Imperial College
London

Novel Ceramic Hollow Fibre Membranes for Fluid Separation and Chemical Reaction

By

Yutie Liu

B.Sc. (Hefei University of Technology, China),
M.Phil. (Dalian Institute of Chemical Physics,
Chinese Academy of Science, China)

A thesis submitted for the degree of Doctor of Philosophy of the University of London,
and for the Diploma of Imperial College London.

Department of Chemical Engineering
Imperial College London
London SW7 2AZ

August 2005

IMPERIAL COLLEGE LONDON

ABSTRACT

Polymeric membranes are in current use for a number of process applications, including filtration, desalination, gas separation and biochemical reactions. Ceramic membranes have been developed for similar applications, especially where harsh (alkaline, acid or organic solvent) feed solution or high temperature operation precludes the use of existing polymeric membranes. However, currently produced ceramic membranes are usually in the form of finite sized tubes with diameters of at least several millimetres or flat discs and consequently have low surface area/volume ratios (typically a maximum of 500 m^2/m^3). These low area/volume ratios compare unfavourably with polymeric hollow fibre modules where area/volume ratios of several thousand are obtainable; this limits the application of current ceramic tubular and disc membranes. This limitation is most evident in a number of application areas such as catalytic membrane reactor/separator where it is desirable to maximise the area of the membrane module to increase the permeation rate to remove the product species from the reaction zone.

This thesis concerns the development of ceramic hollow fibre membranes for reaction/separation. The hollow fibre membranes have been prepared from perovskite materials such as mixed oxygen ion-electron conducting oxide $La_{0.6}Sr_{0.4}Co_{0.8}Fe_{0.2}O_3$ (LSFC) and mixed proton-hole conducting oxide $SrCe_{0.95}Yb_{0.05}O_3$ (SCYb) using a combined phase inversion and sintering method. Emphasis has been placed on the development of the relationships between the conditions of membrane preparation, membrane structure and its performance in oxygen or proton permeation and in the oxidative coupling and non-oxidative coupling reactions of hydrocarbons. The variables examined include the types of starting solutions used, spinning conditions in preparing the ceramic hollow fibre precursors and sintering procedures. The membrane structures have been characterised by its permeation characteristics and its morphology, while performance of the prepared membranes in separation and coupling reactions have been examined under different operating pressures and flow rates.

ACKNOWLEDGEMENTS

First and foremost, I would like to sincerely thank my academic supervisor, Dr. Kang Li for his invaluable guidance, constant support, unbelievable patience, tireless help throughout this thesis. His serious attitude towards academic research and strict requirement will benefit me the rest of my life.

A special thank to Dr. Xiaoyao Tan for his countless help in my experiments, results discussion of this thesis.

I am also thankful to have received a great deal of help and collaboration from Peter Chapman for correcting my English, Dr. Shengfu Zhang, Robert Lian-huey Liu, Michalis Koutinas, Frederico Ferreira and Ludmila G. Peeva on GC analysis.

Many thanks to all the technical and clerical staff in the department for their assistance and help, especially to Mrs June Talbot and Ann Sewell, Miss Laia Santamaria-Ortega and Jacqueline Demontague, Dr. Alcina Mendes for helping on the documental work, Keith Walker and Peter Poggioli in the Stores for helping with material orders, Malcolm Dix and Richard Oxenham in the electronics workshop, Darren Palmer, Richard Wallington and Tony Meredith in the workshop for building my equipments and testing instruments, Nam Ly for computer assistance, and Patricia Carry in the analytical lab.

Thanks for those staff from other departments for their assistance and help, especially to Dr. Mahmoud Andakani for helping with SEM analysis, Mr. Hugh J. MacGillivary for helping on three-point bending test, and Mr. Richard Sweeney, for helping with XRD analysis.

Thank you to all colleagues, Champe Sirichai Koonaphapdeelert, Ram Shpiner, Rogelio Valadez-Blanco, Pedro Silva, Pook Apichat Boontawan Guy Ohandja, Alan Yung-Chih Hu, Just Lin, Lun Zhao, Cherry Chayaporn Roengpithya, Muhammad Dastgir, and Gavin R Daisley, etc. whom I enjoyed working with. You all made my life in London so much more interesting.

I would also like to express my gratitude to my good friends: Mr. Jin Xu and his wife from America, Dr. Jianfeng Kong and his wife Suxia, Liu, Dr. Jianjun Qin and his wife Juan Gu from Singapore, Dr. Jizhong Ren and Dr. Zhansheng Li also from Singapore, Dr. Mayling Yeow, Dr, Alan Thursfield, Dr. Rongsheng Zhang and his wife Yu Gan, Dr. Fan Zhang and his wife Yanhai Cui from UK and Dr. Xuehua Liu from Beijing, as well as my former supervisors and colleagues: Professor Chenzhang Jiang, Professor Yizheng Lin, Mr. Hengshan Zhang, Mrs. Jingbo Fan, Dr. Yiming Cao, and Mr. Huamu Zhou from Dalian, Dr. Geert-henk Koops from Twente, and Dr. Fook Sin Wong from Singapore for their encouragement and support.

I am grateful for the financial support and training that I received from the British Engineering and Physical Science Research Council (EPSRC).

Finally, I would like to thank my wife and daughter, as well as my parents, sister, brothers and all my families for their constant patience, love and encouragement during this study.

TABLE OF CONTENTS

ABSTRACT..... i

ACKNOWLEGEMENTS..... ii

TABLE OF CONTENTS..... iv

LIST OF FIGURES..... viii

LIST OF TABLES..... xii

Chapter 1 Introduction..... 1

1.1 General background..... 1

1.2 Research outline and objectives..... 3

1.3 Thesis organization and presentation..... 4

References..... 5

Chapter 2 Novel mixed conducting ceramic materials, membranes and applications... 6

Abstract..... 6

2.1 Introduction..... 7

2.2 Fundamentals of mixed conducting ceramic materials..... 8

2.2.1 Structure of perovskite-type of materials..... 9

2.2.2 Doping strategies..... 11

2.2.3 Properties of materials..... 12

2.3 Current status of the mixed-conducting membranes..... 13

2.3.1 Oxygen permeable materials and membranes..... 13

2.3.1.1 Perovskite-type oxides..... 14

2.3.1.2 Non-perovskite-type oxides..... 25

2.3.1.3 Summary of oxygen permeable materials..... 26

2.3.2 Proton conducting materials and membranes..... 28

2.3.2.1 Perovskite-type oxides..... 29

2.3.2.2 Non-perovskite-type oxides..... 31

2.3.3 Dual phase membranes..... 32

2.4 Transport of the mixed conducting membranes..... 35

2.4.1 Oxygen transport..... 35

2.4.1.1 Transport mechanism..... 35

2.4.1.2 Transport equations..... 37
2.4.2 Proton transport..... 41
2.4.2.1 Transport mechanism..... 41
2.4.2.2 Transport equations..... 43
2.5 Potential applications in the separations and chemical reactions..... 46
2.5.1 Air separation for oxygen production..... 46
2.5.2 Hydrogen production 48
2.5.3 Partial oxidation of methane for syngas production..... 50
2.5.4 Oxidative coupling of methane for C_2 products..... 52
2.5.5 Non-oxidative coupling of methane for C_2 products..... 54
2.5.6 Other applications..... 56
2.6 Further development-challenges and prospects..... 56
2.7 Conclusions..... 58
Notation..... 59
References..... 61

Chapter 3 Preparation of $SrCe_{0.95}Yb_{0.05}O_{3-\delta}$ hollow fibre membranes: study on sintering processes 83
Abstract..... 83
3.1 Introduction..... 84
3.2 Experimental 86
3.2.1 Materials..... 86
3.2.2 Sintering Processes 86
3.2.3 Characterization using SEM..... 86
3.3 Results and Discussions 87
3.3.1 Investigation of sintering temperature..... 89
3.3.2 Investigation of sintering time..... 93
3.4 Conclusions..... 98
References..... 99

Chapter 4 $SrCe_{0.95}Yb_{0.05}O_{3-\delta}$ hollow fiber membrane and its property in proton conduction 102
Abstract..... 102
4.1 Introduction..... 103

4.2 Experiemntal.....104
4.2.1 Preparation of SCYb hollow fiber membranes..... 104
4.2.2 Characterization methods..... 104
4.2.3 Measurement of hydrogen permeation..... 106
4.3 Theory and model development..... 108
4.3.1 Mechanism of hydrogen permeation..... 108
4.3.2 Transfer equations of charged defects in the SCYb membrane..... 110
4.3.3 SCYb hollow fiber membrane module for proton permeation.....111
4.3.4 Solution method..... 115
4.4 Results and discussion.....116
4.4.1 Characterization of the SCYb hollow fiber membranes.....116
4.4.2 Hydrogen permeation in the hollow fiber membrane module.....120
4.5 Conclusions..... 127
Notations..... 128
References..... 129

Chapter 5 Non-oxidative methane coupling in a $SrCe_{0.95}Yb_{0.05}O_{3-\delta}$ (SCYb) hollow fibre membrane reactor..... 131
Abstract..... 131
5.1 Introduction..... 132
5.2 Experiemntal.....134
5.2.1 Materials.....134
5.2.2 Preparation and characterization of the SCYb hollow fiber membranes 134
5.2.3 SCYb hollow fiber membrane reactor and methane coupling experiment135
5.3 Theory description.....138
5.3.1 Formation and transport of defects in SCYb membrane.....138
5.3.2 Mechanism of methane coupling on SCYb membranes..... 140
5.3.3 Model equations for the SCYb hollow fibre membrane reactor..... 142
5.4 Results and discussion.....145
5.5 Conclusions..... 152
Notations..... 153
References..... 154

Chapter 6 Preparation and characterization of $La_{0.6}Sr_{0.4}Co_{0.2}Fe_{0.8}O_{3-\alpha}$ (LSFC) hollow fibre membranes..... 158
Abstract..... 158
6.1 Introduction..... 159
6.2 Experimental.....161
6.2.1 Materials.....161
6.2.2 Preparation of LSCF hollow membranes..... 162
6.2.3 Oxygen permeation measurement method.....163
6.3 Results and discussion.....165
6.3.1 Morphology of the LSCF hollow fibre membranes..... 165
6.3.2 Sealing at high temperatures..... 169
6.3.3 Oxygen permeation through the hollow fibre membrane.....170
6.4 Conclusions..... 172
References.....173

Chapter 7 Mixed conducting ceramic $La_{0.6}Sr_{0.4}Co_{0.2}Fe_{0.8}O_{3-\alpha}$ (LSCF) hollow fibre membrane for air separation.....175
Abstract..... 175
7.1 Introduction.....176
7.2 Experimental.....178
7.2.1 Gas-tightness of the hollow fibre membranes.....178
7.2.2 Fabrication of the LSCF hollow fibre membrane module.....179
7.2.3 Air separation using the LSCF hollow fibre membrane module.....180
7.3 Theory description.....182
7.3.1 Oxygen permeation rate through a hollow fibre membrane.....182
7.3.2 Models for air separation in a hollow fibre membrane module..... 183
7.4 Results and discussion.....188
7.4.1 Gas-tightness of the hollow fibre membranes.....188
7.4.2 Temperature profile in the membrane module..... 189
7.4.3 Air separation results..... 190
7.5 Conclusions.....196
Notations..... 197
References.....198

Chapter 8 Conclusions and recommendations.....200
8.1 Conclusions.....200
8.2 Future work and recommendations.....203

LIST OF PUBLICATIONS.....205
APPENDIX A Data tables of the experimental results.....206
APPENDIX B Computing programs.....223

LIST OF FIGURES

Fig. 2-1	Different principles for oxygen permeable membrane: (a) solid electrolyte cell (oxygen pump), (b) mixed ionic electronic.	8
Fig. 2-2	Structure of ABO_3, emphasizing the coordination number of the A cation at the body centre.	9
Fig. 2-3	Schematic description of dual phase membranes: (a) Composite membrane, (b) Structure of the composite membrane, (c) General dual phase membrane.	33
Fig. 2-4	Schematic diagram of oxygen migration in membranes.	37
Fig. 2-5	Proton formation in mixed conducting oxides.	42
Fig. 2-6	Proton migration in hopping form in SCYb Oxides.	43
Fig. 2-7	Transport diagram of ion permeation in the SCYb membrane.	43
Fig. 2-8	Thin-film support membrane structure. This pressure resistant structure may be fabricated in a flat plate or tubular configuration (Ref: Dyer et al. 2000).	47
Fig. 3-1	SEM photographs of the cross-sectional structures of SCYb hollow fibre membranes (before sintered: (A) hollow fibre, (B) whole cross section and (C) middle part) and (after sintered: (a) hollow fibre, (b) whole cross section and (c) middle part).	88
Fig. 3-2	SEM photographs of surface morphology of SCYb hollow fibres before and after calcination at different temperatures; (A) before sintering, (B) 600 °C, (C) 800 °C, (D) 1200 °C, (E) 1300 °C, and (F) 1400 °C, Calcination time: 120 minutes.	90
Fig. 3-3	SEM photographs of surface morphology of the SCYb hollow fibre calcined at 1500 and 1600 °C.	91
Fig. 3-4	The Effect of calcination temperatures on shrinkage and weight loss of SCYb hollow fibres.	92
Fig. 3-5	Effect of sintering time on the shrinkage of the SCYb hollow fibres at different temperatures.	93
Fig. 3-6	The effect of calcination time at 800 °C; (A) 30 minutes, (B) 60 minutes, (C) 240 minutes, and (D) 480 minutes.	94
Fig. 3-7	The effect of calcination time at 1300 °C; (A) 30 minutes, (B) 60 minutes, (C) 240 minutes, and (D) 480 minutes.	95

Fig. 3-8	The Effect of calcination time at 1400 ºC, (A) 30 minutes, (B) 60 minutes, (C) 240 minutes, and (D) 480 minutes.	96
Fig. 3-9	The effects of calcination temperature and time on the shrinkage of the SCYb hollow fibres.	97
Fig. 4-1	Diagram of the experimental setup for hydrogen permeation.	106
Fig. 4-2	Schematic mechanism of ion permeation in the SCYb membrane.	108
Fig. 4-3	Flow pattern in the SCYb hollow fibre membrane module (A) Cocurrent flow, (B) Countercurrent flow.	112
Fig. 4-4	Algorithm of the numerical solution.	115
Fig. 4-5	SEM photographs of the SCYb hollow fiber membrane: (a) cross-section of the hollow fiber precursor; (b) wall of the hollow fiber precursor; (c) central sponge layer of the hollow fiber precursor; (d) outer surface of the hollow fiber precursor; (A) cross-section of the sintered fiber; (B) wall of the sintered fiber; (C) central layer of the sintered fiber; (D) outer surface of the sintered hollow fiber.	117
Fig. 4-6	Mechanical strength of the SCYb hollow fibers sintered at different temperatures.	118
Fig. 4-7	XRD patterns of the SCYb powders and hollow fiber membranes. (A) SCYb fibre after permeation (p-perovskite; c-CeO_2; s-$SrCO_3$); (B) SCYb fiber before permeation; (C) SCYb powder.	119
Fig. 4-8	Effect of hydrogen partial pressure in shell feed on the permeation flux at various temperatures (p_{O2}=0.21 atm).	121
Fig. 4-9	Effect of oxygen partial pressure in lumen feed on the permeation flux at various temperatures (p_{H2}=0.142 atm).	122
Fig. 4-10	Hydrogen permeation flux under various membrane thickness (T=850 °C, p_{O2}=0.21 atm).	123
Fig. 4-11	Effect of the water vapor concentration in the air feed on the permeation of proton and oxygen vacancy (T=850 °C, p_{H2}=0.2 atm, p_{O2}=0.21 atm).	124
Fig. 4-12	Permeation flux as a function of the length of SCYb hollow fibre (T=850 °C, p_{H2}=0.2 atm, p_{O2}=0.21 atm).	125

Fig. 4-13	Comparison between the countercurrent and cocurrent flow operations (T=850 °C, p_{H2}=0.2 atm, p_{O2}=0.21 atm).	126
Fig. 5-1	Experimental setup for methane coupling in the SCYb hollow fibre membrane module.	135
Fig. 5-2	Mechanism of methane coupling reaction on the SCYb membrane.	140
Fig. 5-3	Flow pattern in the SCYb hollow fibre membrane reactor.	142
Fig. 5-4	C_2 formation rate against feed concentration at different temperatures (feed flow rate of methane stream = 4.3 cm^3/min, feed flow rate of air stream = 40 cm^3/min) (A), (a)-800°C; (B), (b)-850°C; (C), (c)-900°C; (D), (d)-950°C.	146
Fig. 5-5	Plot of reaction kinetic parameters against the reciprocal of temperature.	147
Fig. 5-6	Effect of temperature on the C_2 formation rate (feed flow rate of methane stream =3.96 cm^3/min, methane feed concentration=9.22%, air feed flow rate=40 cm^3/min).	148
Fig. 5-7	C_3-C_5 formation rates as a function of temperature (feed flow rate of methane stream =4.3 cm^3/min, methane feed concentration=9.22%, air feed flow rate=40 cm^3/min).	149
Fig. 5-8	Effect of methane feed flow rate on the C_2 formation rate (temperature=950 °C, methane feed concentration=9.22%, air feed flow rate=40 cm^3/min).	150
Fig. 5-9	Effect of methane feed flow rate on the formation rate of higher hydrocarbons (temperature=950 °C, methane feed concentration=9.22%, air feed flow rate=40 cm^3/min).	151
Fig. 6-1	Schematic experimental setup for oxygen permeation measurements.	163
Fig. 6-2	SEM micrographs of the LSCF hollow fibe precursor.	165
Fig. 6-3	SEM micrographs of the LSCF hollow fibre sintered at 1100°C.	166
Fig. 6-4	SEM micrographs of the LSCF hollow fibre sintered at 1280°C.	167
Fig. 6-5	XRD patterns of the LSCF powder and of the hollow fibre membrane.	169
Fig. 6-6	Effect of temperature on the oxygen permeation (V_{Ar}=32.4 cm^3/min).	170

Fig. 6-7	Plot of oxygen flux against down stream oxygen partial pressure at different temperatures.	171
Fig. 7-1	Experimental setup for gas-tightness test.	178
Fig. 7-2	Configuration of the LSCF hollow fibre membrane module.	179
Fig. 7-3	Experimental setup for air separation.	181
Fig. 7-4	Operating modes of the membrane module for air separation.	184
Fig. 7-5	Pressure change with time in the gas-tightness test of hollow fibre membranes.	188
Fig. 7-6	Temperature profile in the membrane module.	189
Fig. 7-7	Oxygen permeation rate as a function of the gas flow rate for the shell-feed and cocurrent operating mode (A) Air feed flow rate is constant; (B) Argon feed flow rate is constant (Experimental data: ▲800°C, ■ 850°C, ● 900°C).	190
Fig. 7-8	Comparison between the lumen-feed and shell-feed operations (T_s=850°C).	192
Fig. 7-9	Modeling results for the shell-feed, cocurrent flow operation at different temperatures.	193
Fig. 7-10	Comparison between the countercurrent and cocurrent flow patterns.	194
Fig. 7-11	Oxygen permeation rate against vacuum level (absolute pressure).	195

LIST OF TABLES

Table 2-1	Conductivity and oxygen permeability values of mixed conducting oxides.	21
Table 2-2	TEC values in air and phase transformation temperature of the mixed conducting oxides.	24
Table 2-3	Properties of typical proton conducting materials.	30
Table 2-4	Conductivity and activated energy of some complex perovskite type materials.	31
Table 2-5	Properties of $Ce_{0.8}Yb_{0.2}O_{1.9}$ at H_2O/H_2 atmosphere.	32
Table 2-6	Comparison of cryogenic versus ion transport membrane (ITM) air separation technology in integrated gasification combined cycle (IGCC) power applications (Ref: Stiegel, 2000).	48
Table 2-7	Mixed conducting oxide membrane reactors for oxidation reaction.	51
Table 2-8	Mixed conducting oxide membrane reactors for methane oxidative coupling.	54
Table 2-9	Performance data of proton conducting membranes in methane coupling reaction.	55
Table 4-1	Preparation conditions of the SCYb hollow fibre.	104
Table 4-2	Characteristic parameters of the SCYb hollow fiber membrane and kinetic parameters used for calculations (Condon JB, Schober, 1997, Schober, et al., 1995, Souza, et al., 1997, Uchida, et al., 1989, Guan, et al., 1998).	120
Table 5-1	Parameters for the preparation of the $SrCe_{0.95}Yb_{0.05}O_{3-\delta}$ (SCYb) hollow fibre membranes.	134
Table 5-2	Parameters for the SCYb hollow fiber membrane reactor and operating conditions.	145
Table 5-3	Reaction constants by regression with the experimental data	147
Table 6-1	Fire cements for the assembling of the membrane modules (All from FortaFix Inc).	161
Table 6-2	Preparation conditions of LSFC hollow fibre membranes.	162
Table 6-3	Shrinkage of the LSCF hollow membranes after sintering.	168
Table 7-1	Properties of the hollow fibre membrane module.	180

Chapter 1

Introduction

1.1 General background

In essence, a membrane is a barrier separating two distinct phases that is classically defined as "***a region of discontinuity interposed between two phases***" (Hwang and Kammermeyer, 1975). The membrane may possess a porous or dense structure depending on the manufacturing processes. Membrane separation technology presents many clear advantages over conventional separation technologies (such as filtration, distillation, adsorption, and extraction) in terms of process efficiency, energy efficiency and ease of operation. Majority of the existing industrial membrane applications utilise membranes of polymeric nature.

The development of asymmetric membranes via phase inversion technique in the 1960s (Loeb and Sourirajan, 1963) is the major breakthrough that facilitate the penetration of membrane separation technology into large scale industrial applications. These membranes consist of a very thin layer of dense skin (0.2-0.5 μm) that acts as the active separating layer, while the much thicker porous substrate (50-200 μm) beneath acts as a support and provides the mechanical strength required. This ingenious combination enables permeation flux enhancement without compromising membrane selectivity.

In recent years, alternative ceramic membranes have attracted considerable attention primarily for its greater chemical and thermal tolerances. These attributes enable membrane technology to gain access to applications involving strong chemicals at elevated temperatures, as well as withstanding rigorous cleaning procedure without the fear of structural damage.

Development of a novel ceramic membrane using mixed ionic-electronic conduction material is one of the most actively pursued investigation in ceramic membrane research. Oxygen permeable materials such as yttria-stabilized-zironia (YSZ) and $La_{0.6}Sr_{0.4}Co_{0.8}Fe_{0.2}O_{3-\alpha}$ (LSFC) as well as mixed proton/hole conducting materials

such as $SrCe_{0.95}Yb_{0.05}O_{3-\delta}$ (SCYb) are extensively used due to their great application potential in gas separations and chemical/electrochemical reactions.

With its ability to conduct ions and electrons (or holes), mixed-conducting membranes can operate in a very simple way without the need to attach any electrodes to the oxide surface or external circuitry. Mixed conducting membranes work on a different transport mechanism from the conventional molecule diffusion. For instance, oxygen separation from oxygen containing gases using mixed conducting membranes is obtained via the migration of oxygen ions through the membrane. Dissociated and ionized oxygen emerges on both feed and permeate sides of membrane surfaces whereby the individual oxygen ions part with their electrons and recombine again to form oxygen molecules. In the presence of a dense and gas tight mixed conducting membrane (to prevent the direct passage of oxygen molecules), an extremely pure oxygen stream can be generated. In addition, the high membrane selectivity guarantees mixed conducting membrane a competitive advantage over the present commercial processes such as cryogenics, pressure-swing adsorption and polymeric membranes. Meanwhile, the non-conventional transport mechanism of mixed conducting membrane is desirable in chemical reactions such as coal gasification and light hydrocarbon conversions.

Currently, most research activities in this area use small disc membranes of 1 mm thick with very limited membrane area. Relatively larger membrane area could be obtained by using tubular membranes. This type of membrane, however, has a high transport resistance due to it symmetric structure. To overcome this problem, considerable attempts have been focusing on introducing a layer of highly selective dense membrane coating on top of a porous membrane substrate. Unfortunately, the low membrane area per unit packing volume of disc and tubular membranes render this technology economically unviable. In summary, these are the two major restrictive factors that limit the industrial application of novel ceramic membranes. Hollow fibre membranes, on the other hand, appeared to be a promising alternative offering substantially higher packing capacity per unit volume of 9000 m^2/m^3 as compared to packing capacities of around 30-500 m^2/m^3 offered by the plate-frame and tubular membrane format. The greatest challenge in the preparation of a ceramic hollow fibre membrane lies in overcoming the physical brittleness often associated

with ceramic hollow fibre membrane, especially for high temperature industrial applications.

1.2 Research outline and objectives

The general objective of this research is to develop a novel mixed conducting ceramic hollow fibre membrane for chemical reactions and fluid separations applications. The emphasis of this study is placed on the effects of various preparation parameters on the resulting membrane's structure and the associating performances. Two types of perovskite membranes included in this study are $SrCe_{0.95}Yb_{0.05}O_{3-\delta}$ (SCYb), a proton-hole conducting membrane and $La_{0.6}Sr_{0.4}Co_{0.8}Fe_{0.2}O_{3-\alpha}$ (LSFC), a oxygen ion-electron conducting membrane. The SCYb will be used in studying methane coupling reaction while the LSCF will be used in air separation application.

The specific objectives of this research include:

1. Preparation of dense SCYb hollow fibre membranes with special emphasis on the effect of sintering parameters (including temperature and time) on various membrane properties such as membrane structure, gas tightness and mechanical strength. The aim is to obtain the best sintering programme that produces the flawless dense SCYb hollow fibre membranes.
2. Investigation on the proton conduction properties of the SCYb hollow fibre membranes prepared both experimentally and theoretically using a mathematically model developed.
3. Investigation on the performances of the SCYb hollow fibre membrane reactor designed to perform methane coupling reaction both experimentally and theoretically using a mathematically model developed.
4. Preparation and optimisation of LSCF hollow fibre membranes (as an example of mixed oxygen ion-electron conducting membranes) using the appropriate characterisation techniques.
5. Investigation on the performances of the LSCF hollow fibre membrane in air separation application to produce oxygen. The effects of various operating conditions on the membrane separation performance is studied using a

comprehensive mathematical model developed which takes into consideration both surface exchange reactions and bulk transport factors.

1.3 Thesis organization and presentation

This thesis consists of eight chapters, covering from Introduction and literature review, 5 stand alone chapters focusing on different aspect of the experimental works, i.e. (1) the preparation of SCYb hollow fibre membrane: study on the sintering process, (2) characterization of SCYb hollow fibre membrane in proton conduction and methane coupling reaction, (3) preparation of LSCF hollow fibre membrane and its application in air separation. General conclusions and future work are in Chapter 8.

Chapter 1 offers an introduction to the subject matter with brief description on the research background and thesis outline. An extensive review on the structures and properties of various mixed conducting materials is covered in Chapter 2. This chapter also includes a comprehensive account on the research and development activities within the framework of mixed conducting materials and their potential industrial applications. Chapter 3 focuses on the preparation of mixed conducting SCYb hollow fibre membrane. Here, the major emphasis lies on a well-controlled sintering process that is capable of producing SCYb hollow fibre membranes with improved performance and enhanced mechanical strength. In chapter 4, experimental and theoretical analysis on the proton conduction performance of the SCYb hollow fibre membrane is presented and discussed. The performance of methane coupling reaction using the SCYb hollow fibre membrane reactor is presented in Chapter 5. Here, the effects of temperature, feed concentration and flow rate on the formation of C_2 compounds are discussed. The preparation of a mixed oxygen ion-electron conducting hollow fibre membrane is described in Chapter 6, with particular attention on the preparation conditions that led to a gas tight LSCF hollow fibre membrane. Further experimental and theoretical study on the performance of LSCF hollow fibre membranes in air separation application are extensively discussed in Chapter 7. Chapters 3 to 7 are independent chapters with respective conclusions and references. The general conclusions and recommendations for future work are addressed in Chapter 8. All the relevant experimental data and computing programs for the simulations are compiled in the Appendix section at the end of this thesis.

References

Hwang, S.-T. and K. Kammermeyer (1975). Membrane in Separation, in *Techniques of Chemistry*, **Vol.** VII, John Wiley and Sons, Inc, **p.** 2.

Loeb, S. and S. Sourirajan (1963). Sea Water Demineralization by Means of an Osmotic Membrane, in *Saline Water Conversion–II, Advances in Chemistry*, **Vol.** 28, edited by A. C. Society, Washington, DC, **p.** 117–132.

Chapter 2

Novel mixed conducting ceramic materials, membranes and applications

Abstract

This article presents a review on recent development of mixed conducting ceramic materials, membranes and its potential applications in separations and chemical reactions. A basic knowledge of the materials including their structure, composition and properties is first introduced briefly, followed by a short discussion on the relation between the material structures and properties as well as strategies for new material development and screening. The main part of this review gives an intensive discussion on the progress achieved up to early 2005. Performances of the mixed conducting materials for both oxygen and hydrogen and their function as membranes or membrane reactors are summarized. Some examples in gas/vapour separations and catalytic chemical reactions are presented. Current problems related to the fabrication of the mixed conducting membranes are addressed and future technology challenges are also outlined.

Key words: mixed conducting materials, catalytic ceramic membranes, separation, and reaction.

2.1 Introduction

Research into ionic conducting materials and membranes has been in progress for long time. Initial work was mainly focused on the development of solid oxide fuel cells and sensors (Gopel *et al.*, 1991; Minh and Takahashi, 1995; Dyer *et al.*, 2000; Tuller *et al.*, 2000; Knauth and Tuller, 2002). Interest in membranes prepared from these type of materials for industrial gas separations such as oxygen separation from air and hydrogen separation from hydrogen containing gases, and for chemical reactions such as production of syngas by partial oxidation of methane and production of C_2 hydrocarbons by methane coupling reaction, arose after the 1980s when a number of new materials such as $SrCo_{0.8}Fe_{0.2}O_{3-\delta}$ and $SrCe_{0.95}Yb_{0.05}O_{3-\delta}$ were developed (Iwahara *et al.*, 1981; Teraoka *et al.*, 1985). These new materials show a mixed conducting property as they are not only capable of conducting ions, but also electrons/holes. Similar to conventional ionic conducting materials, these materials also possess a unique separation mechanism, i.e. oxygen or hydrogen is transported through the membranes in a dissociated or ionized form rather than the conventional molecular diffusion. Therefore, an extremely high selectivity (theoretically up to 100%) can be achieved. The electronic conductivity of the mixed conducting materials plays an important role. It acts as an internal short circuit such that the mixed conducting membranes do not need electrodes and an external circuit. If a mixed ionic oxygen and electronic conducting membrane is placed under an oxygen chemical potential gradient, oxygen anions permeate from the high oxygen chemical potential side to the low oxygen chemical potential side while overall charge neutrality is maintained by a counterbalancing flux of electrons. Fig. 2-1 shows schematically the operating principle of the mixed conducting materials and the difference to that of purely ionic conducting materials. Because the external circuit is unnecessary, fabrication and operation of the mixed conducting membranes is much simplified. Thus, significant cost reduction can be expected and so the mixed conducting materials have attracted considerable research interest in recent years.

In the past ten years efforts in efficient utilization of energy and reduction of emissions have indirectly stimulated research in mixed conducting membranes. A number of potential applications of mixed conducting ceramic membranes have been identified. These include high-purity oxygen production and catalytic membrane reactors for

hydrocarbon processing (Bouwmeester and Burggraaf, 1996; Iwahara, 1996; Steele, 1998; Norby, 1999; Bouwmeester, 2003). Significant advances have been achieved through several major initiatives that have brought the technology close to the point of commercial readiness. Currently, research in this area concentrates on:

- Identifying new materials. The required functional properties include ionic and electronic conductivity, catalytic activity and desired reliability,
- Developing cheaper membrane fabrication technologies,
- Developing application processes and analyzing their economic feasibility.

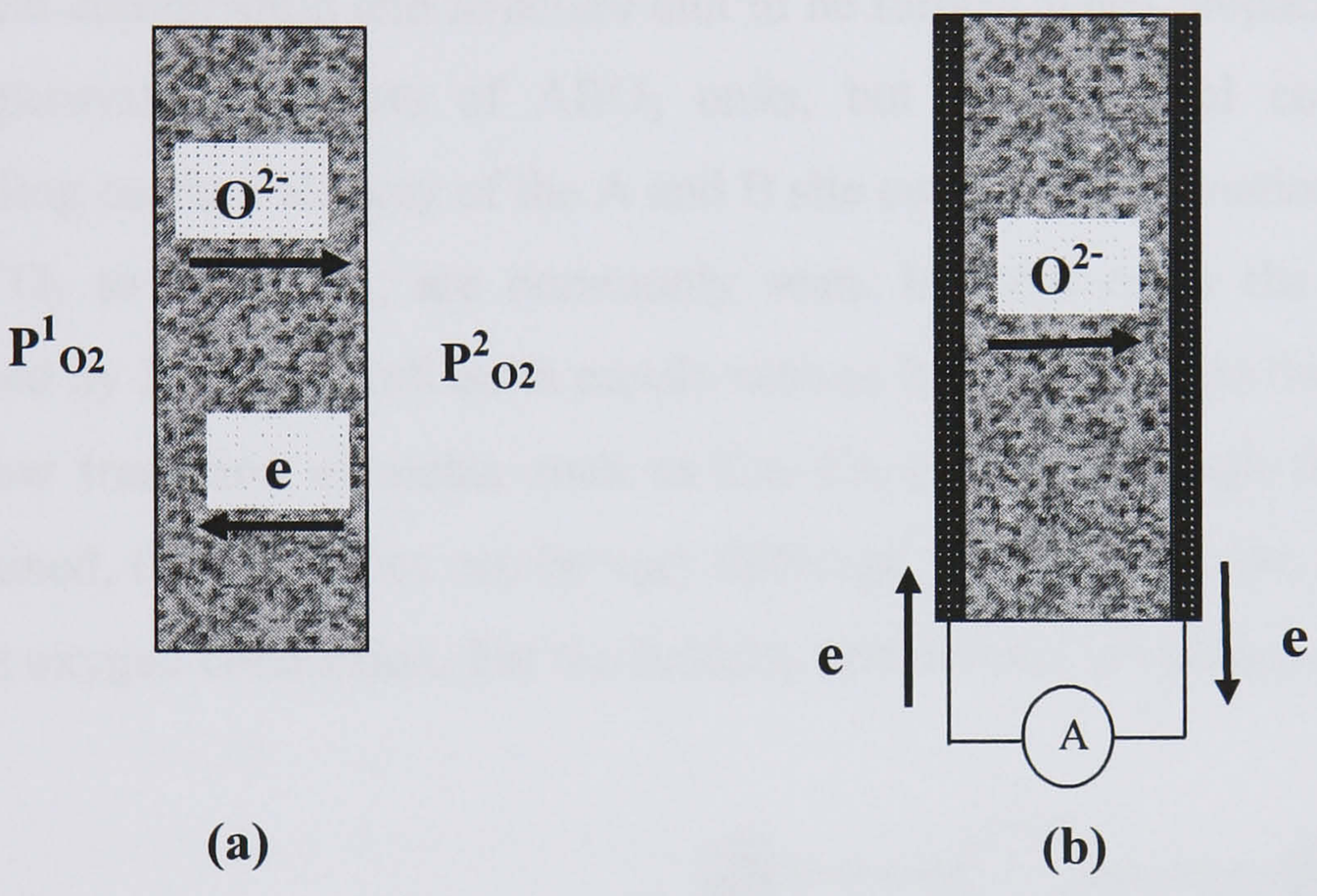


Fig. 2-1 Different principles for oxygen permeable membrane: (a) mixed ionic-electronic conductor. (b) solid electrolyte cell (oxygen pump).

This article presents a review on recent development of mixed conducting ceramic materials, membranes and its potential applications in separations and chemical reactions. It provides a detailed discussion on the progress achieved up to early 2005.

2.2 Fundamentals of mixed conducting ceramic materials

The performance of mixed conducting ceramic membranes is strongly dependant on properties of its materials, which are mainly governed by the material compositions and structures. In order to discuss the relationship between the materials and the membrane performances, basic knowledge and understanding of the composition, structure and property of the materials are required.

2.2.1 Structure of perovskite-type of materials

It has been found that most mixed conducting materials are perovskites which are originally named from a mineral oxide of $CaTiO_3$. The basic structure of this mineral was first thought to be cubic although it was later found to be orthorhombic, the name perovskite has been retained for this type of structure. Such a structure makes the material very stable at high temperatures. A simple cubic structure emphasizing the coordination environment about the A site cation is shown in Fig. 2-2. It can be seen that the A site cation is coordinated to 12 oxygen ions forming a cuboctahedral coordination environment while the B site cation is coordinated to six oxygen ions with an octahedral geometry. This structure provides an indication in consideration of chemical composition and structure unit to be formed when preparing the materials. An ideal perovskite consists of ABO_3 units, but the chemical composition can vary depending on the valencey of the A and B site cations. Combinations such as $A^{1+}B^{5+}O_3$, $A^{2+}B^{4+}O_3$ to $A^{3+}B^{3+}O_3$, are commonly seen. In most cases the A site is generally occupied by 2^+ large alkali earth metals such as Ba, La or Sr and the B site by 4^+ smaller first row transition elements such as Ce, Co or Fe. Although the same structure is maintained, the properties can be very different. For example, the $BaCoO_3$ and $SrCoO_3$ exhibit oxygen conduction, but the $BaCeO_3$ and $SrCeO_3$ are proton conductors.

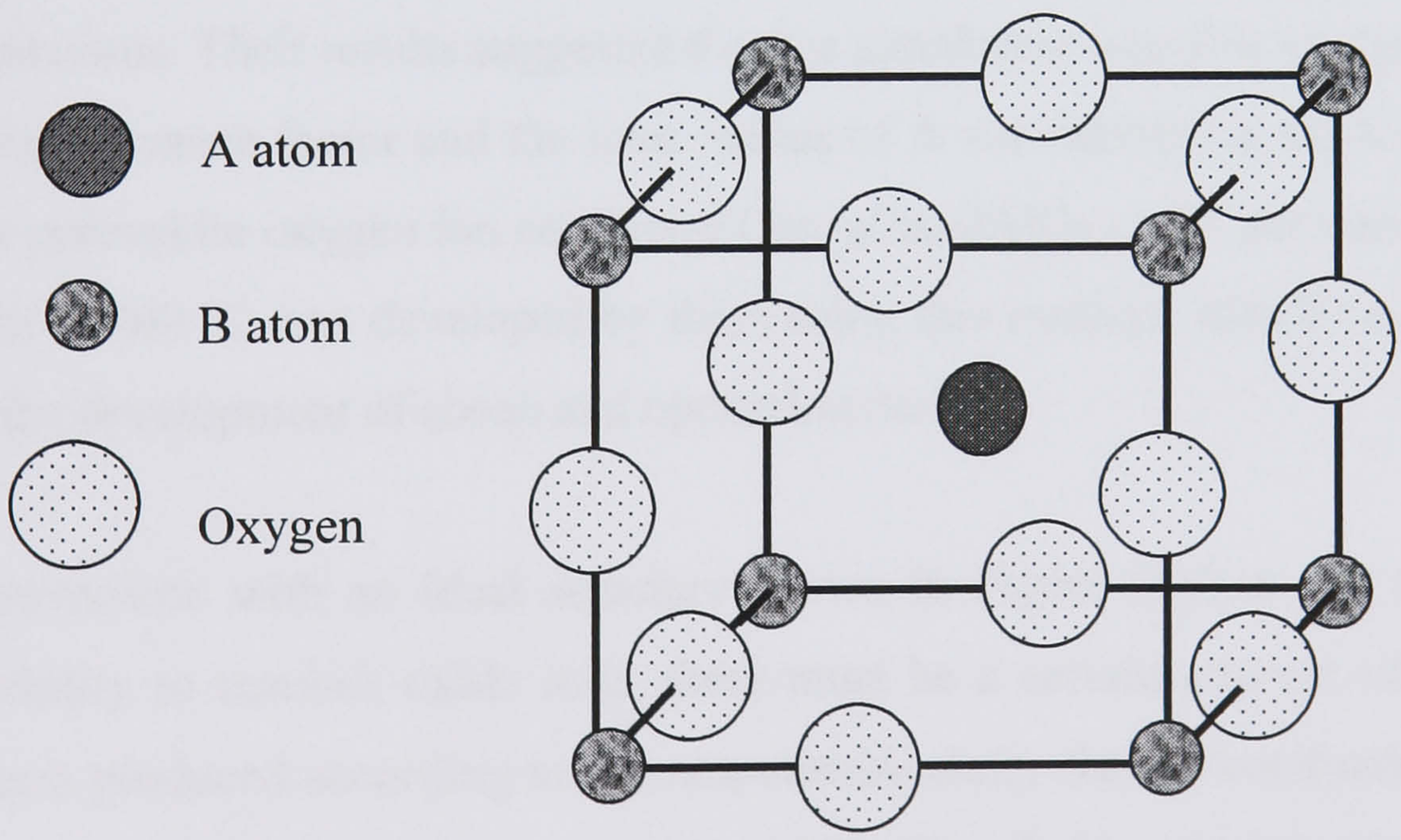


Fig.2-2 Structure of ABO_3, emphasizing the coordination number of the A cation at the body centre.

In a perovskite structure, the A site cation is normally larger than the B site cation because of the different coordination environment. Hayashi *et al.* (1999) examined a correlation between the electrical conductivity and structurally related parameters such as tolerance factor and specific free volume of lattice. The tolerance factor is defined for indicating the deformation from the cubic lattice as:

$$\text{Tolerance factor} = (r_A + r_O)/2^{1/2}(r_B + r_O) \qquad (2\text{-}1)$$

where r_A, r_B and r_O are the ionic radii of the A site cation, B site cation and oxygen. A high conductivity is found to occur in a composition with a large specific free volume and with a tolerance factor of around 0.96. The following two guides were suggested (Hayashi *et al.*, 1999):

(1) A site cation should have a large ionic radii in order to achieve the large free volume;
(2) B site cation should be chosen for adjusting the tolerance factor to around 0.96.

Yamamura *et al.* (2003) studied the effect of the radii of A and B sites cations on the oxygen ion conductivity with La and Nd series of materials using molecular dynamic simulations. Their results suggested that the simulation was able to reproduce the effects of the tolerance factor and the ionic radius of A site cations on the ion conductivity. A new perovskite oxygen ion conductor $(Sm_{0.8}Ca_{0.2})AlO_{2.9}$ with the conductivity of 0.037 S/cm at 800 °C was developed by them using this method, which could be very useful for the development of cheap and optimal materials.

A perovskite with an ideal structure shown in Figure 2 does not show to have the capability to conduct oxide ions, there must be a certain amount of imperfections or defects produced according to the non-stoichiometry for the conduction or diffusion to take place (Gellings and Bouwmeester, 1992; Thursfield and Metcalfe, 2004). The basic concepts of defect chemistry have been adapted to describe the conduction properties of mixed conducting ceramic materials. Kroger and Vink (1964) first employed notations to describe the defect chemical reactions. For example, the oxide ZrO_2 doped with Y_2O_3 to create mobile oxygen vacancies is described in terms of defect chemical notation as $Y_2O_3(ZrO_2) \rightarrow 2Y'_{Zr} + V^{\bullet\bullet}_O + 3O_O$ (Knauth and Tuller, 2002). The subscript usually

shows the site of the defect in the Kroger-Vink notations, the effective defect charge is written as a superscript by a dot ($^{\bullet}$) for a positive excess charge, and by a prime ($'$) for a negative excess charge, and the vacancy is written as V. Ion defects may take the form of vacancies (vacant lattice sites), interstitial ions (placed at normally unoccupied sites), impurities or dopants with charges different from those expected from the overall stoichiometry. Electron defects may arise in the form of ions present with charges deviating from the normal lattice ions, as well as a consequence of the transition of electrons from normally filled energy levels to normally empty levels. In those cases where the electron is missing, i.e. when there is an electron deficiency, this is usually called a hole (or electron hole). The vacancies and electron holes could be considered the point defects where the ions and electrons move. As a mixed ion and electron conductor, its overall conductivity performance arises from contributions from both ionic and electronic defects.

2.2.2 Doping strategies

Doping is a principal method to tailor the physical properties of the mixed conducting materials through formation of non-integral stoichiometry phases or solid solutions by homogeneous doping with appropriate elements (Galasso, 1969). The early and most successful example is ZrO_2 doped with various rare-earth oxides (Knauth and Tuller, 2002), which was previously thought as a preliminary doping strategy. Fluorite-type structural ZrO_2 can form an extended solid solution with oxides of lower-valence cations such as CaO, Y_2O_3, and other rare-earth oxides. Doping with Y_2O_3 creates mobile oxygen vacancies and stabilizes the structure of ZrO_2, and the tetragonal-monoclinic phase transition can be avoided at high-temperature (so-called stabilized ZrO_2).

For the perovskite-structured oxides ABO_3, it is often seen that a lower valence dopant B′ is introduced on the B site to produce $AB_{1-x}B'_xO_{3-\delta}$ and thus form defects (Kharton *et al.*, 1998a). The symbol δ expresses the amount of the vacancies (defects). Ion vacancies provide the pathway for ions. A wide range of compounds with the perovskite structure can also be produced with substitutions occurring for either the A atom, the B atom or both to form a structure of $A_xA'_{1-x}B_yB'_{1-y}O_{3-\delta}$ (Teraoka *et al.*, 1985). In addition to the ABO_3 perovskites, Nowick and Du (1995) introduced two other perovskite-type oxides, $A_2(B'B'')O_6$, where B′ and B″ are 3+ and 5+, and $A_3(B'B'')O_9$, where B′ and B″

are 2+ and 5+. Vacancies can also be produced by changing the B′/B″ ratio. These materials also showed very good mixed conductivity (Norwick and Vaysleyb, 1997). Having so many possible alternatives, the proper selection of effective doping strategies would be essential.

2.2.3 Properties of materials

The conducting property of mixed conducting materials is usually expressed by conductivity for both ions and electrons. The total conductivity of a mixed-conducting material can be given as the sum of the ionic conductivity and electronic conductivity:

$$\sigma_{total} = \sigma_{ion} + \sigma_e \tag{2-2}$$

The total and ionic conductivities can be measured directly using the conventional four-probe method and the electron-blocking four-probe method, respectively (Ma *et al.*, 1996). The electronic conductivity can, thus, be obtained by subtracting the ionic conductivity from the total conductivity. A useful concept of transport (or transference) number t_k is more frequently used to describe the property of the mixed-conducting materials in practice. For any carrier k, t_k is defined by:

$$t_k = \sigma_k/\sigma_{total} \tag{2-3}$$

In the case of mixed conduction,

$$\sigma_{total} = \sigma_{ion} + \sigma_e = \sigma_{total}\,(t_{ion} + t_e) \tag{2-4}$$

where t_{ion} and t_e represent the transport numbers of ionic and electronic defects respectively. t_{ion} plus t_e always equals unity to retain electron neutrality. The t_{ion} and t_e should be as close as possible at the same time for a good mixed conducting material. For an ideal mixed conducting material, t_{ion} and t_e should both be equal to 0.5. Normally, t_e is much smaller than t_{ion} in most mixed conducting materials. When the t_e is too low, an external circuit may be needed to assist electronic conduction so that the ions' transport can take place. The increase in both t_e and t_{ion} values can be obtained by doping with appropriate elements, which has been one of the frequently used strategies in the development of good mixed conducting materials.

Some mixed conducting oxides show interesting chemical properties including catalytic activity for oxidative reactions (McCarty and Wise, 1990; Gellings and Bouwmeester, 1992) and it is normally dependant on the nature of the B-site cation. The A-site cations strongly affect the mobility of the oxygen ion in the bulk phase (Lin and Zheng, 1996). Membrane reactors prepared from such materials can simultaneously be used as membranes for separation of oxygen from air and catalysts for oxidation processes. As a result, additional catalysts are no longer required (Zeng *et al.*, 1998; Lu *et al.*, 2000b). However, for mixed conducting materials without catalytic activities, but with high oxygen permeability, they can also be used for fabricating membrane reactors but additional catalysts would be required (Balachandran *et al.*, 1997; Jin *et al.*, 2000a; Jin *et al.*, 2000b; Maiya *et al.*, 2000; Shao *et al.*, 2001a; Shao *et al.*, 2001b).

2.3 Current status in mixed-conducting membranes

Mixed conducting materials is categorized into two types based on their different ion-transport properties, one exhibits mixed oxygen ionic and electronic conducting property, and the other exhibits mixed proton and electron/hole conduction. Most research work has been focused on the oxygen conducting materials, but the mixed proton electron/hole conducting materials have also attracted much interest in the recent years. The recent progress in the development of both oxygen permeable and hydrogen permeable materials and membranes is outlined in the following sections.

2.3.1 Oxygen permeable materials and its membranes

Oxygen permeable dense membranes with high ionic and electronic conductivities were first reported by Teraoka *et al.*(1985). A perovskite-type of oxide, $LaMO_3$ with Co and/or Fe on the M-site was doped partially with Sr^{2+} on the La site, yielding a solid oxide solution with the general formula of $La_{1-x}Sr_xCo_{1-y}Fe_yO_{3-\delta}$. This material exhibited that the oxygen permeation flux is two to four orders of magnitude higher than those of stabilized zirconia, and attracted considerable attention. The highest oxygen permeation rate was observed as 2.3×10^{-6} mol/cm^2.s at 850 °C and 1 atm oxygen pressure difference using a 1.0 mm thick disk membrane prepared from $SrCo_{0.8}Fe_{0.2}O_{3-\delta}$ (Teraoka *et al.*, 1985). This permeation result is only slightly smaller than those found in meso-porous membranes ($1\text{-}3\times10^{-5}$ mol/cm^2.s) with 5 μm thickness and 3 nm pores, but bigger than

those observed from microporous membranes (1-0.1×10^{-6} mol/cm^2.s) with 50 nm thickness and 0.5-1.0 nm pores (Bouwmeester and Burggraaf, 1996; Lin, 2001). It was noted by Steele (Steele, 1998) that an oxygen permeation flux higher than 1 cm^3/cm^2.min (7.4×10^{-7} mol/cm^2.s) is always required for a process to be economical, and usually a flux around 3.5 cm^3/cm^2.min (2.6×10^{-6} mol/cm^2.s) is favourable for most technological applications. Materials that meet this target must be chemically and thermodynamically stable as well.

So far, many oxygen ionic and electronic conducting materials have been developed and studied for their transport properties, chemical and thermal stabilities, and performances in some potential applications by a number of researchers (Kharton *et al.*, 1997a; Kharton *et al.*, 1997b; Ishihara *et al.*, 1998; Kharton *et al.*, 1998a; Kharton *et al.*, 1999a; Kharton *et al.*, 1999b; Li *et al.*, 1999; Xu and Thomson, 1999; Kharton *et al.*, 2000b; Kharton *et al.*, 2000d; Luyten *et al.*, 2000; Shao *et al.*, 2000a; Shao *et al.*, 2000b; Shao *et al.*, 2001c; Tong *et al.*, 2002b; Tong *et al.*, 2002c; Tong *et al.*, 2003; Akin and Lin, 2004). Most of the materials are of a perovskite structure including several important families of $Sr(Co,Fe)O_3$, $La(Co,Fe)O_3$ and $LaGaO_3$, etc, some is of non-perovskite structures. Increasing ion conductivity and/or electron conductivity and improving the stability of the materials are the two major tasks in current development of the materials and membranes (Ma and Balachandran, 1998; Ma *et al.*, 1998b; Mitchell *et al.*, 2002; Wachsman and Clites, 2002; Tong *et al.*, 2003; Wang *et al.*, 2003). Recent progress shows the following few types of materials are very promising.

2.3.1.1 Pervoskite-type oxides

$Sr(Co,Fe)O_{3-\delta}$ (SCFO)

A typical perovskite oxide that has been extensively studied is the $SrCoO_3$ or $SrFeO_3$ based materials. They are exceptional among other perovskite-type of oxides due to their high oxygen permeation rate, the maximum value was up to 3.1 cm^3/cm^2.min (2.3×10^{-6} mol/cm^2.s) at 850 °C (Teraoka *et al.*, 1985). It was found that the properties of these materials are very dependent on the chemical compositions and are able to be changed substantially when Sr or Co(Fe) is partially substituted using other metal ions with different valence by different doping strategies. The doping cation and its

concentration remarkably affect the performance of the oxides including the total electrical conductivity, ionic transference number and phase stability.

Cation deficiency in sublattice B of the SCFOs has a lower influence on oxygen permeability in comparison with that in sublattice A. Both oxygen permeability and ionic conductivity of oxides reduce while decreasing the mean radius of the cations in the sublattice A. For example, in solid solutions $Sr_{0.7}M_{0.3}CoO_{3-\delta}$ (M=La, Nd, Sm, Gd), the sequence by which they reduce is La>Nd>Sm>Gd (Kovalevsky *et al.*, 1998). Li *et al* (Li *et al.*, 1998) studied the effect of the partial substitution of Sr with Bi on the oxygen permeation flux through $Sr_{1-x}Bi_xFeO_3$ oxides (without cobalt). It was found that the permeability increases with increasing Bi content.

The oxygen permeability of SCFOs depends not only on their ionic and electronic conductivity, but also on rate of oxygen exchange between the oxides and gas phase (Qiu *et al.*, 1995; Lee *et al.*, 1997a; Lee *et al.*, 1997b; Kovalevsky *et al.*, 1998). Accordingly, some type of surface modification of the oxides such as acid treatment could greatly improve the oxygen permeability (Liu *et al.*, 2000). Miura et. al (Miura *et al.*, 1995) attributed this result to the removal of some impurities such as SrO by the acid treatment. Since the surface exchange rates and oxygen ionic conductivity increases and decreases, respectively with the increase of the oxygen pressure in SCFOs, the bulk oxygen permeation becomes the permeation-determining factor at high oxygen pressures (Kharton *et al.*, 1999b).

However, SCFO perovskites are usually regarded to be thermodynamically and structurally unstable at lower temperatures and a low partial pressure of oxygen, especially in reducing environments owing to the presence of alkaline-earth metal cations. The stability of the materials must be paid considerable attention during the development of the new materials and modification of current available materials.

The oxygen conductivity of Ti-containing $SrFeO_3$ was studied by Kharton *et al*. (2000a; 2000c), because it was thought that the phase stability of the material could be improved by Ti. It was found that the ion transference numbers of the oxide in air vary from 0.005 to 0.08, increasing with temperature. Since the oxygen permeation through the oxide membranes is limited by both bulk ionic conductivity and surface exchange rates,

depositing porous layers of the same material or a mixture of platinum and praseodymium oxide onto the membrane feed-side surface leads to a significant increase in the oxygen permeability (Kharton *et al.*, 2000a; Kharton *et al.*, 2000c). The oxide is stable at temperatures above 770 K with respect to CO_2 but unstable at lower temperatures with the surface decomposition of the perovskite, associated with the formation of strontium carbonate. The average thermal expansion coefficient of strontium ferrite-titanate is $(27.0\pm0.4) \times 10^{-6}K^{-1}$ at 780-1040 K. (Kharton *et al.*, 2000a).

The effect of partial substitution of Co(Fe) with various metal cations such as Cr, Cu, Mn, Ni, Ti etc. were studied by several researchers (Kharton *et al.*, 1996; Kharton *et al.*, 1997b; Jurado *et al.*, 1999; Kharton *et al.*, 2000c; Shao *et al.*, 2000b; Shao *et al.*, 2001c). It was found that the introduction of moderate amounts of higher valence cations such as Ti or Cr into the Co or Fe sublattice might decrease the electron conductivity and thus oxygen permeability, but improve the structural stability (Kharton *et al.*, 2000c). In addition, the stability of these perovskites in CO_2-containing atmospheres can be improved by creation of a moderate cation deficiency in the Sr sublattice although the conductivity also decreases (Jurado *et al.*, 1999; Kharton *et al.*, 2000c).

Shao *et al* (2000b; 2001b) studied the effect of barium, Ba in doping $SrCo_{0.8}Fe_{0.2}O_{3-\delta}$. The partial substitution of Sr with barium ions of a larger radius forms a perovskite oxide in the form of $Ba_{1-x}Sr_xCo_{0.8}Fe_{0.2}O_{3-\delta}$. It was found that the phase stability is greatly improved by the introduction of barium into $SrCo_{0.8}Fe_{0.2}O_{3-\delta}$ while the conductivity is not decreased. The highest oxygen permeation rate is up to 1.19 cm^3/cm^2 min for a 1.5 mm thickness membrane at 850 °C. The suitable Ba doping content was in the range of x=0.3-0.5 and 0.3 was found to be the optimum value. A long-term oxygen permeation study of more than 1000 h at 850 °C indicated that only a very slow decay of the performance for $Ba_{0.5}Sr_{0.5}Co_{0.8}Fe_{0.2}O_{3-\delta}$ occurred due to the surface segregation and bulk phase decomposition (Shao *et al.*, 2000b). Recently, Wang *et al.* (2003) applied a $Ba_{0.5}Sr_{0.5}Co_{0.8}Fe_{0.2}O_{3-\delta}$ tubular membrane reactor packed with LiLaNiO/γ-Al_2O_3 catalyst in partial oxidation of methane to syngas. Their results proved to be very promising with a 94% methane conversion and higher than 95% CO selectivity achieved by operating steadily in pure methane for 500 hours. However, more than 500 hours operating in a syngas atmosphere was not performed. In order to improve the

stability of $Ba_{0.5}Sr_{0.5}Co_{0.8}Fe_{0.2}O_{3-\delta}$, the strontium ions in the A site of SCFO can be completely substituted with the same valence state but larger radius size barium ions and stable higher valence state titanium ions to form an oxide of $BaTi_{0.2}Co_{0.5}Fe_{0.3}O_{3-\delta}$. Its oxygen permeability could also be kept at a relative high level, about 0.9 cm^3/cm^2.min at 950 °C (Tong *et al.*, 2002c; Tong *et al.*, 2003). They also studied novel zirconium-doped materials of $BaCo_{0.4}Fe_{0.6-x}Zr_xO_{3-\delta}$ (x = 0-0.4) (Tong *et al.*, 2002c). $BaCo_{0.4}Fe_{0.4}Zr_{0.2}O_{3-\delta}$ shows a high oxygen permeation rate of 0.9 cm^3/cm^2.min and a long-term stable operation at 800 °C.

La(Co,Fe)$O_{3-\delta}$ (LCFO)

La(Co,Fe)$O_{3-\delta}$ based ceramics are another type of mixed conducting oxides, which exhibits significant oxygen ionic conductivity with prevailing electronic conduction (Kharton *et al.*, 1995; Kharton *et al.*, 1996; Stevenson *et al.*, 1996; Chen *et al.*, 1997a; Kharton *et al.*, 2000b). Its total electrical conductivity may attain a value up to 1000 S cm^{-1} (Aasland *et al.*, 2000). Although the oxygen permeability is much less than that of Sr(Co, Fe)$O_{3-\delta}$ based oxides, some problems suffered in the most perovskites derived from Sr(Co, Fe)$O_{3-\delta}$ is minimized in La(Co,Fe)$O_{3-\delta}$ based ceramics.

In La(Co, Fe)$O_{3-\delta}$ oxides, La can be partially substituted with M^{2+} metal cations (M=Sr, Ba, Ca). The substituted metal cations for Co in $LaCoO_{3-\delta}$ include Ga, Cr, Fe, Pb or Ni and so on. The partial substitution of B-site Co with different metal cations was studied in details by Kharton *et al.* (1998a; 1998b; 1999a; 2000b; 2000d) who found that the oxygen permeation fluxes, electrical conductivity and thermal expansion of $LaCo_{1-x}Cr_xO_3$ (x=0.1–0.4) solid solutions all decrease with increasing chromium concentration. The surface-exchange is the rate-limiting step of the oxygen transport. Their study (Kharton *et al.*, 1998a) further showed that introduction of nickel into the cobalt sublattice of $LaCo_{1-x}Ni_xO_3$ was found to result in a sharp decrease of the oxygen ionic conductivity which was the flux-limiting factor. However, the electronic conductivity of the solid solutions increases with nickel content. The substitution of cobalt with either chromium or nickel led to decrease in thermal expansion, while the substitution of Co(Fe) with titanium in the oxides led to increase in thermal expansion as well as oxygen ionic and electronic conductivities.

The cobalt may also be substituted simultaneously with both Ni and Fe cations with the formation of a rhombohedrally-distorted perovskite structure (Kharton *et al.*, 1998a; Kharton *et al.*, 1998b). In the $LaCo_{1-x-y}Fe_xNi_yO_3$ (x=0.1–0.2; y=0.1–0.3) oxide system, the introduction of nickel into the perovskite lattice leads to increasing oxygen non-stoichiometry and electrical conductivity and decreasing thermal expansion, but the effect of doping by iron is the opposite. Oxygen permeation through $LaFe_{1-x}Ni_xO_{3-\delta}$ membranes was found to increase with nickel content due to increasing oxygen vacancy concentration and bulk ionic conductivity, which are the permeation flux-limiting factors (Kharton *et al.*, 1999a). For solid solutions with equal concentrations of nickel and iron, oxygen permeation is limited predominantly by the bulk ionic conductivity. Further substitution of cobalt with nickel results in a sharp increase in the permeation flux due to increasing oxygen non-stoichiometry which is accompanied by an occurrence of the surface exchange limitations of oxygen transport (Kharton *et al.*, 1998a; Kharton *et al.*, 1998b).

For the substitution of A-site La, strontium was found the best candidate. The oxygen permeation in $La_{0.3}Sr_{0.7}CoO_{3-\delta}$ is predominantly controlled by bulk diffusion across the membrane with the range of thickness 0.57- 2.15 mm, and the characteristic thickness, which determines the transition from predominant control by diffusion to that by surface exchange, is extrapolated to be about 80 μm (Chen *et al.*, 1997a).

The partial substitution of La with Pb was also studied by Kharton *et al.* (1998c) who found that the catalytic and electrochemical activities of the ceramic were enhanced remarkably. Furthermore, a higher degree of stability was observed in lead-substituted perovskites in relation to poisoning by sulphur dioxide, compared with strontium-substituted ones. In the oxide system of $La_{1-x}\ Pb_xFeO_{3-\delta}$ (x=0.1–0.3), electrical conductivity and oxygen permeation fluxes increase with increasing x, but both the oxygen permeability and conductivity values of the oxides are considerably less than those of $La_{1-x}Sr_xFeO_{3-\delta}$. Permeation fluxes through $La_{1-x}\ Pb_xFeO_{3-\delta}$ were limited by the bulk ionic conductivity.

It was found that the double-site-substitution perovskite oxides in the form of $La_{1-x}Sr_xCo_{1-y}Fe_yO_{3-\delta}$ (LSCF) give high oxygen permeability and also possess good stability

under air atmosphere, thus they were recognized as a very promising material for air separation (Teraoka *et al.*, 1985; Bouwmeester *et al.*, 1994; Tai *et al.*, 1995; Xu and Thomson, 1998). Armstrong *et al.* (Armstrong *et al.*, 2001) also studied the properties of $LaSr_3Fe_{3-x}Co_xO_{10}$ oxides, the total conductivity increases with increasing Co content. However, above a transition temperature $T>T_t\approx400°C$, the conductivity decreases with increasing temperature due to the loss of oxygen vacancy (Armstrong *et al.*, 2001). The oxygen permeation flux across the oxide membranes at high temperatures $800°C\leq T\leq950°C$ increases with increasing Co content and the flux values are approximately one order of magnitude lower than that of perovskite $SrFe_{0.2}Co_{0.8}O_{3-\delta}$, but exhibits better crystal structural stability in low oxygen partial pressures and at high temperatures compared to the latter. Xu and Thomson (1998) found that $La_{0.6}Sr_{0.4}Co_{0.2}Fe_{0.8}O_{3-\delta}$ is very stable under air/nitrogen gradients at a temperature up to 960°C. Its phase transition temperature is around 825°C (Zeng *et al.*, 1998). In other work (Li *et al.*, 1999; Li *et al.*, 2000), the LSCF showed a slight decline in oxygen permeation after long-term operation over 1100h. Another composite of $La_{0.2}Sr_{0.8}Co_{0.2}Fe_{0.8}O_{3-\delta}$ perovskite oxide was studied by Li *et al.* (2000).

The cubic perovskite $La_{0.2}Sr_{0.8}Cu_{0.4}Co_{0.6}O_{3-x}$ also has high electronic and ionic conductivities at high temperatures. The electronic conductivity increases with increasing temperature initially but then decreases due to the loss of oxygen atoms from the structure. The oxygen permeability is comparable to the values reported for other cobalt containing perovskite oxides with high strontium contents. The temperature of phase transformation from the disordered cubic perovskite to an ordered structure related to Brownmillerite is 975°C under an oxygen partial pressure of 0.01 atm (Kim *et al.*, 1997).

$LaGaO_3$(LGO)

$LaGaO_3$ based oxides exhibit lower relative electronic conductivity but a higher ionic conductivity (Kharton *et al.*, 2000d) and thus attracted much attention in solid oxide fuel cells. The concept of substitution of cobalt by gallium is assumed to increase the ionic character of the B-O bonds in the ABO_3 perovskite lattice. This can increase the stability of $LaCoO_3$ in a reducing atmosphere but would decrease the electronic conductivity (Kharton *et al.*, 1997a). $LaGaO_3$ also shows a relatively low thermal

expansion coefficient (TEC) and a large electrolyte domain (Ishihara *et al.*, 2000). Kharton *et al.* (2000d) investigated the effects of different cation dopants (Ti, Cr, Fe, Co, Ni) and the dopant concentrations on the physico–chemical and transport properties of $LaGaO_3$ based materials. Oxygen-ion transference numbers vary from 2×10^{-6} to 0.98 throughout the series and p-type electronic conductivity increases with increasing transition metal content. Substitution of Ga with higher valence cations (Ti, Cr) decreases ionic conductivity whereas small amounts of Fe or Co (~5%) increase ionic conductivity. The $LaGa_{1-x}Ni_xO_{3-\delta}$ (x = 0.2–0.5) perovskites have significant oxygen permeation fluxes as well as thermal expansion coefficients (Kharton *et al.*, 1999c).

Ishihara *et al.* (1994) studied doping of $LaGaO_3$ with Sr for La site and Mg for Ga site and found that the electrical conductivity increases with the level of Sr-doping and reaches a maximum value at x=0.1. The electrical conductivity of $La_{0.9}Sr_{0.1}GaO_3$ increases with partial substitution of Mg, Al or In for Ga, with Mg (concentration 0.2 mol) producing the largest increase in the conductivity (Ishihara *et al.*, 1994). As a result, $La_{0.8}Sr_{0.2}Ga_{0.83}Mg_{0.17}O_{2.815}$ (LSGM) is the optimum composition exhibiting a stable ionic conductivity (Huang *et al.*, 1998). The high oxide ionic conductivity in LSGM results from the high mobility of oxygen vacancies in addition to the high concentration of oxygen vacancies. Meanwhile, the oxygen diffusion coefficient was found to be higher than the surface exchange coefficient in LSGM (Ishihara *et al.*, 1998). However, LSGM is a pure ionic conductor that barely possesses electronic conductivity. By further doping with other cations, it can become a mixed conductor. Ullmann *et al* (Ullmann and Trofimenko, 1999; Ullmann *et al.*, 1999) studied the perovskite-type oxides $La_{1-x}A_xM_{1-y}B_yO_{3-\delta}$ with A=Sr^{2+}, Ln^{3+}, Ce^{4+}, M=Fe, Co, Ga and B=Co, Fe, Mg in the concentration range of x=0.1–1 mol and y=0.1–0.5 mol. The electrical conductivity of the LSGM could be increased by doping Co or Fe. Increasing Co or Fe doping concentrations leads to the increased p-type conductivity. By applying higher Co or Fe doping concentrations the oxide becomes a mixed conductor.

The characteristic values of above three types of perovskite and related oxides are summarized in Table 2-1 and Table 2-2.

Table 2-1 Conductivity and oxygen permeability values of mixed conducting oxides.

Composition [film thickness]	**Conductivity (800-1000°C) σ, S·cm^{-1}**	**Transference number t_{ion}**	**Permeation flux (800-1000°C) J, mol·cm^{-2}·s^{-1}**	**Ref**
$SrCo_{0.33}Fe_{0.67}O_{3-\delta}$ [1.5 mm]	~100	0.012	(0.89~2.06) ×10^{-6}	(Aasland *et al.*, 2000)
$SrCo_{0.8}Fe_{0.2}O_{3-\delta}$ [1.5 mm]	~100		(4.3~9.3) ×10^{-7}	(Lee *et al.*, 1997b)
$Sr_{0.7}M_{0.3}CoO_{3-\delta}$ (M=La,Nd,Sm,Gd) [1.4 mm]			(2.6~0.41)×10^{-7} ↓ at 1153 K	(Kharton *et al.*, 1999c)
$Sr_{1-x}La_xCoO_{3-\delta}$ (x=0.3-0.35) [1.4 mm]			(2.8~1.7)×10^{-7} ↓	
$Sr_{0.97}Fe_{0.8}Ti_{0.2}O_{3-\delta}$ [1.0 mm]	10~31.6	0.0044-0.012	(0.66~3.98)×10^{-7}	(Kharton *et al.*, 2000a; Kharton *et al.*, 2000)
$Sr_{0.97}Fe_{0.4}Ti_{0.6}O_{3-\delta}$ [1.0 mm]	~1	0.009-0.041	(0.25~1.12)×10^{-7}	
$SrCo_{0.8}Ti_{0.2}O_{3-\delta}$	63.1~100			
$Ba_{0.5}Sr_{0.5}Co_{0.8}Fe_{0.2}O_{3-\delta}$ [1.5 mm]			(0.67~1.15)×10^{-7}	(Shao *et al.*, 2000b)
$BaBi_xCo_{0.2}Fe_{0.8-x}O_{3-\delta}$ (x=0.1~0.5) [1.5 mm]			(2.23~7.44)×10^{-7}	(Shao *et al.*, 2000a)
$LaCo(M)O_{3-\delta}$ [1.0 mm]	~800		_1.86×10^{-7}	(Kharton *et al.*, 2000b)
$LaCo_{0.9}Cr_{0.1}O_{3-\delta}$ [1.4 mm]	400~500		(0.4~0.8)×10^{-7}	(Kharton *et al.*, 1998a)
$LaCo_{0.8}Cr_{0.2}O_{3-\delta}$ [1.4 mm]	~355			
$LaCo_{0.7}Cr_{0.3}O_{3-\delta}$ [1.4 mm]	316~355			
$LaCo_{0.6}Cr_{0.4}O_{3-\delta}$ [1.4 mm]	158~200			
$LaCo_{0.9}Ni_{0.1}O_{3-\delta}$	~1000			

$LaCo_{0.7}Ni_{0.3}O_{3-\delta}$ [1.0 mm]	630~794		$(0.4\sim1.2)\times10^{-7}$	
$LaFe_{1-x}Ni_xO_{3-\delta}$ (x=0.2-0.5) [1.0 mm]	50~316		$(0.43\sim8.6)\times10^{-8}$	(Kharton *et al.*, 1999a)
$LaCo_{0.8}Fe_{0.1}Ni_{0.1}O_{3-\delta}$ [1.0 mm]	630~660		$(0.46\sim1.08)\times10^{-9}$	(Kharton *et al.*, 1998b)
$LaCo_{0.7}Fe_{0.1}Ni_{0.2}O_{3-\delta}$ [1.0 mm]	760~800		$(1.68\sim3.20)\times10^{-9}$	
$LaCo_{0.6}Fe_{0.2}Ni_{0.2}O_{3-\delta}$ [1.0 mm]	530~580		$(0.27\sim1.17)\times10^{-9}$	
$LaCo_{0.5}Fe_{0.2}Ni_{0.3}O_{3-\delta}$ [1.0 mm]	470~500		$(1.57\sim3.11)\times10^{-9}$	
$La_{0.2}Sr_{0.8}CoO_{3-\delta}$ [0.5 mm]			6.44×10^{-7}	(Zeng *et al.*, 1998)
$La_{0.9}Pb_{0.1}FeO_{3-\delta}$ [1.0 mm]	0.5~0.8		$(1.0\sim2.0)\times10^{-8}$ at 1000°C	(Kharton *et al.*, 1998c)
$La_{0.8}Pb_{0.2}FeO_{3-\delta}$ [1.0 mm]	2.5~4.0			
$La_{0.7}Pb_{0.3}FeO_{3-\delta}$ [1.0 mm]	3.5~5.0			
$La_{0.6}Pb_{0.4}FeO_{3-\delta}$ [1.0 mm]	~17			
$La_{0.6}Sr_{0.4}Co_{0.2}Fe_{0.8}O_{3-\delta}$	252	0.0009	$(0.3\sim3.0)\times10^{-7}$	(Li *et al.*, 1999; Xu and Thomson, 1999; Li *et al.*, 2000)
$La_{0.4}Sr_{0.6}Co_{0.2}Fe_{0.8}O_{3-\delta}$	219	0.0018		
$La_{0.2}Sr_{0.8}Co_{0.2}Fe_{0.8}O_{3-\delta}$	120	0.0052	$(1.1\sim8.9)\times10^{-7}$	
$La_{0.2}Sr_{0.8}Co_{0.8}Fe_{0.2}O_{3-\delta}$	310	0.0028		
$La_{0.8}Sr_{0.2}Co_{0.8}Fe_{0.2}O_{3-\delta}$ [0.5 mm]			$(2.5\sim8.3)\times10^{-7}$	(Ishihara *et al.*, 2000)
$La_{0.6}Sr_{0.4}Co_{0.8}Fe_{0.2}O_{3-\delta}$			4.46×10^{-9}	(ten Elshof *et al.*, 1995)
$La_{0.2}Sr_{0.8}Co_{0.6}Cu_{0.4}O_{3-\delta}$ [0.8 mm]	250~600		$(1.2\sim6.0)\times10^{-7}$	(Kim *et al.*, 1997)
$LaGa_{1-x}Ni_xO_{3-\delta}$ (x=0.2-0.6) [1.0 mm]			$(1.9\sim6.6)\times10^{-8}$	(Kharton *et al.*, 1999a)

$LaGa_{0.8}Ni_{0.2}O_{3-\delta}$ (1.0 mm)	~2	0.0008~0.012	(4.47~8.91) $\times 10^{-8}$	(Yaremchenko
$LaGa_{0.5}Ni_{0.5}O_{3-\delta}$	20~32	0.00012~0.002		*et al.*, 1999;
		2		Kharton *et al.*,
$LaGa_{0.4}Co_{0.6}O_{3-\delta}$	12.6~63			2000b)
$LaGa_{0.6}Co_{0.4}O_{3-\delta}$	2~4			
$LaGa_{0.85}Mg_{0.15}O_{3-\delta}$	0.02~0.09	0.94~0.92		
$LaGa_{0.4}Mg_{0.2}Cr_{0.4}O_{3-\delta}$	0.32~0.33	0.0044~0.031		
$LaGa_{0.4}Mg_{0.2}Fe_{0.4}O_{3-\delta}$	~5	0.012~0.046		
$LaGa_{0.4}Mg_{0.2}Co_{0.4}O_{3-\delta}$	~18	0.0008~0.0017	(5.0~6.31) $\times 10^{-8}$	
[1.0 mm]				
$LaGa_{0.3}Mg_{0.1}Co_{0.6}O_{3-\delta}$	79~126	(0.22~4.1)$\times 10^{-4}$	(0.04~1)$\times 10^{-8}$	
[1.0 mm]				
$LaGa_{0.4}Mg_{0.25}Co_{0.35}O_{3-\delta}$	9~10		(3.8~5.0)$\times 10^{-8}$	
[1.0 mm]				
$La_{0.8}Sr_{0.2}Ga_{0.8}Fe_{0.2}O_{3-\delta}$			(0.35~0.52)$\times 10^{-6}$	(Ishihara *et al.*,
[0.5 mm]				2000)
$La_{0.8}Sr_{0.2}Ga_{0.7}Fe_{0.3}O_{3-\delta}$	0.33~0.79		(0.41~1.03)$\times 10^{-6}$	
[0.5 mm]				
$La_{0.8}Sr_{0.2}Ga_{0.6}Fe_{0.4}O_{3-\delta}$			(0.43~0.83)$\times 10^{-6}$	
$La_{0.8}Sr_{0.2}Ga_{0.6}Fe_{0.4}O_{3-\delta}$			(0.37~0.73)$\times 10^{-6}$	
$La_{0.8}Sr_{0.2}Ga_{0.7}Ni_{0.3}O_{3-\delta}$	~3.98		(0.25~1.0)$\times 10^{-6}$	
[0.5 mm]				
$La_{0.8}Sr_{0.2}Ga_{0.7}Co_{0.3}O_{3-\delta}$	2~10		(0.23~1.1)$\times 10^{-6}$	
[0.5 mm]				
$La_{0.9}Sr_{0.1}GaO_{3-\delta}$	0.025~0.076	0.97~0.98		
$La_{0.9}Sr_{0.1}Ga_{0.95}M_{0.05}O_{3-\delta}$	0.015~0.126	0.77~0.95		
M=Cr, Fe, Co				
$La_{0.9}Sr_{0.1}Ga_{0.8}Fe_{0.2}O_{3-\delta}$	0.033~0.071	0.14~0.47		
$La_{0.86}Sr_{0.14}Ga_{0.96}Ti_{0.04}O_{3-\delta}$	0.019~0.060	0.91~0.89		

Table 2-2 TEC values in air and phase transformation temperature of the mixed conducting oxides.

Composition	$\alpha\times10^6$, K^{-1} (800-1000°C)	Ref
$SrCo_{0.8}Fe_{0.2}O_{3-\delta}$	29.4±0.8	(Kharton *et al.*, 2000a;
$SrCo_{0.8}Ti_{0.2}O_{3-\delta}$	28.8±0.9	Kharton *et al.*, 2000)
$Sr_{0.97}Co_{0.8}Ti_{0.2}O_{3-\delta}$	27.0±0.4	
$Sr_{0.97}Fe_{0.4}Ti_{0.6}O_{3-\delta}$	16.6±0.1	
$Sr_{0.70}La_{0.30}CoO_{3-\delta}$	28.8	(Kovalevsky *et al.*, 1998;
$Sr_{0.70}Nd_{0.30}CoO_{3-\delta}$	31.5	Ishihara *et al.*, 2000)
$Sr_{0.70}Sm_{0.30}CoO_{3-\delta}$	25.9	
$Sr_{0.70}Gd_{0.30}CoO_{3-\delta}$	20.4	
$Sr_{1-x}La_xCoO_{3-\delta}$ (x=0.3~0.4)	27.9~18↓	
$Sr_{0.65}La_{0.35}Co_{0.9}O_{3-\delta}$	16.9±0.9	
$Sr_{0.89}Co_{0.1}Fe_{0.1}Cr_{0.01}O_{3-\delta}$	30.5±0.9	
$Ba_{0.5}Sr_{0.5}Co_{0.8}Fe_{0.2}O_{3-\delta}$		(Shao *et al.*, 2000b)
$LaCoO_{3-\delta}$	21.9±0.3	(Kharton *et al.*, 2000b)
$LaCo_{1-x}Cr_xO_{3-\delta}$ (x=0.1-0.4)	23.7~20.3	(Kharton *et al.*, 1998a;
$LaCo_{1-x}Ni_xO_{3-\delta}$ (x=0.1,0.3)	19.6, 17.3	Kharton *et al.*, 1998b)
$LaCo_{0.9-y}Fe_{0.1}Ni_yO_{3-\delta}$ (y=0.1,0.2)	20.8, 18.6	
$LaCo_{0.8-y}Fe_{0.2}Ni_{0.2}O_{3-\delta}$ (y=0.2,0.3)	19.2, 18.0	
$La_{0.8}Sr_{0.2}Co_{0.6}Fe_{0.4}O_{3-\delta}$		(Zeng *et al.*, 1998)
$La_{1-x}Pb_xFeO_{3-\delta}$ (x=0.1,0.2,0.3)	10.0, 10.4, 10.1	(Kharton *et al.*, 1998c)
$LaGa_{0.3}Co_{0.6}Mg_{0.1}O_{3-\delta}$	19.8±0.3	(Yaremchenko *et al.*,
$LaGa_{0.4}Co_{0.4}Mg_{0.2}O_{3-\delta}$	15.4±0.3	1999)
$LaGa_{0.4}Co_{0.35}Mg_{0.25}O_{3-\delta}$	12.4±0.2	
$LaGa_{1-x}Ni_xO_{3-\delta}$ (x=0.2~0.6)	10.8~11.6	(Kharton *et al.*, 1999c)
$LaCo_{0.6}Ga_{0.3}Mg_{0.1}O_{3-\delta}$	20.0±0.3	
$LaCo_{0.9}Mg_{0.1}O_{3-\delta}$	19.5±0.3	
$LaFe_{1-x}Ni_xO_{3-\delta}$ (x=0.2~0.5)	8.9~11.9↑	

Apart from the advantages mentioned above, the perovskite-type or related oxides still have a few disadvantages:

- Relatively low oxygen permeability. Oxygen permeation rate of most materials in this class is lower than 7.4×10^{-7} mol/cm^2.s (1 cm^3/cm^2.min),
- Peroviskite-related phase (highest oxygen permeability in oxidizing conditions) thermodynamically and/or dimensionally unstable, under large oxygen chemical potential gradients such as air/methane,
- Perovskite-type oxides exhibit an ordering in the oxygen sublattice and a high reactivity with gas species such as CO_2 at a temperature below 1000-1070 K, leading to degradation in behaviour with time.

2.3.1.2 Non-perovskite-type oxides

Apart from the perovskite oxides mentioned above, some non-perovskite-type oxides also exhibit mixed oxygen ionic and electronic conducting properties and have attracted a considerable attention (Balachandran *et al.*, 1995; Balachandran *et al.*, 1998). One type of the mixed phase oxides, $SrFeCo_{0.5}O_x$, given by Balachandran *et al.* (1998) shows a comparable electronic and ionic transference number, making it unique among other mixed conductors. The properties and the phase stability of this oxide were investigated (Balachandran *et al.*, 1998; Ma and Balachandran, 1998) and a tubular membrane was also fabricated as a reactor for methane conversion to syngas by Balachandran *et al.* (1995) who found that the methane conversion efficiency was higher than 98% and CO selectivity was up to 90% at 850 °C. An oxygen permeation rate of 2-4 cm^3/cm^2.min was also achieved. Under such a reducing atmosphere, high structural stability was observed whilst operating for more than 1000 hours (Balachandran *et al.*, 1997). This clearly suggests that the structural stability and mechanical integrity of the material in reducing atmospheres are better than many other cobalt-containing perovskite oxides. In addition, studies carried out by Kim *et al.* (1998a; 1998b) concluded that the oxygen transport in this oxide is dependent primarily on the bulk diffusion rate. Recently, a study further suggested that a suitable preparation technique could improve the oxygen permeation properties of $SrFeCo_{0.5}O_x$ (Ikeguchi *et al.*, 2003). The relationships between structures and properties of a more complex oxides, $Sr_4Fe_{6-x}Co_xO_{13+\delta}$ with $1\leq x\leq 3$ were also extensively studied by Ma *et al.* (Ma *et al.*, 1998b) who found that the total conductivity and the oxygen flux increase with

cobalt substitution and temperature. The conductivity of $Sr_4Fe_4Co_4O_{13+\delta}$ was found to be 20 and 6 Scm^{-1} at 900 °C in flowing air and argon environments, respectively. Its ionic transference number is about 0.4. The oxygen permeation rate was observed up to 10 $cm^3/cm^2.min$ for a 0.75-mm-thick tubular membrane in a methane-conversion-reaction condition for more than 1000 hours. Based on the above studies, it is concluded that this oxide exhibits a better structural and chemical stability at high temperatures and in low oxygen partial pressure atmosphere compared to the perovskite $SrFe_{0.2}Co_{0.8}O_{3-\delta}$ although the oxygen permeability has been shown to be lower than that of the latter (Ma *et al.*, 1998a; Armstrong *et al.*, 2000). The preparation procedure of this material on the phase relationships was also investigated systematically (Xia *et al.*, 2000).

Other type of non-perovskite-type mixed conductors are $La_2Cu_{1-x}Co_xO_{4+\delta}$ with $0 \leq x \leq 0.3$ investigated by Bochkov *et al.* (1999). The $La_2Cu_{1-x}Co_xO_{4+\delta}$ ($0 \leq x \leq 0.3$) solid solutions with orthorhombic K_2NiF_4-type structure was found to be a mixed conductor also, with the electrical conductivity of up to 13 S cm^{-1} (Bochkov *et al.*, 1999). Incorporating cobalt into the copper sublattice of $La_2CuO_{4+\delta}$ leads to increasing oxygen content, and the oxygen permeability increases with cobalt concentration at x=0.02–0.10 but decreases with the further dopant additions. Since no alkaline-earth metal cations are contained in the oxide, the sintered ceramics of this material exhibit sufficient stability, maintaining a single phase for more than 12 months.

2.3.1.3 Summary of oxygen permeable materials

Due to the large number of oxygen permeable materials available, it is quite difficult to have an extensive comparison. Some general observations are summarized below:

1. The $A^{III}B^{III}O_3$-type perovskites. (i.e., $La(Co,Fe)O_{3-\delta}$) have higher oxygen ionic conductivity than the $A^{II}B^{IV}O_3$ -type perovskites which are not good as an oxygen ionic conductor (Knauth and Tuller, 2002).

2. The optimum tolerance factor is near unity from the viewpoint of lattice stability and equivalency in oxygen sites. A large specific free volume is desirable in view of the mobility of oxygen. The specific free volume linearly increases with the decrease of the

tolerance factor for each series with a fixed A site cation. The optimum tolerance factor for $A^{III}B^{III}O_3$ -type perovskites to obtain the maximum electrical conductivity is around 0.96 due to the balance between the specific free volume and the tolerance factor. The change of the tolerance factor due to doping should be as small as possible (Knauth and Tuller, 2002).

3. The optimum oxygen deficiency δ to obtain the maximum electrical conductivity is around 0.2. When δ is considerably larger than 0.2, the electrical conductivity decreases due to short range interaction among vacancies (Knauth and Tuller, 2002).

4. The SrCoFeO based solid solutions with cubic perovskite structure exhibit the highest oxygen permeation fluxes compared to other mixed oxide membranes. However, high thermal expansion coefficients and interaction with gas species such as carbon dioxide and water vapour complicate the employment of SrCoFeO as an oxygen separation membrane.

5. The perovskite-type oxides containing alkaline-earth metal cations were reported to exhibit a high reactivity with gas species such as CO_2, SO_2 and water vapour, whereas relatively low oxygen permeation fluxes are typical for perovskites without alkaline-earth elements.

6. In LaSrFeO and LaGaO oxides, La-site doping with a cation of a lower oxidation state leads to a large number of oxide vacancies being formed and, therefore, to an increase in oxide-ion conductivity.

7. A-site cations strongly affect the oxygen non-stoichiometry of the oxide and the mobility of oxygen ions in the bulk phase (Mizusaki *et al.*, 1989). The creation of vacancies in both cation sublattices of ABO_3 perovskites results in a decrease in the oxygen permeation flux (Kovalevsky *et al.*, 1998).

8. Oxygen permeation in most perovskite-type oxide membranes is controlled by both bulk diffusion and surface exchange rates. The critical membrane thickness that is introduced to distinguish between the regions where bulk diffusion and surface exchange kinetics are rate limiting has been reported to be in the range of 20 to 3000

μm depending upon composition, temperature and oxygen partial pressure (Aasland *et al.*, 2000).

2.3.2 Proton conducting materials and membranes

The high temperature protonic conducting material $SrCe_{0.95}Yb_{0.05}O_{3-\delta}$ was firstly described by Iwahara (1981). This material is a substituted solid solution based on the perovskite-type oxide $SrCeO_3$, in which 5% of Ce is replaced by Yb and exhibits protonic conduction under a hydrogen-containing atmosphere at elevated temperatures (Iwahara, 1996). However, the un-doped oxide $SrCeO_3$ does not show the proton-conducting properties. Oxygen vacancies generated by doping play an important role in the formation of proton-conducting properties including the formation and transport of protons. The interest in proton-conducting materials is due to their following possible applications:

- As an electrolyte in hydrogen sensors (Iwahara, 1995). Commercialized hydrogen analyzers have been developed using $CaZr_{0.9}In_{0.1}O_{3-\delta}$ as a solid electrolyte and porous platinum as an electrode material. This represents an important milestone for the practical application of protonic conduction materials,
- As an electrolyte in hydrogen fuel cell, it can work stably at 800-1000 °C (Iwahara *et al.*, 1983),
- As a solid electrolyte in a steam electrolyzer (Iwahara, 1995),
- As a hydrogen pump for hydrogen extraction from various gas mixtures (Iwahara, 1996),
- As a chemical reactor for hydrogenation or dehydrogenation of organic compounds (Hamakawa *et al.*, 1993).

Currently, two topics which become to be of more and more interest are hydrogen production from hydrogen containing gases and improvement of thermodynamically unfavourable reactions by continuous hydrogen removal using proton conducting membranes (Hamakawa *et al.*, 1993; Guan *et al.*, 1997; Liu *et al.*, 2001a; Schober, 2003; Iwahara *et al.*, 2004). Although, Pt or Pd alloy membranes have been studied for many years, they suffer from some fatal limitations (Lin, 2001). Ceramic proton-conducting membranes provide an interesting alternative (Liu *et al.*, 2001a).

2.3.2.1 Pervoskite-type oxides

The mixed proton and electron (or hole) conducting materials have many aspects in common with mixed oxygen ionic and electronic conducting materials, but unlike oxygen permeable membranes which work under either oxidising vs. reducing conditions (e.g. air vs. methane) or oxidising conditions on both sides of the membrane, the hydrogen permeable membranes would mostly work under reducing conditions on both sides. Some special considerations on the stability of the membranes would be needed in the development strategies of hydrogen permeable materials (Norby, 1999).

Compared with large number of oxygen conducting materials, the choice of the proto-conducting material is, so far, limited. Several perovskite-type of oxides have been identified to have a good capability in protonic conduction including doped $BaCeO_3$, $BaZrO_3$ (Kreuer, 1999; Norby, 1999; Schober and Bohn, 2000), $BaPrO_3$ (Fukui *et al.*, 1999; Norby, 1999), $SrZrO_3$, $CaZrO_3$ (Huang *et al.*, 1991; Yajima *et al.*, 1991b; Iwahara *et al.*, 1993) and $SrTiO_3$ (Sata *et al.*, 1996), since the first protonic conductor of $SrCe_{0.95}Yb_{0.05}O_{3-\delta}$ was reported. The general formula is written as $AB_{1-x}M_xO_{3-\delta}$, where the A element is taken from the group consisting of Ca, Sr or Ba; the B element is taken from the group consisting of Ce, Tb, Zr or Th; the M element is taken from the group consisting of Ti, Tm, Cr, Mn, Co, Ni, Cu, Al, Ga, Y, Yb, In, or Sn, and x is less than its upper limit of solid solution formation range (normally less than 0.2) and δ is the oxygen deficiency per unit cell (Iwahara *et al.*, 1981; Norwick and Du, 1995). Their protonic conductivities in hydrogen atmosphere are of order of $10^{-3} - 10^{-2}$ Scm^{-1} at 600 – 1000 °C. $BaCeO_3$ based oxides show the highest conductivity, but oxygen ions contribute to the conduction as the temperature is increased, and result in the transport number of protons decreases with the increase of the temperature (Yajima *et al.*, 1991a). Although the conductivity of $SrCeO_3$ based oxides is lower, the transport number of protons is higher than that of $BaCeO_3$ based ones. The zirconate based oxides such as $SrZrO_3$ or $CaZrO_3$ show good chemical stability and good mechanical strength and they are more stable against carbon dioxide gas which reacts with cerates materials below 800 °C (Yajima *et al.*, 1991b; Yajima *et al.*, 1992), but the conductivity of zirconates is lower than those of cerates (Matzke and Cappadonia, 1996). The major properties of these materials are summarized in Table 2-3.

Table 2-3 Properties of typical proton conducting materials.

Composition	T (°C)	Properties	Ref
$BaCe_{0.95}Y_{0.05}O_{3-\delta}$	500-600	$\sigma_H > \sigma_O$	(Guan *et al.*, 1997)
	700-800	$\sigma_H < \sigma_O$	
	800	$\sigma_H = 1.93\times10^{-3}\Omega^{-1}cm^{-1}$	
		$\sigma_O = 8.2\times10^{-3}\ \Omega^{-1}cm^{-1}$	
$BaCe_{0.95}Nd_{0.05}O_{3-\delta}$		E=0.54/eV (lowest)	(Liu and Norwick, 1992)
		$\sigma_H=8.5\times10^{-3}\Omega^{-1}cm^{-1}$	
$SrCe_{0.95}Yb_{0.05}O_{3-\delta}$	600-800	$\sigma_H = 3.47\times10^{-3} - 1.27\times10^{-2}\Omega^{-1}cm^{-1}$	(Guan *et al.*, 1997)
		$\sigma_O = 1.2\times10^{-4} - 2.1\times10^{-3}\Omega^{-1}cm^{-1}$	
		$\sigma_e = 7\times10^{-4} - 3.2\times10^{-3}\Omega^{-1}cm^{-1}$	
	700	$\sigma_H = 7.2\times10^{-3}\Omega^{-1}cm^{-1}$	
		$\sigma_e = 2.1\times10^{-3}\Omega^{-1}cm^{-1}$	
		E= 0.62/eV,	
	800	$\sigma_e = 8.5\times10^{-3}\Omega^{-1}cm^{-1}$	
	900	$J_H = 1.7\times10^{-8}mol/cm^2.s$	(Hamakawa *et al.*, 1994)
$SrCe_{0.95}Tm_{0.05}O_{3-\delta}$	800	$\sigma_e = 1.29\times10^{-2}\Omega^{-1}cm^{-1}$	(Qi and Lin, 2000)
	900	$J_H = 2.9\times10^{-8}mol/cm^2.s$	
$SrZr_{0.9}Sc_{0.1}O_{3-\delta}$		E= 0.59eV, $\delta_H=2.8\times10^{-2}\Omega^{-1}cm^{-1}$	(Liang and Nowick, 1993)
$SrZr_{0.95}Yb_{0.05}O_{3-\delta}$			
$SrYb_{0.05}(Ce_{1-x}Zr_x)_{0.95}O_{3-\delta}$	<500°C	E=0.74-0.79/eV in O_2	(Matzke and Cappadonia, 1996)
		E=0.56-0.62/eV in H_2/H_2O	

A new series of protonic materials with more complex perovskite structure have also been reported, in which their conductivity is as high as that of $BaCeO_3$ based oxides at high temperature (Norwick and Du, 1995). Their general formulas are $A_2(B'B'')O_6$ and $A_3(B'B''_2)O_9$, where A ions always have charge 2+ and B' and B'' ions have charges 3+ and 5+ for $A_2(B'B'')O_6$ and 2+ and 5+ for $A_3(B'B''_2)O_9$. To become protonic conductors, they must be taken off stoichiometry to create negative charges which protons (or oxygen vacancies) can compensate (Liang and Nowick, 1993; Liang *et al.*, 1994). Their formulas are written $A_2(B'_{1+x}B''_{1-x})O_{6-\delta}$ and $A_3(B'_{1+x}B''_{2-x})O_{9-\delta}$. In particular, these systems such as $A_3(Ca_{1+x}Nb_{2-x})O_{9-\delta}$ are extremely sensitive to cation non-stoichiometry x, with major effects on structural order, proton mobility, and

mechanical properties. The protonic conduction in these complex perovskite-related structural oxides were systematically studied (Norwick and Vaysleyb, 1997; Norwick *et al.*, 1999). These structures can accommodate many dopant cations on the A, B' and B" sites, which provides more opportunities to improve the ion and/or electron conductivities and other favoured properties. The properties of this new type of proton-conducting materials are summarized in Table 2-4.

Table 2-4 Conductivity and activated energy of some complex perovskite type materials.

Composition	**E $(eV)^{-1}$**	**σ**	**Ref.**
$A_2(B'B")O_6$			
$SrScNbO_6$	0.58±0.09		(Liang and Nowick, 1993)
$Sr_2Ca_{1.1}Nb_{0.9}O_{6-\delta}$	0.81	$1.8\times10^{-2}\Omega^{-1}cm^{-1}$	
$Sr_2Ca_{1.1}Ta_{0.9}O_{6-\delta}$	0.89	$3.4\times10^{-2}\Omega^{-1}cm^{-1}$	
$Sr_2(Nd_{1.1}Nb_{0.9})O_{6-\delta}$	1.04	$3.6\times10^{-2}\Omega^{-1}cm^{-1}$	
$A_3(B'B")O_9$			
$Sr_3(Ca_{1.18}Nb_{1.82})O_{9-\delta}$	0.66	$5.5\times10^{-2}\Omega^{-1}cm^{-1}$	(Norwick and Du, 1995)
$Sr_3(Sr_{1.18}Nb_{1.82})O_{9-\delta}$	0.97	$2.3\times10^{-2}\Omega^{-1}cm^{-1}$	(Liang *et al.*, 1994)
$Ba_3(Ca_{1.18}Nb_{1.82})O_{9-\delta}$	0.54	$2.1\times10^{-2}\Omega^{-1}cm^{-1}$	

2.3.2.2 Non-pervoskite-type oxides

Some fluorite type of oxides such as Y_2O_3 and CeO_2 have been found to have a possibility of being electron-proton mixed conductors in an H_2/H_2O atmosphere and at high temperatures (Nigara *et al.*, 1998; Nigara *et al.*, 1999). Although the hydrogen permeability of those materials is very low, their chemical and thermodynamic stabilities are very good. With a proper dopant, their hydrogen permeability can be greatly improved (Nigara *et al.*, 2000), for example, $Ce_{0.8}Yb_{0.2}O_{1.9}$ was found to have a hydrogen permeation 100 times higher than that of un-doped CeO_2 (Sakai *et al.*, 1999). Some characteristics of $Ce_{0.8}Yb_{0.2}O_{1.9}$ are listed in Table 2-5.

Table 2-5 Properties of $Ce_{0.8}Yb_{0.2}O_{1.9}$ at H_2O/H_2 atmosphere.

	T (K)	E $(eV)^{-1}$	σ_H (Scm^{-1})	J_H $(mol/cm^2.s)$
$Ce_{0.8}Yb_{0.8}O_{1.9}$	1000-1200	0.58 ± 0.05	1×10^{-6} - 2×10^{-6}	1.7×10^{-7}-8×10^{-7}
	1300-1500	1.10 ± 0.06	8×10^{-6} - 2×10^{-5}	2×10^{-6}-7.5×10^{-6}
	1500-1800	0.92 ± 0.06	2×10^{-5} - 1×10^{-4}	7.5×10^{-6}-1.5×10^{-5}

A few other non-perovskite-types of oxides have been known to exhibit protonic conductivity at high temperature, for example, $Ln_2Zr_2O_7$ and $LaPO_4$ systems (Norby and Christiansen, 1995; Shimura *et al.*, 1996). However, their conductivity is rather low.

For the mixed electron-proton conducting materials, it was thought that the total conductivity derived from both the protonic and electronic conductivities must usually be 0.1 Scm^{-1} at least, depending on membrane thickness and other factors (Norby and Larring, 2000). The technological challenges in the applications of protonic conducting materials from the viewpoint of the material are their relatively low protonic conductivity possibly caused by the low electronic conductivity and poor chemical and thermodynamic stability of some high conductivity materials due to the reducing environment where the proton-conducting membranes work. The mechanical strength of these protonic materials may be another concern.

2.3.3 Dual phase membranes

Normally, the oxygen permeation rate is proportional to $[(\sigma_i\sigma_e)/(\sigma_i + \sigma_e)]$ (Lin *et al.*, 1994). Therefore, a good mixed conducting material must have high ionic conductivity as well as considerable electronic conductivity. It is not easy to meet all the requirements in a single component material. Mazanec *et al.* (Mazanec *et al.*, 1992) introduced the dual phase membrane concept for partial oxidation of methane, which was composed of yttria-stabilized zirconia (YSZ) for oxygen ionic conduction and a metal such as Ag or Au for improving the electronic conduction. In the dual phase membranes, the ionic conductor is usually the continuous phase and the metal is uniformly dispersed, but networked in the whole membrane. By using the dual phase membrane, an enhanced oxygen permeation flux is thus achieved. The concept of the dual phase membranes gives rise to additional opportunities in the selection of materials

and fabrication methods of the membranes, and thus it is interesting to touch on this subject briefly in this review.

Fig. 2-3 gives a schematic description of a dual phase membrane in which one continuous phase is for ion conduction and the other is dispersed in for improving electron conduction. Following this idea, Chen and his co-workers (Chen *et al.*, 1995; Chen *et al.*, 1997b; Chen and Burggraaf, 1999) carried out a detailed research on dual phase membranes using a several dual phase composites such as yttria-stablized zircornia-palladium (Chen *et al.*, 1995; Chen *et al.*, 1996), erbia-stablized bismuth-sliver or gold (Chen *et al.*, 1996; Chen *et al.*, 1997b; Chen and Burggraaf, 1999). It was found that in order to form a networked electron-conducting phase, about 40 vol% of a metal is needed to mix with the ceramic material. The oxygen transport kinetics are believed to be controlled by the bulk diffusion of oxygen ions in the oxide phase for membranes with a thickness down to about 1.0 mm and jointly controlled by bulk diffusion and surface exchange when the membrane thickness decreases further (Chen *et al.*, 1997b).

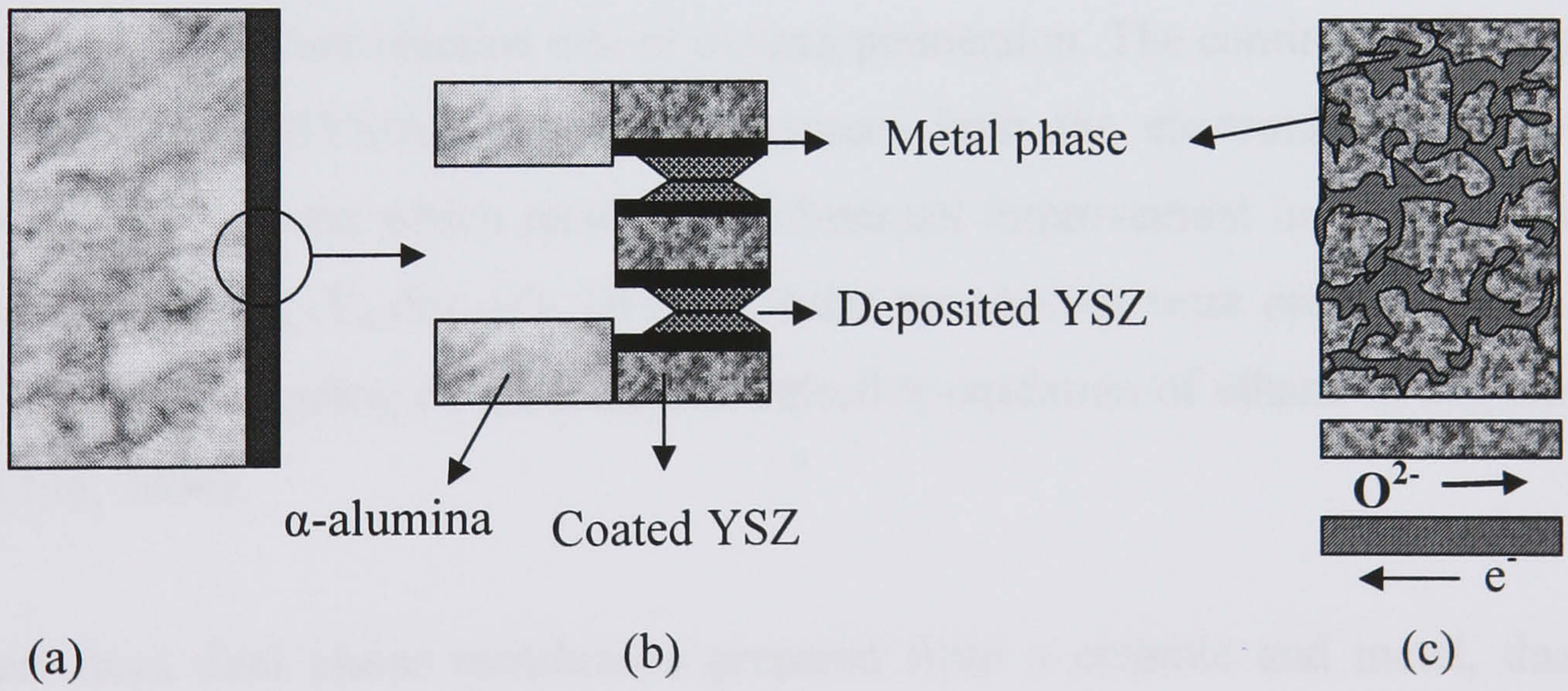


Fig. 2-3 Schematic description of dual phase membranes: (a) Composite membrane, (b) Structure of the composite membrane, (c) General dual phase membrane.

Kim and Lin (2000b) prepared a number of dual phase membranes by coating a porous YSZ layer on α-alumina support membranes and then impregnating a continuous Pd

phase on the wall of the pores of the YSZ layer. The residual pores of the Pd-modified YSZ layer were then plugged with the YSZ using a chemical vapour deposition technique (CVD). The structure of the prepared membranes is shown in Fig. 2-3 (a-b), and a general structure of the dual phase membrane is also schematically described in Fig. 2-3 (c).

Some more complex fluorite-type of materials were also studied such as $Bi_{1.5-x}Y_{0.5}Cu_xO_{3-\delta}$ in the fluorite phase (δ phase) with different CuO concentrations (x=0.005-0.015) (Han *et al.*, 1997) and $Bi_{1.5}Y_{0.3}Sm_{0.2}O_3$ (BYS) (Kim and Lin, 2000a). The oxygen permeation fluxes through the $Bi_{1.5-x}Y_{0.5}Cu_xO_{3-\delta}$ membranes with a thickness of 2 mm is in the range of (5.0-9.2) $\times 10^{-9}$ mol/cm^2.s at 800°C, and is controlled by bulk diffusion (Han *et al.*, 1997). In other work (Kim and Lin, 2000a), percolative and non-percolative fluorite type $Bi_{1.5}Y_{0.3}Sm_{0.2}O_3$ (BYS) and silver dual-phase membranes were prepared by mixing BYS and Ag powders. The percolative BYS/Ag 40% and non-percolative BYS/Ag 30% membranes exhibit about a 50-fold and 10-fold increase, respectively, in oxygen permeation flux compared to BYS membranes. For a 1.3 mm thick BYS/Ag 40% membrane, an oxygen permeation flux of 5.8×10^{-7} mol/cm^2 .s was measured at 850°C. For the non-percolative BYS/Ag membrane, the presence of Ag enhances the surface reaction rate of oxygen permeation. The continuous silver phase in the percolative BYS/Ag membrane increases both the electronic conductivity and surface reaction rate which result in a substantial improvement in oxygen permeance. Recently, the $Bi_{1.5}Y_{0.3}Sm_{0.2}O_3$ (BYS) tubular membranes were prepared and tested in the oxidative coupling of methane and selective oxidation of ethane to ethylene (Akin and Lin, 2004).

Apart from dual phase membranes prepared from a ceramic and metal, dual phase membranes have also been prepared successfully using both ceramic materials, one with a large ionic conductivity and the other exhibiting good electronic conductivity (Kharton *et al.*, 2003; Wang *et al.*, 2003). The oxygen permeability and structural properties of the dual phase membranes fabricated from gadolinia-doped ceria electrolyte $Ce_{0.8}Gd_{0.2}O_{2-\delta}$-perovskite-type $La_{0.8}Sr_{0.2}Fe_{0.8}Co_{0.2}O_{3-\delta}$ (Kharton *et al.*, 2003) and $La_{0.15}Sr_{0.85}Ga_{0.3}Fe_{0.7}O_{3-\delta}$-$Ba_{0.5}Sr_{0.5}Fe_{0.2}Co_{0.8}O_{3-\delta}$ (Wang *et al.*, 2003) were studied in oxygen separation and the performance of the membranes were examined.

Although most of dual phase membranes studied are for the enhancement of oxygen permeation, attempts made by Argonne National Laboratory (Siriwardane *et al.*, 2000; Zhang *et al.*, 2003) for improvement of hydrogen permeation by preparing a dual phase membrane has also been carried out recently. The $BaCe_{1-x}Y_xO_3$ ceramic membranes mixed with various concentrations of nickel were prepared. It was found that the surface properties of the membranes are significantly affected by the concentration of nickel (Siriwardane *et al.*, 2000) and the interfacial resistance of Ni and $BaCe_{1-x}Y_xO_3$ is much higher than the bulk resistance. A suggestion for further improve the hydrogen permeation by reducing the interfacial resistance to a reasonable level is proposed (Zhang *et al.*, 2003).

2.4 Transport of mixed conducting membranes

In this section, mechanisms for oxygen and hydrogen (proton) permeation through mixed conducting membranes is presented. Bulk transport coupled with surface exchange has been considered to quantify a net flux of oxygen or hydrogen (proton) transferred through a dense mixed conducting membrane.

2.4.1 Oxygen transport

2.4.1.1 Transport mechanism

Lattice diffusion in oxides, often synonymously termed as bulk diffusion, takes place because of the presence of point defects such as vacancies and interstitial atoms. It follows different mechanisms depending on the types of the defects (Shaw, 2001, PhD thesis):

1) Vacancy mechanism: when an atom or ion on a normal site jumps into an adjacent unoccupied lattice site, the vacancy moves into the site left by the atom.

2) Interstitial mechanism: it occurs when an atom on an interstitial site moves to one of the neighboring interstitial site. The jump of the interstitial atom involves a considerable distortion of the crystal lattice, hence this mechanism would only be likely when the diffusing atom is smaller than the atoms on the normal lattice positions. Diffusion of interstitially dissolved atoms (e.g. H, C, N, or O) in metals provides the best-known examples of this mechanism.

3) Interstitialcy mechanism: if the distortion of the regular lattice is too large for interstitial diffusion to be favorable, interstitial atoms may migrate via the interstitialcy mechanism. This mechanism involves the movement of an interstitial atom onto a normal lattice site, displacing the atom located on that site into another interstitial position.

4) Other mechanisms: the crowdion is a variant of the interstitialcy mechanism. In this case it is assumed that an extra atom is crowed into a line of atoms, and that it thereby displaces several atoms along the line from their equilibrium positions. The energy to move such a defect is small, but it can move only along the line or along equivalent direction.

As is known, a large number of oxygen vacancies are generated in the solid oxides formed by doping aliovalent cations. In the presence of oxygen, the oxygen vacancies tend to be filled with oxygen atom with formation of two electron holes at high temperatures as a result of charge compensation:

$$\frac{1}{2}O_2 + V_O^{\bullet\bullet} \Leftrightarrow O_O^{\times} + 2h^{\bullet} \tag{2-5}$$

where the charged defects are defined using the Kröger-Vink notation. That is, $O_O^{\times}$ stands for lattice oxygen, $V_O^{\bullet\bullet}$ for oxygen vacancy and $h^{\bullet}$ for positive electron hole.

Obviously, vacancy mechanism is the best one to describe the oxygen transport in mixed conducting oxides. In addition to the bulk diffusion, oxygen permeation through a mixed conducting oxide membrane also undergoes the surface exchange reactions at both the oxygen-rich and oxygen-lean sides of the membrane, which involves many sub-steps such as oxygen adsorption, dissociation, recombination, and charge transfer (Ishihara *et al.*, 1998; Lane and Kilner, 2000). Therefore, the mechanism for oxygen permeation through a mixed ionic-electronic conducting membrane can be schematically described in Fig. 2-4. It can be seen that the permeation process from the high oxygen partial pressure side to the low oxygen partial pressure side includes the

following steps in series: 1) mass transfer of gaseous oxygen from the gas stream to the membrane surface (high pressure side); 2) reaction between the molecular oxygen and oxygen vacancies at the membrane surface (high pressure side); 3) oxygen vacancy bulk diffusion across the membrane; 4) reaction between lattice oxygen and electron-hole at the membrane surface (low pressure side); and 5) mass transfer of oxygen from the membrane surface to the gas stream (low pressure side). However, the resistances between the gas phase and membrane (steps 1 and 5) are usually small and negligible (Xu and Thomson, 1999), as a result, only the membrane bulk diffusion and the surface reactions need to be taken into consideration in developing transport equations.

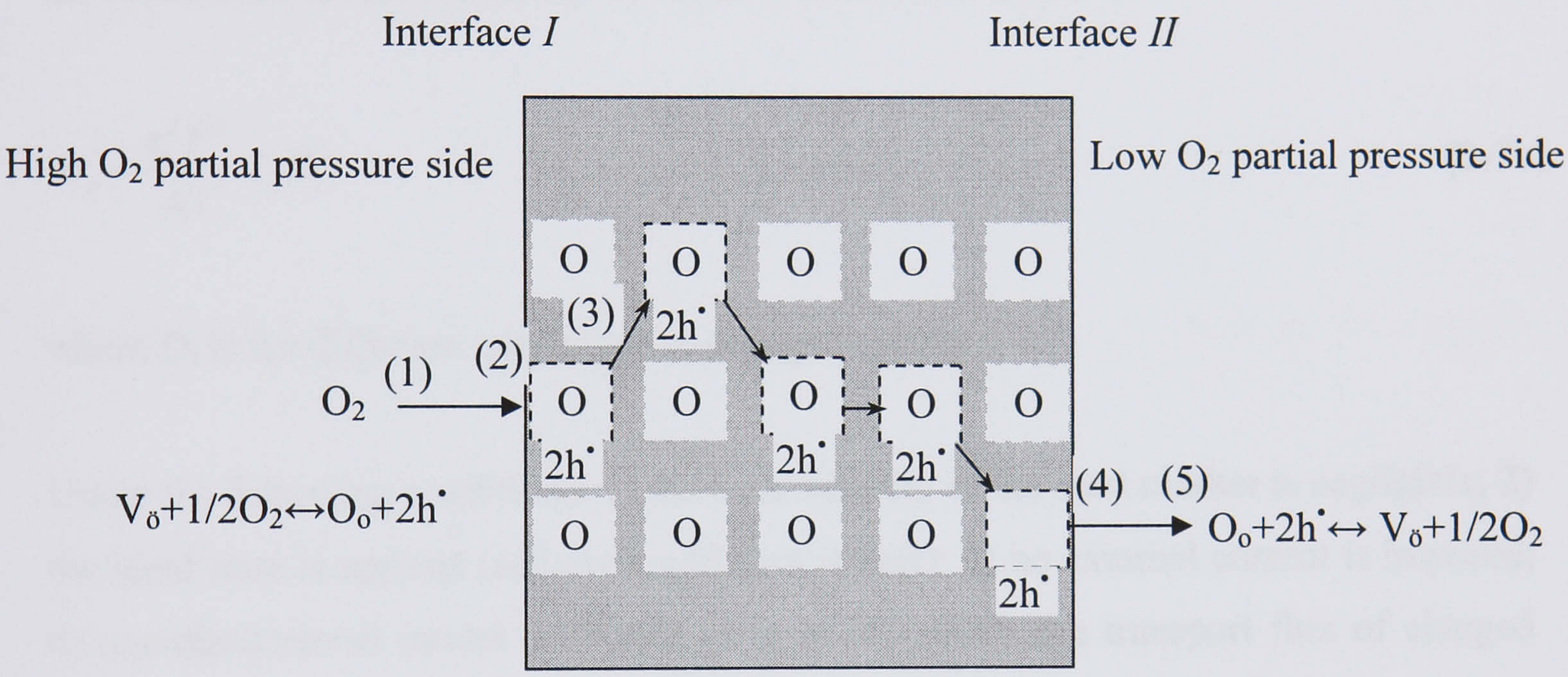


Fig.2-4 Schematic diagram of oxygen migration in membranes.

2.4.1.2 Transport equations

The flux of charged species (oxygen ion, oxygen vacancy, proton, electron, and electron hole) in a mixed conductor is usually described by the Nernst-Planck equation (Goto, 1988):

$$J_i = -\frac{\sigma_i}{z_i^2 F^2}\nabla\mu_i + C_i\upsilon \qquad (2\text{-}6)$$

where μ_i and υ are the electrochemical potential of charged species and the local velocity of the inert marker, respectively. The electrochemical potential for each

charged species consists of a chemical potential or an activity term and a local electrostatic potential term ϕ.

$$\mu_i = \mu_i^0 + RT \ln a_i + z_i F \phi \tag{2-7a}$$

where μ_i^0 a_i, and ϕ are the standard chemical potential, activity and the Galvanic (internal) potential respectively.

In eq.(2-6), the σ_i is the conductivity of charged species *i*, which may be correlated to the concentration and diffusivity by the Nernst-Einstein equation:

$$\sigma_i = \frac{z_i^2 F^2}{RT} C_i D_i \tag{2-7b}$$

where D_i is the diffusion coefficient of charged species *i*.

Under the following conditions: 1) the local velocity of the inert marker is negligible; 2) the ideal state is applied (activity coefficient is unit); 3) no external current is imposed; 4) one-dimensional model is applied (Tan *et al.*, 2000), the transport flux of charged defects at steady state expressed in terms of diffusivity and concentration can be obtained by substituting Eqs. (2-7a) and (2-7b) into Eq. (2-6):

$$J_i = -D_i C_i \left[\frac{1 - t_i}{C_i} \cdot \frac{dC_i}{dx} - \sum_{j \neq i} \frac{z_i}{z_j} \cdot \frac{t_j}{C_j} \cdot \frac{dC_j}{dx} \right] \tag{2-8}$$

where *t* is the transport number of defect *i*:

$$t_i = \frac{\sigma_i}{\sum \sigma_j} = \frac{z_i^2 D_i C_i}{\sum_j z_j^2 D_j C_j} \tag{2-8a}$$

For the mixed ionic-electronic conducting membranes, oxygen vacancy, $V_O^{\cdot\cdot}$ and electron hole, $h^{\cdot}$ are the only mobile charge (Xu and Thomson, 1999). As a result, Eq. 2-8 is then reduced to:

$$J_V = -\frac{(C_h + 4C_V)D_V D_h}{C_h D_h + 4C_V D_V} \cdot \frac{dC_V}{dx} \tag{2-9}$$

Furthermore, for the perovskite membranes whose ionic transference number closes to zero ($C_hD_h >> C_VD_V$ and $C_h >> C_V$) (Qiu *et al.*, 1995; Kharton *et al.*, 1996), Eq. 2-9 is further simplified as:

$$J_V = -D_V \cdot \frac{dC_V}{dx} \tag{2-10}$$

Based on the stoichoimetric relations of oxygen and the oxygen vacancy, the oxygen flux can be written as:

$$J_{O_2} = -\frac{D_V}{2} \cdot \frac{dC_V}{dx} \tag{2-11}$$

or

$$J_{O_2} = \frac{D_V (C_V^{''} - C_V^{'})}{2L} \tag{2-11a}$$

On the membrane surfaces, the following reversible reactions take place at the high and low pressure sides, respectively:

$$\tfrac{1}{2}O_2 + V_O^{\bullet\bullet} \xleftrightarrow{k_f / k_r} O_O^{\times} + 2h^{\bullet} \tag{2-12a}$$

$$O_O^{\times} + 2h^{\bullet} \xleftrightarrow{k_f / k_r} \tfrac{1}{2}O_2 + V_O^{\bullet\bullet} \tag{2-12b}$$

where k_f and k_r are, respectively, the forward and reverse reaction rate constants of the above surface reactions.

Because of the high electronic conductivity, the electron hole concentrations are essentially constant on both membrane surfaces, and thus the reverse and forward reaction rates of the surface reactions of (2-12a) and (2-12b) are pseudo zero-order at steady state under isothermal conditions (Xu and Thomson, 1999). Therefore, the local rate of oxygen consumed (step 2) or formed (step 4) on the membrane surfaces can be, respectively, expressed in the following two equations if they are assumed to be elementary:

$$J_{O_2} = k_f \left(p_{O_2}^{'}\right)^{0.5} C_V^{'} - k_r \tag{2-13a}$$

$$J_{O_2} = k_r - k_f \left(p_{O_2}^{''}\right)^{0.5} C_V^{''} \tag{2-13b}$$

where $p_{O_2}^{'}$ and $p_{O_2}^{''}$ are the partial pressures of oxygen in the upstream and downstream, respectively. Combination of Eq. 2-11 and 2-13 gives the oxygen permeation flux in term of oxygen partial pressures as:

$$J_{O_2} = \frac{k_r D_V \left[(p_{O_2}^{'})^{0.5} - (p_{O_2}^{''})^{0.5}\right]}{2Lk_f (p_{O_2}^{'} p_{O_2}^{''})^{0.5} + D_V \left((p_{O_2}^{'})^{0.5} + (p_{O_2}^{''})^{0.5}\right)} \tag{2-14a}$$

It can be seen that the total permeation resistance is composed of three parts: one by exchange reaction at upstream membrane surface, one by bulk diffusion and one by exchange reaction at downstream membrane surface.

For the tubular or hollow fibre membranes, the local oxygen permeation flux with respect to log-mean membrane area, $dA_m = 2\pi R_m dl$ in which $R_m = (R_o - R_{in}) / \ln(R_o / R_{in})$ can be expressed by (Tan and Li, 2002):

$$J_{O_2} = \frac{k_r D_V \left[(p'_{O_2})^{0.5} - (p''_{O_2})^{0.5} \right]}{2(R_o - R_{in}) \cdot k_f (p'_{O_2} p''_{O_2})^{0.5} + \frac{R_m}{R_{in}} \cdot D_V (p'_{O_2})^{0.5} + \frac{R_m}{R_o} \cdot D_V (p''_{O_2})^{0.5}} \quad (2\text{-}14b)$$

where R_o and R_{in} are the outer and inner radius of the tubular membrane. It can be seen the membrane thickness here is referred to tube's wall thickness.

2.4.2 Proton transport

2.4.2.1 Transport mechanism

Proton-conducting oxides have no host constituent that liberates conducting protons but take protons from water vapor or hydrogen molecules in ambient gas. The protons bond to oxygen ions, forming substitutional hydroxyl defects, $OH_O^{\bullet}$ which may be supported by the IR study (Hibino *et al.*, 1992):

$$H_2O + V_O^{\bullet\bullet} + O_O^{\times} \xleftrightarrow{K_2} 2OH_O^{\bullet} \quad (2\text{-}15)$$

$$H_2 + 2O_O^{\times} + 2h^{\bullet} \xleftrightarrow{K_3} 2OH_O^{\bullet} \quad (2\text{-}16)$$

For simplicity, the oxygen ion in $OH_O^{\bullet}$ may be considered a part of the perfect lattice and thus denoted as an interstitial proton, $H_i^{\bullet}$.

Fig. 2-5 shows the proton formation in $SrCe_{0.95}Yb_{0.05}O_3$ (SCYb). It suggests the oxygen vacancies formed by doping aliovalent cations play an important role in the formation of proton-conduction.

Two mechanisms were usually applied to describe the proton transportation in oxides: the free proton transport mechanism (Grotthuss type) and the vehicle proton transport mechanism (Norby and Larring, 1996). In free proton transport, protons jump between stationary oxygen ions. Each jump is followed by a rotation around the oxygen ion to get in position for the next jump. The jump is normally considered the rate-limiting step and the rotation is easier. In vehicle mechanism, the proton moves as a passenger on a larger species like oxygen ions. The vehicle mechanism can only account for dominant long-range transport processes in oxides when proceeding on interstitial lattice sites.

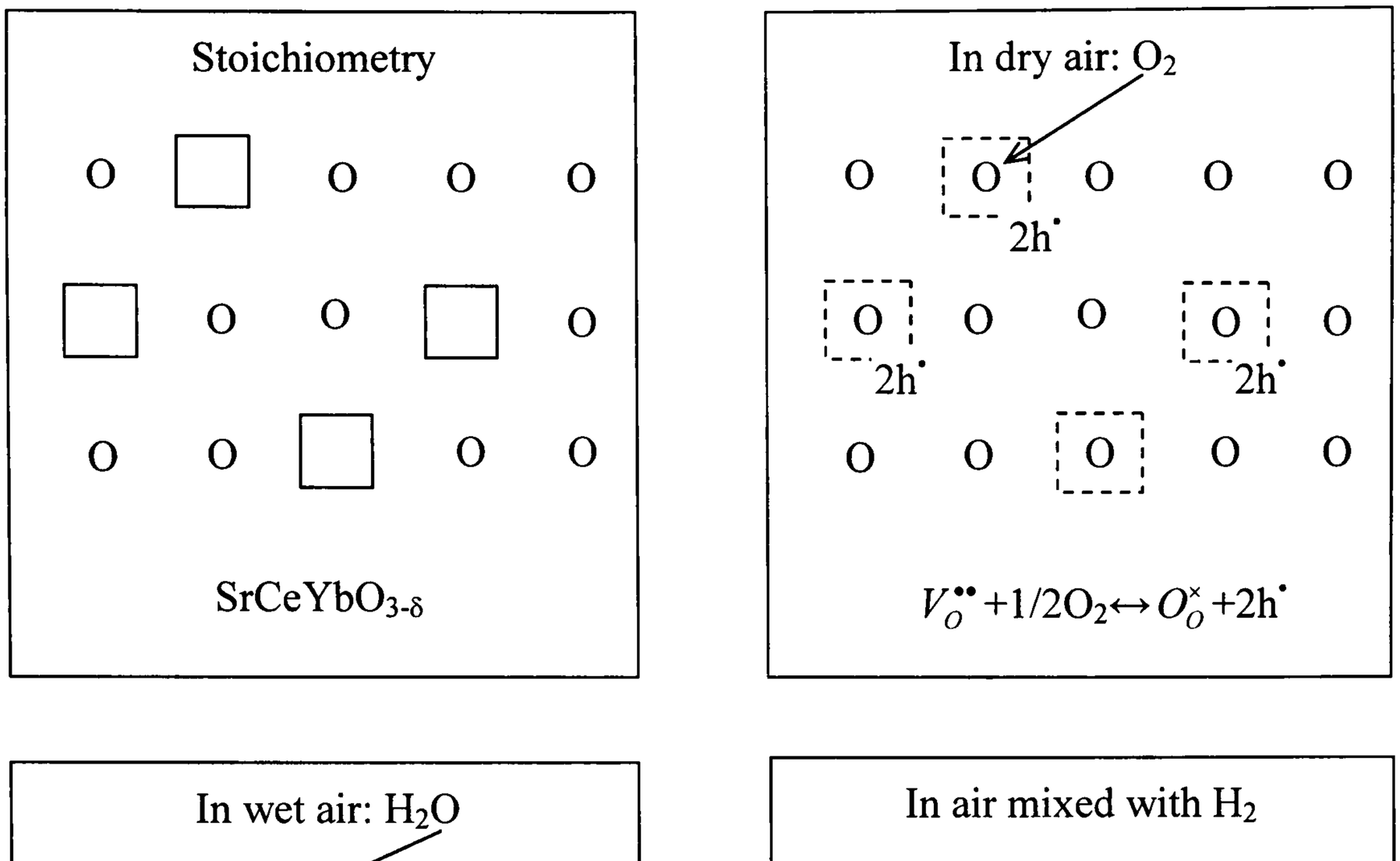


Fig. 2-5 Proton formation in mixed conducting oxides.

Therefore, hydroxygl ion transport cannot provide a dominant conductivity but accomplish minority oxygen transport in a proton conductor. Fig. 2-6 shows the migration of protons in the mixed conducting oxides, following the free proton transport mechanism by changing the OH-bond one after another (Norwick and Vaysleyb, 1997). This mechanism is further supported by physical phenomena observed in the experiments on quasielastic photo scattering and a hole burning experiment (Yugami *et al.*, 1995). The mobility of proton in the oxide is limited by proton transfer between fixed oxygen sites, but is facilitated by the thermal fluctuation of the oxygen ion separation (Kreuer *et al.*, 1995). In fact, the free proton transport is strongly related to the oxygen sublattice vibrations and thus has the activation energies similar to (and generally somewhat lower than) those for oxygen vacancy mobility.

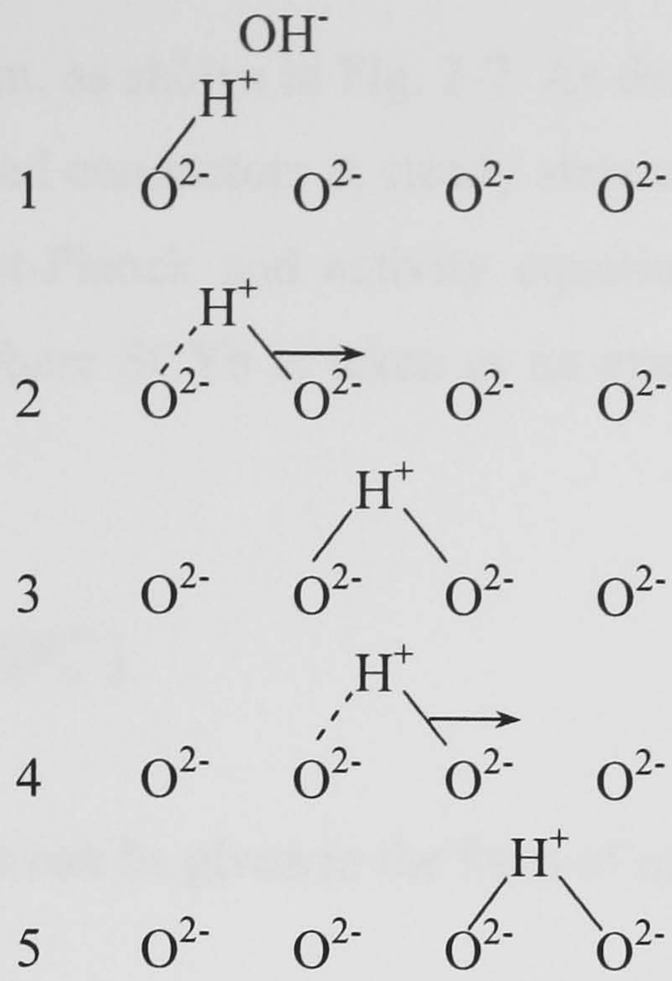


Fig. 2-6 Proton migration in hopping form in $SrCe_{0.95}Yb_{0.05}O_{2.975}$ oxide.

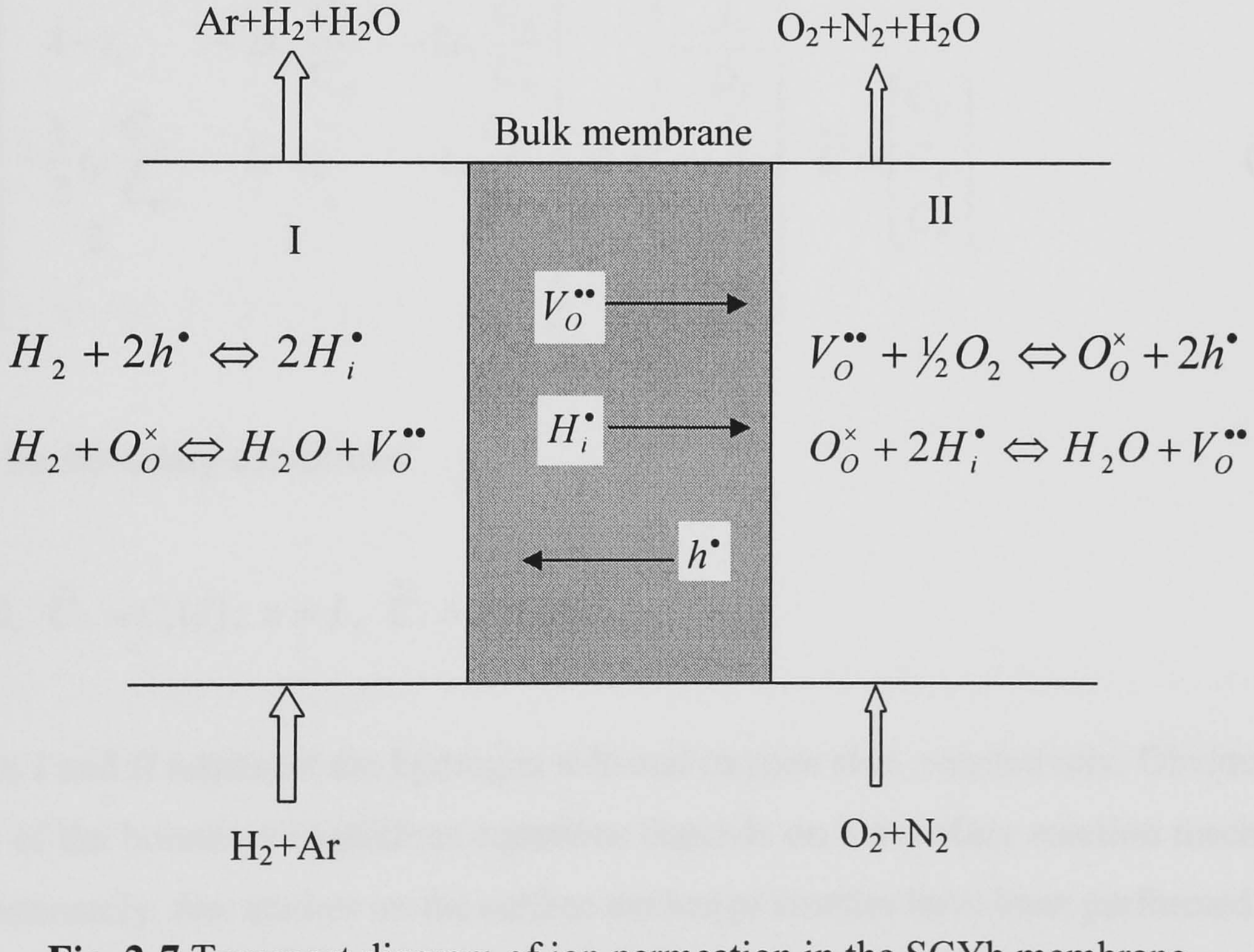


Fig. 2-7 Transport diagram of ion permeation in the SCYb membrane.

2.4.2.2 Transport equations

When the mixed proton conducting membrane is exposed to gaseous hydrogen on one side and to oxygen on the other side at high temperatures (i.e. asymmetrical gas environment), the charged defects would move in certain directions under the

electrochemical gradient, as shown in Fig. 2-7. As described above, the transport flux of charged defects in mixed conductors at steady state can be described by Eq. 2-8, which is derived from Nernst-Planck and activity equations. Along with the local electric neutrality condition, where SCYb is taken as an example and oxygen vacancy, proton and hole are included:

$$[Yb_{Ce}^{'}] = [H_i^{\bullet}] + [h^{\bullet}] + 2[V_O^{\bullet\bullet}] \tag{2-17}$$

The transport equations can be given in the form of matrix as (Tan *et al.*, 2000):

$$\overline{A} \cdot \frac{d\overline{C}}{dx} = \overline{B} \tag{2-18}$$

where,

$$\overline{A} = \begin{bmatrix} 1 - t_V & -2t_p \dfrac{C_V}{C_p} & -2t_h \dfrac{C_V}{C_h} \\ -\dfrac{1}{2} t_V \dfrac{C_p}{C_V} & 1 - t_p & -t_h \dfrac{C_p}{C_h} \\ 2 & 1 & 1 \end{bmatrix} \quad \overline{B} = \begin{bmatrix} -\dfrac{J_V}{D_V} \\ -\dfrac{J_p}{D_p} \\ 0 \end{bmatrix} \quad \overline{C} = \begin{bmatrix} C_V \\ C_p \\ C_h \end{bmatrix} \tag{2-18a}$$

with the boundary conditions:

$$x = 0,\ \overline{C}_i = C_i(I);\ x = L,\ \overline{C}_i = C_i(II) \tag{2-19}$$

where *I* and *II* represent the hydrogen side and oxygen side, respectively. Obviously the form of the boundary conditions equations depends on the surface reaction mechanism. Unfortunately, few studies on the surface exchange kinetics have been performed except for an equilibrium model (Tan *et al.*, 2000), in which all the surface reactions, namely Eqs. 2-5, 2-15 and 2-16, are assumed to be in the equilibrium. As a result, the charged defect concentrations on the membrane surfaces can be given by:

$$C_p(I) = \frac{\sqrt{\left(1 + 1/\sqrt{K_3 p_{H_2}}\right)^2 + 8[Yb_{Ce}']/K_2 p_{H_2O}} - \left(1 + 1/\sqrt{K_3 p_{H_2}}\right)}{4/K_2 p_{H_2O}} \tag{2-20a}$$

$$C_V(I) = C_p(I)^2 / K_2 p_{H_2O} \tag{2-20b}$$

$$C_h(I) = C_p(I) / \sqrt{K_3 p_{H_2}} \tag{2-20c}$$

and

$$C_V(II) = \frac{1}{16}\left[\sqrt{\left(\sqrt{K_1 p_{O_2}^{1/2}} + \sqrt{K_2 p_{H_2O}}\right)^2 + 8[Yb_{Ce}']} - \left(\sqrt{K_1 p_{O_2}^{1/2}} + \sqrt{K_2 p_{H_2O}}\right)\right]^2 \tag{2-21a}$$

$$C_h(II) = \sqrt{K_1 p_{O_2}^{1/2} C_V(II)} \tag{2-21b}$$

$$C_p(II) = \sqrt{K_2 p_{H_2O} C_V(II)} \tag{2-21c}$$

where the equilibrium constants are defined as:

$$K_1 = \frac{C_h^2}{C_V p_{O_2}^{1/2}},\ K_2 = \frac{C_p^2}{C_V p_{H_2O}},\ K_3 = \frac{C_p^2}{C_h^2 p_{H_2}} \tag{2-22}$$

which were studied and measured by Uchida *et al* (1989) and Schober *et al* (1996). Therefore, the proton flux may be obtained by solving numerically the transport Eq. 2-18 with the boundary condition equations.

On a condition that the oxygen ion conductivity is negligible, the transport equation may be reduced to:

$$J_p = -\frac{D_p D_h (C_p + C_h)}{D_p C_p + D_h C_h} \cdot \frac{dC_p}{dx} \tag{2-23}$$

Integration of the above equation gives the proton permeation flux as:

$$J_p = -\frac{D_p D_h \left[C_p(II) + C_h(II)\right]}{L(D_p - D_h)} \cdot \ln\left[\frac{D_p C_p(II) + D_h C_h(II)}{D_p C_p(I) + D_h C_h(I)]}\right] \qquad (2\text{-}23a)$$

For the tubular membranes, the membrane thickness is only replaced by the tube's wall thickness, i.e., (R_o-R_{in}).

2.5 Potential applications in the separations and chemical reactions

Although mixed ionic and electronic conductors have already found possible applications in electrodes of SOFC and gas sensors, some other important applications in the separation and chemical reactions are being investigated (Dyer *et al.*, 2000; Liu *et al.*, 2001a; Iwahara *et al.*, 2004). A several promising applications which attract more attention are discussed in this section.

2.5.1 Air separation for oxygen production

Separation of oxygen from air or other oxygen-containing gas mixtures has an increasing interest in a number of applications which range from small scale oxygen production to large scale combustion processes or partial oxidation of light hydrocarbons (Guizard and Julbe, 1999). Among the current technologies for oxygen separation, membranes can be considered as a clean, efficient and economic means of producing oxygen, and ionic conducting or ionic and electronic conducting ceramic dense membranes are of particular interest because:

- These membranes are 100% selective for oxygen. This results in production of high-purity gas products, which cannot be achieved with even the best organic membranes,
- Additionally, the flux of these membranes is 3-4 orders of magnitude higher than that offered by the organic membranes.

Most materials of interest to produce such ceramic membranes are based on fluorite (ZrO_2 or CeO_2) or perovskite (ABO_3) related structures. Perovskite materials such as

$La_xSr_{1-x}Co_yFe_{1-y}O_{3-\delta}$, are able to provide higher oxygen permeation flux without using an external electric circuit. Air Products has been developing ion or mixed conducting membrane technology for many years, more than 47 U.S. patents were issued at the end of the last century (Stiegel, 1999; Dyer *et al.*, 2000). Recently, this technology has entered the commercial stage with three different processes for oxygen production or supply (Dyer *et al.*, 2000). The first one is electrically driven SEOS^{TM} Oxygen Generator using membranes fabricated from oxygen ion conductor with low electronic conductivity materials. With the aid of an external electric circuit, oxygen can be separated and compressed by this equipment from a low-pressure side to a high-pressure side. The second one is the pressure driven ITM Oxygen using membranes fabricated from mixed conducting materials. A multi-layer membrane structure is designed as shown in Fig. 2-8. An oxygen partial pressure differential imposed across the membrane at high temperature drives oxygen ions from the high partial pressure side to the low partial pressure side. The feed side pressure can be very high. To minimize the mechanical load imposed by the driving force, the process operating conditions constitute a medium-pressure air feed stream, typically 100 – 300 psi and a low-pressure oxygen permeate stream, typically at a fraction of an atmosphere. The cost and performance of cryogenic based case and the ITM oxygen-integrated IGCC facility were compared in Table 2-6.

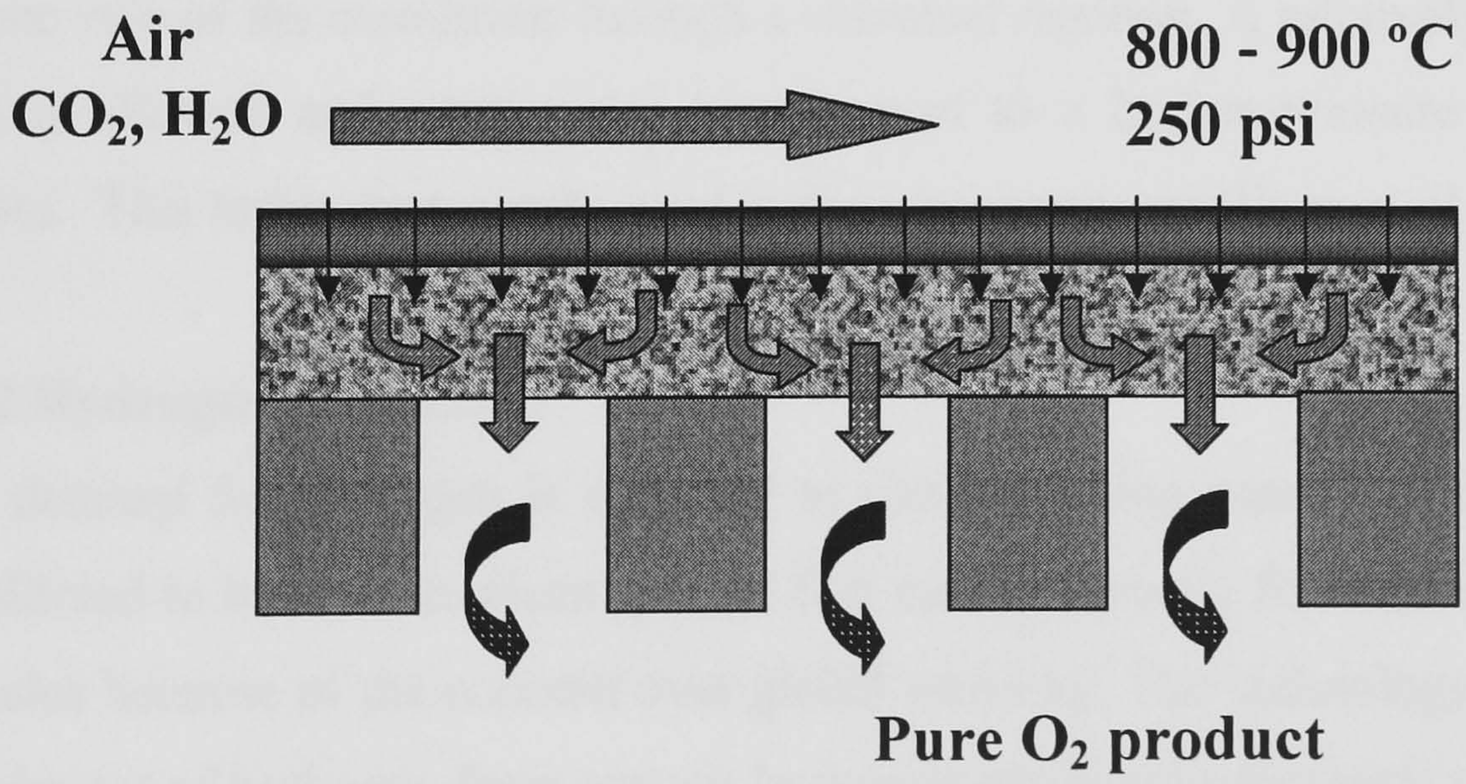


Fig. 2-8 Thin-film support membrane structure. This pressure resistant structure may be fabricated in a flat plate or tubular configuration (Dyer *et al.*, 2000).

Table 2-6 Comparison of cryogenic versus ion transport membrane (ITM) air separation unit (ASU) in integrated gasification combined cycle (IGCC) power applications (Stiegel, 1999).

	Cryogenic based case	**ITM based case**	**Delta**	**% change**
Capital investment, US$m	641	610	-31	-4.8
Capital investment, US$/kw	1567	1453	-114	-7.3
ASU capital investment, US$m	60.2	41.6	-18.6	-31
Power generation, MW	409	420	11	2.7
Thermal efficiency, % HHV	45.2	46.5	1.3	2.9
Cost of electricity, mills/kwh	55.5	51.9	-3.6	-6.5

Potential cost reduction in capital investment and electricity consumption can possibly be achieved with additional integration and increase of capacities of the factory. Better environmental performance would be another benefit of using this technology.

The last process is the chemical potential driven ITM Syngas technology using membranes. It is also fabricated from mixed conducting materials. The driving force for oxygen transport in the membrane is developed by depleting the oxygen partial pressure on one side of the membrane through a chemical reaction. A relatively low pressure air feed is allowed and oxygen can be transport to a higher pressure reaction product stream. This technology can be used in the syngas process (Dyer *et al.*, 2000).

2.5.2 Hydrogen production

The demand for hydrogen is expected to rise in coming years, especially hydrogen is considered to be a future clean fuel (or fuel carrier) directly for both electric power and vehicles because of the concern over global warming. The technology for separation or enrichment of hydrogen from various hydrogen production processes will be required in the near future. Currently a few methods exist to produce hydrogen such as methane partial oxidation ($CH_4 + 1/2O_2 = CO + 2H_2$), steam reforming of natural gas ($CH_4 + H_2O = CO + 3H_2$), the water gas shift reaction ($CO + H_2O = CO_2 + H_2$) or the gasification of heavy carbonaceous materials. These generally proceed at high temperature and/or pressures and produce hydrogen mixed with other gases. The recovery of hydrogen

from high temperature, high pressure streams without the need for cooling or depressurization would enhance the efficiency and performance of systems. Membrane technologies in removal of hydrogen from the reaction mixtures will provide the possibility to improve these methods by shifting the equilibrium towards the production of hydrogen. The purity of recovered hydrogen will also be very high, thus reducing the cost of hydrogen production. There are two main processes, water-gas shift and water dissociation, that have been investigated and thought as having potential for hydrogen production using high temperature mixed proton conducting membranes.

The water-gas shift reaction has been studied extensively as a basis for improving the yield of hydrogen production by Argonne National Laboratory (ANL) and National Energy Technology Laboratory (NETL) of America (Guan *et al.*, 1997;1998a;b; Maiya *et al.*, 2000). A membrane made from $BaCe_{0.8}Y_{0.2}O_{3-\delta}$ (BCY) was studied during their early stage, where they found the electronic conductivity of BCY is still not sufficient to support hydrogen flux (Guan *et al.*, 1997;1998a). In order to increase the electronic conductivity, various dual phase (i.e. 40-50% of a metal is dispersed in a ceramic matrix) membranes were developed (Guan *et al.*, 1998b). The hydrogen permeability was increased by the increase in electronic conductivity, but the stability of the membranes still requires further investigation.

It has also been considered to produce hydrogen from water splitting into oxygen and hydrogen at high temperatures (H_2O (g) = H_2 + $1/2O_2$), because the water resources is almost unlimited. But very low concentrations of hydrogen (0.1%) and oxygen (0.042%) are generated at 1600 °C, because of the small equilibrium constant of the water dissociation reaction (Ihara, 1977). The equilibrium can be disturbed and shifted towards the product side using either an oxygen permeable or hydrogen permeable mixed conducting membrane with an advantage of no electric power or electrical circuitry required compared with the use of steam electrolysis (Naito and Arashi, 1995; Maiya *et al.*, 2000; Balachandran *et al.*, 2004). A ZrO_2-TiO_2-Y_2O_3 membrane was used to separate hydrogen directly from water splitting by Naito and Arashi (Naito and Arashi, 1995). A production rate of 4.5×10^{-7} mol/cm^2.s of hydrogen was reported at 1683 °C. Recently, a production rate of 4.5×10^{-6} mol/cm^2.s of hydrogen has been achieved at a much moderate temperature (< 900 °C) by Balachandran *et al.* (2004)

LON IN. UNIV

using a 0.13-mm-thick dual phase membrane made from 60 vol% gadolinium-doped CeO_2 mixed with a 40vol% metal.

2.5.3 Partial oxidation of methane for syngas production

Of all the potential applications for mixed conducting ceramic membranes, the partial oxidation of methane to syngas ($CO+H_2$) is thought to be one of the most commercially important applications (Balachandran *et al.*, 1997; Dyer *et al.*, 2000). Using mixed-conducting membranes, air is allowed to use as the oxidant without introducing nitrogen in the reaction compartment, which avoids the further purification of product streams. Hence, the syngas production costs can be potentially reduced. Recent progress in applying mixed conducting membranes in partial oxidative methane to syngas has been reported (Foster *et al.*, 1998; Udovich, 1998; Sammells, 1999; Hamakawa *et al.*, 2000; Ritchie *et al.*, 2001; Shao *et al.*, 2001b). Developing a mixed conducting membrane with a high oxygen flux and long term phase stability would be the main challenge for the successful application in the syngas production process. Although membranes made from La-Sr-Co-Fe family materials exhibit high ionic and electronic conductivity, hence the high oxygen permeation rate, considerable doubts on these cobalt-containing perovskite membranes are still remained due to their poor phase stability under a reducing environment. Partial decomposition of the membrane surface exposed to the reducing environment has been observed (Martin and Schmackpfeffer, 1994; Pei *et al.*, 1995; Bouwmeester, 2003). Recently, much effort has been placed on the improvement of the oxygen permeability and chemical stability of the mixed conducting materials (Jin *et al.*, 2000a; Jin *et al.*, 2000b; Maiya *et al.*, 2000; Ritchie *et al.*, 2001), especially, several new materials including Ba-Sr-Co-Fe by Shao *et al.* (Shao *et al.*, 2001a; Shao *et al.*, 2001c) and Ba-Co Fe-Zr by Tong *et al.* (Tong *et al.*, 2002a) have been developed and found to be of good stability in syngas generation. Membranes made from $A_2B_2O_5$ brownmillerite structure materials have been tested by Eltron Research, and a high yield of syngas and long term operation have been reported (Sammells, 1999). The performance of these recently studied materials is summarised in Table 2-7.

Table 2-7 Mixed conducting oxide membrane reactors for oxidation reaction.

Membrane	Temp. (°C)	Stability	Remarks X(CH_4 conversion) S_{CO} (CO selectivity)	Ref.
$La_{0.6}Sr_{0.4}Co_{0.2}Fe_{0.8}O_{3-\delta}$: Tube with catalyst	825-885	Fail, 7 hrs	X>96, S_{CO}>97	(Jin *et al.*, 2000a)
$La_{0.6}Sr_{0.4}Co_{0.2}Fe_{0.8}O_{3-\delta}$: Disk			X=5~25%	(Ishihara *et al.*, 2000)
$La_{0.8}Sr_{0.2}Ga_{0.6}Fe_{0.4}O_{3-\delta}$: Disk		good	X=5~42%; Sco=100%	
$La_{0.5}Sr_{0.5}Fe_{0.8}Ga_{0.2}O_{3-\delta}$: Tube with catalyst	850		X=97%; S_{CO}=100% J_{O2}=0.35 ml/cm^2.min	(Ritchie *et al.*, 2001)
$SrFeCo_{0.5}O_3$: Tube with catalyst	850	1000 hrs	X>99%; S_{CO}>98% J_{O2}=0.3 ml/cm^2.min	(Balachandran *et al.*, 1997; Ma and Balachandran, 1998)
$Sr_4(Fe_{1-x}Co_x)_6O_{13\pm\delta}$: Tube	850	1000 hr	X>98, J_{O2}=10 ml/cm^2.min	(Ma and Balachandran, 1998)
$A_2B_2O_5$ Brownmillerite structure: Tube	900	One year	X=90; S_{CO}>96 J_{O2}=10-12 ml/cm^2.min	(Sammells, 1999)
$BaCo_{0.4}Fe_{0.4}Zr_{0.2}O_{3-\delta}$: Disk with catalyst	850	2200 hrs	X=98; Sco=100 J_{O2}=5.6 ml/cm^2.min	(Tong *et al.*, 2002a)

It was reported that two industrial alliances have been formed in America for enhancing R&D work in order to commercialise ceramic membrane technology for syngas production (Dyer *et al.*, 2000; Lin, 2001). One includes five large global oil and gas companies, BP/Amoco, Praxair, Sasol, Statoil and Phillips Petroleum, helped with a numbers of universities, and the other one is headed by Air Products and Chemicals and Ceramatec, and a number of other industrial partners. The progress achieved by the Air Products group revealed that a 25-50% reduction in the capital cost for syngas is possible if the cryogenic air separation and high-temperature syngas generation can be combined into a single process step (Dyer *et al.*, 2000). Their ITM (ion transport membranes) technology for syngas production is for this purpose. On the other hand, a high active reforming catalyst is required in this reaction because of the poor catalytic properties of the membrane materials themselves.

2.5.4 Oxidative coupling of methane for C_2 products

Methane oxidative coupling to ethylene or ethane (C_2 products) is an interesting reaction which has been studied using conventional catalytic technologies for many years. However, some problems still exist (Amenomiya *et al.*, 1990; Lu *et al.*, 2000a). One of the main problems is the selection of oxidant, which is the same problem as in the partial oxidative of methane for syngas production, i.e. when air is used as an oxidant, the large amount of introduced nitrogen is not easy to separate from the mixtures of methane or products. Another problem is the formation of CO_x in the gas phase reaction of methyl radicals and oxygen. In addition, the yield of C_2 products was limited to about 25% in conventional reactors, lower than the economically attractive C_2 yield threshold of 30%.

Dense mixed conducting ceramic membranes have an excellent permselectivity towards oxygen. Therefore, air is allowed to be used directly as an oxidant during the reaction without any nitrogen introduced into the reaction compartment. On the other hand, the distinct oxygen transport mechanism of the mixed conducting ceramic membranes delivers the oxygen into the reaction compartment in a form of dissociated and ionized oxygen. The ionized oxygen reacts with methane on the membrane surface would follow different reaction mechanism so that the formation of CO_x from by-reactions due to the presence of gas phase oxygen could be minimized, and thus an increased selectivity of C_2 hydrocarbons could be expected. Recently, a great deal of efforts has

been placed on oxidative methane coupling using dense oxygen permeable ceramic membranes to improve the methane coupling reaction. Hazbun (1988;1989) conducted the methane oxidative coupling reaction for C_2 compound conversion using a two layer tubular membrane in the earlier studies, a $10\%Y_2O_3$-$89\%ZrO_2$-$1\%TiO_2$ layer for oxygen permeation and a $LiO/MgO/ZrO_2$ layer as the catalyst. A product yield of 20 to 25 % C_2 compounds achieved with 50 to 60% selectivity and 35 to 45 % conversion at 700 – 750 °C showed a feasibility of using a dense membrane reactor for oxidative coupling of methane. Since then, a variety of mixed conducting perovskite-type oxides have been reported as promising OCM catalysts, which are very active and selective in converting methane into C_2 (C_2H_4, C_2H_6) products (Nomura *et al.*, 1993; Omata *et al.*, 1994; Lin and Zheng, 1996). $La_{0.2}Sr_{0.8}CoO_3$ showed good OCM catalytic properties in terms of C_2 yield (>14%) and selectivity (>50%), while $SrCo_{1-x}Fe_xO_3$ showed very poor OCM catalytic properties (Lin and Zeng, 1996). $La_{1-x}Sr_xCo_{1-y}Fe_yO_{3-\delta}$ series materials were also investigated in the OCM reactions and higher yields of C_2 products were observed (ten Elshof *et al.*, 1995; Zeng *et al.*, 1998). Zeng *et al* (1998) found that the surface catalytic properties for OCM of LSCF membranes strongly depend on the oxygen activity of the membrane surface exposed to the methane stream. A more comprehensive analysis of the performance of the oxygen permeable membranes made from perovskite oxides formulae $(La_{1-x}A_x)(Co_{1-y}Fe_y)O_{3-\delta}$ for methane coupling was performed by Xu and Thomson (1997).

More recently, other mixed conducting oxides were studied for OCM including $Ba_{0.5}Sr_{0.5}Co_{0.8}Fe_{0.2}O_{3-\delta}$ (BSCF) (Shao *et al.*, 2001a) and $BaCe_{0.8}Gd_{0.2}O_{3-\delta}$ (Lu *et al.*, 2000a) and and show promising performances in OCM reactions. C_2 hydrocarbon selectivity of $Ba_{0.5}Sr_{0.5}Co_{0.8}Fe_{0.2}O_{3-\delta}$ is from 40–70%, while the maximum yield to C_2 of $BaCe_{0.8}Gd_{0.2}O_{3-\delta}$ attained is 16%. Some reported results are summarized in Table 2-8.

Compared with mixed conducting perovskite materials, membrane made from other materials, such as, $Bi_{1.5}Y_{0.3}Sm_{0.2}O_{3-\delta}$ (Akin and Lin, 2002) also showed good performance in methane coupling reaction. A 35% yield of C_2 product was obtained using a $Bi_{1.5}Y_{0.3}Sm_{0.2}O_{3-\delta}$ membrane reactor. The material $Bi_{1.5}Y_{0.3}Sm_{0.2}O_{3-\delta}$ was found to be not only highly oxygen permeable and catalytically active for OCM but also chemically and mechanically stable under OCM conditions.

Table 2-8 Mixed conducting oxide membrane reactors for methane oxidative coupling.

Membrane	Temp. (°C)	Reaction	Remarks Y (yield) S (selectivity)	Ref
$La_{0.8}Sr_{0.2}CoO_3$: Disk	800 – 850	No Cat.	Y_{C2}= 12-14 S_{C2}=40-56%	(Lin and Zheng, 1996)
$La_{0.8}Sr_{0.2}Co_{0.6}Fe_{0.4}O_{3-\delta}$ Dsk 1.85 mm,	850	No Cat.	Y_{C2}=10-18%, S_{C2}=70-90%	(Zeng *et al.*, 1998)
$La_{0.6}Sr_{0.4}Co_{0.8}Fe_{0.2}O_{3-\delta}$ Disk 0.5-2 mm		No Cat.	Y_{C2}=13%, S_{C2}=70%	(ten Elshof *et al.*, 1995)
$BaCe_{0.8}Gd_{0.2}O_3$: Tube 0.7mm		No Cat.	Y_{C2}=16.5%	(Lu *et al.*, 2000a)
$Ba_{0.5}Sr_{0.5}Co_{0.8}Fe_{0.2}O_3$: Disk		No Cat.	X=40-70; S_{C2}=0.5-0.3	(Shao *et al.*, 2001a)
$La_{0.2}Sr_{0.8}CoO_{3-\delta}$	800	With Cat.	Y_{C2}=14%, S_{C2}=40%	(Lin and Zeng, 1996)
$SrCo_{0.8}Fe_{0.2}O_{3-\delta}$	850	With Cat.	Y_{C2}=6.3%, S_{C2}=30.4%	(Lin and Zeng, 1996)

There is still a gap to be closed between the currently achieved yield results and desirable industrial values. It is possible to increase the yield by matching the oxygen permeation rate of the membrane and surface catalytic activation of the methane on the membrane surface because the overall C_2 yield is determined by the combined effects of the both important factors. When the oxygen permeation rate is greater than the rate consumed in the methane coupling, deep oxidation of methyl radical and C_2 products to CO_x would occur and the C_2 yield would be reduced. The surface catalytic activation of the methane must be improved while the oxygen permeation rate is increased, and this may be performed by fixing a catalyst on the membrane surface.

2.5.5 Non-oxidative coupling of methane for C_2 products

Non-oxidative coupling of methane to produce C_2 products is recently attracted attention (Gellings and Bouwmeester, 2000; Liu *et al.*, 2001a). This reaction is equilibrium limited and may be improved by using membranes (Chiang *et al.*, 1991;

Hamakawa *et al.*, 1993;1994; Marnellos *et al.*, 1997; White *et al.*, 1998; Li *et al.*, 2002). The principle idea is that hydrogen in the form of protons produced during dehydrogenation reaction of methane is removed continuously using a mixed proton-hole conducting membrane, the equilibrium of the reaction is thus disturbed so that a potential and significant improvement of C_2 yield by shifting the conversion towards the product side can be achieved. On the other hand, CO_x by-product can also be restrained since no oxygen is introduced into the methane compartment and thus, C_2 selectivity is possible to achieve up to 100% (Chiang *et al.*, 1991). Recently, some progress has been achieved in this research area and the results are listed in Table 2-9.

Table 2-9 Performance data of proton conducting membranes in methane coupling reaction.

Membrane	**T (°C)**	**Yield C_2 (%)**	**Selectivity (%)**	**Reference**
$SrCe_{0.95}Yb_{0.05}O_{3-\delta}$: Disk 0.75mm	650-750	0.17		(Chiang *et al.*, 1991;1993)
$SrCe_{0.95}Yb_{0.05}O_{3-\delta}$: Tube, 1mm	900	0.15-0.54	100	(Hamakawa *et al.*, 1993;1994)
$SrCe_{0.95}Yb_{0.05}O_{3-\delta}$: Disk 1 mm	815-820	0.1	100	(Woldmann and Sokolovskii, 1991)
$BaCe_{0.95}Mn_{0.05}O_{3-\delta}$: Tube 1mm	950, no catalyst	Ethylene production of 0.2 ml(STP)/cm^2.min	100	(White *et al.*, 1998)

Further research interests in applying mixed proton-hole conducting ceramic membranes in direct coupling of methane into C_2 products has been focused on preparation of the membranes with ultrathin separation layer and large ratio of membrane area to volume of membrane module, as well as the improvement of catalytic properties of the membranes through loading an appropriate catalyst on the membranes by various methods (Liu *et al.*, 2001a). The preparation of ultrathin ceramic membrane is, so far, a big challenge in membrane fabrication technology.

2.5.6 Other applications

Other attractive and possible applications include the reduction of sulphur and nitrogen oxides, chemical oxidation reactions, hydrogen sulphide and ammonia decomposition, as well as hydrogenation and dehydrogenation reactions (White *et al.*, 1998; Kobayashi *et al.*, 2000).

2.6 Further development-challenges and prospects

Although significant advances have been made in the last decade, there are still many challenges that have to be faced so as to allow the utilization of ceramic mixed conducting membranes in the practical applications mentioned above.

First of all, the permeation rate of either oxygen or hydrogen through the membranes must be high enough to satisfy the requirements of industrial applications. Currently, most of the related research work uses small disc membranes, as they are relatively easier to fabricate and have been used to test the properties of the materials during the stage of material development and screening. Such disk membranes only supply very limited membrane area and are also too thick. Some researchers use tubular membranes because the tubular membranes provide a relatively large active area compared to disk membranes. However, transport resistance of the tubular membranes is very high due to their symmetric structure. The rate of oxygen or hydrogen permeation depends on the thickness of the membrane, usually being inversed relation to the membrane thickness. Therefore, it is necessary to develop a technique in fabricating thin membranes to maximize the permeation flux. Many attempts are being made to reduce the thickness of the membranes (Itoh *et al.*, 1997; Kosacki and Anderson, 1997; Lee *et al.*, 1997a; Jin *et al.*, 2001; Hamakawa *et al.*, 2002). Most of these efforts were based on the concept of composite membranes where a dense thin film is coated on a porous substrate by various methods such as spin-coating or dip-coating, chemical vapour deposition and some other methods. The film thickness could be well controlled. About 2 μm of thickness of the membrane was obtained by spin coating of the $SrCe_{0.95}Yb_{0.05}O_{3-\delta}$ suspension on a porous $SrZr_{0.95}Y_{0.05}O_{3-\delta}$ substrate (Hamakawa *et al.*, 2002). Hydrogen permeation rate is as much as 500 times higher than that of 1 mm disk and reached 6×10^{-4} mol/cm^2.min. When the toplayer material is different from substrate material, the toplayer is usually unstable especially at elevated temperature. Jin *et al* (2001)

successfully prepared a crack-free asymmetric membrane using the same materials for both toplayer and substrate by simply coating a slurry containing $La_{0.6}Sr_{0.4}Co_{0.2}Fe_{0.8}O_{3-\delta}$ powders directly on the surface of a green support, followed by a sintering process. This asymmetric membrane has a 200 μm thick dense toplayer and exhibited the oxygen flux about three to four times higher than that of a 2 mm dense disk. The same idea was also taken and applied by Air Products to produce a large membrane consisting of a dense thin top layer and a thick porous support. A multiple planner stack module containing such membranes has been used in a pilot plant for air separation (see section 5.1) (Stiegel, 1999; Dyer *et al.*, 2000). Although a multiple planar stack can be employed to enlarge the membrane area to that required at a plant scale (Dyer *et al.*, 2000), many problems such as sealing, connecting and pressure-resistance have to be faced. Also the packing density of both planner stack and tubular membrane modules is still too low and leads to a high fabrication cost.

Hollow fibre membranes are, in this context, a good alternative. So far, ceramic hollow fibre membranes are not commercially available mainly due to the lack of techniques available to produce the ceramic membrane with a thin and dense separation layer in a hollow fibre form. Hollow fibre membranes are frequently produced from polymeric materials and can provide the largest membrane area per unit packing volume, as high as 8000-10000 m^2/m^3 of packing density has been achieved. However, this configuration is seldom used in ceramic membranes because of the poor mechanical strength. An early effort was made for gas separation by the development of glass hollow fibre membranes (Way and Roberts, 1992), but the membranes were too fragile to be used in industrial processes. Many other attempts have been made to develop fabrication techniques for making hollow fibre ceramic membranes (Smid *et al.*, 1996; Brinkman *et al.*, 2000; Luyten *et al.*, 2000; Liu *et al.*, 2001b; Tan *et al.*, 2001; Liu and Li, 2003; Liu *et al.*, 2003; Xu *et al.*, 2004). Brinkman (2000) developed aluminium-oxide and silica-nitride hollow fibre membranes using an extrusion technique, but these membranes are porous and symmetric. One step multi-layer inorganic hollow fibres were also explored using a triple orifice spinneret (de Jong *et al.*, 2004). Xu *et al* (2004) reported a composite hollow fibre membrane by synthesis of NaA zeolite on a porous ceramic hollow fibre. Unfortunately, the fabrication of such a thin membrane presents considerable difficulties such as mismatch of the ceramic material with the porous substrate. Luyten *et al* (2000) synthesised dense hollow fibre $LaSrCoFeO_{3-x}$ membranes

and porous multilayer substrates, but no performance was reported. A several ceramic hollow fibre membranes prepared from different materials were developed by Li's group (Liu *et al.*, 2001b; Tan *et al.*, 2001; Liu and Li, 2003; Liu *et al.*, 2003; Liu and Li, 2005; Tan *et al.*, 2005) using a combined phase inversion and sintering method where a typical asymmetric structure is obtained because of the phase inversion. The fabrication process by the phase inversion is fast and simple. The characteristics of the hollow fibres produced the via phase inversion are that the membrane structure is asymmetric and possesses a very thin toplayer which is self supported by a porous sub-layer. In their research, the phase inversion technique was applied using a polymer solution containing suspended ceramic powders. A dry-jet wet spinning process was carried out to spin hollow fibre precursors, which were then sintered at high temperature to obtain performance and strength. Effects of sintering temperature and ratio of polymer to ceramic powder on the gas tight property and strength were investigated. Secondly, the membrane materials must possess good thermal and chemical stability whilst also maintaining high ionic and electronic conductivities. Also, for use in chemical reactions, a high catalytic activity is also desirable. Therefore, development of membrane materials is always an important challenge in future. Finally, design and engineering problems such as connecting and sealing of the membrane systems at high temperatures have to overcome before the extensive commercial applications can be realized.

2.7 Conclusions

The recent development of mixed conducting materials, membranes and its applications in separations and catalytic chemical reactions has been reviewed. These novel ceramic materials have shown promising applications in gas separation such as production of purified oxygen from air and in utilization of natural gas such as partial oxidation of methane for syngas production or methane coupling reactions. Although significant progresses have been achieved, there is still a long way to go before the successful applications of these ceramic membranes in separation/reaction can be made in industrial scales. Significant achievements in this new research area would become feasible if joint efforts were established from both material scientists and chemical engineers.

Notation

a	-	Activity of charged defect
C	-	Defect concentration, mol•cm^{-3}
D	-	Effective diffusivity of defect, cm^2•s^{-1}
F	-	Faraday constant
J	-	Permeation flux of defect, $\mathrm{mol \cdot cm^{-2} \cdot s^{-1}}$
k_r	-	Reverse surface reaction rate constant of eq. (12), mol/(m^2 s)
k_f	-	Forward surface reaction rate constant of eq. (12), m/(Pa$^{0.5}$ s)
K_1	-	Equilibrium constant of eq. (5), $\mathrm{Pa^{-1/2} \cdot mol \cdot cm^{-3}}$
K_2	-	Equilibrium constant of eq. (15), $\mathrm{Pa^{-1} \cdot mol \cdot cm^{-3}}$
K_3	-	Equilibrium constant of eq. (16), Pa^{-1}
L	-	Thickness of membrane, cm
l	-	Length variable of tubular membrane, cm
p	-	Gas partial pressure, Pa
p'_{O_2}	-	Oxygen partial pressures in the shell side, Pa
p''_{O_2}	-	Oxygen partial pressures in the lumen side, Pa
r	-	Ionic radius
R	-	Ideal gas constant
R_{in}	-	Inner radius of tubular membrane, cm
R_m	-	Log-mean radius of tubular membrane, $R_m = (R_o - R_{in}) / \ln(R_o / R_{in})$
R_o	-	Outer radius of tubular membrane, cm
t	-	Transference number of defect
T	-	Temperature, K
$V_O^{\cdot\cdot}$	-	Oxygen vacancy
x	-	Location coordinate, cm
Yb_{Ce}'	-	Substitution of Yb for Ce
z	-	Charge number of defect

Greek letters

σ	-	Conductivity
μ	-	Chemical potential
μ_i^0	-	Standard chemical potential

ϕ - Electric potential

υ - Local velocity of inert defect

Subscripts

e - Electron

h - Electron hole

i, j - Hole, proton or vacancy

p - Proton

V - Vacancy

o - Oxygen

References

Aasland, S., I. L. Tangen, K. Wiik and R. Odegard (2000). Oxygen permeation of $SrFe_{0.67}Co_{0.33}O_{3-\delta}$, *Solid State Ionics*, **Vol.** 135, **pp.** 713-717.

Akin, F. T. and Y. S. Lin (2002). Oxidative coupling of methane in dense ceramic membrane reactor with high yields, *AIChE J.*, **Vol.** 48, **pp.** 2298-2306.

Akin, F. T. and Y. S. J. Lin (2004). Oxygen permeation through oxygen ionic or mixed-conducting ceramic membranes with chemical reactions, *J. Membr. Sci.*, **Vol.** 231, **pp.** 133-146.

Amenomiya, Y., V. I. Birss, M. Goledzinowski, G. J. and A. R. Sanger (1990). Conversion of methane by oxidative coupling, *Cata. Rew. Sci. Eng.*, **Vol.** 32, **pp.** 163-227.

Armstrong, T., F. Prado and A. Manthiram (2001). Synthesis, crystal chemistry, and oxygen permeation properties of $LaSr_3Fe_{3-x}Co_xO_{10}$ (0 x 1.5), *Solid State Ionics*, **Vol.** 140, **pp.** 89-96.

Armstrong, T., F. Prado, Y. Xia and A. Manthiram (2000). Role of perovskite phase on the oxygen permeation properties of the $Sr_4Fe_{6-x}Co_xO_{13+}$ system, *J., Electrochem. Soc.*, **Vol.** 147, **pp.** 435-438.

Balachandran, U., J. T. Dusek, P. S. Maiya, B. Ma, R. L. Mieville, M. S. Kleefisch and C. A. Udovich (1997). Ceramic membrane reactor for converting methane to syngas., *Catal. Today*, **Vol.** 36, **pp.** 265-272.

Balachandran, U., J. T. Dusek, R. L. Meieville, R. B. Poeppel, M. S. Kleefisch, S. Pei, T. P. Kobylinski, C. A. Udovich and A. C. Bose (1995). Dense ceramic membranes for partiasl oxidation of methane to syngas, *Applied Catal. A: Gen.*, **Vol.** 133, **pp.** 19-29.

Balachandran, U., T. H. Lee, S. Wang and S. E. Dorris (2004). Use of mixed conducting membranes to produce hydrogen by water dissociation, *International Journal of Hydrogen Energy*, **Vol.** 29, **pp.** 291-296.

Balachandran, U., B. Ma, P. S. Maiya, R. L. Mieville, J. T. Dusek, J. J. Picciolo, J. Guan , Dorris S.E. and M. Liu (1998). Development of mixed-conducting oxides for gas separation, *Solid State Ionics*, **Vol.** 108, **pp.** 363-370.

Bochkov, D. M., V. V. Kharton, A. V. Kovalevsky, A. P. Viskup and E. N. Naumovich (1999). Oxygen permeability of $La_2Cu(Co)O_{4+\delta}$ solid solutions, *Solid State Ionics*, **Vol.** 120, **pp.** 281-288.

Bouwmeester, H. J. M. (2003). Dense ceramic membranes for methane conversion, *Catalysis Today*, **Vol.** 82, **pp.** 141-150.

Bouwmeester, H. J. M. and A. J. Burggraaf (1996). Dense ceramic membranes for oxygen separation, in *Fundamentals of Inorganic Membrane Science and Technology*, **Vol.**, edited by A. J. Burggraaf and L. Cot, **pp**. **43pp.** 435-528, Elsevier Science B.V., Amsterdam.

Bouwmeester, H. J. M., H. Kruidhof and A. J. Burggraaf (1994). Importance of the surface exchange kinetics as rate limiting step in oxygen permeation through mixed-conducting oxides, *Solid State Ionics*, **Vol.** 72, **pp.** 185-194.

Brinkman, H. W., J. P. G. M. van Eijk, H. A. Meinema and R. A. Terpstra (2000). Processing and characteristics of TNO's hollow fibre ceramic membranes, *Int. Ceram.*, **Vol.** 1, **pp.** 45-47.

Chen, C. H., H. J. M. Bouwmeester, R. H. E. van Doorn, H. Kruidhof and A. J. Burggraaf (1997a). Oxygen permeation of $La_{0.3}Sr_{0.7}CoO_{3-a}$, *Solid State Ionics*, **Vol.** 98, **pp.** 7-13.

Chen, C. S., B. A. Boukamp, H. J. M. Bouwmeester, G. Z. Cao, H. Kruidhof, A. J. A. Winnubst and A. J. Burggraaf (1995). Microstructural development, electrical

properties and oxygen permeation of zirconia-palladium composites, *Solid State Ionics*, **Vol.** 76, **pp.** 23-28.

Chen, C. S. and A. J. Burggraaf (1999). Stabilized bismuth oxide±noble metal mixed conducting composites as high temperature oxygen separation membranes, *J. Appl. Electrochem.*, **Vol.** 29, **pp.** 355-360.

Chen, C. S., H. Kruidhof, H. J. M. Bouwmeestera, H. Verweij and A. J. Burggraaf (1996). Oxygen permeation through oxygen ion oxide-noble metal dualphase composites, *Solid State Ionics*, **Vol.** 86-88, **pp.** 569-572.

Chen, C. S., H. Kruidhof, H. J. M. Bouwmeestera, H. Verweij and A. J. Burggraaf (1997b). Thickness dependence of oxygen permeation through stabilized bismuth oxide-silver composites, *Solid State Ionics*, **Vol.** 99, **pp.** 215-219.

Chiang, P. H., D. Eng and M. Stoukides (1991). Electrocatalytic methane dimerization with a Yb-doped $SrCeO_3$ electrolytes, *J. Electrochem. Soc.*, **Vol.** 138, **pp.** L11.

Chiang, P. H., D. Eng and M. Stoukides (1993). Electrocatalytic nonoxidative dimerization of methane over Ag electrodes, *Solid State Ionics*, **Vol.** 61, **pp.** 99-103.

de Jong, J., N. E. Benes, G. H. Koops and M. Wessling (2004). Toward single step production of muti-layer inorganic hollow fibres, *J. Membr. Sci.*, **Vol.** 239, **pp.** 2656-2669.

Dyer, P. N., R. E. Richards, S. L. Russek and D. M. Taylor (2000). Ion transport membrane technology for oxygen separation and syngas production, *Solid State Ionics*, **Vol.** 134, **pp.** 21-33.

Foster, E. P., P. J. A. Tijm and D. L. Bennett (1998). Advanced gas-to-liquids processes for syngas and liquid-phase conversion, *Stud. Surf. Sci. Catal.*, **Vol.** 119, **pp.** 867-874.

Fukui, T., S. Ohara and Kawatsu (1999). Ionic conductivity of gadolinium-doped barium praseodymium oxide, *Solid State Ionics*, **Vol.** 116, **pp.** 331-337.

Galasso, F. S. (1969). *Structure, Properties and Preparation of Perovskite-type Compounds*, Pergamon Press, London.

Gellings, P. J. and H. J. M. Bouwmeester (1992). Ion and mixed-conducting oxides as catalysts, *Catal. Today*, **Vol.** 12, **pp.** 1-101.

Gellings, P. J. and H. J. M. Bouwmeester (2000). Solid state aspects of oxidation catalysis, *Catal. Today*, **Vol.** 58, **pp.** 1-53.

Gopel, W., T. A. Jones, M. Kleitz, I. Lundstrom and T. Seiyama (1991). *Sensors: A Comprehensive Survey, Chemical and Biochemical Sensors*, VCH, New York.

Goto, K. S. (1988). *Solide state electrochemistry and its applications to sensors and electronic devices*, Elsevier, Amsterdam-Oxford-New York-Tokyo.

Guan, J., S. E. Dorris, U. Balachandran and M. Liu (1997). Transport properties of $BaCe_{0.95}Y_{0.05}O_{3-\delta}$ mixed conductors for hydrogen separation, *Solid State Ionics*, **Vol.** 100, **pp.** 45-52.

Guan, J., S. E. Dorris, U. Balachandran and M. Liu (1998a). The effects of dopants and A:B site nonstoichiometry on properties of perovskite-type proton conductors, *J. Electrochem. Soc.*, **Vol.** 145, **pp.** 1780-1786.

Guan, J., S. E. Dorris, U. Balachandran and M. Liu (1998b). Transport properties of $BaCe_{0.95}Y_{0.05}O_{3-\delta}$ and its application for hydrogen separation, *Solid State Ionics*, **Vol.** 110, **pp.** 303-310.

Guizard, C. G. and A. C. Julbe (1999). Nanophase ceramic ion transport membranes for oxygen separation and gas stream enrichment, in *Recent Advances in Gas Separation by Microporous Ceramic Membranes*, **Vol.**, edited by N. K. Kanellopoulos, **pp**. **43pp.** 435-469.

Hamakawa, S., T. Hayakawa, K. Suzuki, K. Murata, K. Takehira, S. Yoshino, J. Nakamura and T. Uchijima (2000). Methane conversion into synthesis gas using an electrochemical membrane reactor, *Solid State Ionics*, **Vol.** 136-137, **pp.** 761-766.

Hamakawa, S., T. Hibino and H. Iwahara (1993). Electrochemical methane coupling using protonic conductors, *J. Electrochem. Soc.*, **Vol.** 140, **pp.** 459-462.

Hamakawa, S., T. Hibino and H. Iwahara (1994). Electrochemical methane coupling in a proton-hole mixed conductor and its application to a membrane reactor, *J. Electrochem. Soc.*, **Vol.** 141, **pp.** 1720-1726.

Hamakawa, S., L. Li, A. Li and E. Iglesia (2002). Synthesis and hydrogen permeation properties of membranes based on dense $SrCe_{0.95}Yb_{0.05}O_{3-a}$, thin film, *Solid State Ionics*, **Vol.** 148, **pp.** 71-81.

Han, J., Y. Zeng and Y. S. Lin (1997). Oxygen permeation through fluorite-type bismuth-yttrium-copper oxide membranes, *J. Membr. Sci.*,, **Vol.** 132, **pp.** 235-243.

Hayashi, H., H. Inaba, M. Matsuyama, N. G. Lan, M. Dokiya and H. Tagawa (1999). Structural consideration on the ionic conductivity of perovskite-type oxides, *Solid State Ionics*, **Vol.** 122, **pp.** 1-15.

Hazbun, E. A. (1988). US4791079,

Hazbun, E. A. (1989). US4827071,

Hibino, T., K. Mizutani, T. Yajima and H. Iwahara (1992). Characterization of proton in Y-doped $SrZrO_3$ polycrystal by IR spectroscopy, *Solid State Ionics*, **Vol.** 58, **pp.** 85-88.

Huang, H. H., M. Ishigame and S. Shin (1991). Protonic conduction in the single crystals of Y-doped $SrZrO_3$, *Solid State Ionics*, **Vol.** 47, **pp.** 251-255.

Huang, K., R. S. Tichy and J. B. Goodenough (1998). Superior perovskite oxide-ion conductor; strontium- and magnesium-doped $LaGaO_3$: I, Phase relationships and electrical properties, *J. Am. Ceram. Soc.*, **Vol.** 81, **pp.** 2565-2575.

Ihara, S. (1977). Approximations for the thermodynamic prperties of high-temperature dissociated water vapour, *Bull. Electrotech. Lab.*, **Vol.** 41, **pp.** 259-280.

Ikeguchi, M., Y. Yoshino, K. Kanie, M. Nomura, E. Kikuchi and M. Matsukata (2003). Effect of preparation method on oxygen permeation properties of $SrFeCo_{0.5}O_x$ membrane, *Sepn. Pur. Tech.*, **Vol.** 32, **pp.** 313-318.

Ishihara, T., J. A. Kilner, M. Honda, N. Sakai, H. Yokokawa and Y. Takita (1998). Oxygen surface exchange and diffusion in $LaGaO_3$ based perovskite type oxides, *Solid State Ionics*, **Vol.** 113-115, **pp.** 593-600.

Ishihara, T., H. Matsuda and Y. Takita (1994). Doped $LaGaO_3$ perovskite type oxide as a new oxide ionic conductor, *J. Am. Chem. Soc.*, **Vol.** 116, **pp.** 3801-3803.

Ishihara, T., T. Yamada, H. Arikawa, H. Nishiguchi and Y. Takita (2000). Mixed electronic-oxide ionic conductivity and oxygen permeating property of Fe-, Co- or Ni-doped $LaGaO_3$ perovskite oxide, *Solid State Ionics*, **Vol.** 135, **pp.** 631-636.

Itoh, H., H. Asano, K. Fukuroi, M. Nagata and H. Iwahara (1997). Spin coating of a $Ca(Ti,Fe)O_3$ dense film on a porous substrate for electrochemical permeation of oxygen, *J. Am. Ceram. Soc.*, **Vol.** 80, **pp.** 1359-1365.

Iwahara, H. (1995). Technological challenges in the application of proton conducting ceramics, *Solid State Ionics*, **Vol.** 77, **pp.** 289-298.

Iwahara, H. (1996). Proton conducting ceramics and their applications, *Solid State Ionics*, **Vol.** 86-88, **pp.** 9-15.

Iwahara, H., Y. Asakura, K. Katahira and M. Tanaka (2004). Prospect of hydrogen technology using proton-conducting ceramics, *Solid State Ionics*, **Vol.** 168, **pp.** 299-310.

Iwahara, H., T. Esaka, H. Uchida and N. Maeda (1981). Proton conduction in sintered oxides and its applications to steam electrolysis for hydrogen production, *Solid State Ionics*, **Vol.** 3-4, **pp.** 359-363.

Iwahara, H., H. Uchida and S. Tanaka (1983). High temperature type proton conductor based on $SrCeO_3$ and its application to solid electrolyte fuel cells, *Solid State Ionics*, **Vol.** 9-10, **pp.** 1021-1026.

Iwahara, H., T. Yajima, T. Hibino, K. Ozaki and H. Suzuki (1993). Protonic conduction in calcium, strontium and barium zirconates, *Solid State Ionics*, **Vol.** 61, **pp.** 65-69.

Jin, W., X. Gu, S. Li, P. Huang, N. Xu and J. Shi (2000a). Experimental and simulation study on a catalyst packed tubular dense membrane reactor for partial oxidation of methane to syngas, *Chem. Eng. Sci.*, **Vol.** 55, **pp.** 2617-2625.

Jin, W., S. Li, P. Huang, N. Xu and J. Shi (2001). Preparation of an asymmetric perovskite-type membrane and its oxygen permeability, *J. Membr. Sci.*, **Vol.** 185, **pp.** 237-243.

Jin, W., S. Li, P. Huang, N. Xu, J. Shi and Y. S. Lin (2000b). Tubular lanthanum cobaltite perovskite-type membrane reactors for partial oxidation of methane to syngas, *J. Membr. Sci.*, **Vol.** 166, **pp.** 13-22.

Jurado, J. R., F. M. Figueiredo and J. R. Frade (1999). Overpotential terms on the electrochemical permeability of $Sr_{0.97}(Ti,Fe)O_{3-y}$ materials, *Solid State Ionics*, **Vol.** 122, **pp.** 197-204.

Kharton, V., A. P. Vispup, E. N. Naumovich and N. M. Lapchuk (1997a). Mixed electronic and ionic conductivity of $LaCo(M)O_3$ (M = Ga, Cr, Fe or Ni): I. Oxygen transport in perovskite $LaCoO_3$-$LaGaO_3$, *Solid State Ionics,*, **Vol.** 104, **pp.** 67-78.

Kharton, V. V., A. V. Kovalevsky, V. N. Tikhonovich, E. N. Naumovich and A. P. Viskup (1998a). Mixed electronic and ionic conductivity of $LaCo(M)O_3$ (M=Ga, Cr, Fe or Ni) II. Oxygen permeation through Cr- and Ni-substituted $LaCoO_3$, *Solid State Ionics*, **Vol.** 110, **pp.** 53-60.

Kharton, V. V., A. V. Kovalevsky, A. P. Viskup, F. M. Figueiredo, J. R. Frade, A. A. Yaremchenko and E. N. Naumovich (2000a). Faradaic efficiency and oxygen permeability of $Sr_{0.97}Ti_{0.6}Fe_{0.4}O_{3-\delta}$ perovskite, *Solid State Ionics*, **Vol.** 128, **pp.** 117-130.

Kharton , V. V., A. V. Kovalevsky, A. P. Viskup, A. P. Shaula, F. M. Figueiredo, E. N. Naumovich and F. M. B. Marques (2003). Oxygen transport in $Ce_{0.8}Gd_{0.2}O_{2-\delta}$-based composite membranes, *Solid State Ionics*, **Vol.** 160, **pp.** 247-258.

Kharton, V. V., E. N. Naumovich, A. V. Kovalevsky, A. P. Viskup, F. M. Figueiredo, I. A. Bashmakov and F. M. B. Marques (2000b). Mixed electronic and ionic conductivity of $LaCo(M)O_3$ (M=Ga, Cr, Fe or Ni) IV. Effect of preparation method on oxygen transport in $LaCoO_{3-x}$, *Solid State Ionics*, **Vol.** 138, **pp.** 135-148.

Kharton, V. V., E. N. Naumovich and A. V. Nikolaev (1996). Materials of high-temperature electrochemical oxygen membranes, *J. Membr. Sci.*, **Vol.** 111, **pp.** 149-157.

Kharton, V. V., E. N. Naumovich, A. A. Vecher and A. V. Nikolaev (1995). Oxide ion conduction in solid solutions $Ln_{1-x}Sr_xCoO_{3-\delta}$ (Ln = La, Pr, Nd), *J. Solid State Chem.*, **Vol.** 120, **pp.** 128-136.

Kharton, V. V., L. Shuangbao, A. V. Kovalevsky and E. N. Naumovich (1997b). Oxygen permeability of perovskites in the system $SrCoO_3$-$SrTiO_3$, *Solid State Ionics*, **Vol.** 96, **pp.** 141-151.

Kharton, V. V., A. P. Viskup, D. M. Bochkov, E. N. Naumovich and O. P. Reut (1998b). Mixed electronic and ionic conductivity of $LaCo(M)O_3$ (M=Ga, Cr, Fe or Ni) III. Diffusion of oxygen through $LaCo_{1-x-y}Fe_xNi_yO_{3-\delta}$ ceramics, *Solid State Ionics*, **Vol.** 110, **pp.** 61-68.

Kharton , V. V., A. P. Viskup, A. V. Kovalevsky, J. R. Jurado, E. N. Naumovich, A. A. Vecher and J. R. Frade (2000). Oxygen ionic conductivity of Ti-containing strontium ferrite, *Solid State Ionics*, **Vol.** 133, **pp.** 57-65.

Kharton, V. V., A. P. Viskup, E. N. Naumovich and V. N. Tikhonovich (1999a). Oxygen permeability of $LaFe_{1-x}Ni_xO_{3-\delta}$ solid solutions, *Mater. Res. Bull.*, **Vol.** 34, **pp.** 1311-1317.

Kharton, V. V., A. P. Viskup, E. N. Naumovich, A. A. Tonoyan and O. P. Reut (1998c). Oxygen ionic transport in a-site-deficient perovskite $La(Pb)FeO_3$, *Mater. Res. Bull.*, **Vol.** 33, **pp.** 1087-1093.

Kharton, V. V., A. P. Viskup, A. A. Yaremchenko, R. T. Baker, B. Gharbage, G. C. Mather, F. F.M., N. E.N. and F. M. B. Marques (2000d). Ionic conductivity of $La(Sr)Ga(Mg,M)O_{3-\delta}$ (M=Ti, Cr, Fe, Co, Ni): effects of transition metal dopants, *Solid State Ionics*, **Vol.** 132, **pp.** 119-130.

Kharton, V. V., A. P. Viskup, A. A. Yaremchenko, P. F. Kerko, E. N. Naumovich and A. V. Kovalevsky (1999b). Ionic transport in $SrCo_{0.85}Ti_{0.15}O_{3-\delta}$ ceramics at high oxygen pressures, *Mater. Res. Bull.*, **Vol.** 34, **pp.** 1921-1928.

Kharton, V. V., A. A. Yaremchenko, A. V. Kovalevsky, A. P. Viskup, E. N. Naumovich and P. F. Kerko (1999c). Perovskite-type oxides for high-temperature oxygen separation membranes, *J. Membr. Sci.*, **Vol.** 163, **pp.** 307-317.

Kim, J. and Y. S. Lin (2000a). Synthesis and oxygen permeation properties of ceramic-metal dual-phase membranes, *J. Membr. Sci.*, **Vol.** 167, **pp.** 123-133.

Kim, J. and Y. S. Lin (2000b). Synthesis and oxygen-permeation properties of thin YSZ/Pd composite membranes, *AIChE J.*, **Vol.** 46, **pp.** 1521-1529.

Kim, S., Y. L. Yang, R. Christoffersen and A. J. Jacobson (1998a). Determination of oxygen permeation kinetics in a ceramic membrane based on the composition $SrFeCo_{0.5}O_{3.25-\delta}$, *Solid State Ionics*, **Vol.** 109, **pp.** 187-196.

Kim, S., Y. L. Yang, A. J. Jacobson and B. Abeles (1998b). Diffusion and surface exchange coefficients in mixed ionic electronic conducting oxides from the pressure dependence of oxygen permeation, *Solid State Ionics*, **Vol.** 106, **pp.** 189-195.

Kim, S., Y. L. Yang, A. J. Jacobson, R. Christoffersen and B. Abeles (1997). Oxygen permeation, electrical conductivity and stability of perovskite oxide $La_{0.2}Sr_{0.8}Cu_{0.4}Co_{0.6}O_{3-x}$, *Solid State Ionics*, **Vol.** 104, **pp.** 57-65.

Knauth, P. and H. L. Tuller (2002). Solid state ionics: roots, status, and future prospects, *J. Am. Ceram. Soc.*, **Vol.** 85, **pp.** 1654-1680.

Kobayashi, T., K. Abe, Y. Ukyo and H. Iwahara (2000). Reduction of nitrogen oxide by steam electrolysis cell using a protonic conductor SrZr0.9Yb0.1O3-d and the catalyst Sr/Al2O3, *Solid State Ionics*, **Vol.** 134, **pp.** 241-247.

Kosacki, I. and H. U. Anderson (1997). The structure and electrical properties of $SrCe_{0.95}Yb_{0.05}O_3$ thin film protonic conductors, *Solid State Ionics*, **Vol.** 97, **pp.** 429-436.

Kovalevsky, A. V., V. V. Kharton, V. N. Tikhonovich, E. N. Naumovich, A. A. Tonoyan, O. P. Reut and L. S. Boginsky (1998). Oxygen permeation through $Sr(Ln)CoO_{3-\delta}$ (Ln=La, Nd, Sm, Gd) ceramic membranes, *Mater. Sci. and Eng.*, **Vol.** B52, **pp.** 105-116.

Kreuer, K. D. (1999). Aspects of the formation and mobility of protonic charge carriers and the stability of perovskite-type oxides, *Solid State Ionics*, **Vol.** 125, **pp.** 285-302.

Kreuer, K. D., A. Fuchs and J. Maier (1995). H/D isotope effect of proton conductivity and proton conduction mechanism in oxides, *Solid State Ionics*, **Vol.** 77, **pp.** 157-162.

Kroger, F. A. (1964). *The chemistry of imperfect crystals*, Wiley, New York.

Lane, J. A. and J. A. Kilner (2000). Oxygen surface exchange on gadolinia doped ceria, *Solid State Ionics*, **Vol.** 136-137, **pp.** 927-932.

Lee, T. H., Y. L. Yang, A. J. Jacobson, B. Abeles and S. Milner (1997a). Oxygen permeation in dense $SrCo_{0.8}Fe_{0.2}O_{3-\delta}$ membranes with porous electrodes, *Solid State Ionics*, **Vol.** 100, **pp.** 87-94.

Lee, T. H., Y. L. Yang, A. J. Jacobson, B. Abeles and M. Zhou (1997b). Oxygen permeation in dense $SrCo_{0.8}Fe_{0.2}O_{3-\delta}$ membranes: surface exchange kinetics versus bulk diffusion, *Solid State Ionics*, **Vol.** 100, **pp.** 77-85.

Li, L., R. W. Borry and E. Iglesia (2002). Design and optimization of catalysts and membrane reactors for the non-oxidative conversion of methane, *Chem. Eng. Sci.*, **Vol.** 57, **pp.** 4594-4604.

Li, S., Y. Cong, L. Fang, W. Yang, L. Lin, J. Meng and Y. Ren (1998). Oxygen permeation properties of the mixed conducting membranes without cobalt, *Mater. Res. Bull.*, **Vol.** 33, **pp.** 183-188.

Li, S., W. Jin, P. Huang, N. Xu, J. Shi and Y. S. Lin (2000). Tubular lanthanum cobalitite perovskite type membrane for oxygen permeation, *J. Membr. Sci.*, **Vol.** 166, **pp.** 51-61.

Li, S., W. Jin, X. N. and J. Shi (1999). Synthesis and oxygen permeation properties of $La_{0.2}Sr_{0.8}Co_{0.2}Fe_{0.8}O_{3-\delta}$ membranes, *Solid State Ionics*, **Vol.** 124, **pp.** 161-170.

Liang, K. C., Y. Du and A. S. Norwick (1994). Fast high-temperature proton transport in nonstoichiometric mixed perovskites, *Solid State Ionics*, **Vol.** 69, **pp.** 117-120.

Liang, K. C. and A. S. Nowick (1993). High-temperature protonic conduction in mixed perovskite ceramics, *Solid State Ionics*, **Vol.** 61, **pp.** 77-81.

Lin, Y. S. (2001). Microporous and dense inorganic membranes: current status and prospective, *Sepn. Pur. Tech.*, **Vol.** 25, **pp.** 39-55.

Lin, Y. S., W. J. Wang and J. H. Han (1994). Oxygen permeation through thin mixed-conducting solid state mmembranes, *AIChE J.*, **Vol.** 40, **pp.** 786-798.

Lin, Y. S. and Y. Zeng (1996). Catalytic Properties of Oxygen Semipermeable Perovskite-Type Ceramic Membrane Materials for Oxidative Coupling of Methane, *Journal of Catalysis*, **Vol.** 164, **pp.** 220-231.

Lin, Y. S. and Y. Zheng (1996). Catalytic properties of oxygen semipermeable perovskite-type ceramic membrane materials for oxidative coupling of methane, *J. Cataly.*, **Vol.** 164, **pp.** 220-231.

Liu, J. F. and A. S. Norwick (1992). The incorporation and migration of protons in Nd-doped $BaCeO_3$, *Solid State Ionics*, **Vol.** 50, **pp.** 131-138.

Liu, S. and K. Li (2003). Preparation of TiO_2/ Al_2O_3 composite hollow fibre membranes, *J. Membr. Sci.*, **Vol.** 218, **pp.** 269-277.

Liu, S., K. Li and R. Hughes (2003). Preparation of porous aluminium oxide (Al_2O_3) hollow fibre membranes by a combined phase-inversion and sintering method, *Ceram. Int.*, **Vol.** 29, **pp.** 875-881.

Liu, S., X. Tan, K. Li and R. Hughes (2001a). Methane coupling using catalytic membrane reactors, *Catal. Rev. Sci. Eng.*, **Vol.** 43, **pp.** 147-198.

Liu, S., X. Tan, K. Li and R. Hughes (2001b). Preparation and characterisation of $SrCe_{0.95}Yb_{0.05}O_{2.975}$ hollow fibre membranes, *J. Membr. Sci.*, **Vol.** 193, **pp.** 249-260.

Liu, W., G. G. Zhang, S. Xie, C. S. Chen, G. Y. Meng and D. K. Peng (2000). Electrical conduction and oxygen transport in $SrFeCo_{0.5}O_x$ oxide membranes, *Solid State Ionics*, **Vol.** 135, **pp.** 727-730.

Liu, Y. and K. Li (2005). Preparation of $SrCe_{0.95}Yb_{0.05}O_{3-\delta}$ hollow fibre membranes: Study on sintering processes, *J. Membr. Sci.*, **Vol.** 259, **pp.** 47-54.

Lu, Y., A. G. Dixon, W. R. Moser, Y. Ma and U. Balachandran (2000a). Oxygen-permeable dense membrane reactor for the oxidative coupling of methane, *J. Membr. Sci.*, **Vol.** 170, **pp.** 27-34.

Lu, Y., A. G. Dixon, W. R. Moser, Y. H. Ma and U. Balachandran (2000b). Oxygen-permeable dense membrane reactor for the oxidative coupling of methane, *Journal of Membrane Science*, **Vol.** 170, **pp.** 27-34.

Luyten, J., A. Buekenhoudt, W. Adriansens, J. Cooymans, H. Weyten, F. Servaes and R. Leysen (2000). Preparation of $LaSrCoFeO_{3-x}$ membranes, *Solid State Ionics*, **Vol.** 135, **pp.** 637-642.

Ma, B. and U. Balachandran (1998). Phase stability of $SrFeCo_{0.5}O_x$ in reducing environments, *Mater. Res.Bull.*, **Vol.** 33, **pp.** 223-236.

Ma, B., U. Balachandran, J. P. Jorgensen, D. J. Miller and J. W. Richardson Jr. (1998a). Phase stability of the mixed-conducting Sr-Fe-Co-O system, *Mater. Res. Soc. Symp. Proc.*, **Vol.** 496, **pp.** 167-172.

Ma, B., U. Balachandran and J.-H. Park (1996). Electrical transport properties and defect structure of $SrFeCo_{0.5}O_x$, *J. Electrochem. Soc.*, **Vol.** 143, **pp.** 1736-1744.

Ma, B., J. P. Hodges, J. D. Jorgensen, D. J. Miller, J. W. Richardson Jr. and U. Balachandran (1998b). Structure and property relationships in mixed-conducting $Sr_4(Fe_{1-x}Co_x)_6O_{13\pm\delta}$ materials, *J. Solid State Chem.*, **Vol.** 141, **pp.** 576-586.

Maiya, P. S., T. J. Anderson, R. L. Mieville, J. T. Dusek, J. J. Picciolo and U. Balanchandran (2000). Maximizing H_2 production by combined partial oxidation of CH_4 and water gas shift reaction, *Appl. Catal. A: Gen.*, **Vol.** 196, **pp.** 65-72.

Marnellos, G., O. Sanopoulou, A. Rizou and M. Stoukides (1997). The use of proton conducting solid electrolyte for improved performance of hydro- and dehydrogenation reactors, *Solid State Ionics*, **Vol.** 97, **pp.** 375-383.

Martin, M. and R. Schmackpfeffer (1994). Demixing of doped oxides: influence of defect interactions, *Solid State Ionics*, **Vol.** 72, **pp.** 67-71.

Matzke, T. and M. Cappadonia (1996). Proton conductive perovskite solid solutions with enhanced mechanical stability, *Solid State Ionics*, **Vol.** 86-88, **pp.** 659-663.

Mazanec, T. J., T. L. Cable and J. J. G. Frye (1992). Electrocatalytic cells for chemical reaction, *Solid State Ionics*, **Vol.** 53-56, **pp.** 111-118.

McCarty, J. G. and H. Wise (1990). Applications of perovskites - perovskite catalysts for methane combustion, *Catal. Today*, **Vol.** 8, **pp.** 231.

Minh, N. Q. and T. Takahashi (1995). *Science and Technology of Ceramic Fuel Cells*, Elsevier, Amsterdam, The Netherlands.

Mitchell, B. J., R. C. Rogan, J. W. Richardson Jr., B. Ma and U. Balachandran (2002). Stability of the cubic perovskite $SrFe_{0.8}Co_{0.2}O_{3-\delta}$, *Solid State Ionics*, **Vol.** 146, **pp.** 311-321.

Miura, N., Y. Okamoto, J. Tamaki, K. Morinaga and N. Yamazoe (1995). Oxygen semipermeability of mixed conductive oxide thick-film prepared by slip casting, *Solid State Ionics*, **Vol.** 79, **pp.** 195-200.

Mizusaki, Y., S. Mima, K. Yamauchi, H. Fukei and Tagawa (1989). Nonstoichiometry of the perovskite-type oxides $La_{1-x}Sr_xCoO_{3-\delta}$, *J. Solid State Chem.*, **Vol.** 80, **pp.** 102-111.

Naito, H. and H. Arashi (1995). Hydrogen production from direct water splitting at high temperature using a ZrO_2-TiO_2-Y_2O_3 membrane, *Solid State Ionic*, **Vol.** 79, **pp.** 366-370.

Nigara, Y., K. Kawamura, T. Kawada and J. Mizusaki (2000). Hydrogen permeability in $Ce_{0.8}Yb_{0.2}O_{1.9}$ at high temperatures, *Solid State Ionics*, **Vol.** 136-137, **pp.** 215-221.

Nigara, Y., K. Kawamura, T. Kawada, J. Mizusaki and M. Ishigame (1999). Hydrogen permeability in sintered CeO_2 at high temperatures, *J. Electrochem. Soc.*, **Vol.** 146, **pp.** 2948-2953.

Nigara, Y., J. Mizusaki, K. Kawamura, T. Kawada and M. Ishigame (1998). Hydrogen permeability in $(CeO_2)_{0.9}(CaO)_{0.1}$ at high temperatures, *Solid State Ionics*, **Vol.** 113-115, **pp.** 347-354.

Nomura, K., T. Hayakawa, K. Takehira and Y. Ujihira (1993). Oxidative coupling of methane on perovskite oxides, $(Ba,Ca)(Co,Fe)O_{3-\delta}$, *Appl. Catal. A: Gen.*, **Vol.** 101, **pp.** 63-72.

Norby, T. (1999). Solid-state protonic conductors: principles, properties, progress and prospects, *Solid State Ionics*, **Vol.** 125, **pp.** 1-11.

Norby, T. and N. Christiansen (1995). Proton conduction in Ca- and Sr-substituted $LaPO_4$, *Solid State Ionics*, **Vol.** 77, **pp.** 240-243.

Norby, T. and Y. Larring (1996). Concentration and transport of protons and oxygen defects in oxides, in *Ceramic oxygen ion conductors and their technological application*, **Vol.**, edited by B. C. H. Steele, The Institute of Materials.

Norby, T. and Y. Larring (2000). Mixed hydrogen ion-electronic conductors for hydrogen permeable membranes, *Solid State Ionics*, **Vol.** 136-137, **pp.** 139-149.

Norwick, A. S. and Y. Du (1995). High-temperature protonic conductors with perovskite-related structures, *Solid State Ionics*, **Vol.** 77, **pp.** 137-146.

Norwick, A. S., Y. Du and K. C. Liang (1999). Some factors that determine proton conductivity in nonstoichiometric complex perovskites, *Solid State Ionics*, **Vol.** 125, **pp.** 303-311.

Norwick, A. S. and A. V. Vaysleyb (1997). Isotope effect and proton hopping in high-temperature protonic conductors, *Solid State Ionics*, **Vol.** 97, **pp.** 17-26.

Omata, K., O. Yamazaki, K. Tomita and K. Fujimoto (1994). Oxidative coupling of methane on an ABO_3-type oxide with mixed conductivity,, *J. Chem. Soc. Chem. Commun.*, **Vol.** 14, **pp.** 1647-1648.

Pei, S., M. S. Kleefisch, T. P. Kobylinski, J. Faber, C. A. Udovich, V. Zhang-McCoy, B. D. Dabrowski, U. Balachandran, R. L. Mieville and R. B. Poeppel (1995). Failure mechanisms of ceramic membrane reactors in partial oxidation of methane to synthesis gas, *Cata. Lett.*, **Vol.** 30, **pp.** 201-212.

Qi, X. and Y. S. Lin (2000). Electrical conduction and hydrogen permeation through mixed proton-electron conducting strontium cerate membranes, *Solid State Ionics*, **Vol.** 130, **pp.** 149-156.

Qiu, L., T. H. Lee, M. L. Liu, Y. L. Yang and A. J. Jacobson (1995). Oxygen permeation studies of $SrCo_{0.8}Fe_{0.2}O_{3-\delta}$, *Solid State Ionics*, **Vol.** 76, **pp.** 321-329.

Ritchie, J. T., J. T. Richardson and D. Luss (2001). Ceramic membranes reactor for synthesis gas production, *AIChE J.*, **Vol.** 47, **pp.** 2092-2101.

Sakai, N., K. Yamaji, H. Horita, H. Yokokawa, Y. Hirata, S. Sameshima, Y. Nigara and J. Mizusaki (1999). Determination of hydrogen solubility in oxide ceramics by using SIMS analyses, *Solid State Ionics*, **Vol.** 125, **pp.** 325-331.

Sammells, A. F. (1999). Catalytic Membrane Reactors for Spontaneous Synthesis Gas Production, Rosebank, Johannesburg, South Africa.

Sata, N., K. Hiramoto, M. Ishigamw, S. Hosoya, N. Nijmuma and S. Shin (1996). Site identification of protons in $SrTiO_3$: Mechanism for large protonic conduction, *Phys. Rew.*, **Vol.** B 54, **pp.** 15795-15799.

Schober, T. (2003). Applications of oxidic high-temperature proton conductors, *Solid State Ionics*, **Vol.** 162-163, **pp.** 277-281.

Schober, T. and H. G. Bohn (2000). Water vapor solubility and electrochemical characterization of the high temperature proton conductor $BaZr_{0.9}Y_{0.1}O_{2.95}$, *Solid State Ionics*, **Vol.** 127, **pp.** 351-360.

Schober, T., W. Schilling and H. Wenzl (1996). Defect model of proton insertion into oxides, *Solid State Ionics*, **Vol.** 86-88, **pp.** 653-658.

Shao, Z., H. Dong, G. Xiong, Y. Cong and W. Yang (2001a). Performance of a mixed-conducting ceramic membrane reactor with high oxygen permeability for methane conversion, *J. Membr. Sci.*, **Vol.** 183, **pp.** 181-192.

Shao, Z., G. Xiong, Y. Cong and W. Yang (2000a). Synthesis and oxygen permeation study of novel perovskite-type $BaBixCo_{0.2}Fe_{0.8-x}O_{3-\delta}$ ceramic membranes, *J. Membr. Sci.*, **Vol.** 164, **pp.** 167-176.

Shao, Z., G. Xiong, H. Dong, W. Yang and Y. S. Lin (2001b). Synthesis, oxygen permeation study and membrane performance of a $Ba_{0.5}Sr_{0.5}Co_{0.8}Fe_{0.2}O_{3-\delta}$

oxygen-permeable dense ceramic reactor for partial oxidation of methane to syngas, *Sep. Purif. Tech.*, **Vol.** 25, **pp.** 97-116.

Shao, Z., G. Xiong, J. Tong, H. Dong and W. Yang (2001c). Ba Effect in doping $Sr(Co_{0.8}Fe_{0.2})O_{3-\delta}$ on the phase structure and oxygen permeation properties of the dense ceramic membranes, *Sept. Purf. Tech.*, **Vol.** 25, **pp.** 419-429.

Shao, Z., W. Yang, Y. Cong, H. Dong, J. Tong and G. Xiong (2000b). Investigation of the permeation behavior and stability of a $Ba_{0.5}Sr_{0.5}Co_{0.8}Fe_{0.2}O_{3-\delta}$ oxygen membrane, *J. Membr. Sci.*, **Vol.** 172, **pp.** 177-188.

Shaw, C. K. (2001, PhD thesis). Mass transport in mixed conducting perovskite related oxides, Imperial College London.

Shimura, T., M. Komori and H. Iwahara (1996). Ionic conduction in pyrochlore-type oxides containing rare earth elements at high temperature, *Solid State Ionics*, **Vol.** 86, **pp.** 685-689.

Siriwardane, R. V., J. A. PostonJr., E. P. Fisher, T. H. Lee, S. E. Dorris and U. Balachandran (2000). Characterization of ceramic hydrogen separation membranes with varying nickel concentrations, *Applied Surface Science*, **Vol.** 167, **pp.** 34-50.

Smid, J., C. G. Avci, V. Gunay, R. A. Terstra and J. P. G. M. van Eijk (1996). Preparation and characterization of microporous ceramic hollow fibre membranes, *J. Membr. Sci.*, **Vol.** 112, **pp.** 85-90.

Steele, B. (1998). Ceramic ion conucting membranes and their technological applications, *C. R. Acad. Sci. Paris*, **Vol.** 1, **pp.** 533-543.

Stevenson, J. W., T. R. Armstrong, R. D. Carneim, L. R. Pederson and W. L. Weber (1996). Electrochemical properties of mixed conducting perovskites $La_{1-x}M_xCo_{1-y}Fe_yO_{3-\delta}$ (M = Sr, Ba, Ca), *J. Electrochem. Soc.*, **Vol.** 143, **pp.** 2722-2729.

Stiegel, G. (1999). Mixed conducting ceramic membranes for gas separation and reaction, *Membrane Technology*, **Vol.** 110, **pp.** 5-7.

Tai, L. W., M. M. Nasrallah, H. U. Anderson, D. M. Sparlin and S. R. Sehlin (1995). Structure and electrical properties of $La_{1-x}Sr_xCo_{1-y}Fe_yO_{3-\delta}$ Part I. The system $La_{0.8}Sr_{0.2}Co_{1-y}Fe_yO_{3-\delta}$, *Solid State Ionics*, **Vol.** 76, **pp.** 259-271.

Tan, X. and K. Li (2002). Modeling of air separation in a LSCF hollow-fiber membrane module, *AIChE J.*, **Vol.** 48, **pp.** 1469-1477.

Tan, X., S. Liu and K. Li (2001). Preparation and characterization of inorganic hollow fibre membranes, *J. Membr. Sci.*, **Vol.** 188, **pp.** 87-95.

Tan, X., S. Liu, K. Li and R. Hughes (2000). Theoretical analysis of ion permeation through mixed conducting membranes and its application to dehydrogenation reactions, *Solid State Ionics*, **Vol.** 138, **pp.** 149-159.

Tan, X., Y. Liu and K. Li (2005). Mixed conducting ceramic hollow-fiber membranes for air separation, *AIChE J.*, **Vol.** 51, **pp.** 1991-2000.

ten Elshof, J. E., H. J. M. Bouwmeester and H. Verweij (1995). Oxidative coupling of methane in a mixed-conducting perovskite membrane reactor, *Appl. Catal. A: Gen.*, **Vol.** 130, **pp.** 195-212.

Teraoka, Y., H. M. Zhang, S. Furukawa and N. Yamazoe (1985). Oxygen permeation through perovskite-type oxides, *Chem. Lett.*, **Vol., pp.** 1743-1746.

Thursfield, A. and I. S. Metcalfe (2004). The use of dense mixed ionic and electronic conducting membranes for chemical production, *J. Mater. Chem.*, **Vol.** 14, **pp.** 2475-2485.

Tong, J., W. Yang, R. Cai, B. Zhu, G. Xiong and L. Lin (2003). Investigation on the structure stability and oxygen permeability of Titanium-doped perovskite-type

oxides of $Ba_{0.8}Ti_{0.2}Co_xFe_{1-x}O_{3-\delta}$ (x = 0.2-0.6),, *Sepn. Pur. Tech.*, **Vol.** 32, **pp.** 289-299.

Tong, J., W. Yang, R. C. B. Zai and L. Lin (2002a). Novel and ideal zirconium-based dense membrane reactors for partial oxidation of methane to syngas, *Catal. Lett.*, **Vol.** 78, **pp.** 129-137.

Tong, J., W. Yang, R. C. B. Zai and L. Lin (2002b). Titanium-based perovskite-type mixed conducting ceramic membranes for oxygen permeation, *Mater. Lett.*, **Vol.** 56, **pp.** 958-962.

Tong, J., W. Yang, B. Zhu and R. Cai (2002c). Investigation ideal zirconium-doped perovskite-type ceramic membrane materials for oxygen separation, *J. Membr. Sci.*, **Vol.** 203, **pp.** 175-189.

Tuller, H. L., J. Schoonman and I. Riess (2000). *Oxygen Ion and Mixed Conductors and Their Technological Applications*, Kluwer Academic,, Dordrecht, The Netherlands.

Uchida, H., H. Yoshikawa and H. Iwahara (1989). Dissolution of water vapour (or hydrogen) and proton conduction in $SrCeO_3$ based oxides at high temperatures, *Solid State Ionics*, **Vol.** 35, **pp.** 229-237.

Udovich, A. (1998). Ceramic membrane reactors for the conversion of natural gas to syngas, *Stud. Surf. Sci. Catal.*, **Vol.** 119, **pp.** 417-422.

Ullmann, H. and N. Trofimenko (1999). Composition, structure and transport properties of perovskite-type oxides, *Solid State Ionics*, **Vol.** 119, **pp.** 1-8.

Ullmann, H., N. Trofimenko, A. Naoumidis and D. Stover (1999). Ionic/electronic mixed conduction relations in perovskite-type oxides by defect structure, *J. Euro. Ceram. Soc.*, **Vol.** 19, **pp.** 791-796.

Wachsman, E. D. and T. L. Clites (2002). Stable mixed-conducting bilayer membranes for direct conversion of methane to syngas, *J. Electrochem. Soc.*, **Vol.** 149, **pp.** A242-A246.

Wang, H., Y. Cong and W. Yang (2003). Investigation on the partial oxidation of methane to syngas in a tubular $Ba_{0.5}Sr_{0.5}Co_{0.8}Fe_{0.2}O_{3-\delta}$ membrane reactor, *Catal. Today*, **Vol.** 82, **pp.** 157-166.

Way, J. D. and D. L. Roberts (1992). Hollow Fiber Inorganic Membranes for Gas Separations, *Separation Science and Technology*, **Vol.** 27, **pp.** 29-41.

White, J. H., M. Schwartz and A. F. Sammells (1998). US5821185,

Woldmann, L. S. and V. D. Sokolovskii (1991). Electrocatalytic methane coupling in the absence of oxygen on a high-temperature proton-conducting electrolyte, *Cata. Lett.*, **Vol.** 8, **pp.** 61.

Xia, Y., T. Armstrong, F. Prado and A. Manthiram (2000). Sol-gel synthesis, phase relationships, and oxygen permeation properties of $Sr_4Fe_{6-x}Co_xO_{13+\delta}$, *Solid State Ionics*, **Vol.** 130, **pp.** 81-90.

Xu, S. J. and W. J. Thomson (1997). Ion-conducting perovskite membrane for the oxidative coupling of methane, *AIChE J.*, **Vol.** 43, **pp.** 2731-2740.

Xu, S. J. and W. J. Thomson (1998). Stability of $La_{0.6}Sr_{0.4}Co_{0.2}Fe_{0.8}O_{3-\delta}$ perovskite membrane in reducing and nonreducing environments, *Ind. Eng. Chem. Res.*, **Vol.** 37, **pp.** 1290-1299.

Xu, S. J. and W. J. Thomson (1999). Oxygen permeation rates through ion-conducting perovskite membranes, *Chemical Engineering Science*, **Vol.** 54, **pp.** 3839-3850.

Xu, X., W. Yang, J. Lui, L. Lin, N. Stron and H. Brunner (2004). Synthesis of NaA zeolite membrane on a ceramic hollow fibre, *J. Membr. Sci.*, **Vol.** 229, **pp.** 81-85.

Yajima, T., H. Iwahara and H. Uchida (1991a). Protonic and oxide ionic conduction in $BaCeO_3$-based ceramics — effect of partial substitution for Ba in $BaCe_{0.9}O_{3-\delta}$ with Ca, *Solid State Ionics*, **Vol.** 47, **pp.** 117-124.

Yajima, T., H. Kazeoka, T. Yogo and H. Iwahara (1991b). Proton conduction in sintered oxides based on $CaZrO_3$, *Solid State Ionics*, **Vol.** 47, **pp.** 271-275.

Yajima, T., H. Suzuki, T. Yogo. and H. Iwahara (1992). Protonic conduction in $SrZrO_3$-based oxides, *Solid State ionics*, **Vol.** 51, **pp.** 101-107.

Yamamura, Y., C. Ihara, S. Kawasaki, H. Sakai, K. Suzuki, S. Takami, M. Kubo and A. Miyamoto (2003). Material design of perovskite-based oxygen ion conductor by molecular dynamics method, *Solid State Ionics*, **Vol.** 160, **pp.** 93-101.

Yaremchenko, A. A., V. V. Kharton, A. P. Viskup, E. N. Naumovich, V. N. Tikhonovich and N. M. Lapchuk (1999). Mixed electronic and ionic conductivity of $LaCo(M)O_3$ (M=Ga, Cr, Fe or Ni). V. Oxygen permeability of Mg-doped $La(Ga, Co)O_{3-\delta}$ perovskites, *Solid State Ionics*, **Vol.** 120, **pp.** 65-74.

Yugami, H., S. Matsuo and M. Ishigame (1995). Presistent spectral hole burning of En^{3+} and Pr^{3+} in $SrZr_{1-x}Y_xO_3$ crystals, *Solid State Ionics*, **Vol.** 77, **pp.** 195-200.

Zeng, Y., L. Y.S. and S. L. Swartz (1998). Perovskite-type ceramic membrane: synthesis, oxygen permeation and membrane reactor performance for oxidative coupling of methane, *J. Membr. Sci.*, **Vol.** 150, **pp.** 87-98.

Zhang, G., S. E. Dorris, U. Balachandran and M. Liu (2003). Interfacial resistances of Ni-BCY mixed-conducting membranes for hydrogen separation, *Solid State Ionics*, **Vol.** 159, **pp.** 121-134.

Chapter 3

Preparation of $SrCe_{0.95}Yb_{0.05}O_{3-\delta}$ hollow fibre membranes: study on sintering processes

Abstract

In this chapter, sintering processes, as one of the critical steps in ceramic processing responsible for final shape and characteristics of products, have been investigated using hollow fibre precursors prepared from a mixed proton/hole conducting material of $SrCe_{0.95}Yb_{0.05}O_{3-\delta}$ (SCYb). The hollow fibre precursors were spun via a phase inversion method using a polyethersulfone (PESf)/N-methyl-2-pyrrollidone (NMP) solution system, which is often used in making polymeric membranes. In order to understand influences of the sintering process on the hollow fibre membranes, some sintering parameters such as sintering temperature, heating rate and sintering time have been investigated. The shrinkage and weight loss of the hollow fibres during the sintering processes have been measured at different calcination temperatures and the surface morphology of resulting hollow fibres has been investigated using scanning electron microscopy (SEM).

Key words: perovskite material, hollow fibre membrane, sintering process

3.1 Introduction

Recently, membranes with mixed ionic-electronic conducting abilities have attracted great research interest for their potential applications in chemical and electrochemical industries, especially in applications of methane conversions (Lee and Oyama, 1988; Iwahara, 1995; Kreuer, 1997; Norby, 1999; Liu *et al.*, 2001a). One of the advantages of using such a mixed conducting membrane is the structural simplicity as no electrodes and external electric loadings are required compared to pure ionic (oxygen ion or proton) conducting membranes. Many studies have been conducted using either oxygen permeable material, such as, $La_{0.6}Sr_{0.4}Co_{0.8}Fe_{0.2}O_{3-\alpha}$ (LSCF) (Teraoka *et al.*, 1985; Teraoka *et al.*, 1988; Zeng *et al.*, 1998; Bouwmeester, 2003) or hydrogen permeable materials, such as $SrCe_{0.95}Yb_{0.05}O_{3-\delta}$ (SCYb) (Hamakawa *et al.*, 1993;1994; Guan *et al.*, 1997; Langguth *et al.*, 1997; Qi and Lin, 2000; Liu *et al.*, 2001b; Hamakawa *et al.*, 2002). Most of the research on the mixed-conducting ceramic membranes allowing permeation of oxygen or hydrogen focused on perovskite disk shaped membranes because preparation of these dense and defect-free ceramic membranes by a press/sintering method is currently available. However, the disk-shaped membrane has a very limited effective area and in addition, up to millimeters thickness of these disk-shaped membranes would impose large mass transfer resistance. Although the thickness of the disk membrane could be reduced by depositing a thin top-layer on a porous support (Hamakawa *et al.*, 2002), for the prospective of industrial applications, hollow fibre membranes are still preferable compared to the disk shaped membranes. Liu et al. (Liu *et al.*, 2001b) first developed the SCYb hollow fibre dense membranes intended to use in methane coupling reactions to produce C_2 products. Their results showed an exciting possibility in developing ceramic hollow fibre membranes using a combined phase inversion and sintering method. However, performance of the module made from these hollow fibres was not very ideal due to the inadequate mechanical strength of the membranes, especially when the modules were operated at elevated temperatures.

There are many factors governing the fabrication of ceramic membranes. The sintering process plays a prominent role, since almost all the ceramic precursors must be fired at

elevated and properly controlled temperatures in order to obtain its mechanical strength and microstructures with desired properties (Rhodes, 1981; Binner, 1990; Richerson, 1992; Chen and Chen, 1996; Akash and Mayo, 1999; Wang *et al.*, 1999).

The objective of this chapter is concerned with the sintering processes. It is intended to observe how the sintering processes take place and influence the microstructural evolution of the hollow fibres prepared from a SCYb perovskite-type material. The effect of sintering temperature and sintering time on the microstructure-related characteristics including surface morphology, grain growth and pore evolution or elimination has been investigated.

3.2 Experimental

3.2.1 Materials

$SrCe_{0.95}Yb_{0.05}O_{2.975}$ (SCYb) powders purchased from Praxair Special Ceramics (99.9%, surface area: 4.05 m^2/g and particle size d_{50} 0.8μm) were used as the hollow fibre material. Polyethersulfone (PESf) (Radel A-300, Ameco Performance, Greenville, SC) and N-methyl-2-pyrrollidone (NMP) (>99%, synthesis grade, Acros) were used to prepare spinning solutions. Polyvinlpyrrolidone (PVP K90, Acros) was used as an additive. Deionized water and tape water were used as the internal and external coagulants, respectively.

3.2.2 Sintering Processes

The hollow fibre precursors were prepared using a phase inversion method described elsewhere (Liu *et al.*, 2001b) and were dry-treated at about 25 °C before sintered in a furnace. The heating rate was of 2 to 5 °C/min applied during all the sintering processes. The sintering temperature is up to 1600 °C. The linear shrinkage and the weight loss of hollow fibres were measured and calculated after calcined at different temperature for different time. An average value was taken from three samples measured for each condition. The effect of sintering on surface morphology of the fibres was investigated using SEM.

3.2.3 Characterization using SEM

Structures of the prepared hollow fibre membranes were visually observed using scanning electron microscopy (JEOL JSM-5610LV, Japan). The hollow fibre precursor was first immersed in liquid nitrogen. After about 10 min, the frozen membranes were slowly flexed in the liquid nitrogen until a clear cross-sectional fracture occurred. These membrane samples were then positioned on a metal holder and gold coated using a sputter coating operated under vacuum.

3.3 Results and Discussions

As generally understood, sintering processes play an important role in the formation of ceramic final configuration and characteristics. The sintering process is usually comprised of three stages (Reed, 1995). Movements of particles exhibit different features at each stage and are attributed to densification, grain coarsening and pores closing. Rapid densification with limited grain growth occurs at lower temperature, followed by rapid grain growth with little densification at higher temperature. Compared to the relatively homogeneous ceramics manufactured using a normal casting method, the sintering process of the membranes prepared by a phase inversion method is more complex because of their highly asymmetric and porous structure. Therefore, careful control of the sintering conditions would be essential.

The SCYb hollow fibre membranes were developed via a combined phase inversion and sintering method using a same composition of dope solution used by Liu, et al. (Liu *et al.*, 2001b). Fig. 3-1 shows the SEM photographs of the SCYb hollow fibre precursor (Fig. 3-1A-C) and its fibres calcined at 1400 ºC (Fig. 3-1a-c). These SEM pictures illustrate the cross section of the whole fibre (Fig. 3-1A and a), of outer part of fibre (Fig. 3-1B and b) and of the middle part (Fig. 3-1C and c) before and after sintering. As can be seen from Fig. 3-1(A) and (a), the o.d./i.d. of the hollow fibre precursor and sintered fibre were measured to be 1.85/0.80 and 1.45/0.65 mm, respectively. The dimension shrinkage of the SCYb hollow fibre membrane was very substantial after the sintering process. Fig. 3-1(B) shows the structure of the cross section of the outer fibre, which is attributed to the rapid precipitation occurred at the outer-layer resulting in thin and dense skin layer and to the slow precipitation giving the porous sub-layer structure. The middle part structure shown in Fig. 3-1 (C) is also very porous. Corresponding to the structures shown in Fig. 3-1(B) and (C), Fig. 3-1(b) shows the outer skin layer of the sintered fibre. The dense skin layer was composed by tightly contacted relative uniform grains, the porosity of sub-layer was reduced and the grain shape can be observed in Fig. 3-1(c).

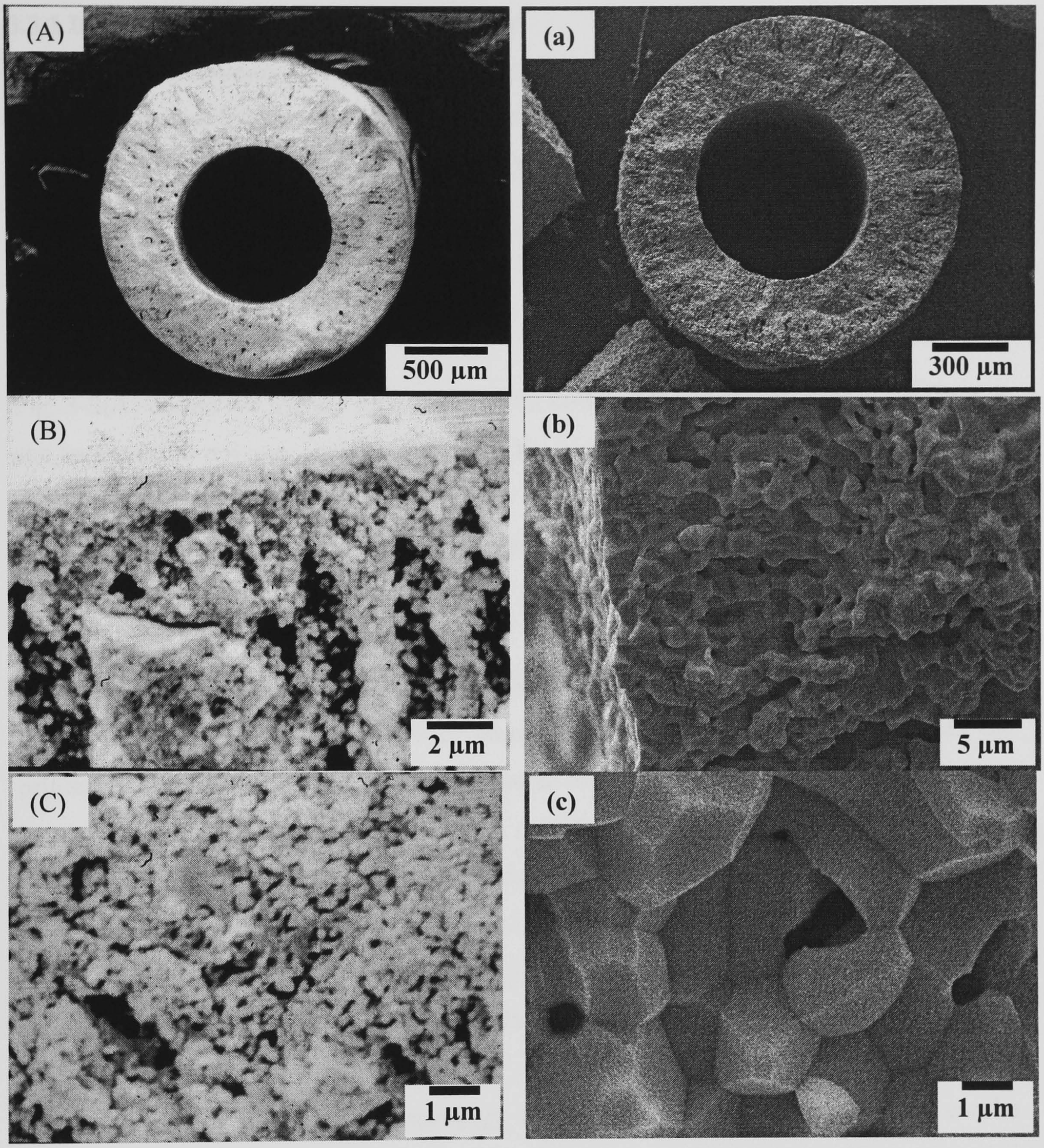


Fig. 3-1 SEM photographs of the cross-sectional structures of SCYb hollow fibre membranes (before sintering: (A) whole cross section, (B) outer layer and (C) middle part) and (after sintering: (a) whole cross section, (b) outer layer and (c) middle part).

3.3.1 Investigation of sintering temperature

The sintering temperature was investigated using the SCYb hollow fibres at 600-1600 ºC. The heating or cooling rate was kept constant at 2-5 ºC/min. SEM pictures in Fig.3-2 and Fig.3-3 show the surface morphology of SCYb hollow fibre precursor and hollow fibres calcined at temperatures between 600 and 1600 ºC for duration of two hours. The membrane shrinkage and weight loss were measured for the SCYb hollow fibre membranes calcined at different temperatures and the results are shown in Fig. 3-4.

Fig. 3-2(A) shows the surface morphology of a hollow fibre precursor before sintering. It can be seen that polymer nodules instead of the ceramic particles were compacted on the membrane surface without obvious boundary and the surface characteristics are similar to those of polymeric membranes because of the polymer binder (about 8.8 wt%) presented in the fibre precursor.

Fig. 3-2(B) shows the surface of the fibre precursor heated at 600 ºC. It can be seen that the membrane surface is composed of large granular ceramic particles (large than the original SCYb particle size). It is obvious that at 600 ºC the polymer binder at the surface has been burnt out, resulting in a rough membrane surface formed by the granular particles, which were aggregated from original SCYb particles with the polymer binder. Experimental data indicated that the weight loss of the hollow fibre was only 2.5 percent after two hours' heating at 600 ºC, further confirming that removal of the polymer binder from the hollow fibre precursor only takes place at the membrane surface.

Fig. 3-2(C) shows the surface morphology of the membrane heated at 800 ºC. It can be seen that the particles packed on the membrane surface are smaller and uniform compared to that shown in Fig. 3-2(B). As shown in Fig. 3-4, the heating at 800 ºC for two hours results in a dramatic weight loss of the fibre, indicating that bulk of the polymer were burnt out at this stage and the particle size was reduced to its original size. It is interesting to note that the fibre shrinkage remains small suggesting that at this stage the polymer burning out is the dominating step. The morphology of the membrane surface at this stage might show the original particle packing before sintering occurs.

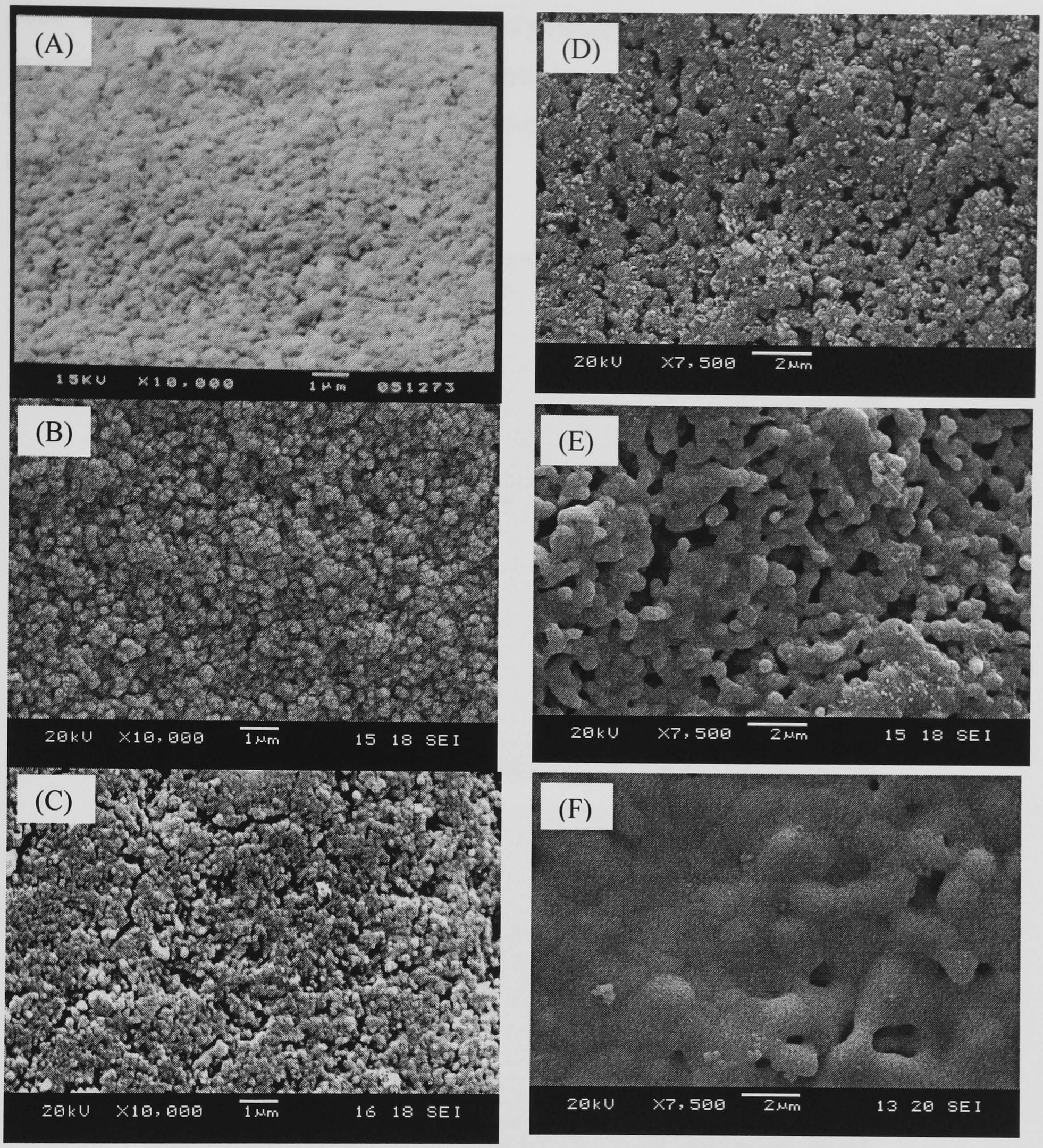


Fig. 3-2. SEM photographs of surface morphology of SCYb hollow fibres before and after calcination at different temperatures; (A) before sintering, (B) 600 ºC, (C) 800 ºC, (D) 1200 ºC, (E) 1300 ºC, and (F) 1400 ºC, Calcination time: 120 minutes.

Fig. 3-2(D) shows the surface morphology of the membrane calcined at 1200 ºC. It can be seen that the membrane surface is very porous. Based on the weight loss data given in Fig 3-4, all the polymer binder has been removed at this stage and thus the membrane surface becomes porous. It should be noted that data obtained for weight loss for SCYb sintered at

1200 °C is slightly larger than the content of polymer binder, which is probably due to the experimental error (i.e., moisture absorption on the hollow fibre precursor). The experimental data, given in Fig. 3-4, also shows that fibre shrinkage started to take place at temperature > 1000 °C.

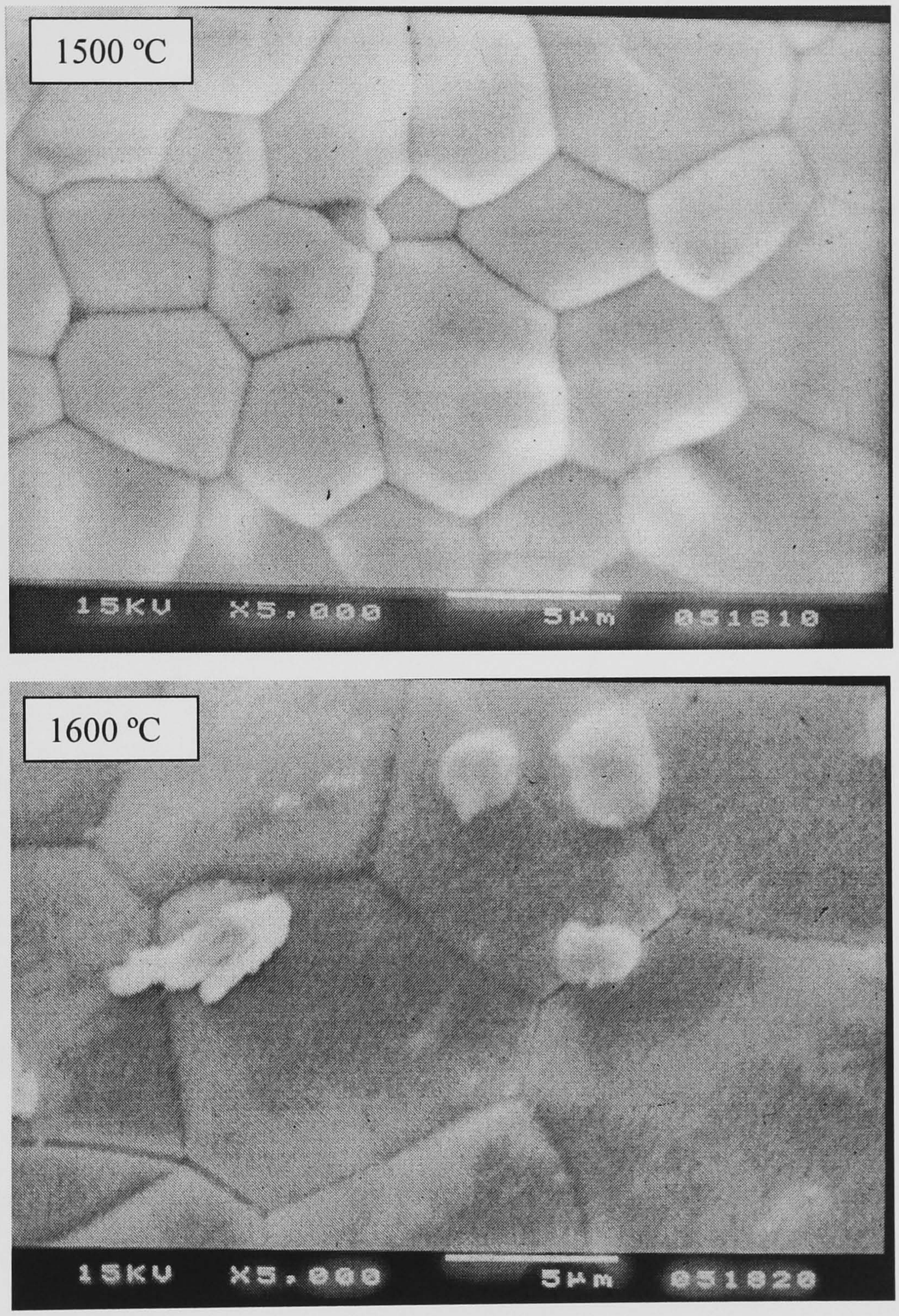


Fig. 3-3. SEM photographs of surface morphology of the SCYb hollow fibre calcined at 1500 and 1600 °C.

Fig. 3-2(E) shows the surface morphology of the membrane sintered at 1300 °C. As can be seen, the obvious sintering occurred, i.e. smaller particle disappeared and grain growth takes place. However, at this stage, the membrane surface is still very porous, indicating the limited grain growth with the shrinkage of the fibre around 11±0.1% as shown in Fig.3-4.

Fig. 3-2(F) shows the surface morphology of the membrane sintered at 1400 °C. It can be seen that the membrane surface becomes dense with isolated cavities. The membrane surface is, in general, dense and smooth. The grain size was further developed, as the sintering temperature is further increased. As shown in Fig. 3-3, the grain size becomes very big at higher temperature and the grain size is about 5 μm at 1500 °C and 10 μm at 1600 °C. The surface of both membranes was dense and smooth.

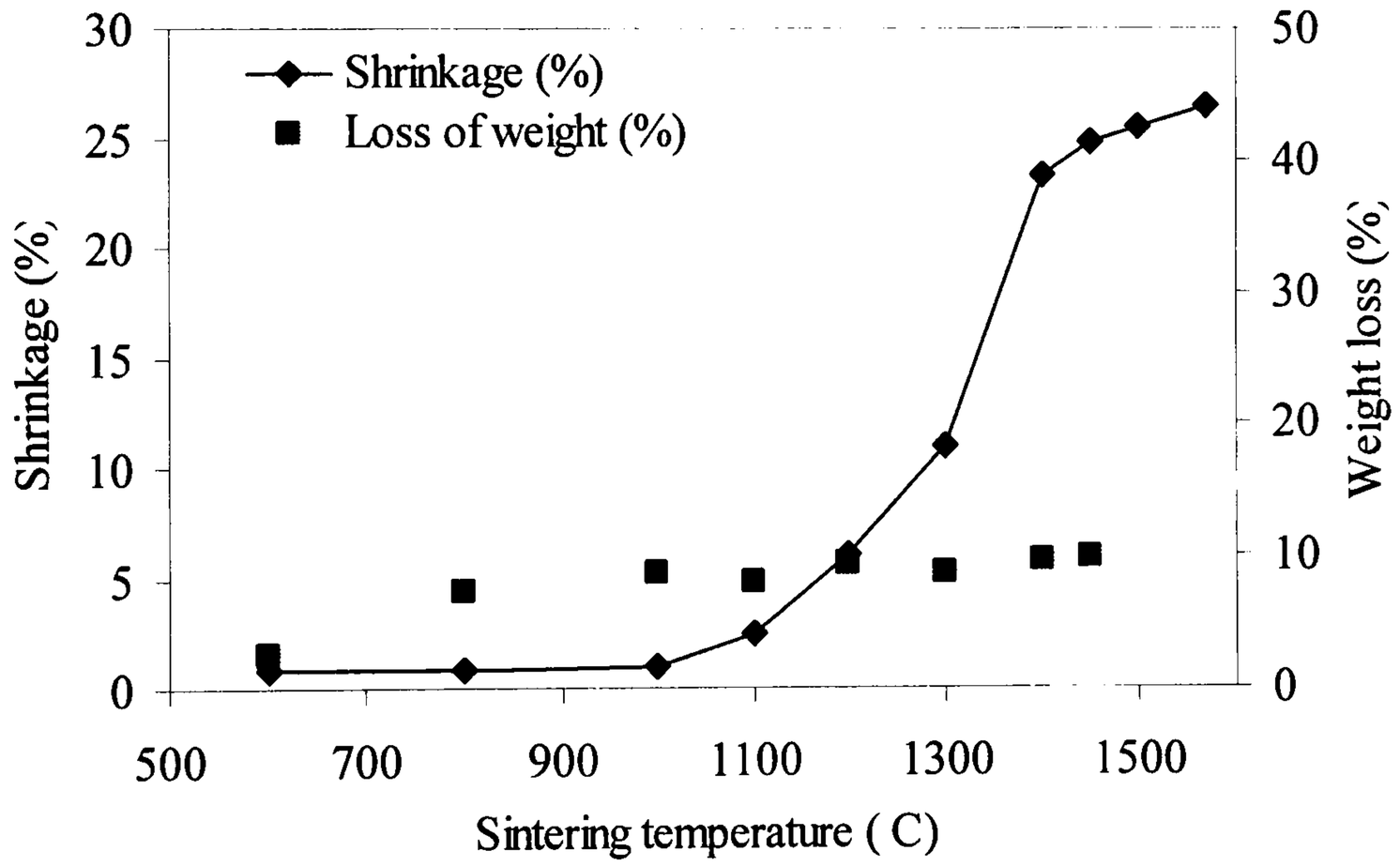


Fig. 3-4 The Effect of calcination temperatures on shrinkage and weight loss of SCYb hollow fibres.

At sintering temperature of 1400 °C, the hollow fibre was shrunk about 23.3±0.2%, which was more than twice of the shrinkage when sintering at 1300 °C. The shrinkages of hollow fibre membranes at higher temperatures of 1450, 1500 and 1570 °C were also measured and the results were shown in the Fig. 3-4 as well. It can be seen that the rate of shrinkage

after 1400 ℃ was considerably decreased. As shown Fig. 3-4, the slopes of shrinkage curve between 1200 and 1400 ℃ are great, indicating the fast rate of fibre shrinkage. At lower (600-1200 ℃) and higher (1450-1570 ℃) temperature ranges, the rate of fibre shrinkage is negligible.

3.3.2 Investigation of sintering time

Except for the sintering temperature, the sintering time is also thought to be another important parameter in the sintering process. Fig. 3-5 gives the effect of sintering time on the shrinkage of fibres at different temperatures. It can be seen that the shrinkage increases sharply at first 60 minutes when the most of shrinkage was completed. Between 60 and 480 minutes, the hollow fibres were not found to be shrinking considerably. At lower temperatures, the shrinkage was very limited. In order to investigate the effect of time at different sintering temperatures, the sintering experiments were carried out at the temperature from 800 to 1400 ℃, which was considered to be the sensitive operating zone. Fig. 3-6 - Fig. 3-8 show the SEM pictures of surface morphology of fibres sintered at 800 ℃, 1300 ℃ and 1400 ℃ for duration from 30 to 480 minutes.

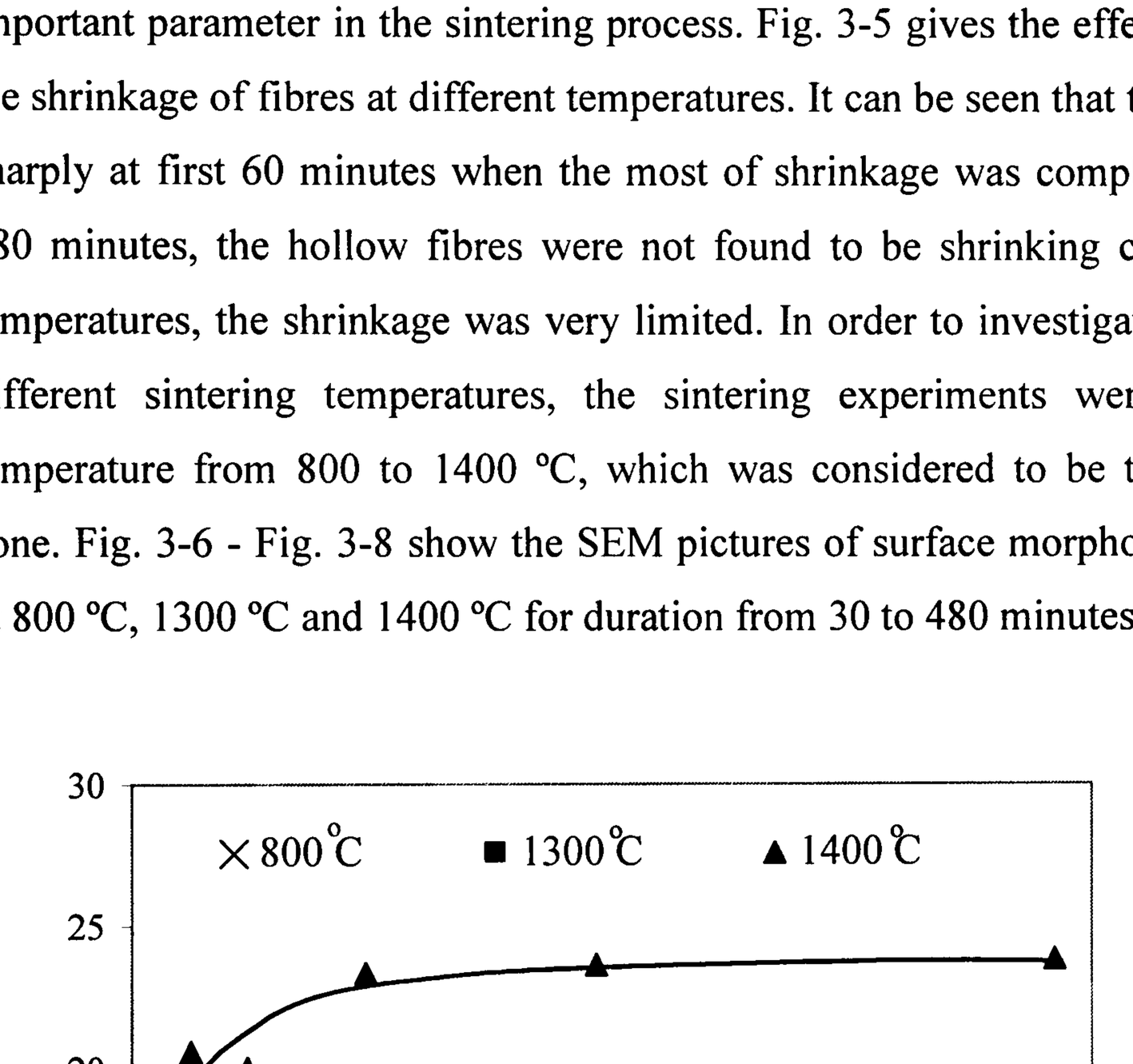


Fig. 3-5 Effect of sintering time on the shrinkage of the SCYb hollow fibres at different temperatures.

Fig. 3-6 depicts surface morphology change with time for the membrane calcined at 800 °C. It can be seen from Fig. 3-6 (A), i.e. calcined for 30 minutes, the membrane surface is dense with identifiable particle shapes. As the calcination continues, the surface of the membrane, which composed by the particles, becomes porous as shown in Fig. 3-6(B)-Fig. 3-6(D). All the particles kept in their original shape and the shrinkage was found to be less than one percent at this stage.

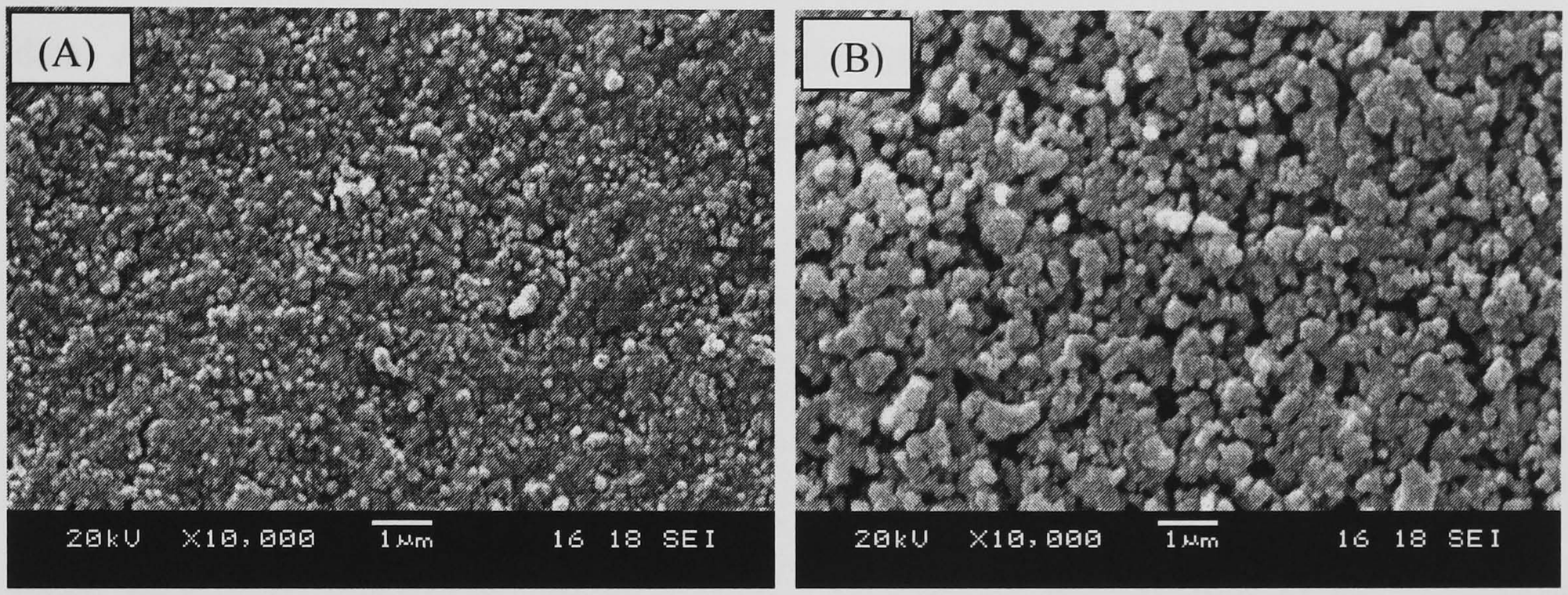


Fig. 3-6 The effect of calcination time at 800 °C; (A) 30 minutes, (B) 60 minutes, (C) 240 minutes, and (D) 480 minutes.

Fig. 3-7 shows the surface morphology change with time for the membrane calcined at 1300 °C. It can be seen from Fig. 3-7(A) that the aggregation of particles takes place within 30 minutes and many large pores are formed on the membrane surface due to the disappearance of polymer binders. The shrinkage of the fibre was up to 9.1±0.1 percent at

this stage where the sintering of the particles could not be observed. The morphology of the membrane surface at this stage is similar to that of the membrane calcined at 800 ℃ over 480 minutes (Fig. 3-6D). As the calcination continues, the aggregated particles are sintered and the porous membrane with a network structure is formed as shown in Fig. 3-7(B). As the sintering process proceeds to 240 (Fig. 3-2C) and then 480 (Fig. 3-7D) minutes, there is no obvious grain growth observed. The membrane surface is porous, and its structure remains relatively unchanged. This can also be confirmed from the shrinkage data. As can be seen from Fig. 3-5, the shrinkage is 9.9±0.1, 11.0±0.2, 12.5±0.1 and 13.2±0.1 percent for 60, 120, 240 and 480 minutes, respectively.

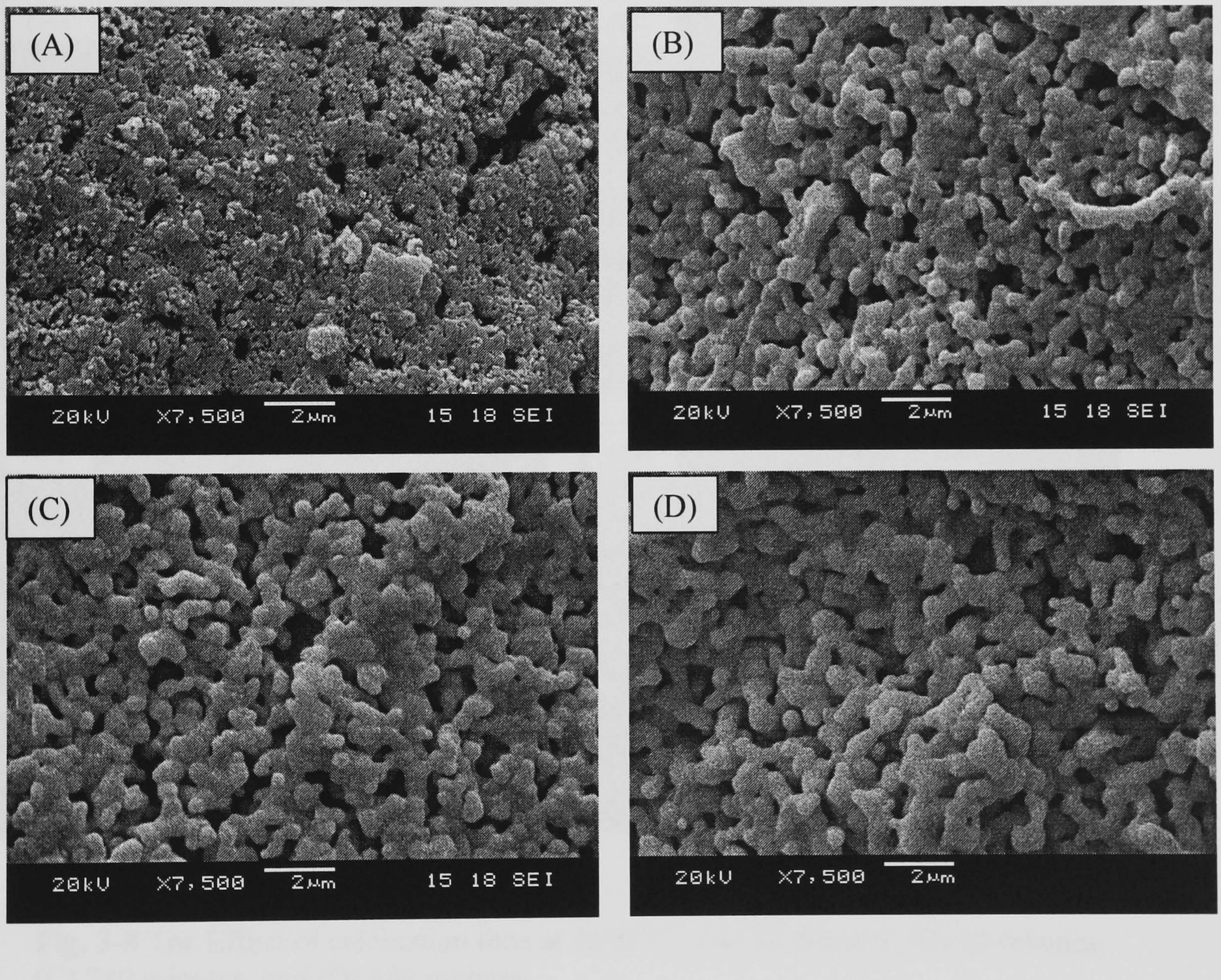


Fig. 3-7 The effect of calcination time at 1300 ℃; (A) 30 minutes, (B) 60 minutes, (C) 240 minutes, and (D) 480 minutes.

Fig. 3-8 shows the surface morphology change with time for the membrane calcined at 1400 °C. It can be seen that the sintering process started within 30 minutes of calcinations. The observed porosity at the membrane surface is low. As the calcination continues, the grain size is increased considerably and the number of surface pores of the membrane is observed to be further reduced. The shrinkage of the fibres calcined at 1400 °C was found to be much higher than that calcined at 1300 °C, i.e. up to 23.3±0.2 percent. The most shrinkage was completed within 30 minutes, i.e. 20.6±0.1 percent.

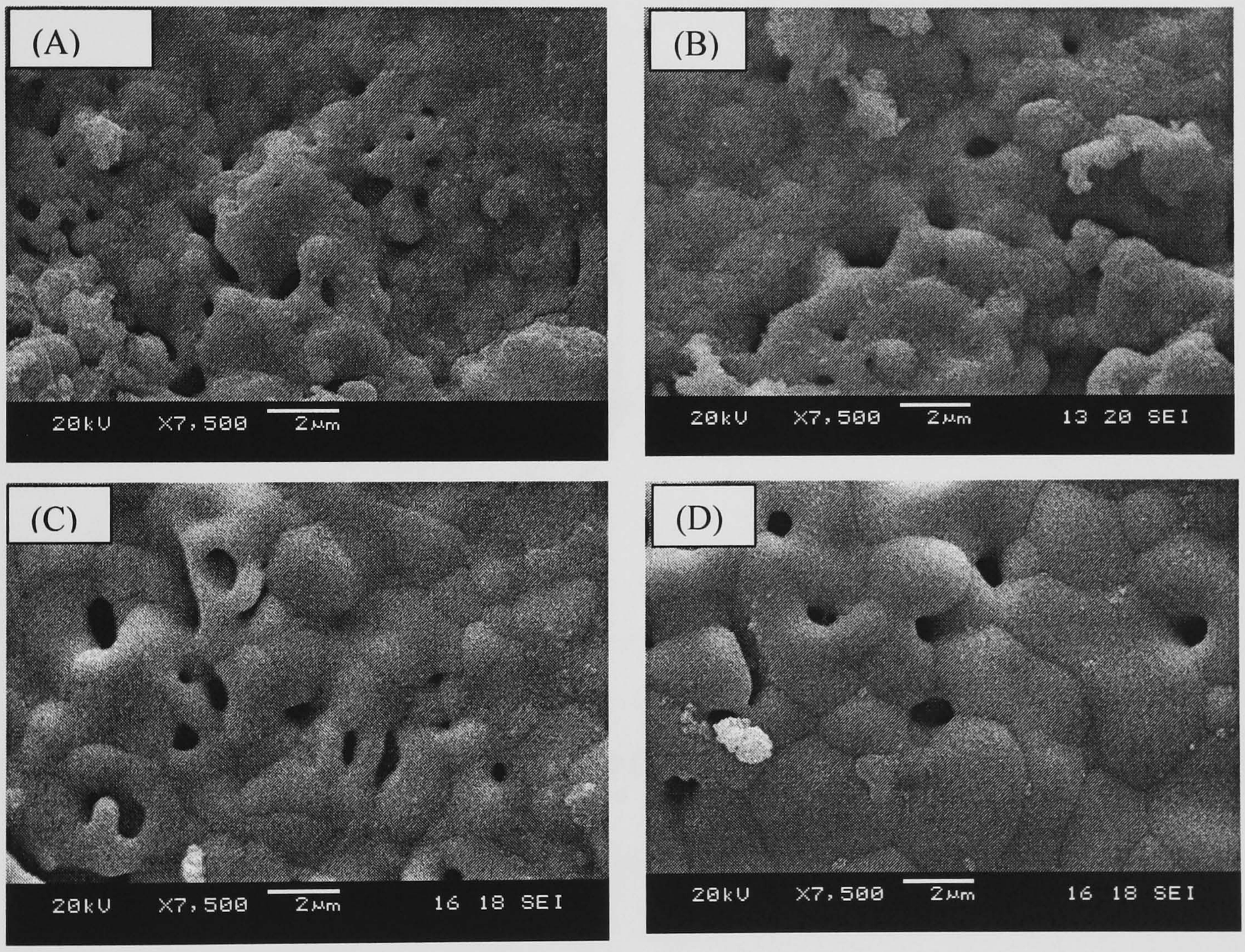


Fig. 3-8 The Effect of calcination time at 1400 °C, (A) 30 minutes, (B) 60 minutes, (C) 240 minutes, and (D) 480 minutes.

In order to demonstrate the combined influences of the sintering temperature and time, the experiment results of shrinkage of the hollow fibres in the sintering process under the

conditions of temperature from 1000 to 1600 °C and calcination time from 30 to 480 minutes were summarized in Fig. 3-9. An area between the two curves was obtained to illustrate the operating zone of calcination corresponding to temperature and time. The large effect of sintering temperature on the shrinkage of the membranes takes place between 1200 to 1400 °C, beyond this temperature range, the membrane shrinkage was relatively small, as calcination time is further increased.

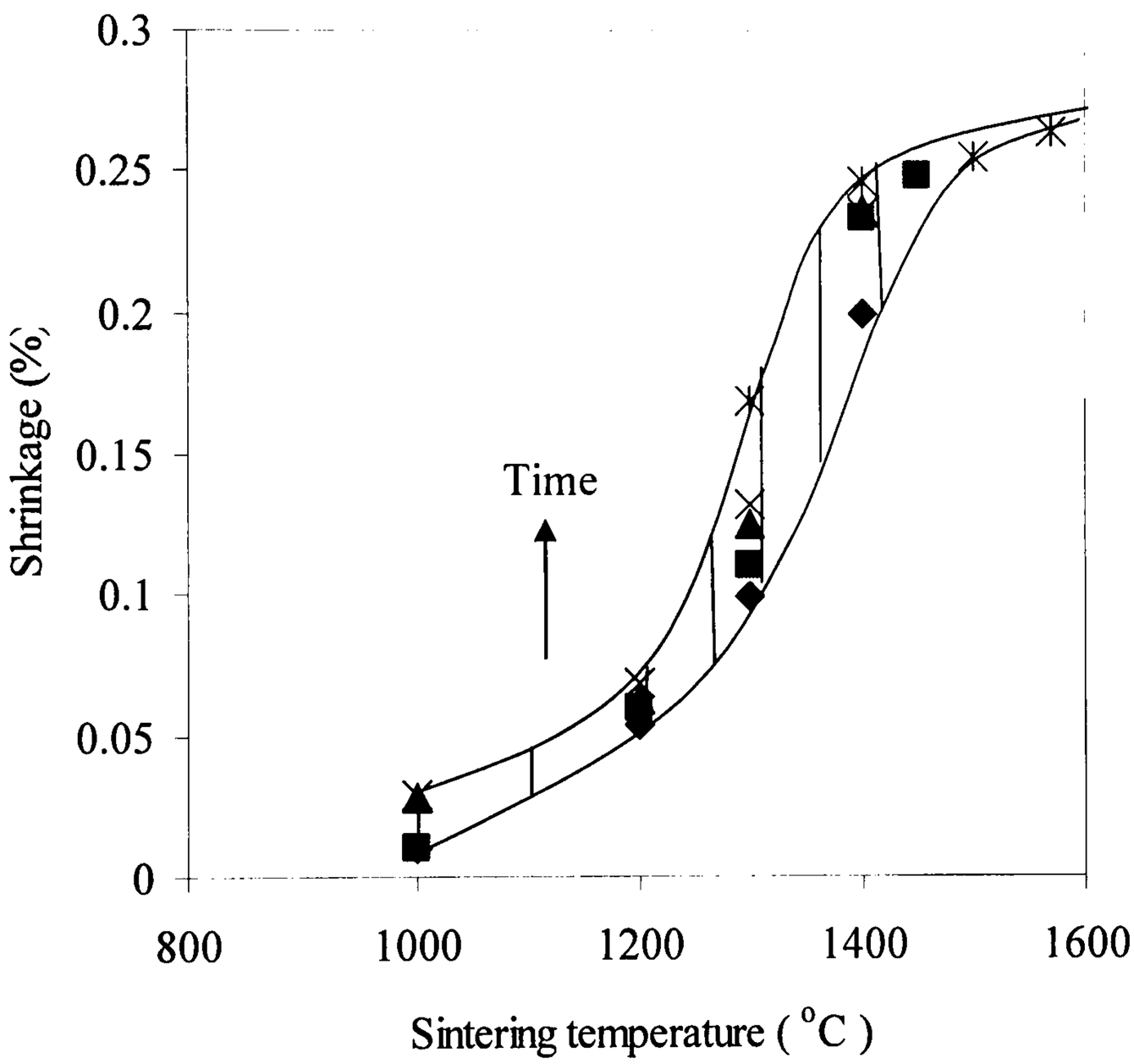


Fig. 3-9 The effects of calcination temperature and time on the shrinkage of the SCYb hollow fibres.

3.4 Conclusions

The SCYb hollow fibre membranes were prepared via a combined phase inversion and sintering method. The membranes have strong asymmetric structure and a very thin toplayer. From above discussions on the effect of sintering temperature and time on the shrinkage, weight loss, gain growth gas permeability and mechanical strength was investigated using SCYb hollow fibre membranes, a few of conclusions related to the sintering behaviors based on the experimental results and SEM pictures could be summarized as:

- The results from weight loss experiments suggest that the polymer binder could not be burnt out completely at temperatures lower than 1000 ºC in 2 hours. Fully dense membrane surface was obtained at sintering temperature of 1500 or 1600 ºC, but fast growing of grain size occurred at such high temperatures.
- The shrinkage of SCYb hollow fibre increases, as the calcination temperature is increased. However, it is not obvious when the temperature is lower than 1100 ºC. As the sintering temperature is operated at 1400 ºC or greater, the increase in the shrinkage of the hollow fibre again becomes limited. The considerable shrinkage of the hollow fibres takes place at temperature between 1200 and 1400 ºC, which indicates that the densification dominates at this temperature range.
- The influences of sintering time between 30 and 480 minutes is found to be different for different sintering temperatures. At lower calcination temperature i.e. less 1100 ºC, the effect of calcination time on the fibre shrinkage is very limited. However, at higher sintering temperature i.e. over 1400 ºC, bulk of shrinkage is completed within 30 or 60 minutes.
- For the SCYb ceramic hollow fibre membranes, the obvious sintering takes place at temperature around 1300 ºC where the grain growth is limited and the membrane surface is porous. The fast growing of the grain size occurs at the temperature higher than 1400 ºC, and the porosity of the membrane surface is observed to be reduced greatly even in a very short sintering time. Precise design of the sintering procedure would be essential for manufacturing of SCYb hollow

fibre membranes with desirable properties and without greatly growing of the grain size.

References

Akash, A. and M. J. Mayo (1999). Pore growth during initial-stage sintering, *J. Am. Ceram. Soc.*, **Vol.** 82, **pp.** 2948-2952.

Binner, J. G. P. (1990). *Advanced Ceramic Processing and Technology*, Noyes Publications, New Jersey.

Bouwmeester, H. J. M. (2003). Dense ceramic membranes for methane conversion, *Catalysis Today*, **Vol.** 82, **pp.** 141-150.

Chen, P.-L. and I.-W. Chen (1996). Sintering of fine oxide powders: I, microstructural evolution, *J. Am. Ceram. Soc.*, **Vol.** 79, **pp.** 3129-3141.

Guan, J., S. E. Dorris, U. Balachandran and M. Liu (1997). Transport properties of $BaCe_{0.95}Y_{0.05}O_{3-\delta}$ mixed conductors for hydrogen separation, *Solid State Ionics*, **Vol.** 100, **pp.** 45-52.

Hamakawa, S., T. Hibino and H. Iwahara (1993). Electrochemical methane coupling using protonic conductors, *J. Electrochem. Soc.*, **Vol.** 140, **pp.** 459-462.

Hamakawa, S., T. Hibino and H. Iwahara (1994). Electrochemical methane coupling in a proton-hole mixed conductor and its application to a membrane reactor, *J. Electrochem. Soc.*, **Vol.** 141, **pp.** 1720-1726.

Hamakawa, S., L. Li, A. Li and E. Iglesia (2002). Synthesis and hydrogen permeation properties of membranes based on dense SrCe0.95Yb0.05O3-a, thin film, *Solid State Ionics*, **Vol.** 148, **pp.** 71-81.

Iwahara, H. (1995). Technological challenges in the application of proton conducting ceramics, *Solid State Ionics*, **Vol.** 77, **pp.** 289-298.

Kreuer, K. D. (1997). On the development of proton conducting materials for technological applications, *Solid State Ionics*, **Vol.** 97, **pp.** 1-15.

Langguth, J., R. Dittmeyer, H. Hofmann and G. Tomandl (1997). Studies on oxidative coupling of methane using high-temperature proton-conducting membranes, *Applied Catalysis S: General*, **Vol.** 158, **pp.** 287-305.

Lee, J. S. and S. T. Oyama (1988). Oxidative coupling of methane to higher hydrocarbons, *Catal. Rev. Sci. Eng.*, **Vol.** 30, **pp.** 249-280.

Liu, S., X. Tan, K. Li and R. Hughes (2001a). Methane coupling using catalytic membrane reactors, *Catal. Rev. Sci. Eng.*, **Vol.** 43, **pp.** 147-198.

Liu, S., X. Tan, K. Li and R. Hughes (2001b). Preparation and characterisation of $SrCe_{0.95}Yb_{0.05}O_{2.975}$ hollow fibre membranes, *J. Membr. Sci.*, **Vol.** 193, **pp.** 249-260.

Norby, T. (1999). Solid-state protonic conductors: principles, properties, progress and prospects, *Solid State Ionics*, **Vol.** 125, **pp.** 1-11.

Qi, X. and Y. S. Lin (2000). Electrical conduction and hydrogen permeation through mixed proton-electron conducting strontium cerate membranes, *Solid State Ionics*, **Vol.** 130, **pp.** 149-156.

Reed, J. S. (1995). *Principles of Ceramics Processing*, John Wiley & Sons, Inc.

Rhodes, W. H. (1981). Agglomerate and partcle size effects on sintering yttria-stabilized zirconia, *J. Am. Ceram. Soc.*, **Vol.** 64, **pp.** 19-22.

Richerson, D. W. (1992). *Modern Ceramic Engineering*, Marcel Dekker Inc, New York.

Teraoka, Y., H. M. Zhang, S. Furukawa and N. Yamazoe (1985). Oxygen permeation through perovskite-type oxides, *Chem. Lett.*, **Vol.**, **pp.** 1743.

Teraoka, Y., H. M. Zhang, K. Okamoto and N. Yamazoe (1988). Mixed ionic-electronic conductivity of $La_{1-x}Sr_xCo_{1-y}Fe_yO_{3-\delta}$ perovskite-type oxides, *Mat. Res. Bull.*, **Vol.** 23, **pp.** 51-58.

Wang, P., P. Huang, N. Xu, J. Shi and Y. S. Lin (1999). Effects of sintering on properties of alumina microfiltration membranes, *J. Membr. Sci.*, **Vol.** 155, **pp.** 309-314.

Zeng, Y., L. Y.S. and S. L. Swartz (1998). Perovskite-type ceramic membrane: synthesis, oxygen permeation and membrane reactor performance for oxidative coupling of methane, *J. Membr. Sci.*, **Vol.** 150, **pp.** 87-98.

Chapter 4

$SrCe_{0.95}Yb_{0.05}O_{3-\delta}$ hollow fiber membrane and its property in proton conduction

Abstract

$SrCe_{0.95}Yb_{0.05}O_{3-\delta}$ (SCYb) hollow fiber membranes have been prepared by a combined phase inversion and sintering method where polyethersulfone (PESf) is used as a binder, N-methyl-2-pyrrollidone (NMP) as solvent and polyvinylpyrrolidone (PVP, K16-18) as an additive, respectively. Via a programmed sintering process, hollow fiber precursors have been successfully sintered into dense membranes. A hollow fiber membrane module has also been fabricated and the hydrogen permeation (proton conduction) properties of the developed SCYb hollow fiber membranes have been studied under different operating conditions such as temperatures and hydrogen/oxygen feed concentrations. Comparison between experimental data and theoretical results indicates that the surface exchange reactions may contribute some resistances to hydrogen permeation. In order to promote the hydrogen permeation, dry air should be used. The hydrogen permeation efficiency would be affected when long SCYb hollow fibers were employed. However, the total hydrogen permeation flux remains relatively unchanged in either cocurrent or countercurrent operation.

Key words: $SrCe_{0.95}Yb_{0.05}O_{3-\delta}$; perovskite; hollow fiber membrane; hydrogen permeation.

4.1 Introduction

High-temperature proton conductors based on mixed oxides with perovskite structures, for example, $SrCe_{0.95}Yb_{0.05}O_{3-\delta}$ (SCYb), have attracted considerable interests due to their potential applications in chemical and electrochemical industries (Iwahara *et al.*, 1981; Iwahara *et al.*, 1982; Iwahara, 1995). However, it is also recognized that many efforts have to be made to improve their proton conductivity (or proton permeation flux when imposed with an asymmetric atmosphere) before they can be found useful in many practical applications. Recently, some progresses have been achieved in preparing dense ceramic membranes with ideal proton permeation fluxes. Hamakawa et al. (Hamakawa *et al.*, 2002) prepared a thin proton conducting film (up to 2 μm) on porous substrates by spin coating colloidal suspensions of ceramic powders, and the hydrogen permeation flux as high as 2×10^{-5} mol/cm^2.s at 950 K was achieved. In addition, a phase inversion-sintering technique has been developed in preparing hollow fibre ceramic membranes with asymmetric structures (Liu *et al.*, 2001; Tan *et al.*, 2001; Tan *et al.*, 2005), which show several advantages over the conventional membranes. Compared to the disk-shaped membranes, the hollow fibre membranes can provide a much larger effective membrane area per unit volume for hydrogen permeation. Also by adopting long hollow fibres and keeping the two sealing ends away from the high temperature zone, problems of high temperature sealing no longer exist. Furthermore, due to the asymmetric structure (i.e. a thin separating dense layer integrated with porous substrate), the membrane's resistance to hydrogen permeation (or proton conduction) is very much reduced compared to the symmetric membranes prepared by the conventional methods.

In this chapter, $SrCe_{0.95}Yb_{0.05}O_{3-\delta}$ (SCYb) hollow fibre dense membranes have been successfully prepared by a phase inversion/sintering technique. The proton permeation properties of the resulting SCYb hollow fibre membranes have also been investigated both experimentally and theoretically.

4.2 Experiemntal

4.2.1 Preparation of SCYb hollow fiber membranes

The phase inversion/sintering technique was applied in preparing the SCYb hollow fiber membranes. The detailed procedures were described in Chapter 3. A spinneret with orifice-diameter/inner-diameter of 3.0/1.2 mm was used to obtain the hollow fiber precursors. The preparation parameters for the resulting SCYb hollow fiber membranes in this work were summarized in Table 4-1.

Table 4-1 Preparation conditions of the SCYb hollow fibre.

Parameter	Value
Dope composition (wt%)	
SCYb	69
PES, Radel A-300	6.5
NMP	23.9
PVP K90	0.6
Dope temperature (°C)	20
Coagulation bath temperature (°C)	20
Internal coagulant temperature (°C)	20
Injection rate of internal coagulant (ml/min)	9.5
Air gap (cm)	2.0
Sintering temperature (°C)	1200-1600

Sintering of the hollow fiber membranes was carried out in a high-temperature tubular furnace (STF16/450, CARBOLITE) where the SCYb hollow fiber precursors were placed and sintered at 1200 °C for 16 hours and further sintered at 1350-1550°C for another 4 hours to form the hollow fiber membrane product. The heating and cooling rates of sintering were both 5°C/min.

4.2.2 Characterization methods

Structures of the prepared hollow fiber membranes were visually observed using a scanning electron microscopy (JEOL JSM-5610LV, Japan). In order to obtain the original cross-sectional fracture, the hollow fiber precursor was immersed in a liquid-nitrogen where the frozen membranes were slowly flexed after about 5-10 min. For the

sintered membranes, the cross-sectional fracture was obtained by directly snapping the fiber. These membrane samples were then positioned on a metal holder and gold-coated using a sputter coating operated under vacuum. The SEM micrographs of both surface and cross-section of the hollow fiber membranes were taken at various magnifications.

The gas-tight property of the prepared hollow fibre membranes was measured using a gas permeation apparatus developed in house. Nitrogen was used as the test gas. The initial amount of the test gas in the cylinder was set at 56 kPa and the pressure change was then recorded continuously. The nitrogen permeance through the membrane pores (or defects) was calculated based on the pressure change in the test cylinder as a function of time. The hollow fibres with a measured permeance of less than 10^{-14} mol/(cm^2.Pa.s) is considered to be gas-tight.

The mechanical strength of the hollow fiber was measured through a bending test performed using Intron Model 4466 provided with a load cell for 1 kN. The hollow fiber samples were fixed in the sample holder with the spec gauge length of 15 mm. The crosshead speed was set at 0.02 cm/min. The load needed to break the hollow fiber was recorded for each sample with which the bending strength σ_F is calculated by the following equation:

$$\sigma_{F\cdot} = \frac{8F_m L_h D_o}{\pi(D_o^4 - D_i^4)} \tag{4-1}$$

where, F_m is the force at which fracture takes place; L_h, D_o and D_i are the length (15 mm), outer diameter and inner diameter of the hollow fiber, respectively. Final results were taken from the average value of four samples for each membrane.

XRD analyse were carried out to determine the crystalline structure using a PW1710 X-ray diffractometer with CuKα radiation on the membrane material (SCYb powders), the fresh hollow fiber membrane (after sintered but before hydrogen (proton) permeation experiments) and on the used membranes taken from the middle sector of the hollow fibers after performing the hydrogen permeation. Both the fresh and used membranes were XRD-analysed on the outer surfaces of snapped fibers. A continuous

scan mode was used to collect 2 θ data from 15 to 75° with a 0.04 sampling pitch and a 2.4° /min scan rate. The generator tension and generator current were 40 kV and 40mA, respectively.

4.2.3 Measurement of hydrogen permeation

The hydrogen permeation (or proton conduction) properties of the resulting SCYb hollow fiber membranes were studied using a membrane module where a gas-tight SCYb hollow fiber 30 cm in length was assembled. Fig. 4-1 schematically illustrates the experimental setup. The membrane module was placed in a tubular furnace (MTF 10/25/130, CARBOLITE) with a constant temperature zone of only 4.0 cm. Therefore, the two sealing joints were kept away from the furnace tube. A short soft silicone rubber tube was used to offset the thermal expansion mismatch of the hollow fiber membrane and the module shell at high temperatures.

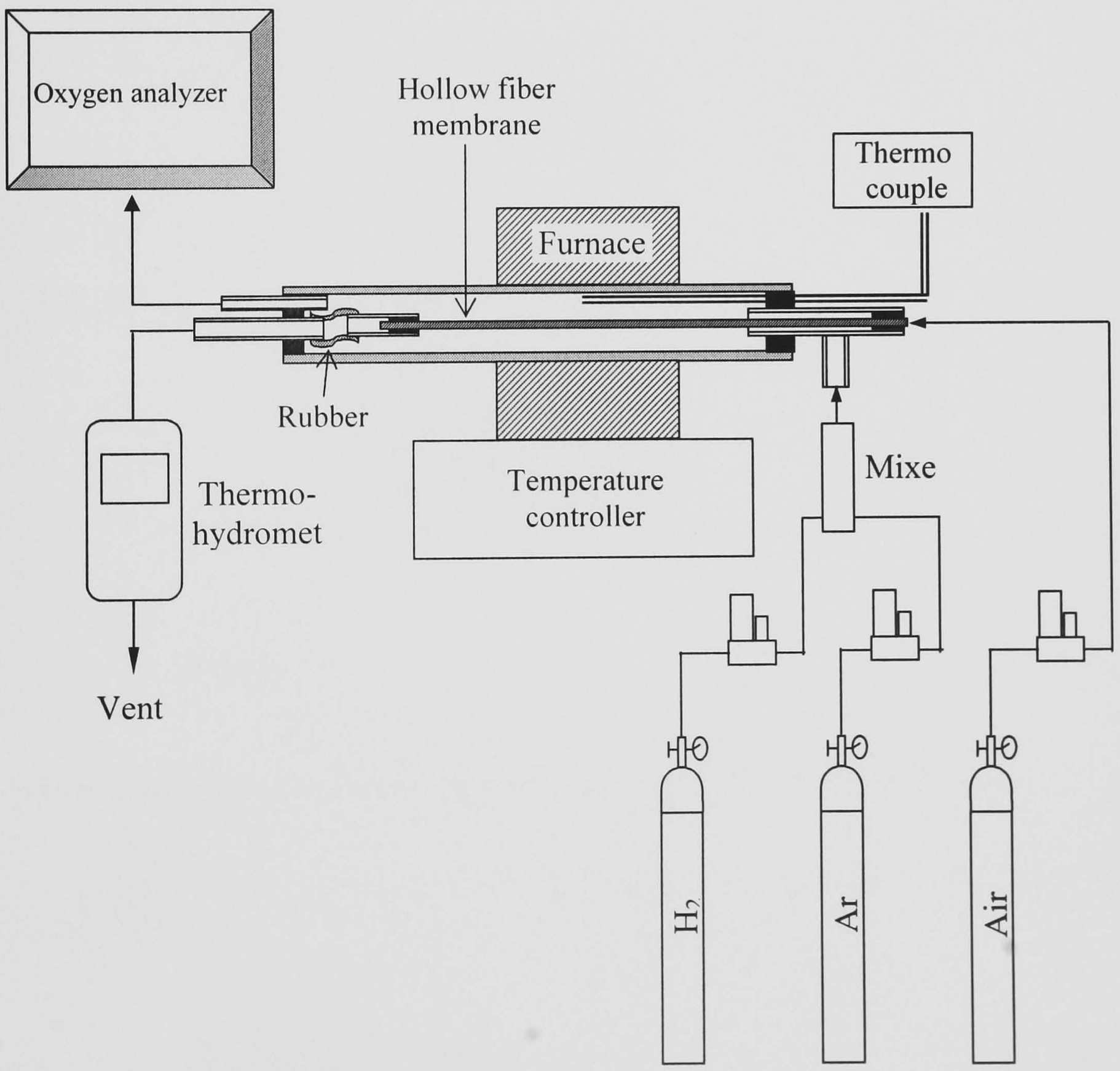


Fig. 4-1 Diagram of the experimental setup for hydrogen permeation.

In the measurements, the mixture of hydrogen and argon was fed into the shell side while air introduced into the lumen side of the module. The gas flow rates were controlled and measured using the mass flow controllers (Smart Mass Flow meter with Read out & Control Electronics Model 0152, Brooks Instrument). The temperature was measured with a type C thermocouple combined with a thermometer supplied by Omega Engineering Inc. Oxygen concentrations were measured with an oxygen meter (Oxygen Analyser 572, Servomex). The concentrations of water vapor in gas streams were measured online in terms of relative humidity (RH) using a thermo-hydrometer supplied by OMEGA (Model RH82). Obviously, the permeation fluxes of hydrogen and oxygen through the membrane can be reflected by the formation rates of water vapor in the air stream and in the hydrogen stream, respectively.

4.3 Theory and model development

4.3.1 Mechanism of hydrogen permeation

It is known that SCYb is a mainly mixed proton-hole conductor (Tan *et al.*, 2000) (its oxygen conduction becomes only noticeable at temperature greater than 1400 K) where the mobile charged defects at elevated temperatures include oxygen vacancy, $V_O^{\cdot\cdot}$, proton $H^{\cdot}$ and electron hole, $h^{\cdot}$ (Uchida *et al.*, 1983; Slade and Singh, 1991). When a SCYb membrane is exposed to an asymmetric gas environment as shown in Fig. 4-2, the charged defects are transferred from one side to the other under the electrochemical potential gradients. The following reactions may take place on the membrane surfaces:

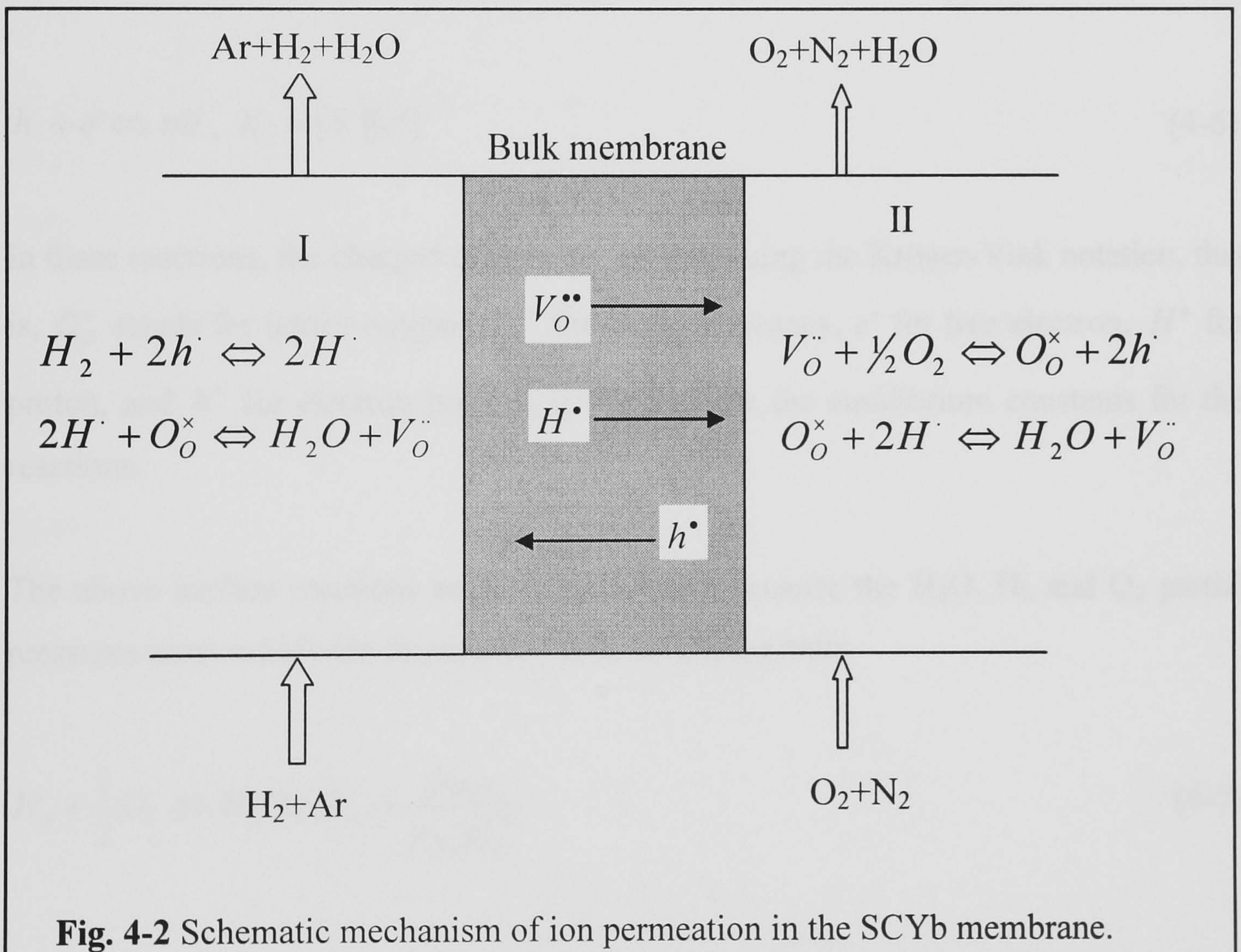


Fig. 4-2 Schematic mechanism of ion permeation in the SCYb membrane.

On the oxygen side,

$$V_O^{\cdot\cdot} + \tfrac{1}{2}O_2 \Leftrightarrow O_O^{\times} + 2h^{\cdot}\ ,\ K_1 = \frac{[h^{\cdot}]^2}{[V_O^{\cdot\cdot}]p_{O_2}^{1/2}} \tag{4-2}$$

$$O_O^{\times} + 2H^{\cdot} \Leftrightarrow H_2O + V_O^{\cdot\cdot},\ K_2 = \frac{[H^{\cdot}]^2}{[V_O^{\cdot\cdot}]p_{H_2O}} \tag{4-3}$$

On the hydrogen side, in addition to eq. 4-2, the following reaction occurs:

$$H_2 + 2h^{\cdot} \Leftrightarrow 2H^{\cdot},\ K_3 = \frac{[H^{\cdot}]^2}{[h^{\cdot}]^2 p_{H_2}} \tag{4-4}$$

It is the linear combination of the following successive reactions:

$$H_2 \Leftrightarrow 2H^{\cdot} + 2e',\ K_4 = \frac{[H^{\cdot}]^2[e']^2}{p_{H_2}} \tag{4-5}$$

$$h^{\cdot} + e' \Leftrightarrow nil,\ K_e = [h^{\cdot}][e'] \tag{4-6}$$

In these reactions, the charged defects are defined using the Kröger-Vink notation, that is, $O_O^{\times}$ stands for lattice oxygen, $V_O^{\bullet\bullet}$ for oxygen vacancy, e' for free electron, $H^{\bullet}$ for proton, and $h^{\bullet}$ for electron hole. K_i (i=1,2,3,4) are the equilibrium constants for the reactions.

The above surface reactions are not independent because the H_2O, H_2 and O_2 partial pressures must satisfy the thermodynamics for the reaction:

$$H_2 + \frac{1}{2}O_2 \Leftrightarrow H_2O,\ K_w = \frac{p_{H_2O}}{p_{H_2} p_{O_2}^{1/2}} \tag{4-7}$$

It should be noted that the above reactions might involve many sub-steps such as adsorption, dissociation, recombination and charge transfer. Meanwhile, local electric neutrality must be satisfied everywhere in the membrane at any time, that is

$$[Yb_{Ce}^{'}] = [H^{\cdot}] + [h^{\cdot}] + 2[V_O^{\cdot\cdot}] \tag{4-8}$$

4.3.2 Transfer equations of charged defects in the SCYb membrane

The transport fluxes of charged defects in mixed conductors at steady state under the electrochemical potential gradient can be expressed by (Tan *et al.*, 2000):

$$J_i = -D_i C_i \left[\frac{1-t_i}{C_i} \cdot \frac{dC_i}{dx} - \sum_{j \neq i} \frac{z_i}{z_j} \cdot \frac{t_j}{C_j} \cdot \frac{dC_j}{dx} \right] \tag{4-9}$$

where D, C, z, t are the diffusivity, concentration, charge number and the transport number of defect i ($i=p$, V, h), respectively. If no external current is applied, the following equation must be satisfied at steady state:

$$\sum z_i J_i = 0 \tag{4-10}$$

At steady state, the concentration profiles of the defects in the membrane may be described by a group of ordinary differential equations that are rewritten in the matrix form as:

$$\overline{A} \cdot \frac{d\overline{C}}{dx} = \overline{B} \tag{4-11}$$

where,

$$\overline{A} = \begin{bmatrix} 1-t_V & -2t_p \dfrac{C_V}{C_p} & -2t_h \dfrac{C_V}{C_h} \\ -\dfrac{1}{2} t_V \dfrac{C_p}{C_V} & 1-t_p & -t_h \dfrac{C_p}{C_h} \\ 2 & 1 & 1 \end{bmatrix} \quad \overline{B} = \begin{bmatrix} -\dfrac{J_V}{D_V} \\ -\dfrac{J_p}{D_p} \\ 0 \end{bmatrix} \quad \overline{C} = \begin{bmatrix} C_V \\ C_p \\ C_h \end{bmatrix} \tag{4-11a}$$

with the boundary conditions:

$$x = 0,\ \overline{C}_i = C_i(I);\ x = L,\ \overline{C}_i = C_i(II) \tag{4-12}$$

The corresponding defect concentrations on the membrane surfaces is given by solving the equilibrium Eqs. 4-2 to 4-7 as:

$$C_p(I) = \frac{\sqrt{\left(1 + 1/\sqrt{K_3 p_{H_2}}\right)^2 + 8[Yb_{Ce}']/K_2 p_{H_2O}} - \left(1 + 1/\sqrt{K_3 p_{H_2}}\right)}{4/K_2 p_{H_2O}} \tag{4-13a}$$

$$C_V(I) = C_p(I)^2 / K_2 p_{H_2O} \tag{4-13b}$$

$$C_h(I) = C_p(I) / \sqrt{K_3 p_{H_2}} \tag{4-13c}$$

and

$$C_V(II) = \frac{1}{16}\left[\sqrt{\left(\sqrt{K_1 p_{O_2}^{1/2}} + \sqrt{K_2 p_{H_2O}}\right)^2 + 8[Yb_{Ce}']} - \left(\sqrt{K_1 p_{O_2}^{1/2}} + \sqrt{K_2 p_{H_2O}}\right)\right]^2 \tag{4-14a}$$

$$C_h(II) = \sqrt{K_1 p_{O_2}^{1/2} C_V(II)} \tag{4-14b}$$

$$C_p(II) = \sqrt{K_2 p_{H_2O} C_V(II)} \tag{4-14c}$$

where *I* and *II* stand for the hydrogen side and the oxygen side, respectively.

It should be noted that the above equations are derived with an assumption that all the surface reactions are in equilibrium, i.e. the defect transfer process is the controlling step.

4.3.3 SCYb hollow fiber membrane module for proton permeation

Establishment of the modeling equations is based on the membrane module consisting of *n* SCYb hollow fibers with the length of *L* housed in a ceramic tube. The mixture of hydrogen and argon is introduced into the shell side of the module under atmosphere while air flows through the fiber lumen either cocurrently or countercurrently. The flow pattern in one SCYb hollow fiber is shown in Fig. 4-3.

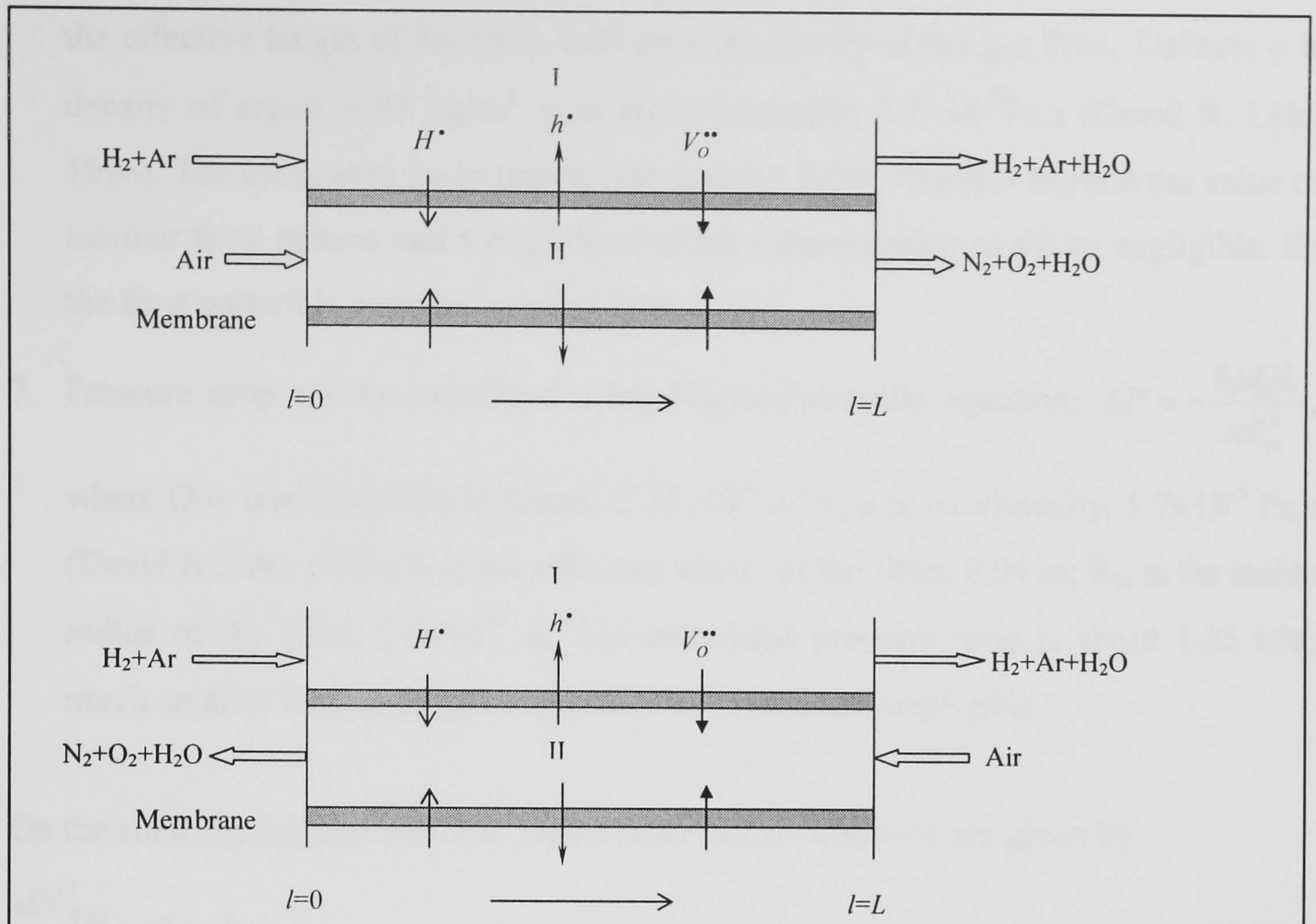


Fig. 4-3 Flow pattern in the SCYb hollow fibre membrane module (A) Cocurrent flow, (B) Countercurrent flow.

The following assumptions are adopted to formulate the mathematical model:

1. The membrane module is isothermally operated at steady state.
2. The transfer of defects in the membrane is the controlling step and the surface reactions are in equilibrium.
3. The transfer of defects in the axial direction within the membrane is negligible due to high ratio of the fibre length and the membrane wall thickness.
4. The mass transfer resistance between gas and the membrane surfaces either on the shell or lumen side is negligible.
5. Ideal gas law may be used to describe the gas behavior of both single component and gas mixture.

6. Reynolds number (Re) of the gas flow can be calculated by Re = Lvρ/μ, where L is the effective length of the fibre, 0.04 m; v is velocity of the gas flow, 7.05m/s; ρ is density of argon, 0.45 kg/m^3; μ is argon viscosity, 5.7×10^{-5}Pa.s (David R. Lide, 1996). The calculated Re in lumen side is about 2230, which is beyond the value of laminar flow pattern and the gradient of the concentration could be negligible. So the flow pattern is assumed as plug flow.

7. Pressure drop can be calculated using Hagen-Poiseuille equation: $\Delta P = -\frac{8\mu QL}{\pi R_{in}^4}$, where Q is feed flow rate in lumen, 2.27×10^{-6} m^3/s; μ is Ar viscosity, 5.7×10^{-5} Pa.s (David R Lide, 1996); L is the effective length of the fibre, 0.04 m; R_{in} is the inside radius of the fibre, 3.2×10^{-4} m. The calculated pressure drop is about 1.25 kPa, much smaller than atmosphere pressure so is assumed negligible.

On the shell (hydrogen) side, the mass conservation equations are given by:

$$\frac{dN_{H_2O}^{I}}{dl} = 2n\pi R_m \cdot J_v \qquad (4\text{-}15a)$$

$$\frac{dN_{H_2}}{dl} = 2n\pi R_m \cdot \frac{1}{2} J_h \qquad (4\text{-}15b)$$

where N is the molar flow rate of each component, mol/s; R_m average membrane radius, $R_m = \frac{R_o - R_{in}}{\ln(R_o / R_{in})}$ in which R_o and R_{in} are respectively the outer and the inner radius of the hollow fiber.

On the lumen (air) side, the mass conservation equations are given by:

For the cocurrent flow,

$$\frac{dN_{H_2O}^{II}}{dl} = 2n\pi R_m \cdot \frac{1}{2} J_p \qquad (4\text{-}16a)$$

$$\frac{dN_{O_2}}{dl} = 2n\pi R_m \cdot \frac{1}{4} J_h \qquad (4\text{-}16b)$$

For the countercurrent flow,

$$\frac{dN_{H_2O}^{II}}{dl} = -2n\pi R_m \cdot \frac{1}{2} J_p \tag{4-16c}$$

$$\frac{dN_{O_2}}{dl} = -2n\pi R_m \cdot \frac{1}{4} J_p \tag{4-16d}$$

With the following boundary conditions:

for the cocurrent flow,

$$l = 0, \quad [N_{H_2O}^{I}, N_{H_2}, N_{H_2O}^{II}, N_{O_2}] = \left[\frac{p_s V_s y_{H_2O,s}}{RT}, \frac{p_s V_s y_{H_2,s}}{RT}, \frac{p_l V_l y_{H_2O,l}}{RT}, \frac{p_l V_l y_{O_2,l}}{RT} \right] \tag{4-17a}$$

for the countercurrent flow,

$$l = 0, \quad [N_{H_2O}^{I}, N_{H_2}] = \left[\frac{p_s V_s y_{H_2O,s}}{RT}, \frac{p_s V_s y_{H_2,s}}{RT} \right] \tag{4-17b}$$

$$l = L, \quad [N_{H_2O}^{II}, N_{O_2}] = \left[\frac{p_l V_l y_{H_2O,l}}{RT}, \frac{p_l V_l y_{O_2,l}}{RT} \right] \tag{4-17c}$$

where p_s and p_l are the operating pressures in the shell side and in the lumen side, respectively; V_s and V_l are the volumetric feed flow rates of hydrogen mixture and of the air stream, respectively; y is the molar fraction of each component in the gas feed; and L is the effective length of the membranes for permeation.

Since the water in the membrane module is produced from the reaction between proton and oxygen, as shown Fig.4-2, the permeation fluxes of proton and oxygen vacancy through the membrane may be given from the formation rates of water on the oxygen side and on the hydrogen side, respectively:

$$J_p = \frac{2}{A_m} \cdot (N^{II}_{H_2O,l=L} - N^{II}_{H_2O,l=0}) \tag{4-18a}$$

$$J_V = \frac{N^{I}_{H_2O,l=L} - N^{I}_{H_2O,l=0}}{A_m} \tag{4-18b}$$

where A_m is the effective membrane area for permeation, $A_m = 2n\pi R_m L$.

4.3.4 Solution method

As described above, the governing equations for the hollow fiber membrane module are a group of implicit ordinary differential equations and can be solved numerically by the Runge-Kutta method. In order to solve the governing equations for the countercurrent flow pattern, the shooting method has been applied. MATLAB software was employed in this study for the calculations. The numerical solution algorithm is given in Fig. 4- 4.

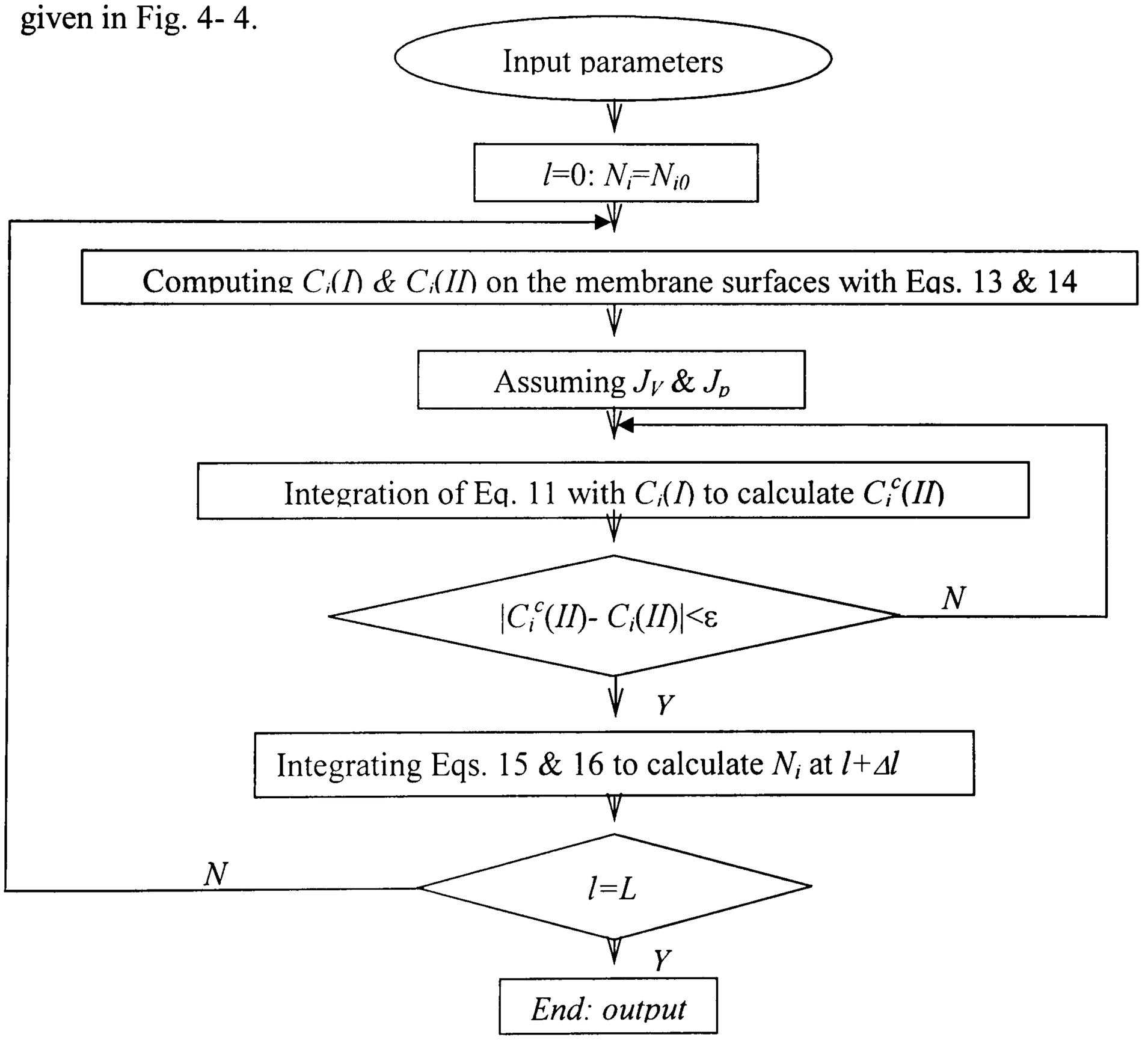


Fig. 4-4 Algorithm of the numerical solution.

4.4 Results and discussion

4.4.1 Characterization of the SCYb hollow fiber membranes

Fig. 4-5 exhibits the microstructures of the SCYb hollow fiber precursors (before sintering) and of the hollow fiber membrane products, which were sintered following a programmed sintering procedure (Liu and Li, in press). The OD/ID of the hollow fiber precursor were 1.85/0.80 mm, as measured from Figure 4-5a. After sintering, the corresponding OD/ID of the fiber product were shrunk to 1.45/0.65 mm, respectively (Fig. 4-5A). Such a considerable shrinkage is resulted from the removal of organic binder and the rearrangement of the SCYb particles in the fibers as well. However, for a certain type of ceramic membranes, the extent of the shrinkage is a function of multi-factor, such as the particle size and its size distribution, the content of the polymer binder in the precursor as well as the sintering temperature (Liu and Li, 2005).

Fig. 4-5a and 5b also illustrates the morphologies of the hollow fiber precursor. It can be seen that a finger-like structure is formed beneath of both the inner and outer skin layers of the hollow fiber precursor, but a sponge-like layer occurs at the center of the fiber precursor. The formation of this type of structure can be attributed to the rapid precipitation occurred at both the inner and outer walls close to coagulants resulting in finger pores beneath of the skin layers, but the slow precipitation at the center of the fiber giving the sponge-like structure, which is also shown in Fig. 4-5(c) under high magnification. Fig. 4-5(d) shows the outer surface of the hollow fibre precursor, from which it can be seen that the SCYb particles are well dispersed and sparsely connected each other by the polymer binder.

After sintering, the original structure can still be observed as shown in Fig. 4-5A and B. However, the quantity and the size of the finger-like pores have greatly reduced after the sintering process. Fig. 4-5(D) shows the membrane outer surface. It can be seen that the surface is completely densified and the SCYb particles are closely connected each other with clear boundaries. Further, most particles are larger than 1 μm instead of the original size of around 1.0 μm, indicating that the particle growth has occurred during the sintering process, where the small discrete particles are combined into larger ones by the sintering. It is interesting to note that all the SCYb

particles at the central layer of the fiber have also been densified and seems to be integrated into a dense layer as shown in Fig. 4-5C.

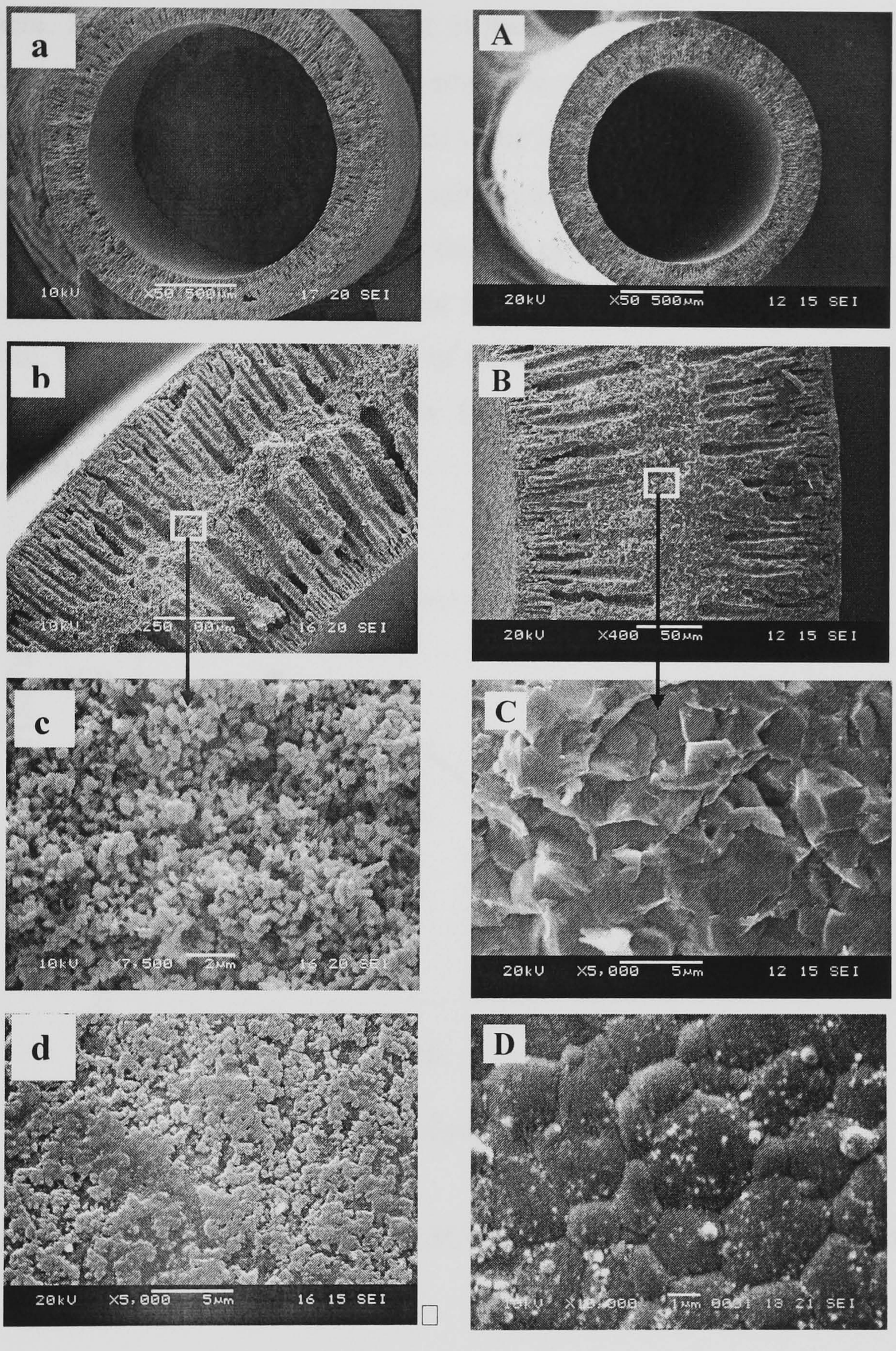


Fig. 4-5 SEM photographs of the SCYb hollow fiber membrane: (a) cross-section of the hollow fiber precursor; (b) wall of the hollow fiber precursor; (c) central sponge layer of the hollow fiber precursor; (d) outer surface of the hollow fiber precursor; (A) cross-section of the sintered fiber; (B) wall of the sintered fiber; (C) central layer of the sintered fiber; (D) outer surface of the sintered hollow fiber.

Gas permeation test was performed to confirm that the SCYb hollow fiber membrane prepared is gas-tight when it is sintered at 1450-1500 °C. The initial pressure in the test cylinder (upstream pressure) was set at 356 kPa while the other side was connected to atmosphere. After 24 hours, the pressure in the test cylinder was changed from 356 kPa to 342 kPa, from which the gas permeance of the fiber was calculated to be 1.66×10^{-15} mol/(cm^2.Pa.s). This permeance value is a few orders of magnitude smaller than the actual proton permeance (see results in the following section). It should also be noted that decrease of the pressure in the test cylinder may not be only due to the gas permeation through the membrane but also due to a possible leakage of joints of the system, the actual permeance value of the fiber should be lower than the above calculated result. Therefore, the hollow fibers of the membrane module can be considered to be gas-tight.

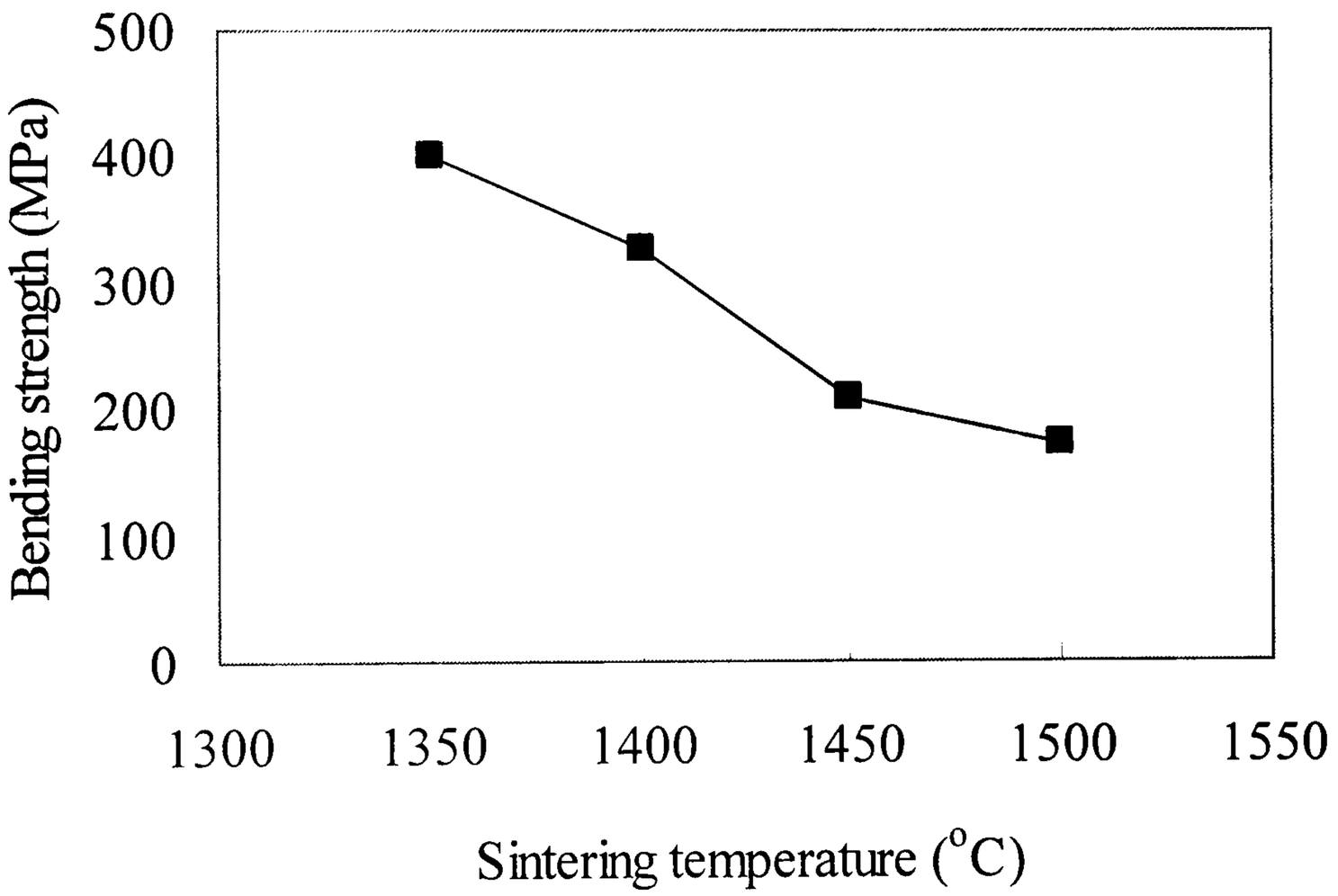


Fig. 4-6 Mechanical strength of the SCYb hollow fibers sintered at different temperatures.

The mechanical strength of the SCYb hollow fiber membranes as a function of sintering temperature is shown in Fig. 4-6. As can be seen, the mechanical strength of the hollow fibers decreases from 401 to 173 MPa as the sintering temperature is increased from 1350 °C to 1500 °C. This is believed to be the result of grain growth as the sintering temperature increases (Liu and Li, 2005). However, the gas permeation tests indicate that the surface defects of the membrane would be only eliminated at

temperatures between 1450-1500 °C, i.e. fibers became gas-tight and further increase of sintering temperature to 1550 °C, the membrane becomes porous again. The same result was observed before (Liu *et al.*, 2001). Therefore, it's essential that sintering of SCYb hollow fiber membranes should be carried out at 1450°C so that these fiber products possess both gas-tight property and enough mechanical strength.

Fig. 4-7 shows the XRD patterns of the membrane material, of the fresh membrane and of the used membranes. It indicates that the fresh membrane remains in the perovskite structure as the SCYb powders after spinning and sintering processes. After performing the hydrogen permeation experiments, a small amount of impurity phase identified as CeO_2 and $SrCO_3$ occurred on the outer surface of the membrane but it still remains mainly in the perovskite structure. Moreover, the hydrogen permeation rate was not noticeably deteriorated after two weeks, which suggests that the SCYb membrane has a satisfactory stability.

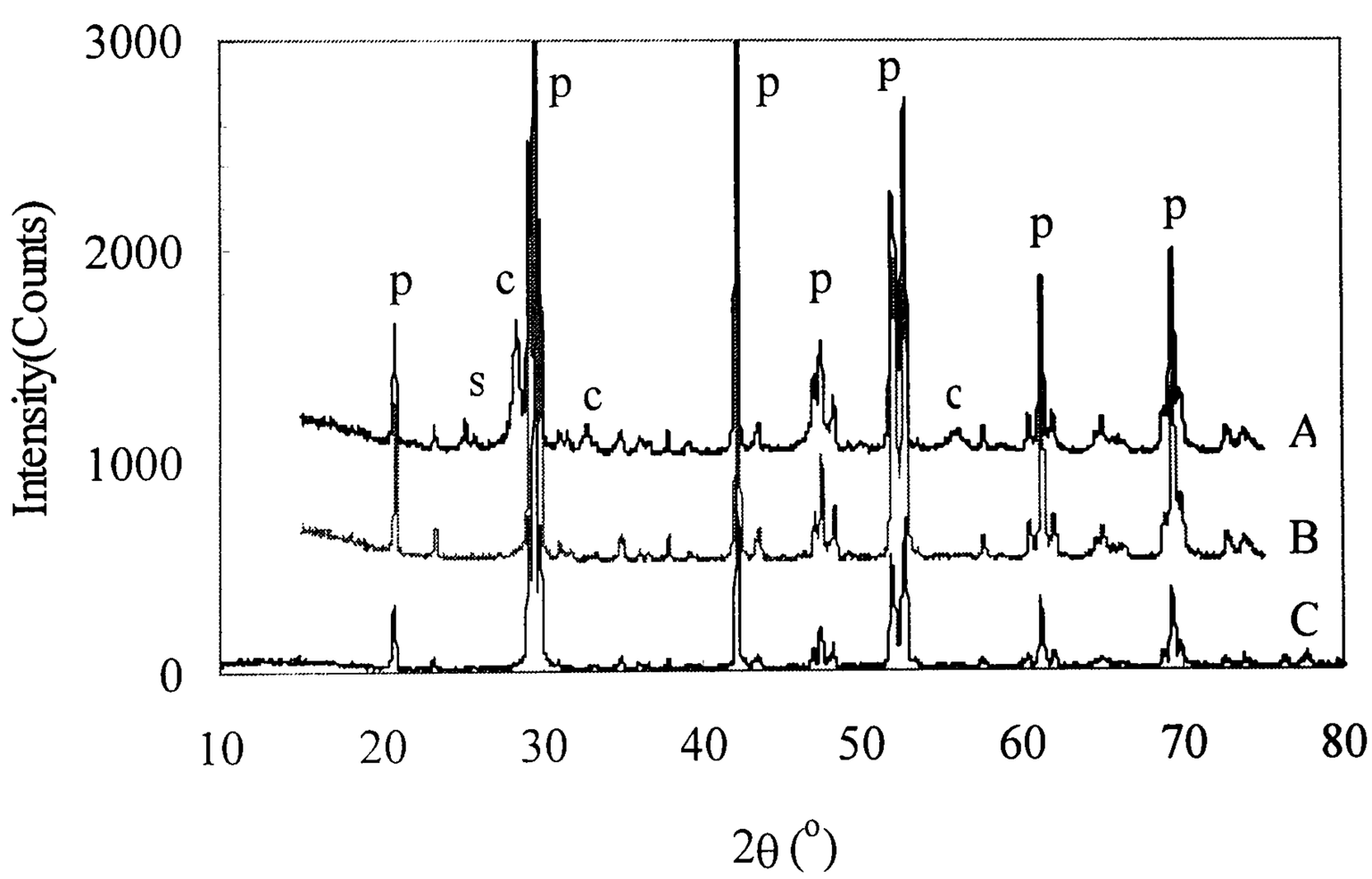


Fig. 4-7 XRD patterns of the SCYb powders and hollow fiber membranes. (A) SCYb fibre after permeation (p-perovskite; c-CeO_2; s-$SrCO_3$); (B) SCYb fiber before permeation; (C) SCYb powder.

4.4.2 Hydrogen permeation in the hollow fiber membrane module

The proton conduction properties of the SCYb hollow fiber membranes under different temperatures and feed concentrations in terms of hydrogen permeation flux are presented in the following section. The membrane characteristics and kinetic parameters for calculation of theoretical hydrogen permeation in the membrane module are summarized in Table 4-2.

Table 4-2 Characteristic parameters of the SCYb hollow fiber membrane and kinetic parameters used for calculations (Uchida *et al.*, 1989; Schober *et al.*, 1995; Condon and Schober, 1997; Souza *et al.*, 1997; Guan *et al.*, 1998).

Kinetic parameters	**Values**
Concentration of Ytterbium	$[Yb_{Ce}']=1.06\times10^{-3}$, mol·cm^{-3}
Diffusivity of proton	$D_p = 0.122\exp(-7851/T), cm^2\cdot s^{-1}$
Diffusivity of oxygen vacancy	$D_V = 24.24\exp(-23467/T),\ cm^2\cdot s^{-1}$
Diffusivity of electron hole	$D_h = 49.38\exp(12588.7/T),\ cm^2\cdot s^{-1}$
Equilibrium constant of reaction (1)	$K_1 = 3.24\times10^{-8}\exp(1371.3/T),$ $mol\cdot atm^{-0.5}\cdot cm^{-3}$
Equilibrium constant of reaction (2)	$K_2 = 1.77\times10^{-10}\exp(21911/T),$ $mol\cdot atm^{-1}\cdot cm^{-3}$
Equilibrium constant of water formation reaction	$K_w = 1.188\times10^{-3}\exp(29709/T)$, atm$^{-1/2}$
Fiber characteristics and experimental conditions	
Number of hollow fibers	n=1
OD of the hollow fiber	d_o=0.145, cm
ID of the hollow fiber	d_i=0.065, cm
Effective length of hollow fiber	L=4, cm
Operating temperature	T=973~1173 K
Feed concentration of hydrogen	y_{H2}=0.035~0.36
Feed concentration of oxygen	y_s=0.017~0.21
Feed flow rate of air stream	Q_s=60, cm^3 min^{-1} (STP)
Feed flow rate of hydrogen stream	Q_f=136, cm^3 min^{-1} (STP)
Vapor concentrations in feed streams	$y_{H2O}=4\times10^{-4}$

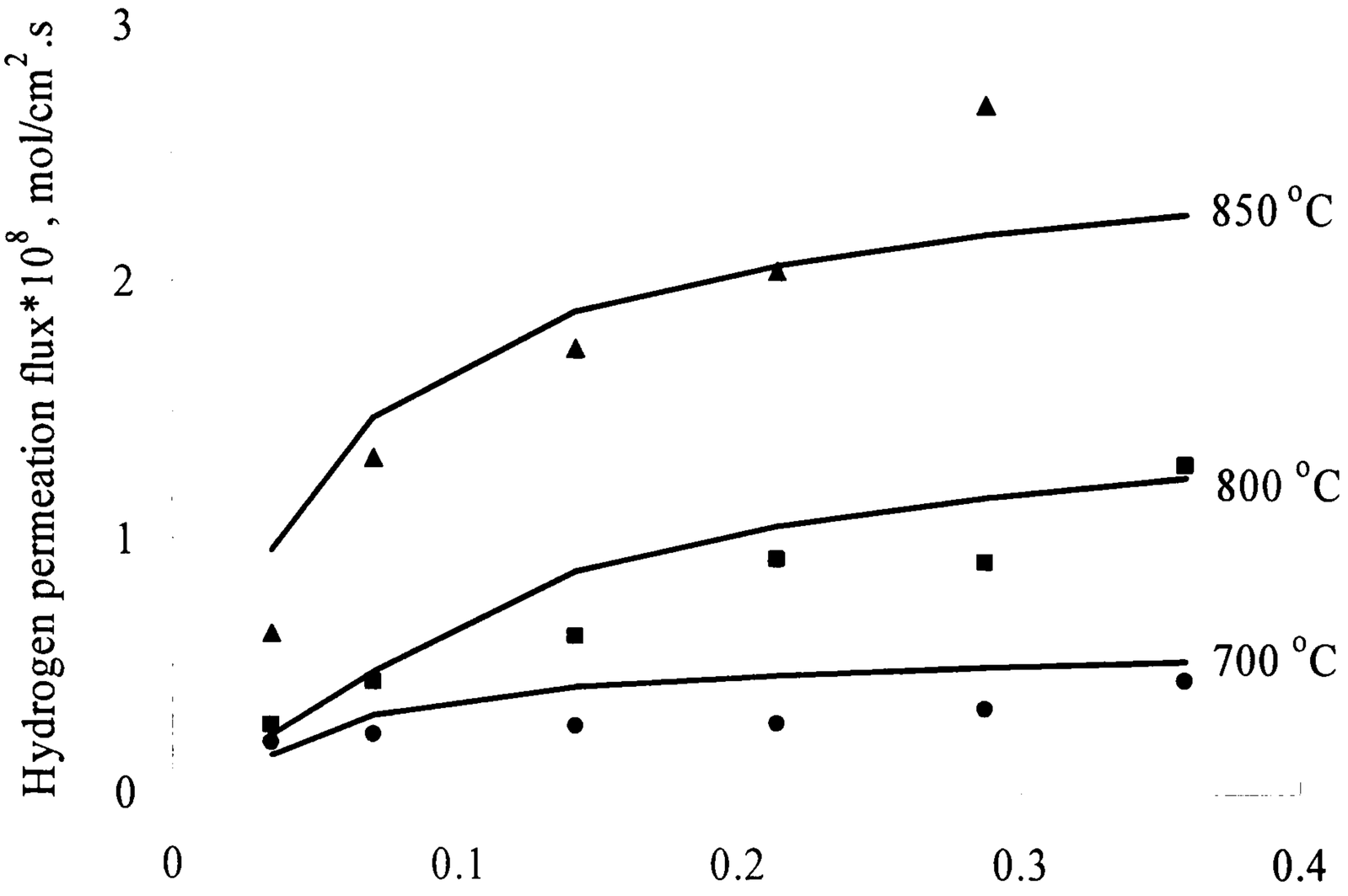


Fig. 4-8 Effect of hydrogen partial pressure in shell feed on the permeation flux at various temperatures (p_{O2}=0.21 atm).

Fig. 4-8 shows hydrogen permeation rates for the SCYb hollow fiber membrane as a function of hydrogen partial pressure, which was obtained by adjusting the flow rates of hydrogen and argon gases, under different temperatures. The oxygen partial pressure in the opposite compartment was kept 0.21 atm, i.e. air was used as the oxygen source. It can be seen that the hydrogen permeation rate increases with increasing hydrogen partial pressure and also increases with increasing temperature. The experimental data, in general, are lower than the theoretical results presented by solid lines. The reason for this might be that the resistances in surface exchange reactions, which were ignored in the mathematical model, may have an effect on hydrogen permeation. Because the hollow fiber shows an asymmetric structure, i.e. dense outer surface of the SCYb hollow fiber, there may be insufficient surface area provided in the outer surface resulting in much reduced surface exchange reaction rate. Therefore, more work should be carried out to increase the surface areas of both the inner and outer surfaces of the membrane. The non-linear relationship between permeation rate and hydrogen partial pressure implies that it follows a different mechanism compared to the conventional gas permeation through porous membranes.

In addition, both the theoretical results and the experimental data indicate that the hydrogen permeation rate may be improved by increasing temperature rather than by increasing the hydrogen partial pressure in the feed.

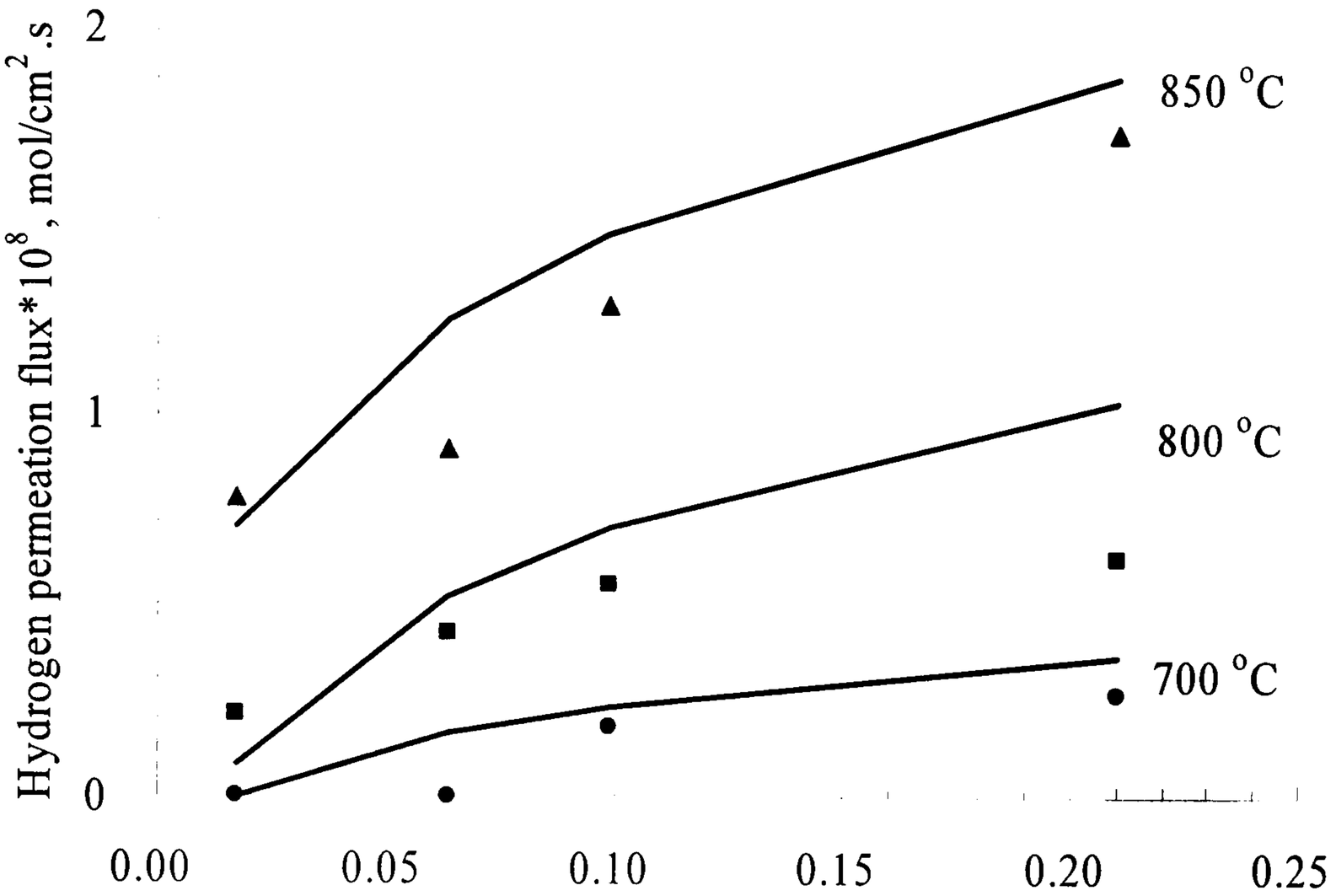


Fig. 4-9 Effect of oxygen partial pressure in lumen feed on the permeation flux at various temperatures (p_{H2}=0.142 atm).

Effects of oxygen partial pressure on the hydrogen permeation rate through the SCYb hollow fiber membrane under different temperatures and partial pressure of oxygen are shown in Fig. 4-9 where the hydrogen partial pressure was kept at constant of 0.142 atm. It can be seen as the oxygen partial pressure increases, more electron holes can be produced according to reaction (4-2) resulting in an increase in the hole-concentration on the membrane surface exposed to the air stream. Therefore, the permeation flux of charged defects or the hydrogen permeation rate is improved due to the increasing driving force as reflected in Fig. 4-8. However, at higher oxygen partial pressures, formation rate of the hole shows less effect in the defect permeation process, which suggests that the permeation process is controlled by other steps such as the formation rate of proton. As a result, the beneficial effect of further increasing oxygen concentration gradually diminishes. Again, in general, the experimental data are lower than the theoretical results as shown in solid lines. However, the general trends are

clear to merit a meaningful comparison between the experimental and theoretical results.

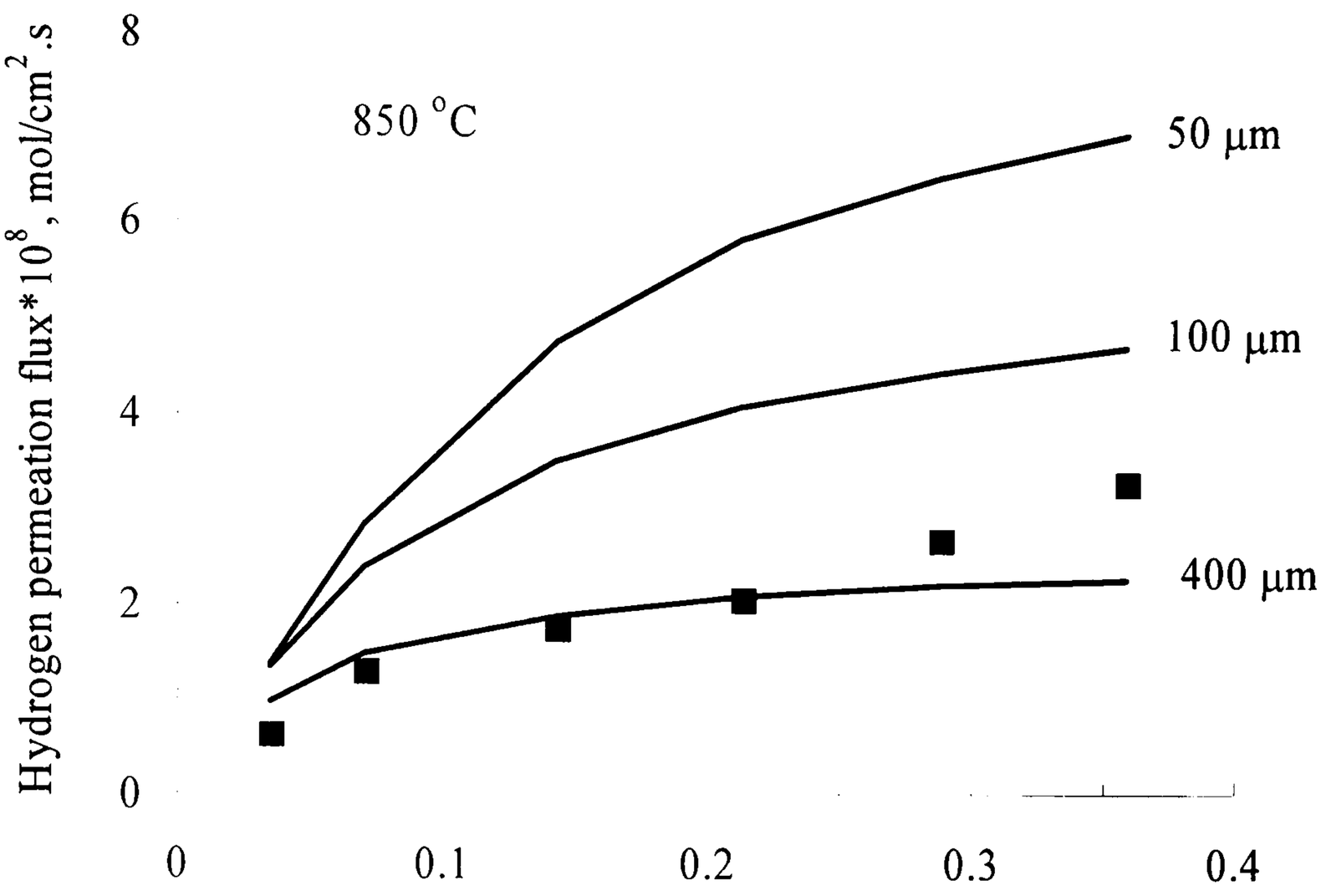


Fig. 4-10 Hydrogen permeation flux under various membrane thickness (T=850 °C, p_{O2}=0.21 atm).

It should be mentioned the membrane thickness used for the calculations is the difference between the outer and inner radius of the hollow fibres, that is, 400 μm. However, if the central dense layer is taken as the actual membrane thickness for hydrogen permeation, that is, 50~100 μm, the theoretical results would be much higher than that of the experimental data as shown in Fig. 4-10. For example, the hydrogen permeation flux for the membrane with thickness of 50 μm at 850°C may approach to 7×10^{-8} mol/cm^2.s, which is similar to the experimental results obtained by Hamakawa et al, whereas the actual permeation flux in the hollow fibre membrane is only 3×10^{-8} mol/cm^2.s (2002). This suggests both inner and outer surfaces of the membrane are dense. Also densification of the middle section of the fiber further leads to the membrane to have its thickness equivalent to the fiber wall thickness. It is envisaged that if both dense skin layers in the inner and outer membrane surfaces are eliminated,

leaving the finger-like pore structures on both the membrane surfaces for enhanced surface reactions and central dense layer for the selective permeation, the hydrogen permeation flux would be expected to be considerably increased.

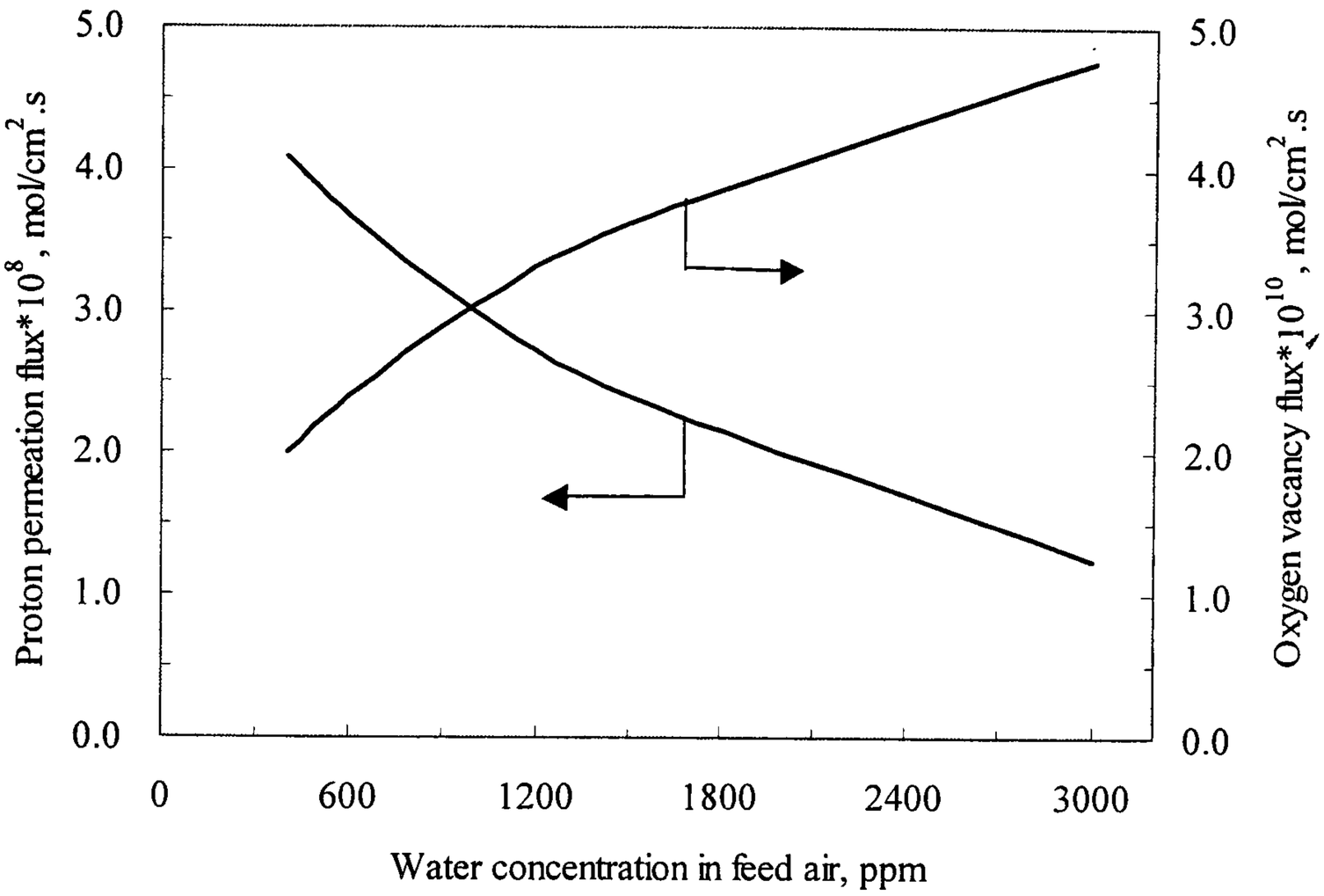


Fig. 4-11 Effect of the water vapor concentration in the air feed on the permeation of proton and oxygen vacancy (T=850 °C, p_{H2}=0.2 atm, p_{O2}=0.21 atm).

Fig. 4-11 shows theoretically the effect of water concentration in the air feed stream on the ionic permeation (conduction) properties of SCYb membrane, where the feed partial pressures of hydrogen and oxygen are 0.2 atm and 0.21 atm, respectively. Since SCYb mainly exhibits proton conduction other than oxygen ion conduction at temperatures of lower than 1300 K (Tan *et al.*, 2000), the permeation flux of oxygen vacancy is two orders of magnitude lower than that of proton, as shown in Fig. 4-11. Therefore, the formation of water vapor takes place mainly on the oxygen side. Furthermore, it can be seen that the proton flux decreases with increasing water concentration in air feed whereas the vacancy permeation flux is increased. According to reaction (4-3), the increase in water vapor concentration on the oxygen side generally leads to the higher proton concentration but lower concentration of oxygen vacancy on the membrane surface. As a result, the driving force for proton permeation is reduced but contrary to the oxygen vacancy permeation. This suggests that the hydrogen permeation is restrained by the water vapor in the air stream. Obviously, in

order to promote proton conduction, dry air should be used. On the other hand, for a given number of hollow fiber membranes in a module, as the module length increases, more water vapor would be produced in the air stream. This would lower the efficiency of membrane for hydrogen permeation. As shown in Fig. 4-12, the proton permeation flux decreases as the membrane length is increased.

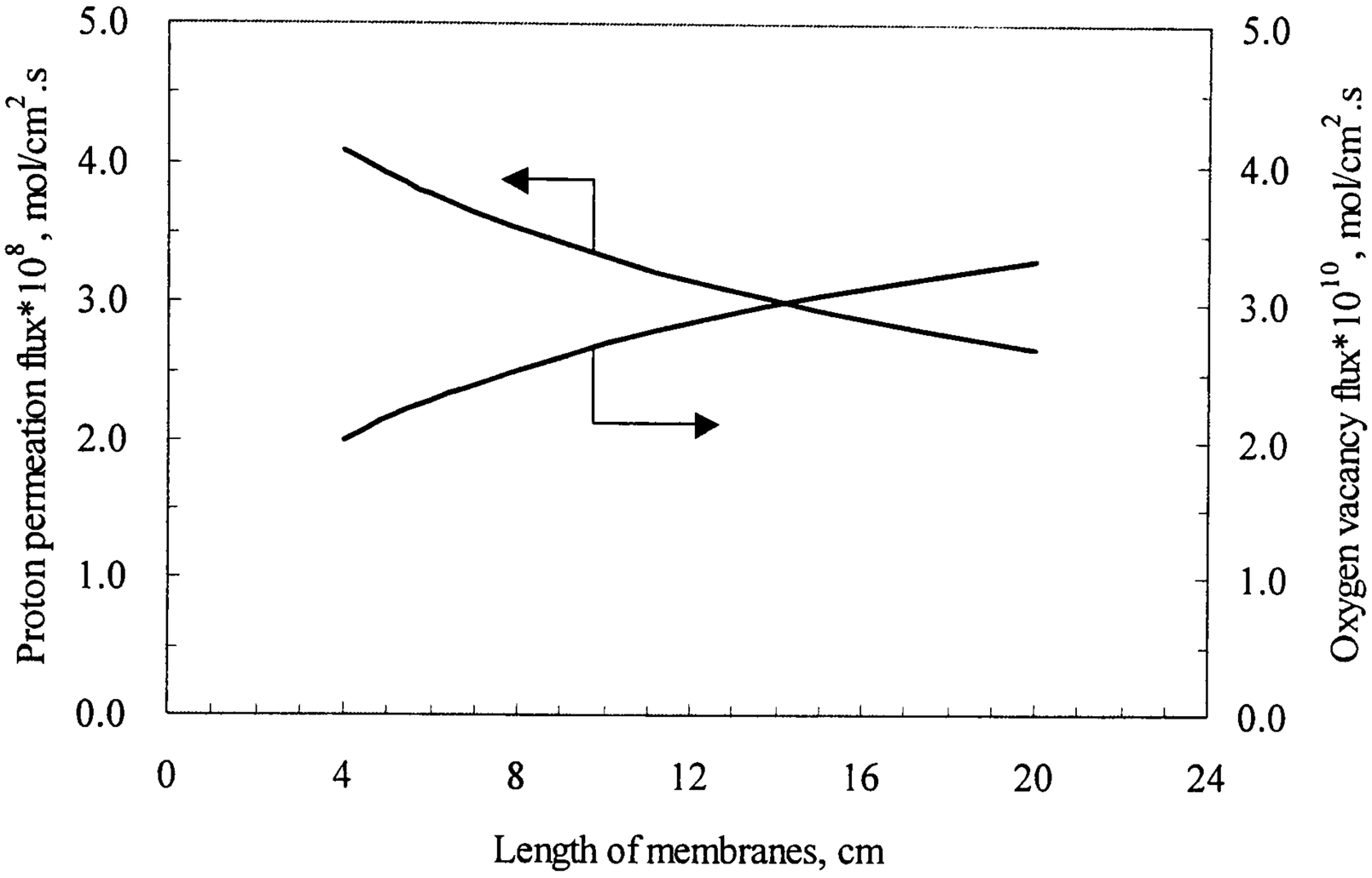


Fig. 4-12 Permeation flux as a function of the length of SCYb hollow fibre (T=850 °C, p_{H2}=0.2 atm, p_{O2}=0.21 atm).

Fig. 4-13 compares theoretically the cocurrent and countercurrent flow patterns where the flow permeation profiles of proton and oxygen vacancy at 850°C are plotted against the effective distance from the air feed entrance. As is expected, the proton permeation rate decreases as the gases pass through the hollow fiber membrane whereas the permeation rate of oxygen vacancy increases. This is because more and more water vapor is produced as the reactions proceeds, leading to the increase in vapor concentration in the oxygen stream. Although the difference in the permeation profile occurs between the cocurrent and the countercurrent flows, the total amount of hydrogen permeation is almost the same. This is because the concentrations of both hydrogen and oxygen are so high that they would be hardly changed due to the permeation and reaction.

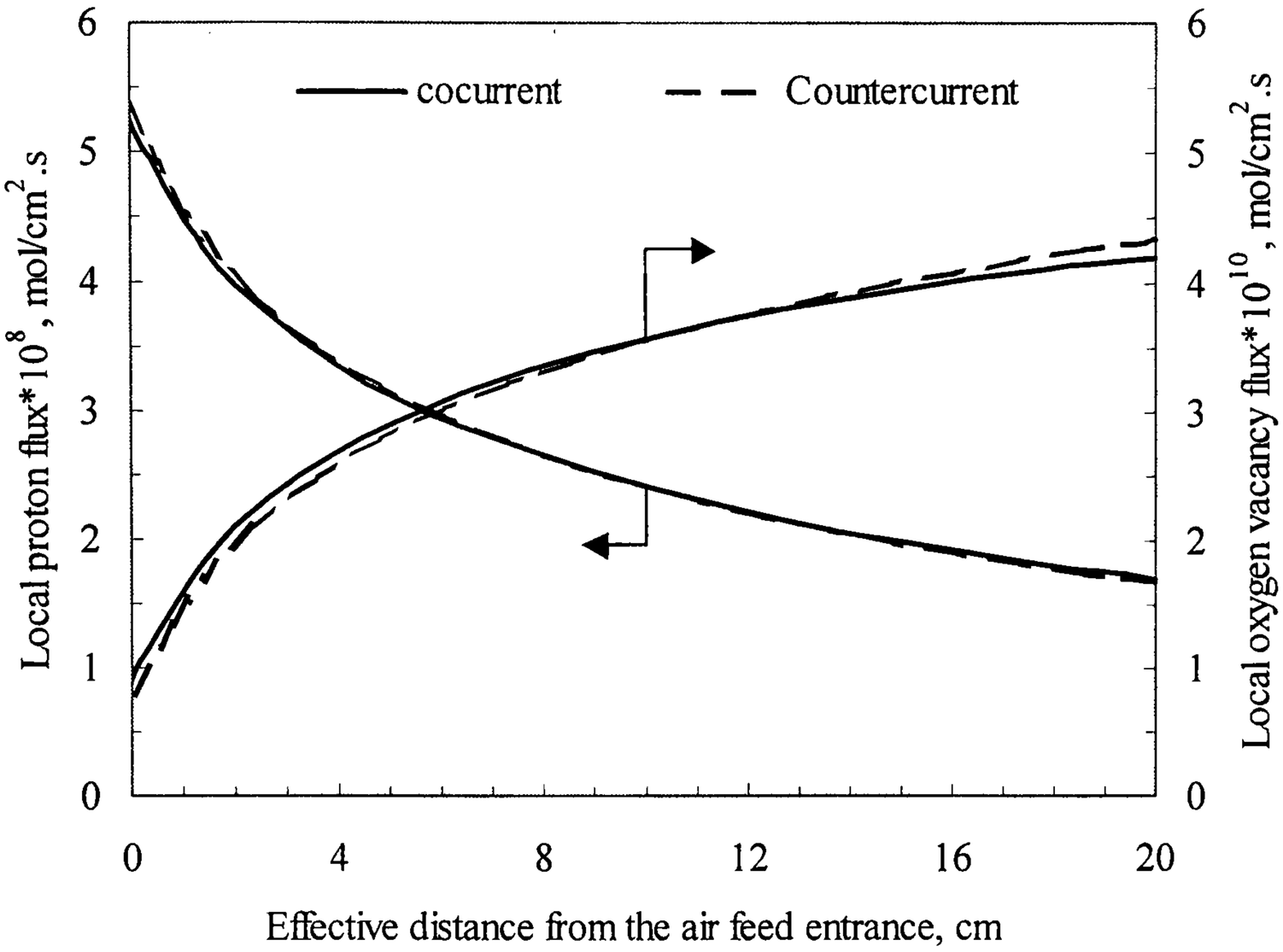


Fig. 4-13 Comparison between the countercurrent and cocurrent flow operations (T=850 °C, p_{H2}=0.2 atm, p_{O2}=0.21 atm).

4.5 Conclusions

$SrCe_{0.95}Yb_{0.05}O_{3-\delta}$ (SCYb) hollow fiber membranes with desirable length were successfully prepared by means of a phase inversion/sintering technique. In order to sinter the SCYb hollow fibers into dense membranes, a programmed sintering process should be adopted. The obvious hydrogen permeation (or proton conduction) through the resulting dense SCYb hollow fiber membranes generally occurs after the temperatures is higher than 700 °C. The hydrogen permeation flux increases with increasing the hydrogen and oxygen concentrations with a nonlinear relationship. As the temperature increases to 850 °C, hydrogen permeation flux is increased noticeably. The surface exchange reactions may contribute some resistances to hydrogen permeation and thus should be taken into the account in a more rigorous mathematical model. However, due to the lack of reaction kinetic data, theoretical calculation with inclusion of surface exchange reactions at this stage is not possible. In order to promote hydrogen permeation, dry air should be used. The hydrogen permeation efficiency could be affected by using the long SCYb hollow fibers. However, operating flow patterns shows no effect on the total hydrogen permeation flux.

Notations

A_m	-	Logarithm average membrane area, cm^2
C	-	Concentration of defects or gas, $mol \cdot cm^{-3}$
D	-	Effective diffusivity of defects, $cm^2 \cdot s^{-1}$
J	-	Molar flux of defects, $mol \cdot cm^{-2} \cdot s^{-1}$
K_1	-	Equilibrium constant for reaction (1), $mol \cdot cm^{-3} \cdot atm^{-0.5}$
K_2	-	Equilibrium constant for reaction (2), $mol \cdot cm^{-3} \cdot atm^{-1}$
K_3	-	Equilibrium constant for reaction (3), atm^{-1}
L	-	Length of the reactor (hollow fiber), cm
n	-	Number of hollow fibers
N	-	Molar flow rate, mol s^{-1}
p_l, p_s	-	Lumen or shell side pressure, atm
V_l, V_s	-	Volumetric feed flow rate of air or hydrogen gas stream, $cm^3 \cdot s^{-1}$ (STP)
R	-	Ideal gas constant
R_o, R_{in}, R_m	-	Outer, inner or log-mean radius of hollow fiber, cm
t	-	Transport number of defects
T	-	Operating temperature, K
y	-	Molar fraction in gas stream
Yb_{Ce}'	-	Concentration of dopant, mol cm^{-3}
z	-	Defect's charge number

Subscripts

h	-	Hole
l	-	Lumen side of the hollow fiber
p	-	Proton
V	-	Vacancy
s	-	Shell side of the hollow fiber
I	-	Hydrogen feed side
II	-	Oxygen feed side

References

Condon, J. B. and T. Schober (1997). Modeling of point defect migration in proton conducting ceramics, *Solid State Ionics*, **Vol.** 97, **pp.** 51-58.

Guan, J., S. E. Dorris, U. Balachandran and M. Liu (1998). Transport properties of $BaCe_{0.95}Y_{0.05}O_{3-\delta}$ and its application for hydrogen separation, *Solid State Ionics*, **Vol.** 110, **pp.** 303-310.

Hamakawa, S., L. Li, A. Li and E. Iglesia (2002). Synthesis and hydrogen permeation properties of membranes based on dense SrCe0.95Yb0.05O3-a, thin film, *Solid State Ionics*, **Vol.** 148, **pp.** 71-81.

Iwahara, H. (1995). Technological challenges in the application of proton conducting ceramics, *Solid State Ionics*, **Vol.** 77, **pp.** 289-298.

Iwahara, H., T. Esaka, H. Uchida and N. Maeda (1981). Protn conduction in sintered oxides and its applications to steam electrolysis for hydrogen production, *Solid State Ionics*, **Vol.** 3-4, **pp.** 359-363.

Iwahara, H., H. Uchida and N. Maeda (1982). High temperature fuel and steam electrolysis cells using proton conductive solid electrolytes, *J. Power Sources*, **Vol.** 7, **pp.** 293-301.

Lide, David R. (1996). CRC Handbook of Chemicstry Physics, 76th edition.

Liu, S., X. Tan, K. Li and R. Hughes (2001b). Preparation and characterisation of $SrCe_{0.95}Yb_{0.05}O_{2.975}$ hollow fibre membranes, *J. Membr. Sci.*, **Vol.** 193, **pp.** 249-260.

Liu, Y. and K. Li (2005). Preparation of $SrCe_{0.95}Yb_{0.05}O_{3-\delta}$ hollow fibre membranes: study on sintering process, *J. Membr. Sci.*, **Vol.** 259, **pp.** 47-54.

Schober, T., J. Friedrich and J. B. Condon (1995). Effective hydrogen diffusivity in $SrCe_{0.95}Yb_{0.05}O_{3-\delta}$ and $SrZr_{0.95}Yb_{0.05}O_{3-\delta}$., *Solid State Ionics*, **Vol.** 77, **pp.** 175-179.

Slade, R. L. T. and N. Singh (1991). Systematic examination of hydrogen ion conduction in rare-earth doped barium cerate ceramics, *Solid State Ionics*, **Vol.** 46, **pp.** 111.

Souza, R. A. D., J. A. Kilner and C. Jeynes (1997). The application of secondary ion mass spectrometry (SIMS) to the study of high temperature proton conductors (HTPC), *Solid State Ionics*, **Vol.** 97, **pp.** 409-419.

Tan, X., S. Liu and K. Li (2001). Preparation and characterization of inorganic hollow fibre membranes, *J. Membr. Sci.*, **Vol.** 188, **pp.** 87-95.

Tan, X., S. Liu, K. Li and R. Hughes (2000). Theoretical analysis of ion permeation through mixed conducting membranes and its application to dehydrogenation reactions, *Solid State Ionics*, **Vol.** 138, **pp.** 149-159.

Tan, X., Y. Liu and K. Li (2005). Preparation of LSCF ceramic hollow fibre membrane for oxygen production by a phase-inversion/sintering technique, *Ind. Eng. Chem. Res.*, **Vol.** 44, **pp.** 61-66.

Uchida, H., N. Maeda and H. Iwahara (1983). Relation between proton and hole conduction in $SrCeO_3$ based solid electrolytes under water-containing atmospheres at high temperatures, *Solid State Ionics*, **Vol.** 11, **pp.** 117-124.

Uchida, H., H. Yoshikawa and H. Iwahara (1989). Dissolution of water vapour (or hydrogen) and proton conduction in $SrCeO_3$ based oxides at high temperatures, *Solid State Ionics*, **Vol.** 35, **pp.** 229-237.

Chapter 5

Non-oxidative methane coupling in a $SrCe_{0.95}Yb_{0.05}O_{3-\delta}$ (SCYb) hollow fibre membrane reactor

Abstract

$SrCe_{0.95}Yb_{0.05}O_{3-\delta}$ (SCYb) hollow fiber membranes have been prepared by a combined phase inversion and sintering method where polyethersulfone (PESf) is used as a binder, N-methyl-2-pyrrollidone (NMP) as solvent and polyvinylpyrrolidone (PVP, K16-18) as an additive, respectively. After the membrane was properly characterised, a membrane reactor was subsequently designed with the SCYb hollow fibers for methane coupling. The performance of the hollow fibre membrane reactor on the methane coupling reaction was investigated both experimentally and theoretically. Extraction of hydrogen through the membrane promotes the formation of ethylene and ethane. Increase of operating temperature favors the formation of ethylene compared to that ethane. Due to the methane carbonisation and formation of higher hydrocarbons (C_3-C_5), a C_2 selectivity of only about 60% was achieved. By increasing the methane feed flow rate, the ethylene formation rate is decreased, but the ethane production is increased. A simple mechanism for methane coupling on the SCYb membrane was presented, with which the performance of the proton conducting membrane reactor on methane coupling reaction could be predicted well with theoretical models.

Key words: $SrCe_{0.95}Yb_{0.05}O_{3-\delta}$; perovskite; hollow fiber membrane; methane coupling.

5.1 Introduction

With the depletion of liquid petroleum, natural gas containing primarily methane (>95%) is increasingly expected to be the main resource for production of chemicals and liquid fuels (Lunsford, 2000; Bouwmeester, 2003). Oxidative coupling of methane (OCM) is an attractive route for utilization of natural gas since it offers direct conversion of methane into valuable chemicals, mainly C_2 products (ethane and ethylene)(Lin and Zeng, 1996; Lu *et al.*, 2000a; Akin and Lin, 2002). Nevertheless, the main problem in commercialization of OCM is that the C_2 yield is too low because the products are more reactive in nature than the starting reactant (methane), leading to deep oxidation and thus low C_2 selectivity. In order to achieve an economically attractive C_2 yield (>30-40%) (Zeng and Lin, 1997), considerable interests have been recently diverted to the development of various membrane reactors (ten Elshof *et al.*, 1995; Wang and Lin, 1995; Ramachandra *et al.*, 1996; Zeng and Lin, 1997; Lu *et al.*, 2000b; Kao *et al.*, 2003; Akin and Lin, 2004). By adding oxygen discretely through either porous or dense oxygen permeable membranes along the length of the reactor, the local methane-to-oxygen ratio in the reaction zone can be kept at certain level so that no excess oxygen is introduced/left in the reaction zone and a much higher C_2 selectivity than that in a conventional reactor can be achieved. As a result, the C_2 yield can be greatly increased if the total amount of oxygen introduced into the reactor is high enough for methane conversion.

Another type of membrane reactors is based on the extraction of part of products out of the reaction zone so that the yield of the desired product is improved. For example, in dehydrogenation reactions, the product yield can be noticeably promoted by removal/extraction of hydrogen continuously through hydrogen permeable membranes such as metal Pd membranes (Hollein *et al.*, 2001; Marigliano *et al.*, 2003; Lin and Chang, 2004). Apart from the Pd membranes, use of the proton-hole mixed conducting membranes is another choice to extract hydrogen (in the form of proton) from the reaction zone (Chiang *et al.*, 1991; Chiang *et al.*, 1992; Chiang *et al.*, 1993; Hamakawa *et al.*, 1993;1994; Langguth *et al.*, 1997). In such operations, methane and oxygen (generally air) are fed into the two compartments separated by the proton-hole mixed conducting membrane. Methane coupling reactions take place on the methane side with the hydrogen permeated through the membrane in form of proton into the oxygen

side, where it reacts with oxygen into water. Therefore, oxygen does not directly take part in the methane coupling reactions (so called non-oxidative methane coupling) and thus a high C_2 selectivity may be expected.

$SrCe_{095}Yb_{0.05}O_{3-\delta}$ (SCYb) is a well-known mixed proton-hole conductor that also exhibits good catalytic activity for methane coupling reaction (Chiang *et al.*, 1991; Chiang *et al.*, 1992; Chiang *et al.*, 1993). In the previous studies, the conversion of methane was usually very low because of the limited membrane area (Hamakawa *et al.*, 1993;1994; Langguth *et al.*, 1997). Another reason for the low methane conversion is that the membrane is not thin enough for the hydrogen permeation. From the view of economic, the use of thin membrane and large membrane area per unit of reactor volume in addition to the high catalytic activity will be more favorable. Recently, hollow fibre ceramic membranes with an asymmetric structure have been prepared successfully by means of a phase inversion spinning/sintering technique (Liu *et al.*, 2001; Tan *et al.*, 2001; Tan *et al.*, 2005a; b). Compared to the disk-shaped membranes, the hollow fibre membranes possess much larger membrane area per unit volume for hydrogen permeation. Also, due to the asymmetric structure, the membrane's resistance to hydrogen permeation is very much lower compared to the symmetric membranes prepared by the conventional methods. In addition, the integrated porous layers on either side or both sides of the membrane may provide larger gas-membrane interfaces for coupling and oxygen exchange reactions thus enhance the reaction rates. Furthermore, by adopting long hollow fibres and keeping the two sealing ends away from the high temperature zone, the problem of high temperature sealing no longer exists.

In this chapter, SCYb hollow fibre membranes with the asymmetric structure were prepared via a combined phase inversion spinning/sintering technique. A membrane reactor was then fabricated in which the methane coupling experiments were carried out. The performances of the membrane reactor for methane coupling at various operating conditions were investigated both experimentally and theoretically.

5.2 Experimental

5.2.1 Materials

Commercially available $SrCe_{0.95}Yb_{0.05}O_{2.975}$ (SCYb) powders [supplied by Praxair Surface Technologies, USA] were used as the membrane material. Polyethersulfone (PESf) (Radel A-300, Ameco Performance, Greenville, SC), N-methyl-2-pyrrollidone (NMP) (>99%, Acros) and polyvinlpyrrolidone (PVP K90, Acros) were used as the binder, the solvent and the additive, respectively. Dionized water and tape water were used as the internal and external coagulants, respectively.

5.2.2 Preparation and characterization of the SCYb hollow fiber membranes

The phase inversion/sintering technique was applied in preparing the SCYb hollow fiber membranes. The detailed procedures were described elsewhere (Liu *et al.*, 2001). A spinneret with orifice- diameter/inner-diameter of 3.0/1.2 mm was used to obtain the hollow fiber precursors in this chapter. Sintering of the SCYb hollow fiber precursors was then carried out in a high-temperature tubular furnace (STF16/450, CARBOLITE). The sintering underwent a program of 1200 °C for 16 hours followed by 1450°C for another 4 hours with the heating and cooling rates of 5°C/min. The preparation parameters for the resulting SCYb hollow fiber membranes in this chapter were summarized in Table 5-1.

Table 5-1 Parameters for the preparation of the $SrCe_{0.95}Yb_{0.05}O_{3-\delta}$ (SCYb) hollow fibre membranes.

Parameters	**Value**
Compositions of the starting solution (wt%)	
$SrCe_{0.95}Yb_{0.05}O_{2.975}$ (SCYb) powder	69
Polyethersulfone (PESf)	7.0
polyvinlpyrrolidone (PVP K90)	0.7
N-methyl-2-pyrrollidone (NMP)	23.3
Internal coagulant	DI water
External coagulant	Tap water
Flow rate of bore liquid (cm^3/min)	9
Spinneret dimension (I.D./O.D) (mm),	1.2/3.0
Temperature (°C)	21
Air gap (mm)	30
Sintering program	1200 °C (16hrs)→1450°C (4hrs)
Heating (cooling) rate (°C/min)	5

The resulting SCYb hollow fiber membranes were characterized by the three-point-bending test for measuring the mechanical strength of the hollow fibre membranes, by the gas permeation test for measuring the gas tightness properties, and by XRD analysis for observing the phase structure of the membranes. These techniques and the test results were described in details in Chapter 4.

5.2.3 SCYb hollow fiber membrane reactor and methane coupling experiments

A simple hollow fibre membrane reactor consists of only one hollow fibre housed in a ceramic tube was prepared for methane coupling experiments. The fibre has the dimensions of 26 cm in length and 0.145/0.065 cm in OD/ID. A soft silicone rubber tube was used on one end of the fibre to offset the thermal expansion of the hollow fibre membranes under high temperature operations, just as shown in Fig. 5-1.

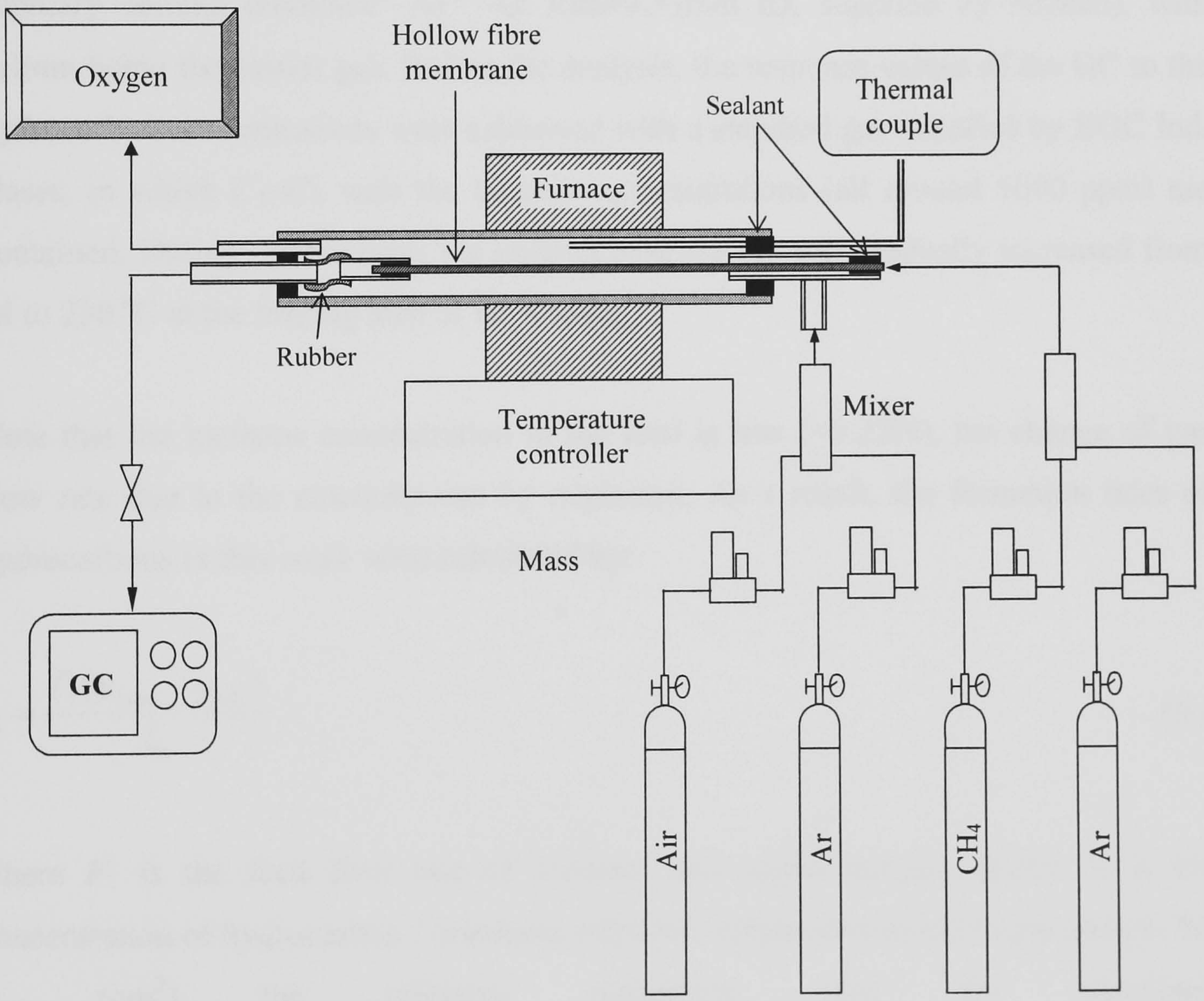


Fig. 5-1 Experimental setup for methane coupling in the SCYb hollow fibre membrane module.

The membrane reactor was located in a tubular furnace (MTF 10/25/130, CARBOLITE) with the length of 13 cm, whereas the constant temperature zone of the furnace is around 4 cm. Thus, the sealing joints were kept out of the furnace tube, preventing the silicone rubber tube from burning. In the experiments, methane mixed with argon was introduced into the lumen side of the module while the mixture of air and argon cocurrently into the shell side. The temperature within the module (inside the alumina tube) was measured using the type C thermocouple with a thermometer supplied by Omega Engineering Inc. The gas flow rates were controlled and measured using a mass flow controller (Smart Mass Flow meter with Read out & Control Electronics Model 0152, Brooks Instrument). An oxygen meter (Oxygen Analyser 572, Servomex) was used to monitor the change of oxygen concentration in the shell side gas stream. The hydrocarbon concentrations in the methane stream were analyzed by a gas chromatography (Shimadzu GC-14A) fitted with FID as the detector and a capillary column (Heliflex® AT™-Q 30m×0.53mm ID, supplied by Alltech), with helium being the carrier gas. Before the analysis, the response values of the GC to the hydrocarbon concentrations were calibrated with a standard gas supplied by BOC Ind. Gases, in which C_1~C_5 with the accurate concentrations (all around 1000 ppm) are contained. During the analysis, the column temperature was gradually increased from 34 to 230 °C at the heating step of 10 °C/min.

Note that the methane concentration in the feed is low (<9.22%), the change of gas flow rate due to the reactions can by neglected. As a result, the formation rates of hydrocarbons in this work were calculated by:

$$r_i = \frac{F_1(y_{i,out} - y_{i,in})}{A_m} \tag{5-1}$$

where F_1 is the feed flow rate of methane and argon mixture, mol/s; y_i is the concentration of hydrocarbon i (methane, ethylene, ethane and so on) in gas stream, %; A_m (cm^2) the effective membrane area for reactions, $A_m = 2m\pi L(R_o - R_{in})/\ln(R_o/R_{in})$, in which L is the membrane length at the constant temperature zone of the furnace, R_o and R_{in} are the outer and the inner radius of the

hollow fibre respectively, m; and m is the number of the hollow fibres (m=1 in this work). The subscripts *out* and *in* represent the effluent and feed, respectively.

C_2 selectivity is defined as the percentage of the reacted methane into C_2 hydrocarbons in the whole converted methane, calculated by:

$$S_{C_2} = 100 \times \frac{2(r_{C_2H_6} + r_{C_2H_4})}{-r_{CH_4}} \tag{5-2}$$

5.3 Theory description

5.3.1 Formation and transport of defects in SCYb membrane

It is known that the partial substitution of trivalent Yb^{3+}cations for the space-centered Ce^{4+} cations in the perovskite oxide $SrCeO_3$ may produce oxygen vacancies (Slade and Singh, 1991):

$$Yb^{3+} \rightarrow Yb'_{Ce} + \tfrac{1}{2}V_O^{\cdot\cdot} \tag{5i}$$

Oxide ions hop into neighboring vacancies, which can be described as vacancy migration to provide the oxide-ion conduction of oxides. On the other hand, an oxygen vacancy can also react with oxygen to generate positive holes:

$$V_O^{\cdot\cdot} + \tfrac{1}{2}O_2 \xleftrightarrow{K_1} O_O^x + 2h^{\cdot} \tag{5ii}$$

In a water or hydrogen-containing environment, protons may form by reactions between the gas and vacancies or holes, so that the oxide may also exhibit proton conduction at high temperature:

$$H_2O + V_O^{\cdot\cdot} \xleftrightarrow{K_2} O_O^x + 2H^{\cdot} \tag{5iii}$$

In above equations, $V_O^{\cdot\cdot}, H^{\cdot}$ and $h^{\cdot}$ represent oxygen vacancy, proton, and electron hole, respectively, while K_1 and K_2 are equilibrium constants.

As a result, three charged defects, including oxygen vacancies, holes and protons, may coexist in the oxide at high temperature so that SCYb exhibits the mixed conducting behaviour. Local electric neutrality must be satisfied anywhere in the membrane at any time. According to previous studies (Uchida *et al.*, 1983), the explicit equation for electroneutrality can be written as:

$$[Yb'_{Ce}] = [H^{\cdot}] + [h^{\cdot}] + 2[V_O^{\cdot\cdot}] \tag{5-3}$$

Once an electrical field or a concentration gradient of the mobile species is imposed on the oxide, the charged defects could move in one direction, resulting in a net ionic flux. The transport fluxes of defects at steady state under the electrochemical potential gradient can be derived as (Tan *et al.*, 2000):

$$J_i = -D_i C_i \left[\frac{1-t_i}{C_i} \cdot \frac{dC_i}{dx} - \sum_{j \neq i} \frac{z_i}{z_j} \cdot \frac{t_j}{C_j} \cdot \frac{dC_j}{dx} \right] \qquad (i = V_O^{\cdot\cdot}, H^{\cdot}, h^{\cdot}) \tag{5-4}$$

where D, C, z and t are the diffusivity, concentration, charge number and transport number of defect i ($i = V_O^{\cdot\cdot}, H^{\cdot}, h^{\cdot}$), respectively. If no external current is applied, the following correlation must be satisfied at steady state:

$$\sum z_i J_i = 0 \tag{5-5}$$

Generally, SCYb mainly shows proton-hole conduction and negligible oxide ion/oxygen vacancy conduction at temperature below 1000°C (Tan *et al.*, 2000). Accordingly, the flux of oxygen vacancy is equal to zero. Therefore, the concentration profiles of defects may be described by a set of ordinary differential equations. In matrix form, they may be rewritten as:

$$\underline{\underline{A}} \cdot \frac{d\underline{C}}{dx} = \underline{B} \tag{5-6}$$

where

$$\underline{\underline{A}} = \begin{bmatrix} 1-t_V & -2t_p C_V / C_p & -2t_h C_V / C_h \\ -\frac{1}{2} t_V C_p / C_V & 1-t_p & -t_h C_p / C_h \\ 2 & 1 & 1 \end{bmatrix} \quad \underline{B} = \begin{bmatrix} 0 \\ -J_p / D_p \\ 0 \end{bmatrix} \quad \underline{C} = \begin{bmatrix} C_V \\ C_p \\ C_h \end{bmatrix} \tag{5-6a}$$

where the subscripts V, p and h represent oxygen vacancy, proton and hole, respectively.

5.3.2 Mechanism of methane coupling on SCYb membranes

In general, methane coupling on the SCYb membrane follows the mechanism of the formation of methyl radical on the membrane's surface and coupling reaction in the gas phase (Hamakawa *et al.*, 1993;1994). This process may be schematically illustrated in Fig. 5-2. As methane passes by the SCYb membrane's surface at a high temperature, it may be catalytically dissociated into methyl radicals by combining with the proton hole transported from the oxygen side:

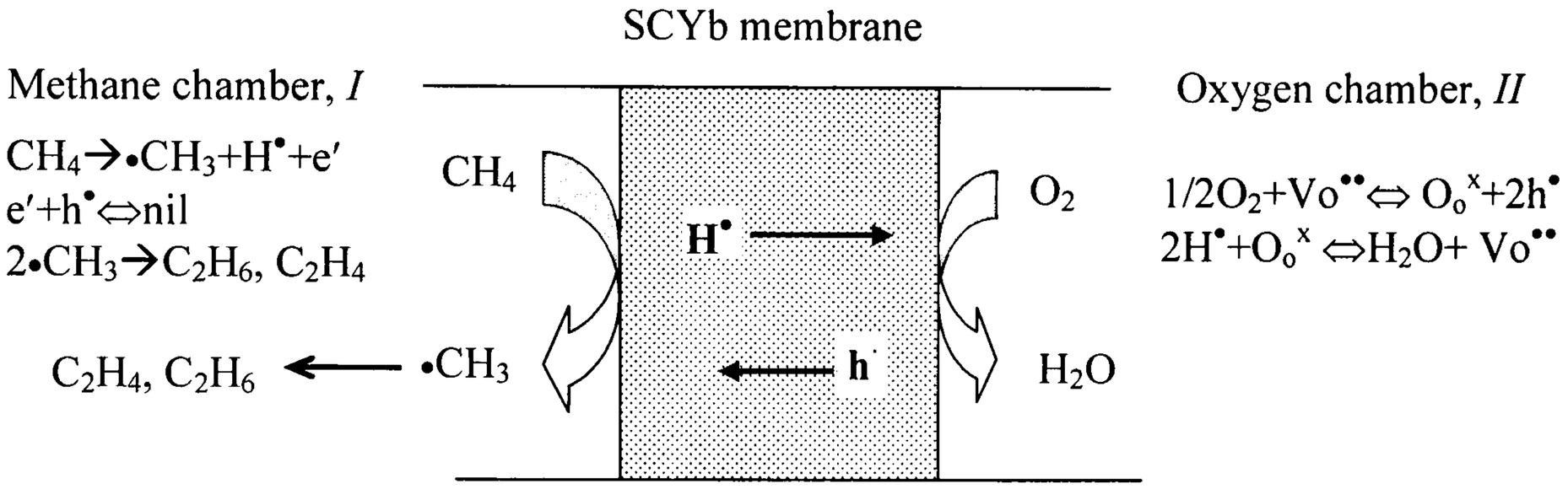


Fig. 5-2 Mechanism of methane coupling reaction on the SCYb membrane.

$$CH_4 + h^{\cdot} \rightarrow \cdot CH_3 + H^{\cdot} \qquad \text{(5iv)}$$

Note that reaction (5iv) is actually the combination of the following two steps:

$$CH_4 \rightarrow \cdot CH_3 + H^{\cdot} + e' \qquad \text{(5v)}$$

$$h^{\cdot} + e' \Leftrightarrow nil \qquad \text{(5vi)}$$

The proton will be transported to the oxygen side under the electrochemical potential gradient and is oxidized by oxygen into water according to reaction (iii). Meanwhile, the methyl radicals are released into the gas phase, where the coupling reaction takes place:

$$2 \cdot CH_3 \rightarrow C_2H_6 \qquad \text{(5vii)}$$

Following the same mechanism, ethylene may be produced from ethane by the formation of ethane radicals:

$$C_2H_6 + h^{\cdot} \Leftrightarrow \cdot C_2H_5 + H^{\cdot} \tag{5viii}$$

$$\cdot C_2H_5 \rightarrow C_2H_4 + \cdot H \tag{5ix}$$

It should be mentioned that higher carbon products (>C_2) could be further produced following the similar mechanism, but neglected in this study. Therefore, the formation rates of ethane and ethylene with respect to the reaction surface may be written as:

$$r_{C_2H_6} = k_1 C_{CH_4} C_{h(I)} - k_2 C_{C_2H_6} C_{h(I)} \tag{5-7}$$

$$r_{C_2H_4} = k_2 C_{C_2H_6} C_{h(I)} \tag{5-8}$$

where k_1 and k_2 are the rate constants for the reaction (5viii) and (5ix), respectively.

On the oxygen side, *II*, local equilibrium reactions of (5ii) and (5iii) may be assumed to take place:

$$K_1 = \frac{C_{h(II)}^2}{C_{V(II)} p_{O_2}^{1/2}} \tag{5-9}$$

$$K_2 = \frac{C_{p(II)}^2}{C_{V(II)} p_{H_2O}} \tag{5-10}$$

Combining Eqs. (5-9), (5-10) with Eq. (5-3) yields the defect concentrations at interface of oxygen side as:

$$C_{V(II)} = \frac{1}{16}\left\{\sqrt{\left[(K_1(p_{O_2})^{1/2})^{1/2} + (K_2 p_{H_2O})^{1/2}\right]^2 + 8[Yb'_{Ce}]} - \left[(K_1(p_{O_2})^{1/2})^{1/2} + (K_2 p_{H_2O})^{1/2}\right]\right\}^2 \tag{5-11a}$$

$$C_{h(II)} = \sqrt{K_1 (p_{O_2})^{1/2} C_{V(II)}} \tag{5-11b}$$

$$C_{p(II)} = \sqrt{K_2 p_{H_2O} C_{V(II)}} \cdots \tag{5-11c}$$

5.3.3 Model equations for the SCYb hollow fibre membrane reactor

Consider that the membrane reactor consists of *n* SCYb hollow fibres, which are housed in a ceramic tube as the reactor shell. Methane diluted with argon gas is fed into the lumen side of the reactor, while air flows on the shell side cocurrently. Fig. 5-3 schematically shows the flow pattern in one SCYb hollow fibre.

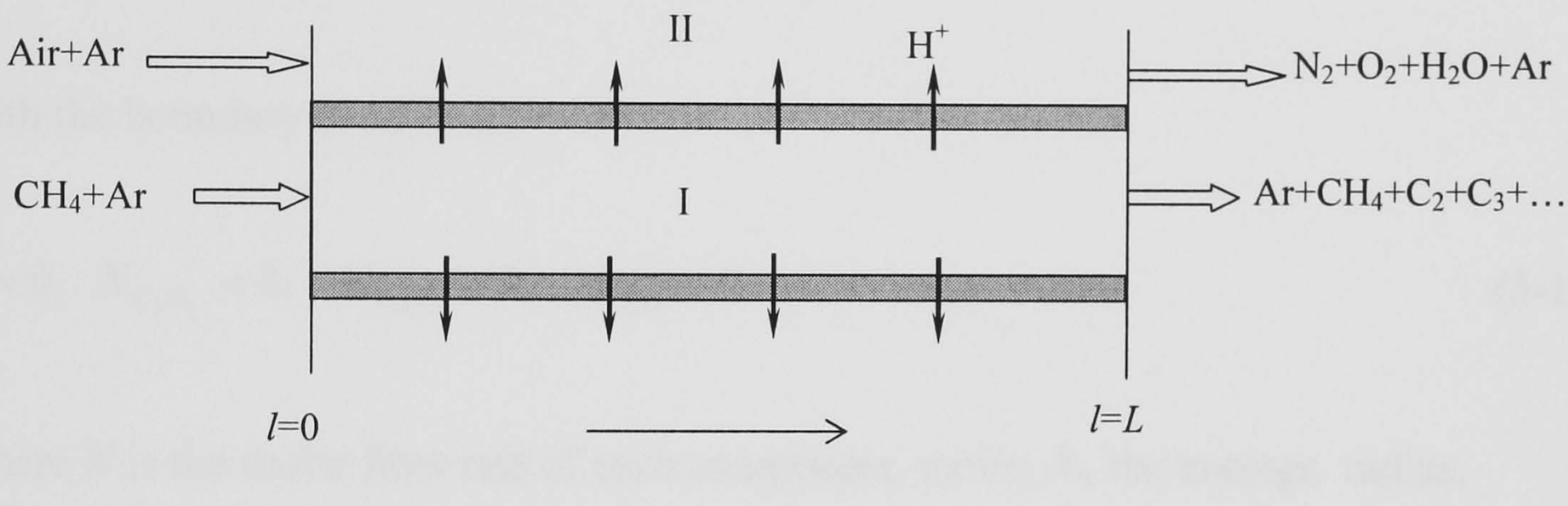


Fig. 5-3 Flow pattern in the SCYb hollow fibre membrane reactor.

In formulating the mathematical model, the following assumptions are adopted:

1. The membrane reactor is operated at steady state under isothermal condition.
2. Since the length of hollow fibre is much greater than the wall thickness, the defect transport in the axial direction within the membrane would be neglected.
3. Gas-solid mass transfer resistances in both shell and lumen sides are negligible.
4. Ideal gas law is used to describe the state of both single component gas and gas mixture.
5. The flow of both reactant streams is plug flow, and the axial dispersion is negligible.
6. Pressure drop in either lumen or shell side is negligible. Unless the reactor is operated under vacuum condition, this assumption can be considered to be reasonable.

The local rates of formation of C_2H_4, C_2H_6 and H_2O in the hollow fibre membrane reactor are given below.

$$\frac{dN_{C_2H_6}}{dl} = 2m\pi R_{in} \cdot r_{C_2H_6} \tag{5-12}$$

$$\frac{dN_{C_2H_4}}{dl} = 2m\pi R_{in} \cdot r_{C_2H_4} \tag{5-13}$$

$$\frac{dN_{H_2O}}{dl} = 2m\pi R_{m} \cdot \frac{1}{2} J_p \tag{5-14}$$

with the boundary conditions:

$$l = 0, \quad N_{C_2H_6} = 0, \quad N_{C_2H_4} = 0, \quad N_{H_2O} = 0 \tag{5-15}$$

where N is the molar flow rate of each component, mol/s; R_m the average radius,

$$R_m = \frac{R_o - R_{in}}{\ln(R_o / R_{in})}, \text{ cm.}$$

The partial pressures of methane and ethane in the lumen phase and of oxygen and water vapor in the shell phase are, respectively, given by:

$$C_{CH_4} = \frac{N_f y_f - 2(N_{C_2H_6} + N_{C_2H_4})}{N_f - (N_{C_2H_6} + N_{C_2H_4})} \cdot \frac{P_l}{RT}, \; C_{C_2H_6} = \frac{N_{C_2H_6}}{N_f - (N_{C_2H_6} + N_{C_2H_4})} \cdot \frac{P_l}{RT} \tag{5-16a}$$

$$p_{O_2} = P_s \cdot \frac{N_s y_s - 0.5N_{H_2O}}{N_s + 0.5N_{H_2O}}, \; p_{H_2O} = P_s \cdot \frac{N_{H_2O}}{N_s + 0.5N_{H_2O}} \tag{5-16b}$$

where N_f and N_s are the molar flow rate of methane feed and oxygen feed, y_f and y_s are the molar fractions of methane and oxygen in the feed mixtures, and P_s and P_l are operating pressures in the shell side and lumen side, respectively.

At steady state, the formation rate of proton is equal to the transfer rate through the membrane, namely,

$$2m\pi R_m \cdot J_p = 2m\pi R_{in}\left(2k_1 C_{CH_4} C_{h(I)} + 2k_2 C_{C_2H_6} C_{h(I)}\right) \tag{5-17}$$

As can be seen above, the governing equations for methane coupling in the hollow fibre membrane reactor are a set of implicit ordinary differential equations and can be solved numerically by the conventional Runge-Kutta method. MATLAB software was applied for the calculations in this chapter.

5.4 Results and discussion

The experimental results together with the theoretical analysis have been presented in this section. In calclations, the reaction and transport parameters of the defects were obtained from published literatures (Tan *et al.*, 2000; Tan *et al.*, 2003) while the coupling reaction kinetic parameters were estimated by regression with the experimental data since no such results are available with respect to SCYb membranes. The characteristic parameters of the reactor and the operating conditions were all based on the experiments (Table 5-2). Effects of various conditions on the performances of the reactor for methane coupling were analyzed both experimentally and theoretically.

Table 5-2 Parameters for the SCYb hollow fiber membrane reactor and operating conditions.

Items	Values
Number of hollow fibers	1
OD of the hollow fiber	D_o=0.145 cm
ID of the hollow fiber	D_{in}=0.065 cm
Length of hollow fiber membranes	26 cm
Effective of heating length in the furnace	4 cm
Operating temperature	750~1000 °C
Feed concentration of methane	2.9~9.22 %
Feed flow rate of methane stream	2.1~12 cm^3 min^{-1} (STP)
Feed concentration of oxygen	2.8~21 %
Feed flow rate of air stream	37~47, cm^3 min^{-1} (STP)

Fig. 5-4 shows the experimental results where the C_2 formation rates at various temperatures are plotted against feed concentrations of methane ((A)-(D)) and oxygen ((a)-(d)), respectively. As is expected, both ethane and ethylene formation rates increase with increasing the methane feed concentration. However, the increase in oxygen feed concentration mainly results in the increase of ethylene formation rate instead of ethane, as shown in Fig. 5-4(a)-(d).

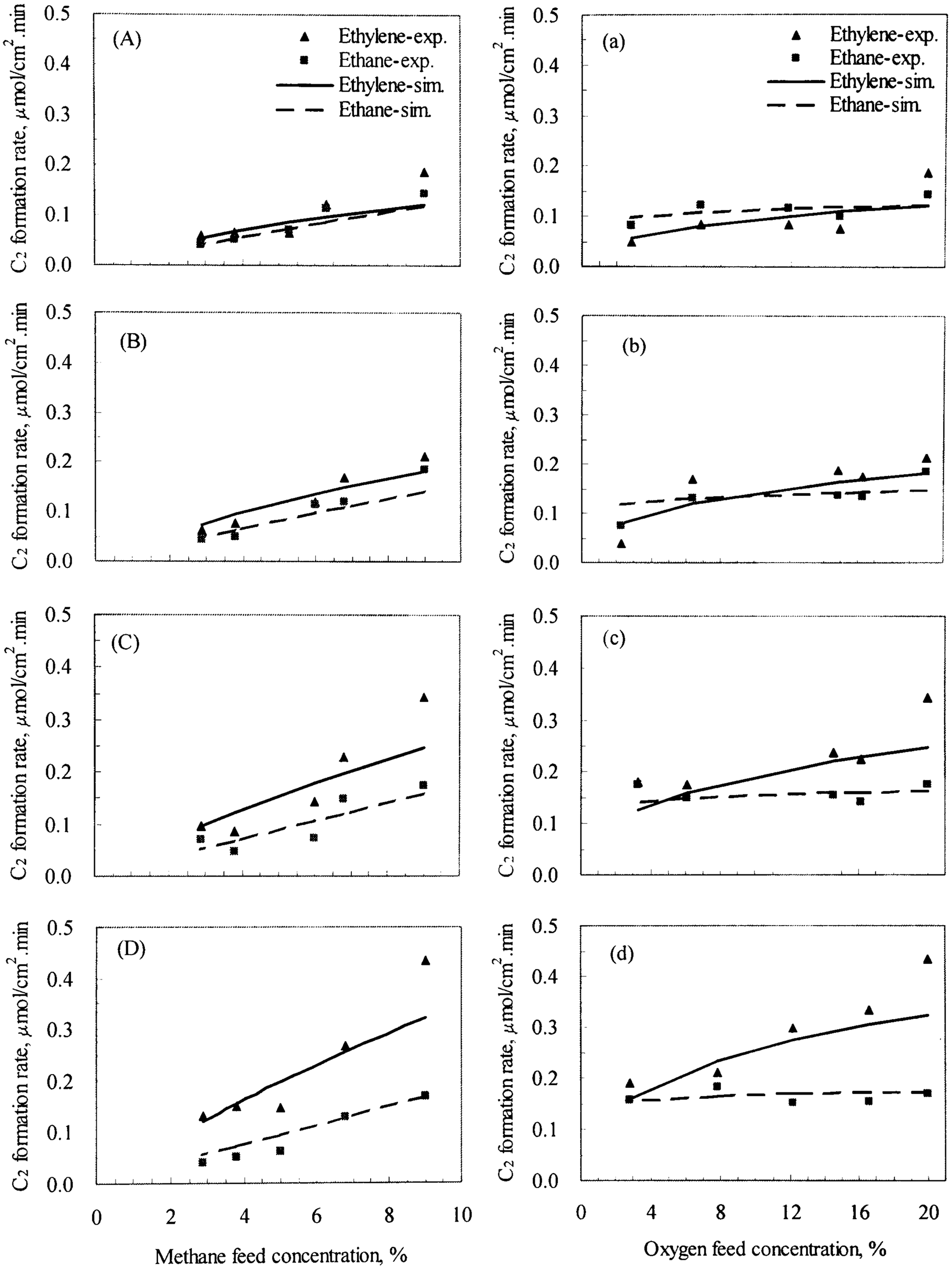


Fig. 5-4 C_2 formation rate against feed concentration at different temperatures (feed flow rate of methane stream = 4.3 cm^3/min, feed flow rate of air stream = 40 cm^3/min) (A), (a)-800°C; (B), (b)-850°C; (C), (c)-900°C; (D), (d)-950°C.

This suggests that increasing the extraction of hydrogen by means of increasing the oxygen concentration promotes the formation of ethylene more than that of ethane, especially at higher temperatures. On the other hand, it can also be seen that as the

temperature increases, the increase in ethylene formation rate is more remarkable than the ethane formation rate. Therefore, higher temperature favors the formation of ethylene other than ethane. This implies that the activation energy for ethylene formation is higher than that for ethane formation. In Fig. 5-4, the regression results are also plotted respectively with the solid line for ethylene and the dashed line for ethane. It can be seen that all the curves are in good agreement with the experimental data. This indicates that the mechanism presented in this work is reliable to describe the methane coupling reactions in the SCYb hollow fibre membrane reactor. Plot of the reaction rate constants obtained by regression with the experimental data against the reciprocal of temperature is shown in Fig. 5-5. It can be seen that both reaction constants are basically in coincidence with the Arrhenius equation, with the correlation coefficients of 0.991 and 0.972, respectively. From the intercept and slop of the lines, the pre-exponential factor and activation energy of the ethylene and ethane formation rates can be obtained as listed in Table 5-3. As can be seen, the activation energy for ethylene formation, 7.16×10^4 J/mol is higher than that for ethane formation, 4.93×10^4 J/mol, leading to the conversion of more ethane into ethylene at higher temperatures.

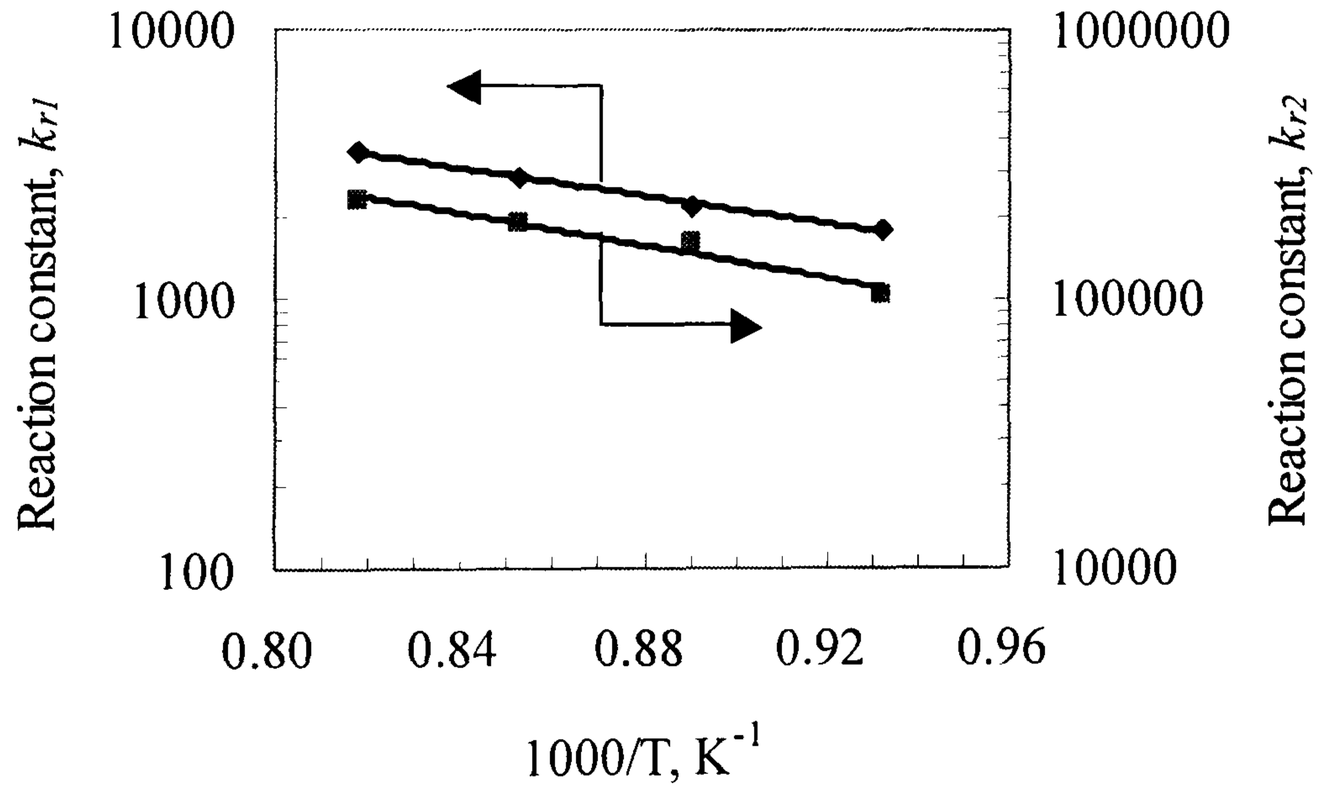


Fig. 5-5 Plot of reaction kinetic parameters against the reciprocal of temperature.

Table 5-3 Reaction constants by regression with the experimental data.

	Regression results				**Expression parameters***		
	800 °C	850 °C	900 °C	950 °C	Pre-exponent factor, kr_0	Activation energy, E_a	R^2 value
k_{r1}	1.82×10^3	2.20×10^3	2.81×10^3	3.57×10^3	4.458×10^5	4.929×10^4	0.991
k_{r2}	1.03×10^5	1.63×10^5	1.92×10^5	2.92×10^5	3.246×10^8	7.166×10^4	0.972

* Expression equation: $k_r = k_{r0}\exp(-E_a / RT)$

Fig. 5-6 illustrates the formation rates of C_2H_4 and C_2H_6 as a function of temperature, where the feed flow rates of methane-argon mixture with the methane concentration of 9.22% and air streams are 3.94 and 40 cm^3/min, respectively. It can be seen that the formation rate of C_2H_4 increases as temperature increases from 700 to 1000 °C, while a maximum formation rate for ethane is present at around 850°C. After the temperature is above 850°C, the formation rate of ethane decreases as temperature is further increased because the increase of ethane formation rate due to the increase of temperature is slower than that of its conversion rate into ethylene. The simulation results using the kinetic parameters obtained above are also been shown in the figure with the solid and dashed lines. They are slightly lower than the experimental data indicating that the real kinetic parameters at higher feed concentrations should be somewhat higher than those by regression with the experimental data in the whole concentration range.

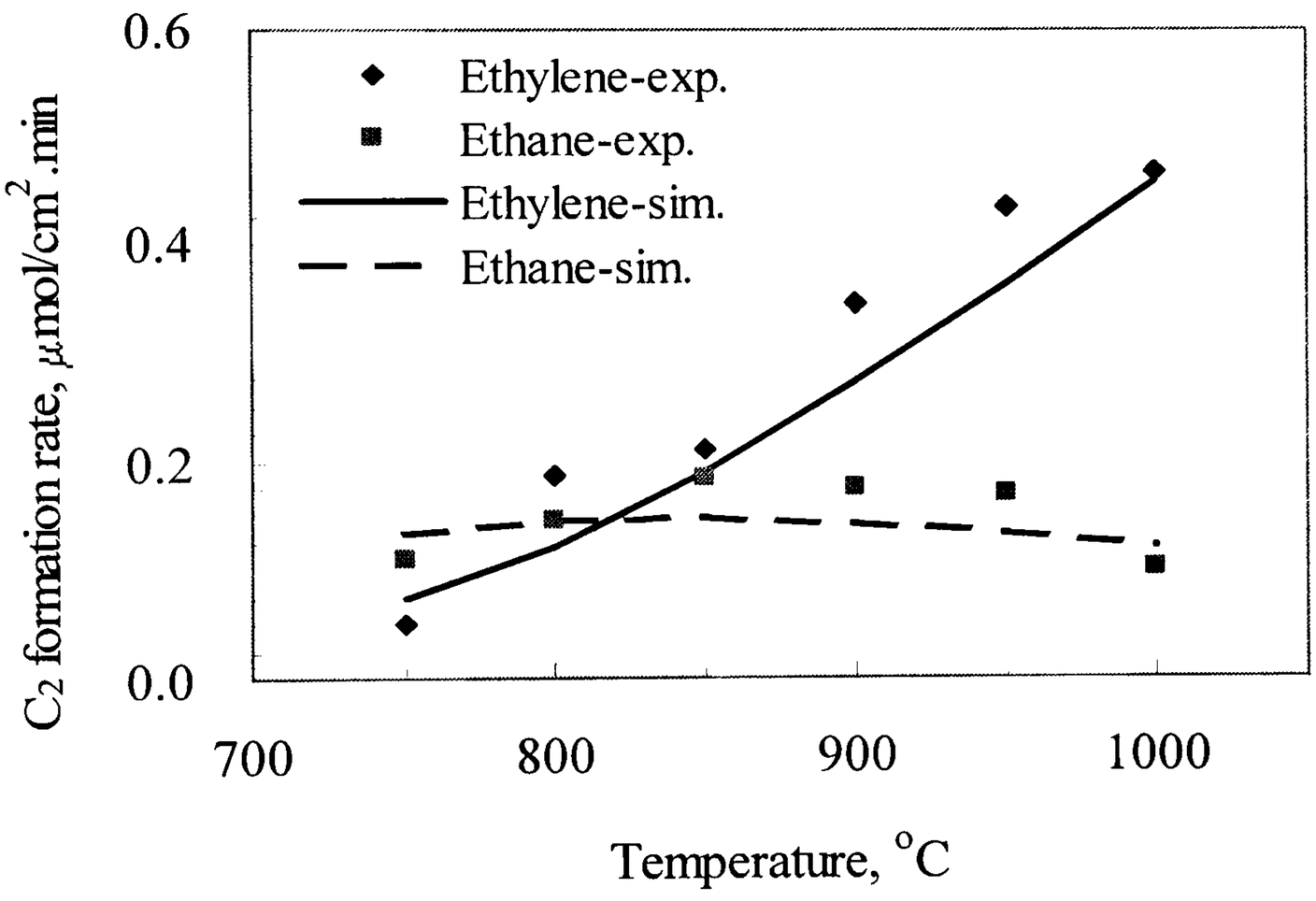


Fig. 5-6 Effect of temperature on the C_2 formation rate (feed flow rate of methane stream =3.96 cm^3/min, methane feed concentration=9.22%, air feed flow rate=40 cm^3/min).

It should be mentioned that the C_2 yield in the experiments was about 9% at 900 °C, which is lower than 35% of the yield obtained in a recent study on oxidative coupling of methane in a $Bi_{1.5}Y_{0.3}Sm_{0.2}O_3$ tube membrane reactor at same temperature (Akin and Lin, 2002). The low yield value indicates the catalytic activity of the SCYb hollow

fibre membrane is not very high. C_2 selectivity in all experiments was found to be about 60%, which is slightly higher than the value of 54% obtained in Akin and Lin's study (2002), but much less than expected in the case that no oxygen takes part in the methane coupling reaction. This is because, on the one hand, methane would be carbonised in the absence of oxygen on the membrane surface at high temperatures. On the other hand, C_2 products can be further converted into higher hydrocarbons such as C_3, C_4 and C_5, following the similar mechanism to the formation of C_2 compounds. Obviously, the formation of these higher hydrocarbons would be the negative contribution to the C_2 selectivity although the formation rates are one to two orders of magnitude lower than the C_2 formation rate. Fig. 5-7 plots the formation rates of C_3, C_4 and C_5 hydrocarbons as a function of temperature. It can be seen that the C_3 formation rate is the highest but the C_5 formation rate is even higher than C_4. Furthermore, as temperature increases, the formation rates of these higher hydrocarbons increase until up to the maximum values at around 950°C and then reduced with further increase in temperature. Obviously, the temperature higher than 950°C promotes the carbonisation of methane with the result of decrease in hydrocarbon production.

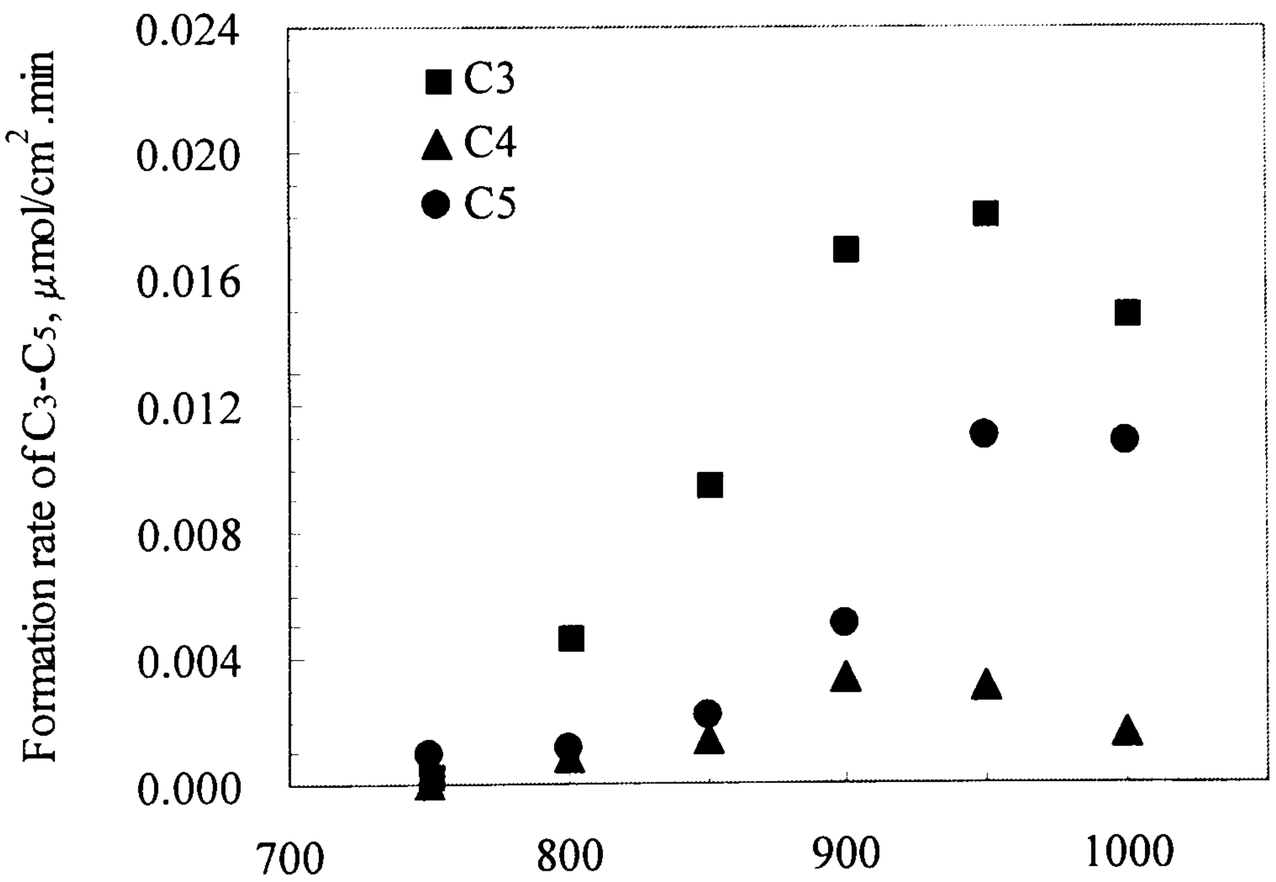


Fig. 5-7 C_3-C_5 formation rates as a function of temperature (feed flow rate of methane stream =4.3 cm^3/min, methane feed concentration=9.22%, air feed flow rate=40 cm^3/min).

Effect of the feed flow rate of methane stream on the C_2 formation rates is shown in Fig. 5-8, where the operation temperature is kept constant to be 950°C. It indicates that as the flow rate of methane stream increases, the ethylene formation rate decreases but the ethane formation rate is increased. As is known that the higher the feed flow rate, the less the residence time for the hydrocarbons in the reactor. According to the mechanism presented before, ethylene is mainly produced by the dehydrogenation of ethane. Therefore, the less residence time means the ethane formed cannot be further converted into ethylene in time before it leaves the membrane reactor, leading to the decrease in ethylene formation rate.

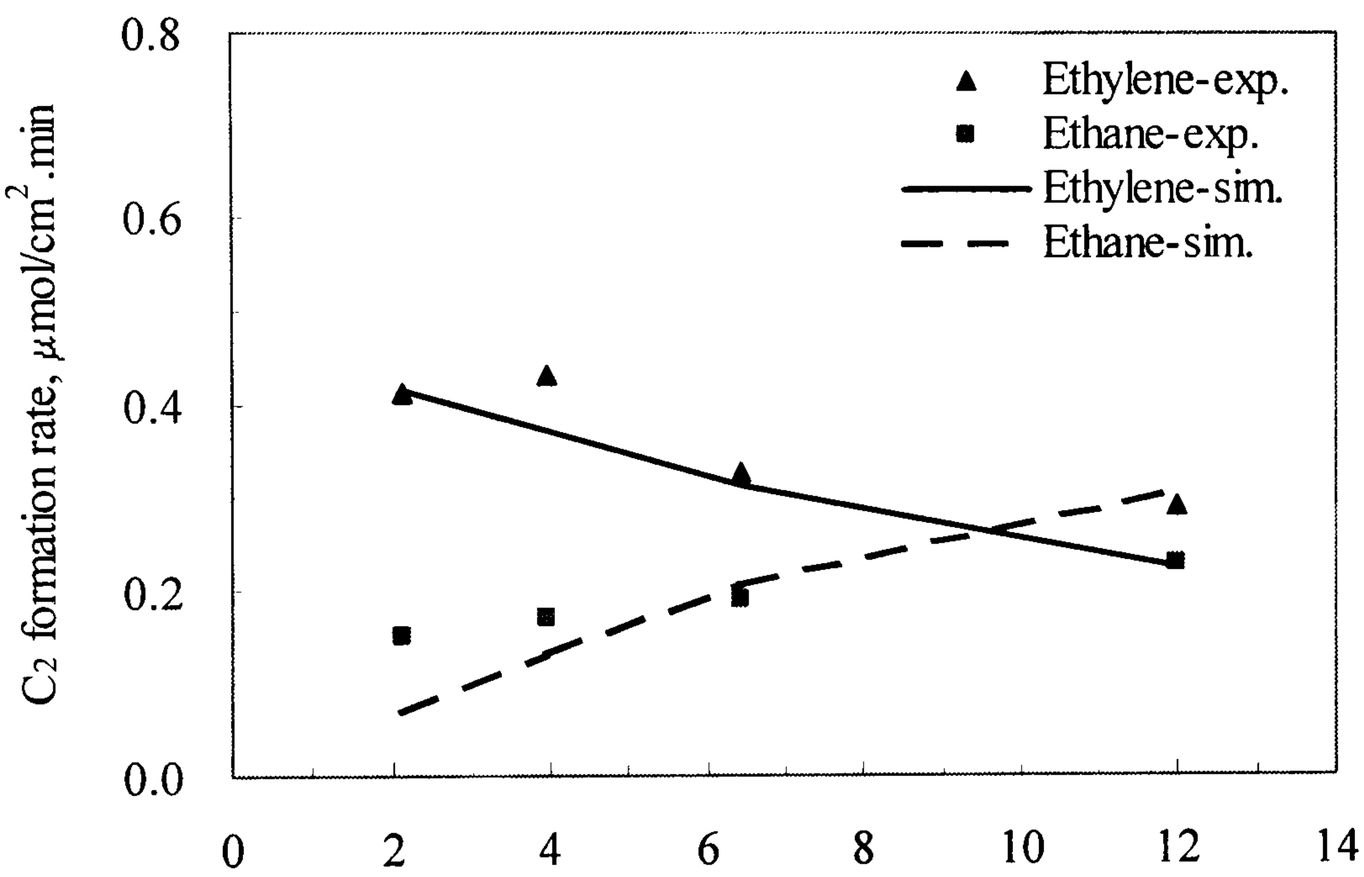


Fig. 5-8 Effect of methane feed flow rate on the C_2 formation rate (temperature=950 °C, methane feed concentration=9.22%, air feed flow rate=40 cm^3/min).

Fig. 5-9 illustrates the effect of methane feed flow rate on the formation rates of C_3-C_5 compounds at 950°C. As can be seen, there are also maximum formation rates for these higher hydrocarbons as the feed flow rate increases, which occur at around 6.4 cm^3/min. Unlike ethylene, formation of the higher hydrocarbons involves the coupling between radicals including $\cdot CH_3$, $\cdot C_2H_5$ and so on. As a result, the increase of radical concentrations due to the increase in methane feed flow rate could improve the formation rate of C_3-C_5 compounds at lower feed flow rates. Meanwhile, just because of the participation of higher hydrocarbon radicals such as $\cdot C_2H_5$, which come from

higher hydrocarbons, the formation rates of C_3-C_5 compounds will be decreased if the feed flow rate is too high since the higher hydrocarbon radicals cannot be formed in time. Therefore, the methane coupling mechanism on the proton conducting membranes is actually very complicated and need to be studied in detail in the future.

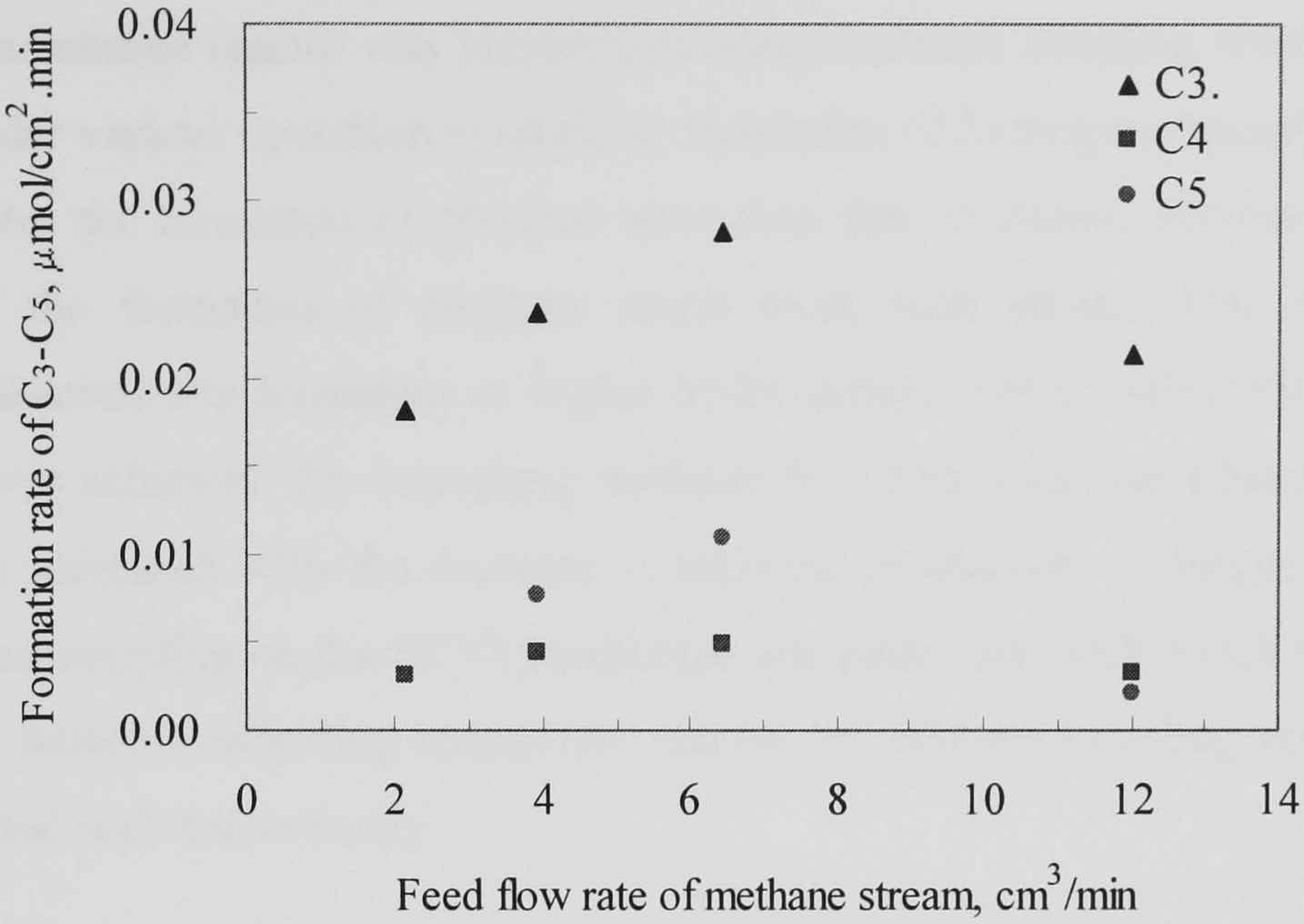


Fig. 5-9 Effect of methane feed flow rate on the formation rate of higher hydrocarbons (temperature=950 °C, methane feed concentration=9.22%, air feed flow rate=40 cm^3/min).

5.5 Conclusions

A proton-hole mixed conducting perovskite, $SrCe_{0.95}Yb_{0.05}O_{3-\delta}$ (SCYb) hollow fibre membrane was successfully prepared by means of a phase inversion/sintering technique. With the resulting dense SCYb hollow fibre membranes, a SCYb hollow fibre membrane reactor was prepared in which methane coupling reaction was carried out under various operation conditions. Extraction of hydrogen through the membrane promotes the formation of ethylene more than that of ethane. Increasing temperature favors the formation of ethylene much more than ethane. Due to the methane carbonisation and formation of higher hydrocarbons, the C_2 selectivity of only about 60% was achieved. By increasing methane feed flow rate, the ethane formation rate can be increased with the decrease in ethylene production. A simple mechanism for methane coupling on the SCYb membrane was presented, with which the performance of the proton conducting membrane reactor on methane coupling reaction could be predicted well theoretically.

Notations

A_m	-	Logarithm average membrane area, cm^2
C	-	Concentration of defects or gas, $mol \cdot cm^{-3}$
D	-	Effective diffusivity of defects, $cm^2 \cdot s^{-1}$
F_1	-	Feed flow rate of methane stream, mol/s
J	-	Molar flux of defects, $mol \cdot cm^{-2} \cdot s^{-1}$
K_1	-	Equilibrium constant for reaction (ii), $mol \cdot cm^{-3} \cdot atm^{-0.5}$
K_2	-	Equilibrium constant for reaction (iii), $mol \cdot cm^{-3} \cdot atm^{-1}$
k_1, k_2	-	Formation rate constants for reaction (viii) and (ix), $cm^4 \cdot mol^{-1} \cdot s^{-1}$
L	-	Effective length of the hollow fiber, cm
m	-	Number of the hollow fibers in the reactor
N	-	Molar flow rate, mol s^{-1}
P_l, P_s	-	Lumen or shell side pressure, atm
R	-	Ideal gas constant
R_o, R_{in}, R_m	-	Outer, inner or log-mean radius of hollow fiber, cm
r_i	-	Formation rate of species i, $mol/cm^2.s$
S_i	-	Selectivity of species i, %
t	-	Transport number of defects
T	-	Operating temperature, K
y_i	-	Molar fraction of species i in gas stream, %
Yb_{Ce}'	-	Concentration of dopant, mol cm^{-3}
z	-	Defect's charge number

Subscripts

h	-	Hole
in	-	Feed
l	-	Lumen side of the hollow fiber membrane reactor
out	-	Effluent
p	-	Proton
V	-	Vacancy
s	-	Shell side of the hollow fiber membrane reactor

References

Akin, F. T. and Y. S. Lin (2002). Oxidative coupling of methane in dense ceramic membrane reactor with high yields, *AIChE J.*, **Vol.** 48, **pp.** 2298-2306.

Akin, F. T. and Y. S. J. Lin (2004). Oxygen permeation through oxygen ionic or mixed-conducting ceramic membranes with chemical reactions, *J. Membr. Sci.*, **Vol.** 231, **pp.** 133-146.

Bouwmeester, H. J. M. (2003). Dense ceramic membranes for methane conversion, *Catalysis Today*, **Vol.** 82, **pp.** 141-150.

Chiang, P. H., D. Eng, H. Alqahtany and M. Stoukides (1992). Nonoxidative methane coupling with the aid of solid electrolytes, *Solid State Ionics*, **Vol.** 53-56, **pp.** 135-141.

Chiang, P. H., D. Eng and M. Stoukides (1991). Electrocatalytic methane dimerization with a Yb-doped $SrCeO_3$ electrolytes, *J. Electrochem. Soc.*, **Vol.** 138, **pp.** L11.

Chiang, P. H., D. Eng and M. Stoukides (1993). Electrocatalytic nonoxidative dimerization of methane over Ag electrodes, *Solid State Ionics*, **Vol.** 61, **pp.** 99-103.

Hamakawa, S., T. Hibino and H. Iwahara (1993). Electrochemical methane coupling using protonic conductors, *J. Electrochem. Soc.*, **Vol.** 140, **pp.** 459-462.

Hamakawa, S., T. Hibino and H. Iwahara (1994). Electrochemical methane coupling in a proton-hole mixed conductor and its application to a membrane reactor, *J. Electrochem. Soc.*, **Vol.** 141, **pp.** 1720-1726.

Hollein, V., M. Thornton, P. Quicker and R. Dittmeyer (2001). Preparation and characterization of palladium composite membranes for hydrogen removal in hydrocarbon dehydrogenation membrane reactors, *Catalysis Today*, **Vol.** 67, **pp.** 33-42.

Kao, Y. K., L. Lei and Y. S. Lin (2003). Optimum operation of oxidative coupling of methane in porous ceramic membrane reactors, *Catal. Today*, **Vol.** 82, **pp.** 255-273.

Langguth, J., R. Dittmeyer, H. Hofmann and G. Tomandl (1997). Studies on oxidative coupling of methane using high-temperature proton-conducting membranes, *Applied Catalysis S: General*, **Vol.** 158, **pp.** 287-305.

Lin, W.-H. and H.-F. Chang (2004). A study of ethanol dehydrogenation reaction in a palladium membrane reactor, *Catalysis Today*, **Vol.** 97, **pp.** 181-188.

Lin, Y. S. and Y. Zeng (1996). Catalytic Properties of Oxygen Semipermeable Perovskite-Type Ceramic Membrane Materials for Oxidative Coupling of Methane, *Journal of Catalysis*, **Vol.** 164, **pp.** 220-231.

Liu, S., X. Tan, K. Li and R. Hughes (2001). Preparation and characterisation of $SrCe_{0.95}Yb_{0.05}O_{2.975}$ hollow fibre membranes, *J. Membr. Sci.*, **Vol.** 193, **pp.** 249-260.

Lu, Y., A. G. Dixon, W. R. Moser and Y. Hua Ma (2000a). Oxidative coupling of methane in a modified [gamma]-alumina membrane reactor, *Chemical Engineering Science*, **Vol.** 55, **pp.** 4901-4912.

Lu, Y., A. G. Dixon, W. R. Moser, Y. Ma and U. Balachandran (2000b). Oxygen-permeable dense membrane reactor for the oxidative coupling of methane, *J. Membr. Sci.*, **Vol.** 170, **pp.** 27-34.

Lunsford, J. H. (2000). Catalytic conversion of methane to more useful chemicals and fuels: a challenge for the 21st century, *Catalysis Today*, **Vol.** 63, **pp.** 165-174.

Marigliano, G., G. Barbieri and E. Drioli (2003). Equilibrium conversion for a Pd-based membrane reactor. Dependence on the temperature and pressure, *Chemical Engineering and Processing*, **Vol.** 42, **pp.** 231-236.

Ramachandra, A. M., Y. Lu, Y. H. Ma, W. R. Moser and A. G. Dixon (1996). Oxidative coupling of methane in porous Vycor membrane reactors, *J. Membr. Sci.*, **Vol.** 116, **pp.** 253-264.

Slade, R. L. T. and N. Singh (1991). Systematic examination of hydrogen ion conduction in rare-earth doped barium cerate ceramics, *Solid State Ionics*, **Vol.** 46, **pp.** 111.

Tan, X., S. Liu and K. Li (2001). Preparation and characterization of inorganic hollow fibre membranes, *J. Membr. Sci.*, **Vol.** 188, **pp.** 87-95.

Tan, X., S. Liu, K. Li and R. Hughes (2000). Theoretical analysis of ion permeation through mixed conducting membranes and its application to dehydrogenation reactions, *Solid State Ionics*, **Vol.** 138, **pp.** 149-159.

Tan, X., Y. Liu and K. Li (2005a). Mixed conducting ceramic hollow-fiber membranes for air separation, *AIChE J.*, **Vol.** 51, **pp.** 1991-2000.

Tan, X., Y. Liu and K. Li (2005b). Preparation of LSCF ceramic hollow fibre membrane for oxygen production by a phase-inversion/sintering technique, *Ind. Eng. Chem. Res.*, **Vol.** 44, **pp.** 61-66.

Tan, X., N. Yang and K. Li (2003). Modeling of the $SrCe_{0.95}Yb_{0.05}O_{3-\delta}$ hollow fibre membrane reactor for methane coupling, *Chinese J. Chem. Eng.*, **Vol.** 11, **pp.** 289.

ten Elshof, J. E., H. J. M. Bouwmeester and H. Verweij (1995). Oxidative coupling of methane in a mixed-conducting perovskite membrane reactor, *Appl. Catal. A: Gen.*, **Vol.** 130, **pp.** 195-212.

Uchida, H., N. Maeda and H. Iwahara (1983). Relation between proton and hole conduction in $SrCeO_3$ based solid electrolytes under water-containing atmospheres at high temperatures, *Solid State Ionics*, **Vol.** 11, **pp.** 117-124.

Wang, W. and Y. S. Lin (1995). Analysis of oxidative coupling of methane in dense oxide membrane reactors, *J. Membr. Sci.*, **Vol.** 103, **pp.** 219-233.

Zeng, Y. and Y. S. Lin (1997). Catalytic properties of yttria doped bismuth oxide ceramics for oxidative coupling of methane, *Appl. Catal. A: Gen.*, **Vol.** 159, **pp.** 101-117.

Chapter 6

Preparation and characterization of $La_{0.6}Sr_{0.4}Co_{0.2}Fe_{0.8}O_{3-\alpha}$ (LSCF) hollow fibre membranes

Abstract

A mixed oxide-electron conducting ceramic, $La_{0.6}Sr_{0.4}Co_{0.2}Fe_{0.8}O_{3-\alpha}$ (LSCF) hollow fibre membrane was prepared by a combined phase inversion/sintering technique. The hollow fibre membrane precursor was first spun from a starting solution containing 66.33 wt% LSCF powder, 6.63 wt% PESf -binder, 0.5 wt% PVP additive and 26.54 wt% NMP, and then sintered at elevated temperatures between 1100-1280°C for 4 hrs to obtain the membranes with gas tight property. The hollow membranes prepared show an asymmetric structure that a sponge-like structure is sandwiched by finger-like structures located at the outer and inner walls of the fibres. Oxygen permeation fluxes through the hollow membranes were measured under different temperatures and downstream oxygen partial pressures. The results indicated that oxygen flux obtained from the hollow fibre membrane is higher than that obtained from conventional LSCF disk-shape or tubular membranes, most probably due to the reduced thickness and porous inner surface of the membranes prepared. The operating temperature plays a more important role in determining the oxygen permeation flux of LSCF membranes. Once the operating temperature is over 700 °C, the oxygen permeation flux increases sharply due to the order–disorder transition of oxygen vacancy.

Key words: Hollow fibre membrane; Oxygen production; Phase inversion

6.1 Introduction

Oxygen production by air separation is of great importance in both environmental and industrial processes. For example, if oxygen instead of air is used in power plants, the waste gas produced in the combustion process is pure carbon dioxide that may be easily reclaimed instead of released as a greenhouse gas to environment. Use of pure oxygen rather than air as the oxidant in chemical industrial processes would be able to decrease the cost remarkably since the separation of nitrogen from subsequent product streams becomes unnecessary. Nowadays, oxygen is usually produced by the cryogenic or by the pressure swing adsorption, which are very costly methods. Alternatively, ceramic membrane processes are economically more promising. In such processes, dense ceramic membranes, which conduct both oxygen ion and electron simultaneously, i.e. the so-called mixed conductor (e.g. $La_{1-x}Sr_xCo_{1-y}Fe_yO_{3-\alpha}$) have been demonstrated to provide pure oxygen fluxes (Kharton *et al.*, 1999; Li *et al.*, 1999; Ullmann and Trofimenko, 1999). When a gradient of oxygen chemical potential is imposed across these dense membranes at high temperatures, oxygen is transported in the form of oxygen ions from the high partial pressure side to the low partial pressure side and released in the downstream without the need of electrodes and external electrical loadings, which makes the system very simple.

In most previous studies, the disc-shaped membranes with only a limited membrane area (<5 cm^2) were usually used for oxygen permeation since they are easily fabricated using the conventional static-pressing method (Zeng and Lin, 1998; Yaremchenko *et al.*, 1999). Although a multiple planar stack can be employed to enlarge the membrane area to a plant scale (Dyer *et al.*, 2000), many problems such as sealing, connection and pressure-resistance have to be faced. Tubular membranes have been developed recently to overcome these difficulties (Li *et al.*, 2000; Lu *et al.*, 2000), but their small surface /volume ratio and the thick membrane wall make them unfavorable in the industrial applications. Alternatively, the hollow fibre membranes possess many advantages over the planar and tubular membranes such as higher surface area /volume ratio and the ease of high temperature sealing (Luyten *et al.*, 2000; Tan *et al.*, 2001). Furthermore, since the membrane cross-section of hollow fibres prepared via the phase inversion is asymmetric (i.e. a thin separating layer integrated with a substrate), the resistance to oxygen permeation may, therefore, be low. As a result, it would be easier

to reach a commercially interesting flux at lower operating temperatures by using the hollow membrane modules (Tan and Li, 2002).

In this chapter, LSCF hollow fibre membranes with the gas-tight property were prepared through a phase inversion/sintering method. The microstructure evolution of the hollow fibre membranes and their performances for oxygen permeation has been investigated in detail.

6.2 Experimental

6.2.1 Materials

Commercially available $La_{0.6}Sr_{0.4}Co_{0.2}Fe_{0.8}O_{3-\alpha}$ (LSCF) powders with the surface area of 6.0 m^2/g and d_{50}<1 μm (purchased from Praxair Surface Technologies, USA) was used as the membrane material. Polyethersulfone, (PESf) (Radel A-300, Ameco Performance, USA), N-methyl-2-pyrrolidone (NMP) (Synthesis Grade, Merck) were used to prepare the starting solution. Polyvinylpyrrolidone (PVP, K16-18) (from Acros Organics, M_w = 8,000) was used as the additive. Deionized water and tap water were used as the internal and external coagulant, respectively. Several inorganic sealants (all purchased from FORTAFIX Inc) were used for the assembling of hollow fibre membrane modules, listed in Table 6-1.

Table 6-1 Fire cements for the assembling of the membrane modules (All from FortaFix Inc.).

Item	Name of sealants	Temperature resistant	Sealing results	Remarks
A	Grade 2001	~ 1400 °C	Leaking	Fail
B	Temcem	>1400 °C	Leaking	Fail
C	Ceramix TC,	~ 1250 °C, gas tight seal	Leaking at temperatures of <1100°C, may react with LSCF membranes	Fail
D	Light	~ 950 °C	>300°C but gas-tight at lower temperatures	Partly ok
E	Chromix	~ 1400 °C, gas tight seal	Leaking at temperatures of <1200°C, may react with LSCF membranes	Fail

6.2.2 Preparation of LSCF hollow membranes

Starting solutions were first prepared for spinning the hollow fibre membrane precursors. A calculated quantity of PESf with the additive PVP was dissolved in the weighted NMP solvent in a 250 ml wide-neck bottle. After the polymer solution was formed, the weighted amount of LSCF powders was then added gradually, while Heidolph RZR 2000 stirrer was used at a speed of around 300 rpm to ensure that all the powders are dispersed uniformly in the polymer solution. The stirring was carried out continuously for at least 48 hrs before spinning. After the starting solution was degassed at room temperature for 30 min, it was then transferred to a stainless steel reservoir and pressurized to 0.5 bar using nitrogen. A spinneret with the orifice diameter/inner diameter of 3.0/1.2 mm was used to obtain the hollow fibre precursors. Deionized water and tap water were used as the internal and external coagulants, respectively. The forming hollow fibre precursors were immersed in a water bath for more than 24 hrs to complete the solidification process. Finally, the resulting hollow fibre precursors were heated in a CARBOLITE furnace at 600°C for 2 hours to remove the organic polymer binder, followed by sintering at high temperatures (1100~1280°C) for 4 hrs to allow the fusion and bonding to occur. The operating conditions employed for preparing the hollow fibre membranes are summarized in Table 6-2.

Table 6-2 Preparation conditions of LSFC hollow fibre membranes.

Parameter	Value
Dope composition (wt.%)	
LSCF	66.33
PESf, Radel A-300	6.63
NMP	26.5
PVP K16-18	0.5
Dope temperature (°C)	20
Internal coagulant temperature (°C)	20
Injection rate of internal coagulant (ml/min)	10
Nitrogen pressure (atm)	0.5
Air gap (cm)	1.5
Sintering temperature (°C)	1100~1280

The prepared hollow fibre precursors and the sintered membranes were characterized by XRD, SEM and gas permeation test, as described in detail elsewhere (Liu *et al.*, 2001; Tan *et al.*, 2001). The XRD patterns of the sintered hollow fibres were from the powders of the crushed membranes.

6.2.3 Oxygen permeation measurement method

Oxygen permeation was conducted only using the dense hollow fibre membranes without defects, which were checked by gas tight measurement before assembling. Here the gas-tightness of hollow fibre membranes is referred to that the N_2 permeability of the membrane tested is less than 1 Barrer. To prepare a membrane module, a hollow fibre membrane with the length of 25 cm was sealed with two Al_2O_3 ceramic tubes (ID/OD = 2/4 mm) at both the ends of the fibre. It was then placed in a CARBOLITE tube furnace (total length of 30 cm) where the effective length of the constant-temperature heating range is 9 cm. The temperatures within the furnace were controlled by the microprocessor temperature controller and checked with a thermal couple at the tube centre and as well as at the sealing spot close to the furnace entrance. In order to lower the temperature at the sealing spot, glass wool was used as thermal barriers to prevent the excessive increase in temperature at the sealing points. The design of the experimental setup is schematically illustrated in Fig. 6-1.

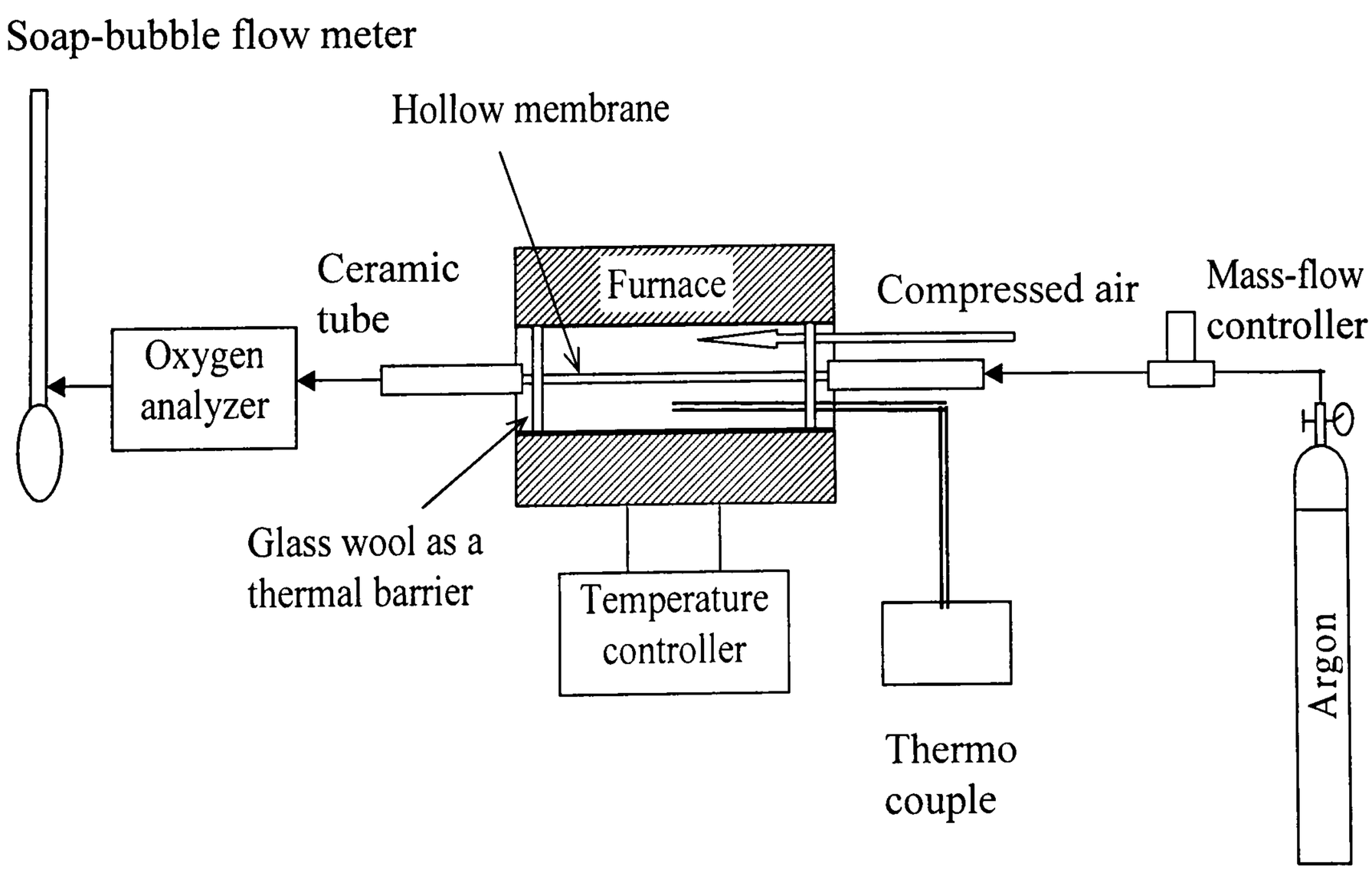


Fig. 6-1 Schematic experimental setup for oxygen permeation measurements.

In operation, argon used as sweep gas was fed into the fibre lumen, while the compressed air was introduced into the furnace tube in order to keep oxygen concentration outside the membrane constant. The flow rate of the sweep gas was controlled using a mass flow controller (Smart Mass Flow meter with Read out & Control Electronics Model 0152, Brooks Instrument). The oxygen concentration in the effluent gas stream was measured online using an oxygen meter (Oxygen Analyser 572, Servomex). In order to check the oxygen permeation, the flow rate of the effluent was measured with a soap-bubble flow meter, as also shown in Fig. 6-1. The oxygen permeation flux may be calculated by:

$$J_{O_2} = \frac{V_t x_{O_2}}{A_m} \tag{6-1a}$$

or

$$J_{O_2} = \frac{V_{Ar} x_{O_2}}{A_m (100 - x_{O_2})} \tag{6-1b}$$

where V_t and V_{Ar} are the volumetric flow rates of the effluent stream and of the sweep Ar gas, respectively, cm^3/min; x_{O2} is the oxygen concentration determined by the oxygen sensor meter, %; A_m (cm^2) is the effective membrane area of the hollow fibre for oxygen permeation, $A_m = \frac{\pi(D_o - D_i)L}{\ln(D_o / D_i)}$, in which D_o and D_i are respectively the outer and the inner diameters of the hollow , cm; and L is the effective heating length, i.e., 9 cm in this chapter.

6.3. Results and discussion

6.3.1 Morphology of the LSCF hollow fibre membranes

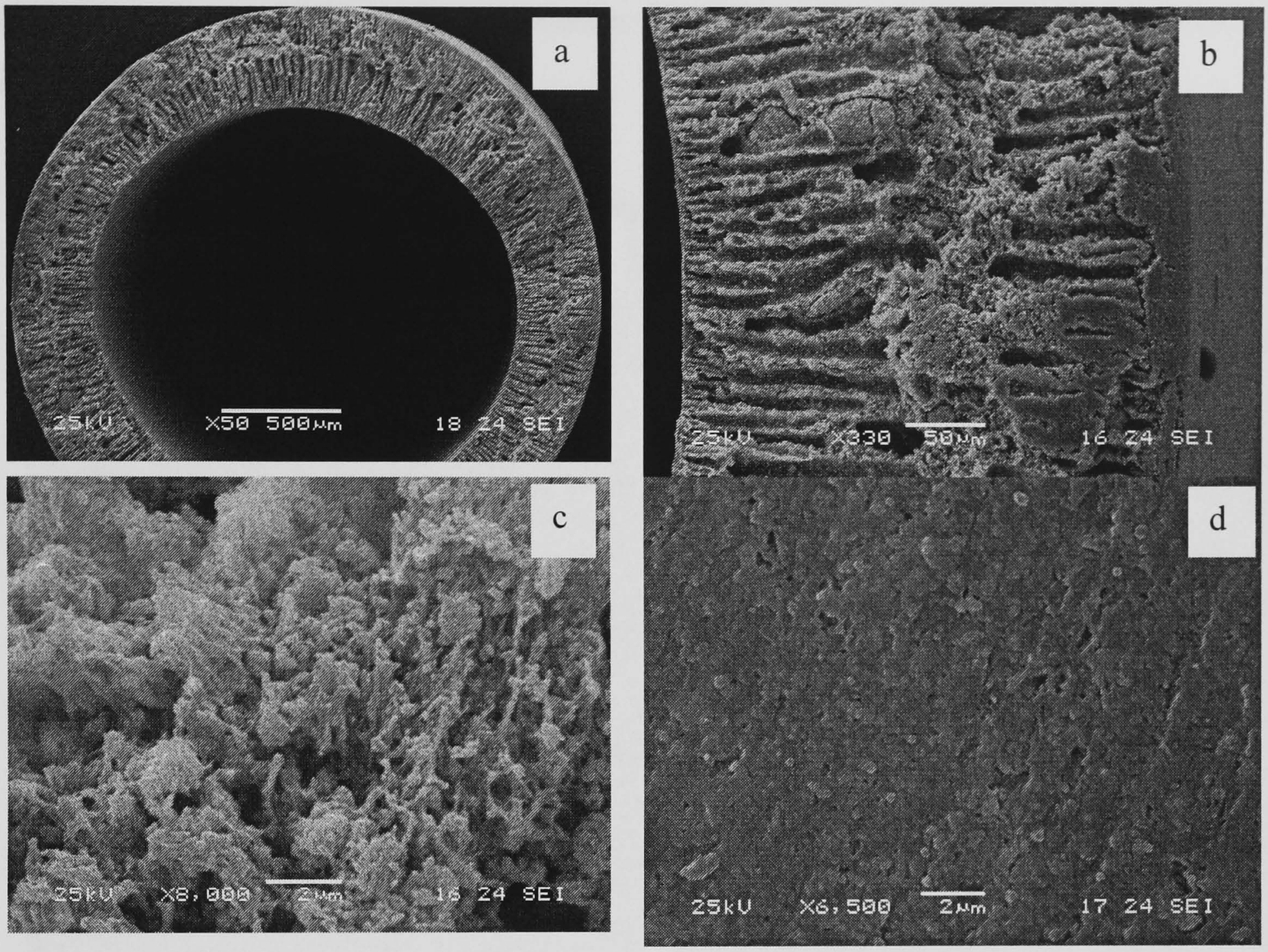


Fig. 6-2 SEM micrographs of the LSCF hollow fibre precursor.

In this chapter, all the hollow fibre membranes discussed were prepared from a starting solution containing LSCF powders 66.33%, PESf 6.63%, PVP 0.5% and NMP 26.54% while deionized water and tap water at room temperature were used as the internal and the external coagulants, respectively. Fig. 6-2 shows the SEM micrographs of the LSCF hollow fibre precursor at different positions. The OD and ID of the fibre precursor prepared are measured from micrograph Fig. 6-2(a) as 2468 μm and 1718 μm, respectively. In addition, it can be seen that finger-like structures have been formed near both the inner and outer walls, but a sponge-like layer occurs at the centre of the fibre precursor. The formation of such asymmetric structures shown in the figure can be attributed to the rapid precipitation occurred at both the inner and outer walls close to coagulants resulting in short finger pores but the slow precipitation at the centre of the fibre giving the sponge-like structure, which is shown in Fig. 6-2(c). Fig.

6-2(d) shows the outer surface of the hollow fibre precursor, from which it can be seen that the LSCF particles are well dispersed and sparsely connected each other by the polymer binder, as also shown in Fig. 6-2(c). This typical structure formed by fast precipitation during phase inversion process is also as same as that of SCYb hollow fibre membranes.

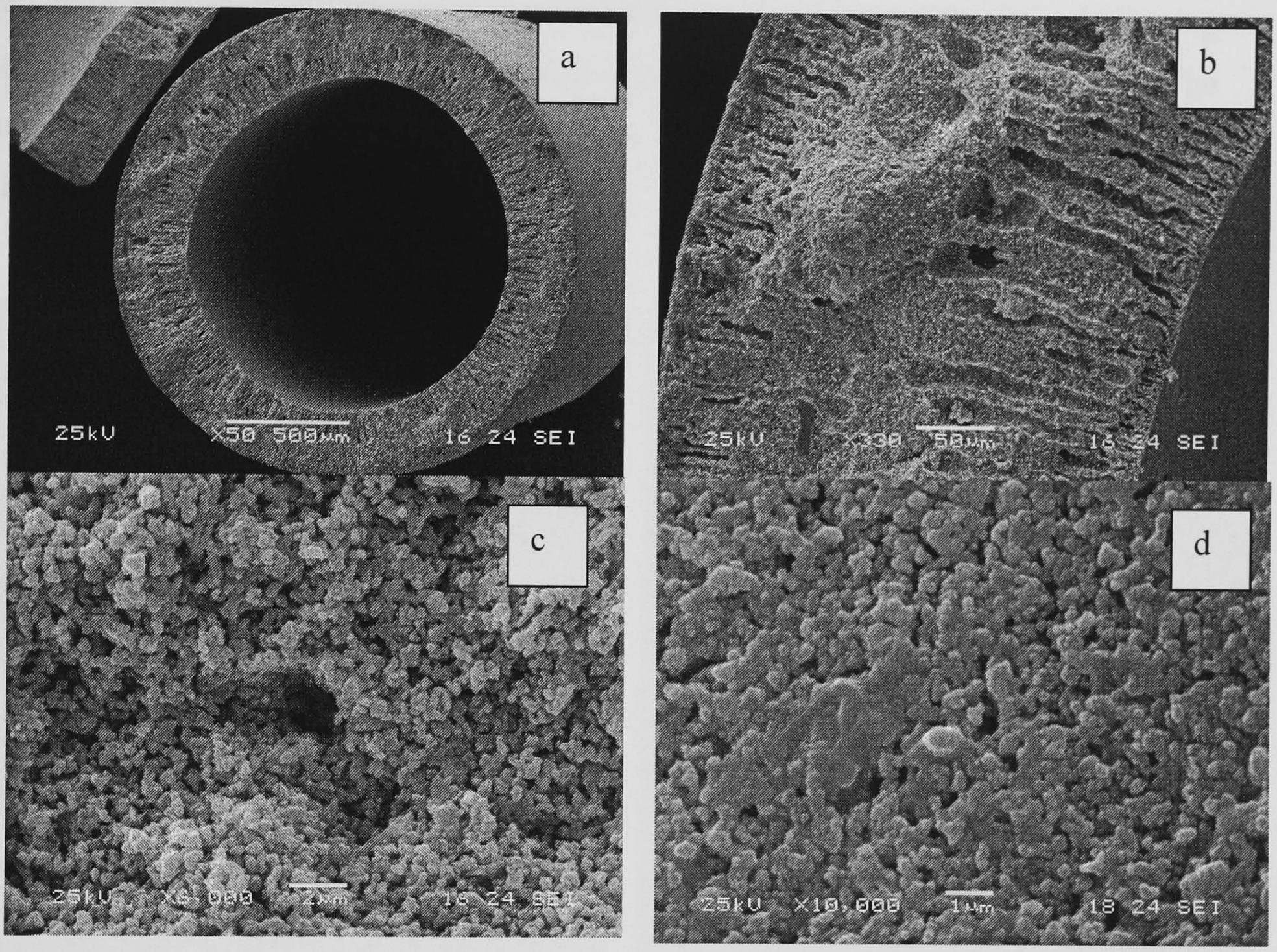


Fig. 6-3 SEM micrographs of the LSCF hollow fibre sintered at 1100°C.

Fig. 6-3 shows the micrographs of the hollow fibre membrane sintered at 1100°C. After sintering, shrinkage of the hollow fibres was observed. For example, the OD/ID of the fibres shrink from 2470/1720 μm to 1780/1310 μm, respectively, as measured from Fig. 6-3(a). Such shrinkage may be due to the removal of organic binder and the combining and sintering of the LSCF particles. However, for a certain type of ceramic membranes, the extent of the shrinkage is a function of multi-factor, such as the particle size and distribution of ceramic powders, the content of the polymer binder in the precursor as well as the sintering temperature, and thus beyond the scope of this study. The cross-sectional structure of the sintered fibre as shown in Fig. 6-3(b) is the

same as that of the fibre precursor, i.e. the sponge-like structure at centre is sandwiched by the short finger-like structures located at the outer and inner walls of the fibre. Fig. 6-3(c) and (d), which show the microstructures of the sponged layer and of the membrane surface respectively, indicate that the organic binders have been removed completely under this temperature. On the other hand, most particles keep their original form although the sintering has already occurred to a certain extent. Both the centre layer and the membrane surface possess the porous structures, indicating that the sintering temperature is not high enough to make the fibres gas-tight. The sintering process at higher temperatures was further conducted as discussed in the following section.

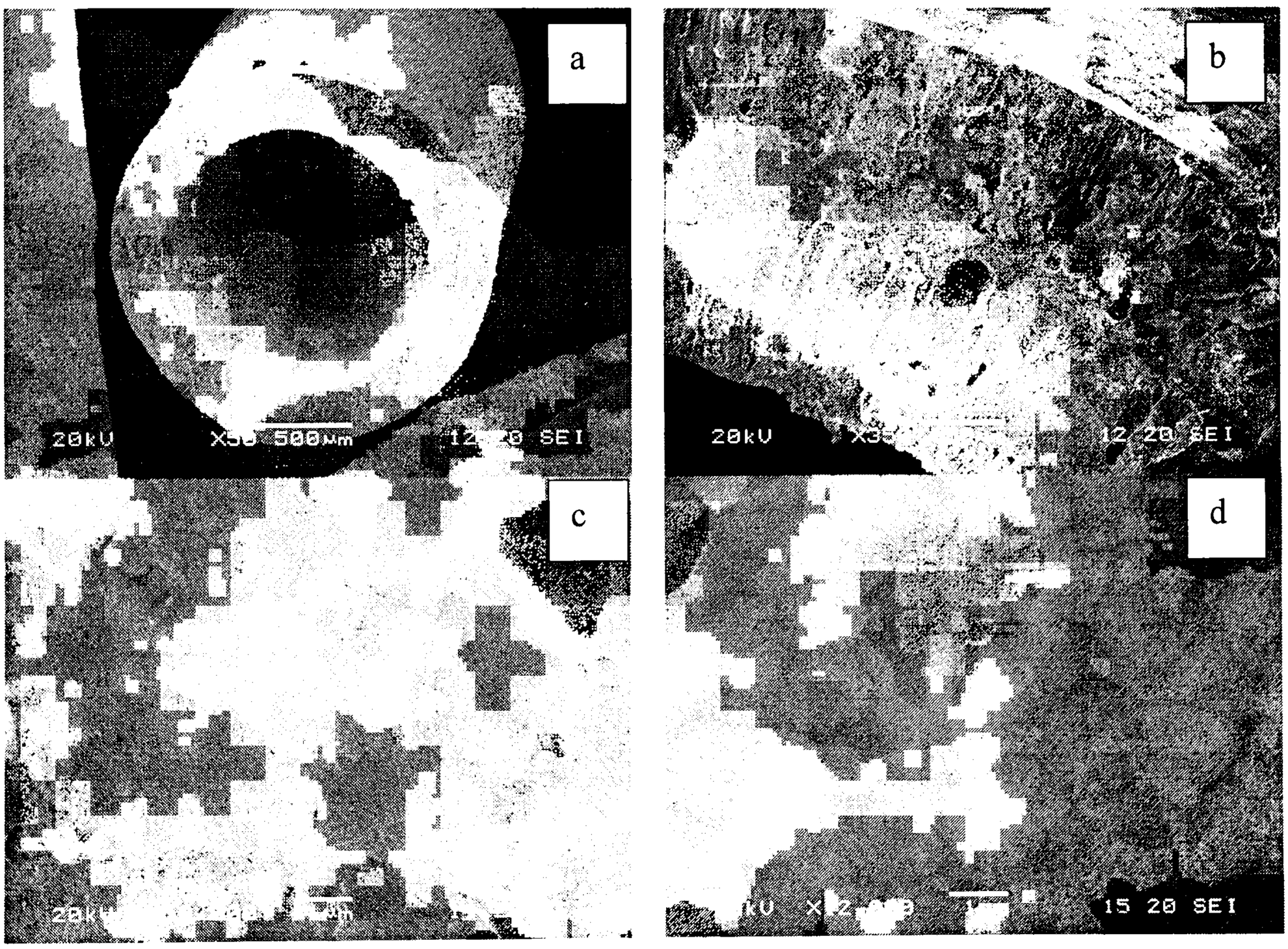


Fig. 6-4 SEM micrographs of the LSCF hollow fibre sintered at 1280°C.

Fig. 6-4 shows the micrographs of the hollow fibre membrane sintered at 1280°C. After sintering, the OD/ID of the fibres are further shrink from 1780/1310 μm to 1560/1120 μm, respectively, as shown in Fig. 6-4(a). Although the sandwiched structure of the sintered fibres still can be observed, as shown in Fig. 6-4(b), the

quantity and the size of the pores have greatly decreased after the sintering process. More importantly, all the LSCF particles at the membrane centre have been molten into an integrated body that is absolutely dense, as shown in Fig. 6-4(c). In fact, the hollow fibre membranes sintered under such a high temperature were proved to be completely gas-tight by means of the gas permeation test. Fig. 6-4 (d) shows the membrane surface. It can be seen that the LSCF particles are closely connected each other with the clear boundaries. Further, most particles are larger than 1 μm instead of the original size of around 0.3 μm, indicating that the particle growth has occurred during the sintering process, where the small discrete particles are combined into larger ones by the sintering.

The shrinkage of the hollow fibre membranes due to the sintering is summarized in Table 6-3. It indicates that the hollow fibres would shrink as much as 36.7±0.3% after being sintered at 1280 °C.

Table 6-3 Shrinkage of the LSCF hollow membranes after sintering.

Membrane	**Dimension of the LSCF hollow**		**Shrinkage %**
	OD (mm)	**ID (mm)**	
Precursor	2.47	1.72	
After sintered at 1100°C	1.78	1.31	27.5±0.2
After sintered at 1280°C	1.56	1.12	36.7±0.3

Fig. 6-5 compares the XRD patterns of the sintered membranes with the original LSCF powders. As can be seen, no changes are observed in the crystalline structure of the LSCF material due to the spinning and sintering processes after the hollow fibre membranes are formed. However, the intensity of the corresponding characteristic peaks for the hollow fibre membranes is much higher than that for the original LSCF powders. This further suggests that the crystallines in the membranes have become larger after sintering at high temperatures.

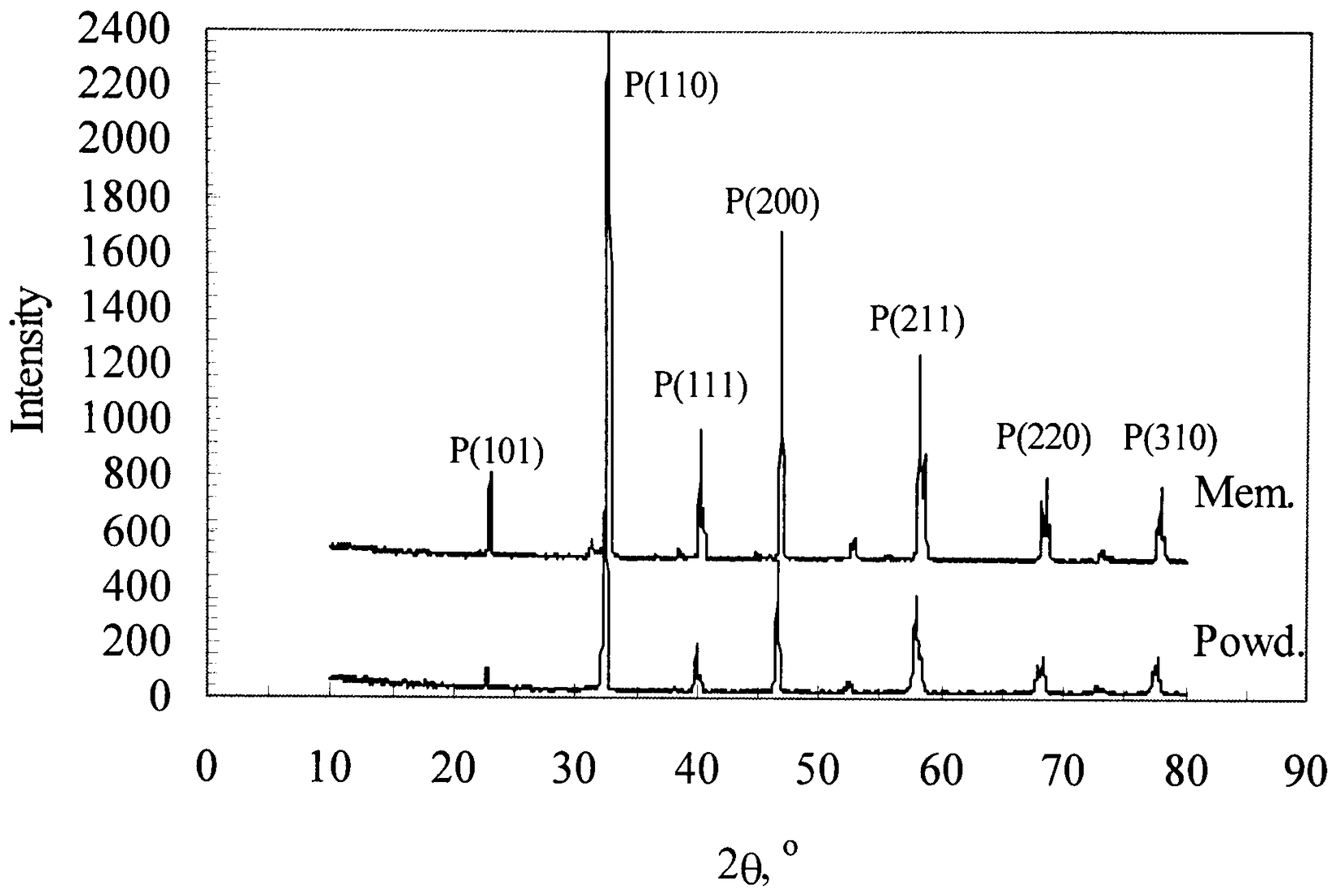


Fig. 6-5 XRD patterns of the LSCF powder and of the hollow fibre membrane.

6.3.2 Sealing at high temperatures

As generally understood, any leakage of air into the fibre lumen during the operation would lead to a questionable result. Therefore, sealing at high temperatures is one of the key challenges to be solved in the assembling of the hollow fibre membrane modules. In this study, five sealants have been tested with the results summarized in Table 6-1. It was found that all the sealants fail to seal the LSCF hollow fibres to the ceramic tubes at high temperatures (300~1000°C). Moreover, sealants C and E even react with the LSCF hollow fibre membrane at high temperatures, resulting in brittleness of the fibres, especially near the glued area. Sealant D possesses a good sealing effect at the temperature lower than 300 °C, but loses the sealing performance at higher temperatures. The sealant D remains inert to the hollow fibres at low temperatures (300 °C) at which the hollow fibre with the good mechanical strength is retained after it is glued. Based on the above experimental results, the sealant D was therefore selected to assemble the hollow fibre membrane module for oxygen permeation experiments. During the oxygen permeation study, care was always taken to ensure that the temperature at the sealing joints was kept below 300°C in order to prevent leakage at the sealing joints.

6.3.3 Oxygen permeation through the hollow fibre membrane

The effect of temperature on the oxygen permeation is shown in Fig. 6-6, where both the oxygen concentration in the downstream and the permeation flux are plotted while the sweep gas flow rate is kept constant, i.e., 32.4 cm^3/min. As can be seen, the oxygen permeation flux increases noticeably with increasing the temperature although the downstream oxygen partial pressure is also increased simultaneously. This means that the operating temperature plays a more important role in the oxygen permeation than the concentration driving force for the LSCF membranes. In addition, Fig. 6-6 also indicates that oxygen permeation flux in the LSCF membrane increases substantially after the temperature approaches to 700 °C due to order–disorder transition of the oxygen vacancy reported by Zeng (Zeng *et al.*, 1998) and Li and his coworkers (Li *et al.*, 2000).

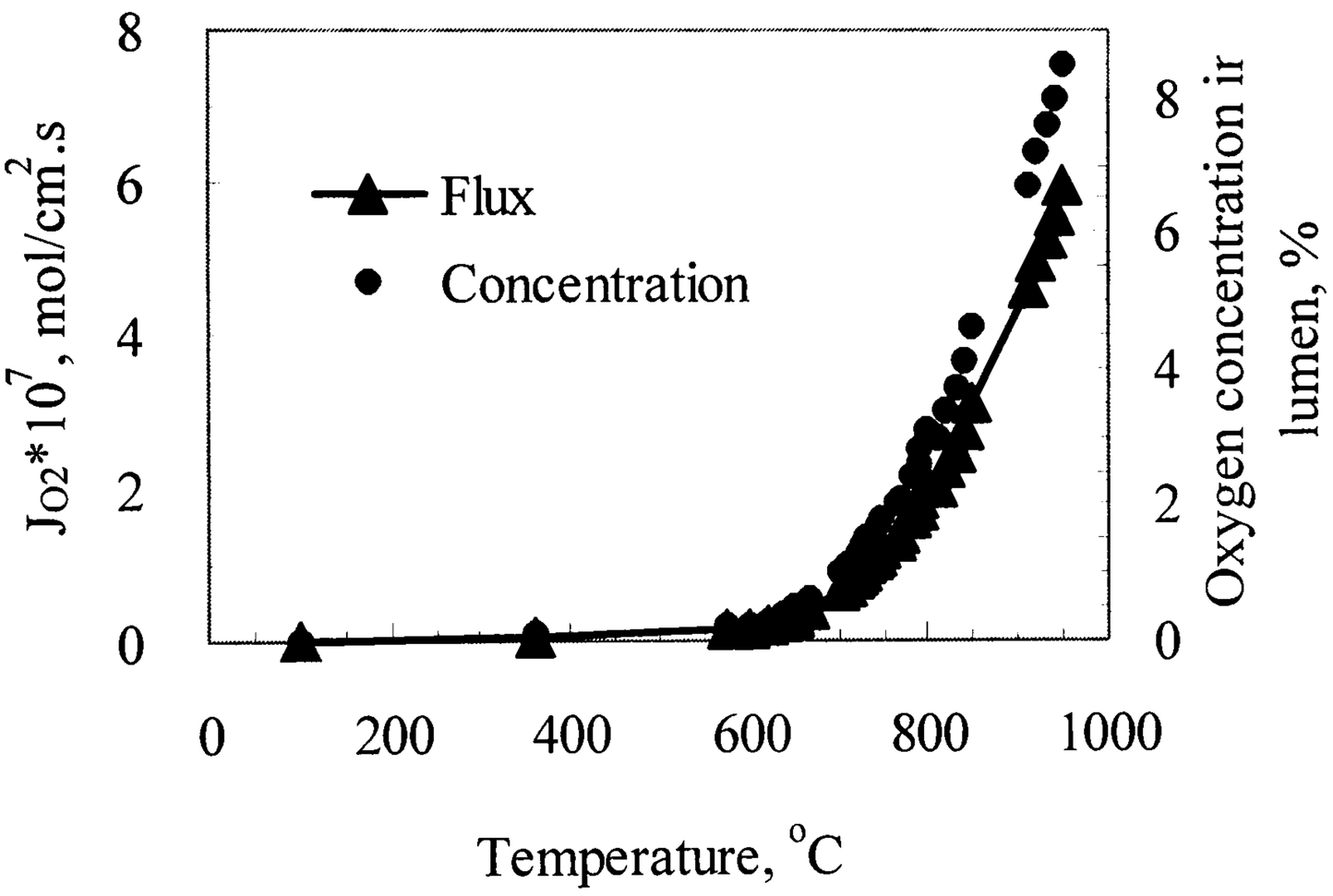


Fig. 6-6 Effect of temperature on the oxygen permeation (V_{Ar}=32.4 cm^3/min).

As the flow rate of sweep gas varies, the oxygen partial pressure on the downstream side (lumen) would be changed with the result of different oxygen permeation fluxes. Fig. 6-7 shows the experimental permeation data as a function of the downstream oxygen partial pressure at different temperatures while the oxygen partial pressure outside the membrane (upstream side) was kept constant (atmosphere) by continuously introducing the air. As is expected, the oxygen permeation flux generally decreases as increasing the downstream oxygen partial pressure since the driving force for oxygen permeation is decreased. However, if the downstream oxygen partial pressure is very

low, the value of the oxygen flux is dependent on the operating temperature and the oxygen permeation flux would slightly decrease even though the downstream oxygen partial pressure is decreased, especially at lower operating temperatures. This implies that the oxygen permeation in the LSCF hollow fibre membranes in this case follows the different mechanism, and should be further studied in the future. Fig. 6-7 also indicates that the oxygen permeation flux increases with increasing the temperature under the same oxygen partial pressure driving force. At the temperature of 900 °C, the oxygen permeation flux reaches 5.49×10^{-7} mol/cm^{2}s while the downstream oxygen partial pressure is 0.017 atm. This value is much higher than the oxygen permeation flux of 0.21 cm^3(STP)/cm^2 min (or 1.57×10^{-7} mol/cm^{2}s) through a LSCF tube membrane obtained at the same operating temperature and at the downstream oxygen partial pressure of 1×10^{-3} atm (Li *et al.*, 2000). Such an increase in the oxygen permeation flux is obviously resulted from the improved membrane design, i.e. better membrane surface morphology and reduced membrane thickness.

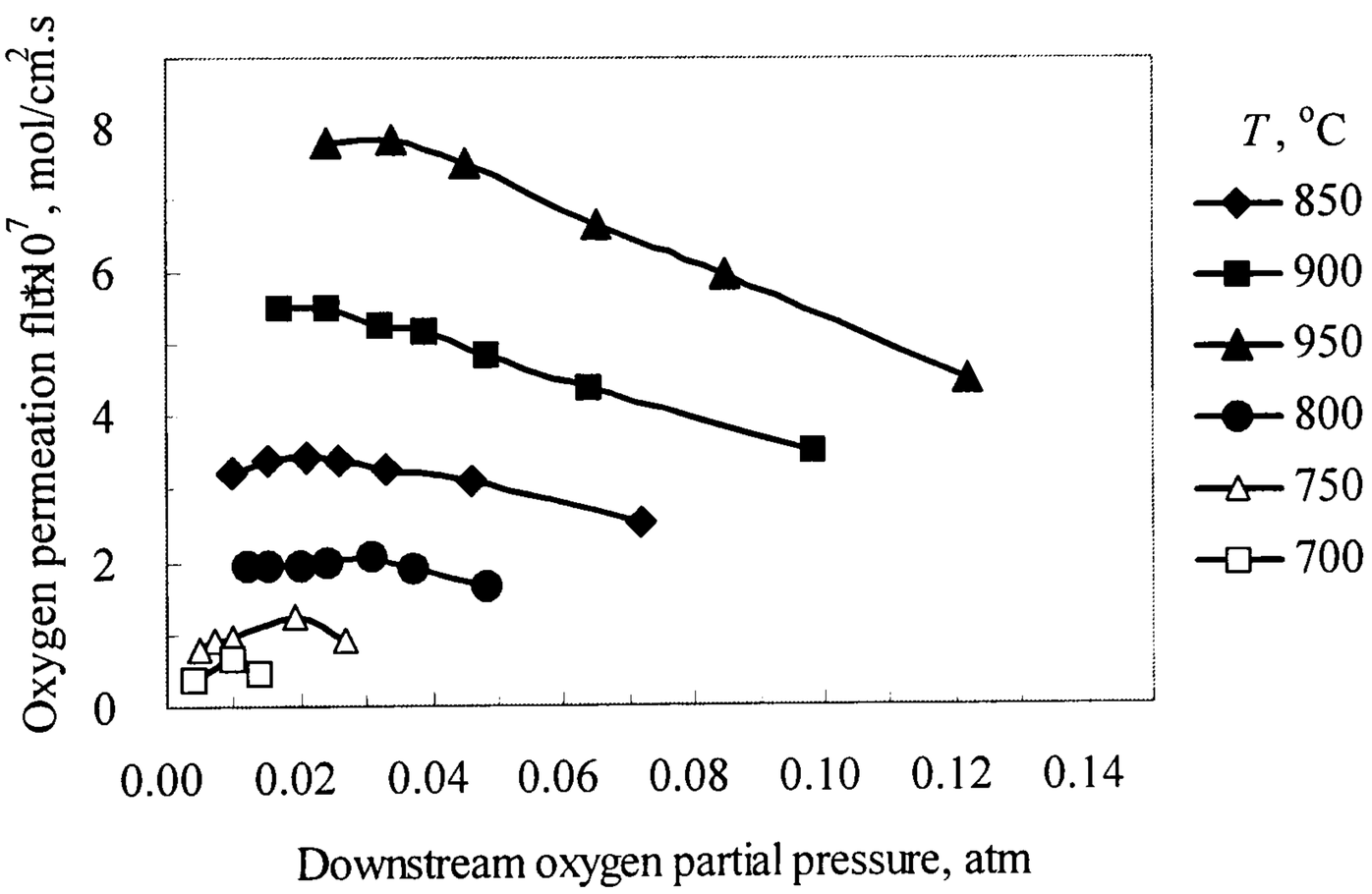


Fig. 6-7 Plot of oxygen flux against down stream oxygen partial pressure at different temperatures.

6.4 Conclusions

The gas tight $La_{0.6}Sr_{0.4}Co_{0.2}Fe_{0.8}O_{3-\alpha}$ (LSCF) hollow fibre membrane has been prepared successfully by a phase inversion/sintering technique. In order to obtain the dense hollow fibre membranes, the hollow fibre precursors, spun from the starting solution containing LSCF powder, PESf binder and PVP additive, must be sintered at temperature of 1280°C for 4 hrs. The operating temperature plays a more important role in oxygen permeation through the LSCF membranes than the concentration driving force. Once the operating temperature is over 700 °C, the oxygen permeation flux would increase sharply due to the order–disorder transition of oxygen vacancy. The oxygen permeation flux through the LSCF hollow membrane is, in general, higher than that through the LSCF disk-shaped or tubular membranes because of the decrease of the improved membrane design, i.e. better membrane surface morphology and reduced membrane thickness.

References

Dyer, P. N., R. E. Richards, S. L. Russek and D. M. Taylor (2000). Ion transport membrane technology for oxygen separation and syngas production, *Solid State Ionics*, **Vol.** 134, **pp.** 21-33.

Kharton, V. V., A. A. Yaremchenko, A. V. Kovalevsky, A. P. Viskup, E. N. Naumovich and P. F. Kerko (1999). Perovskite-type oxides for high-temperature oxygen separation membranes, *J. Membr. Sci.*, **Vol.** 163, **pp.** 307-317.

Li, S., W. Jin, P. Huang, N. Xu, J. Shi and Y. S. Lin (2000). Tubular lanthanum cobalitite perovskite type membrane for oxygen permeation, *J. Membr. Sci.*, **Vol.** 166, **pp.** 51-61.

Li, S., W. Jin, X. N. and J. Shi (1999). Synthesis and oxygen permeation properties of $La_{0.2}Sr_{0.8}Co_{0.2}Fe_{0.8}O_{3-\delta}$ membranes, *Solid State Ionics*, **Vol.** 124, **pp.** 161-170.

Liu, S., X. Tan, L. K. and R. Hughes (2001). Preparation and characterization of $SrCe_{0.95}Yb_{0.05}O_{2.975}$ hollow fibre membranes, *J. Membr. Sci.*, **Vol.** 193, **pp.** 249-260.

Lu, Y., A. G. Dixon, W. R. Moser, Y. Ma and U. Balachandran (2000). Oxygen-permeable dense membrane reactor for the oxidative coupling of methane, *J. Membr. Sci.*, **Vol.** 170, **pp.** 27-34.

Luyten, J., A. Buekenhoudt, W. Adriansens, J. Cooymans, H. Weyten, F. Servaes and R. Leysen (2000). Preparation of $LaSrCoFeO_{3-x}$ membranes, *Solid State Ionics*, **Vol.** 135, **pp.** 637-642.

Tan, X. and K. Li (2002). Modeling of air separation in a LSCF hollow-fiber membrane module, *AIChE J.*, **Vol.** 48, **pp.** 1469-1477.

Tan, X., S. Liu and K. Li (2001). Preparation and characterization of inorganic hollow fibre membranes, *J. Membr. Sci.*, **Vol.** 188, **pp.** 87-95.

Ullmann, H. and N. Trofimenko (1999). Composition, structure and transport properties of perovskite-type oxides, *Solid State Ionics*, **Vol.** 119, **pp.** 1-8.

Yaremchenko, A. A., V. V. Kharton, A. P. Viskup, E. N. Naumovich, V. N. Tikhonovich and N. M. Lapchuk (1999). Mixed electronic and ionic conductivity of $LaCo(M)O_3$ (M=Ga, Cr, Fe or Ni). V. Oxygen permeability of Mg-doped $La(Ga, Co)O_{3-\delta}$ perovskites, *Solid State Ionics*, **Vol.** 120, **pp.** 65-74.

Zeng, Y. and Y. S. Lin (1998). A transient TGA study on oxygen permeation properties of perovskite-type ceramic membrane, *Solid State Ionics*, **Vol.** 110, **pp.** 209-221.

Zeng, Y., L. Y.S. and S. L. Swartz (1998). Perovskite-type ceramic membrane: synthesis, oxygen permeation and membrane reactor performance for oxidative coupling of methane, *J. Membr. Sci.*, **Vol.** 150, **pp.** 87-98.

Chapter 7

Mixed conducting ceramic $La_{0.6}Sr_{0.4}Co_{0.2}Fe_{0.8}O_{3-\alpha}$ (LSCF) hollow fibre membrane for air separation

Abstract

Mixed conducting ceramic hollow fibre membranes which possess an asymmetric structure were prepared via a combined phase inversion and sintering technique where precursors of the hollow fibres were first spun using a polymer solution containing suspended LSCF powders and were then sintered at elevated temperature. By controlling weight ratio of the LSCF powder to the polymer binder, sintering temperature and time, the LSCF hollow fibres with gas-tight properties have been prepared and evaluated using an apparatus developed during the course of this chapter. Using the gas-tight LSCF hollow fibres, a membrane module was assembled for air separation. The performances of the module for air separation have been studied under various operating modes and at different temperatures and feed flow rates both experimentally and theoretically. The results reveal that the surface exchange reaction at the downstream side is much important than that at the upstream side, especially for lower operating temperatures. The porous inner surface of the prepared LSCF hollow fibre membranes favors considerably the oxygen permeation when air is fed in the shell side of the membrane module. At high operating temperatures, oxygen permeation can be enhanced by the countercurrent flow operation. Vacuum operation favors the oxygen permeation kinetically in the LSCF hollow fibre membrane modules.

Key words: Air separation; mixed conducting ceramic; hollow fibre membrane module; perovskite membrane

7.1 Introduction

It is generally believed that some perovskite ceramics such as $La_{1-x}Sr_xCo_{1-y}Fe_yO_{3-\alpha}$ (LSCF) exhibit a good mixed ionic-electronic conducting property (Kharton *et al.*, 1999; Li *et al.*, 1999; Ullmann and Trofimenko, 1999; Dyer *et al.*, 2000; Stefan and Herle, 2004). Dense membranes prepared from these ceramic materials show good oxygen permeation at elevated temperatures without need of external electrical loadings. Furthermore, since no species other than oxygen can be transferred through the membrane, the oxygen permselectivity is theoretically infinite. As a result, pure oxygen production can be achieved by heating such a ceramic membrane system (or called oxygen generator) where air is used as a feedstock. In order to develop the membrane system for industrial use, it is essential to improve not only the oxygen permeation flux of the membrane materials, but also the membrane systems, which are stable in harsh environments.

Many efforts have been made so far to improve oxygen permeation fluxes of perovskite membranes. Oxygen permeation through a dense perovskite membrane is controlled by the oxygen diffusion rate in the membrane as well as the surface oxygen exchange kinetics on either side of the membrane (Xu and Thomson, 1999; Stefan and Herle, 2004). Therefore, it is generally expected that the oxygen flux can be improved once the membrane thickness is reduced (Abrutis *et al.*, 2004) or the surface of the membrane is modified, i.e. application of porous catalytic layers on either or both sides of the membrane, leading to an enhancement of surface oxygen exchange kinetics (Lee *et al.*, 2002; Teraoka *et al.*, 2002; Lee *et al.*, 2003).

In addition, the membrane configuration such as flat sheet, tubular or hollow fibre also plays an important role in the overall ceramic membrane systems for air separation. In most previous studies, disc-shaped membranes with only a limited membrane area (<5 cm^2) were usually employed, as they are easily fabricated using conventional static-pressing methods. Although a multiple planar stack can be adopted to enlarge the membrane area to a plant scale, many problems such as high temperature sealing, connection and pressure-resistance have to be faced (Dyer *et al.*, 2000). Tubular perovskite membranes were developed to reduce the engineering difficulties, especially the problem associated with high temperature sealing (Li *et al.*, 2000; Wang

et al., 2004), but their small surface area/volume ratio and the high membrane thickness, which would lead to low oxygen permeation rates, make them unfavorable in practical applications.

Recently, hollow fibre ceramic membranes with an asymmetric structure have been prepared successfully using a phase inversion spinning/sintering technique (Luyten *et al.*, 2000; Liu *et al.*, 2001; Tan *et al.*, 2001). Compared to the disk-shaped membranes, such hollow fibre membranes posses much larger membrane area per unit volume for oxygen permeation. By adopting long hollow fibres and keeping the two sealing ends away from the high temperature zone, the problem of high temperature sealing no longer exists. Furthermore, due to the asymmetric structure (i.e. a thin separating dense layer integrated with porous layers on either side or both sides), the membrane's resistance to oxygen permeation is very much reduced compared to the symmetric membranes prepared by the conventional methods. In addition, the integrated porous layers on either side or both sides of the membrane also provide much larger gas-membrane interfaces for oxygen exchange reactions, leading to an enhancement of surface oxygen exchange kinetics and thus the improved oxygen permeation rate. All these advantages of the ceramic membrane in asymmetric and hollow fibre configurations would, in a foreseeable future, put the perovskite mixed conducting membranes into commercial applications.

In this chapter, LSCF hollow fibre membranes have been prepared via a combined phase inversion spinning/sintering technique. A membrane module consisting 6 dense LSCF hollow fibres has been fabricated for air separation. The performances of the membrane module for air separation at different operating modes, operating temperatures and feed flow rates have also been investigated both experimentally and theoretically.

7.2 Experimental

7.2.1 Gas-tightness of the hollow fibre membranes

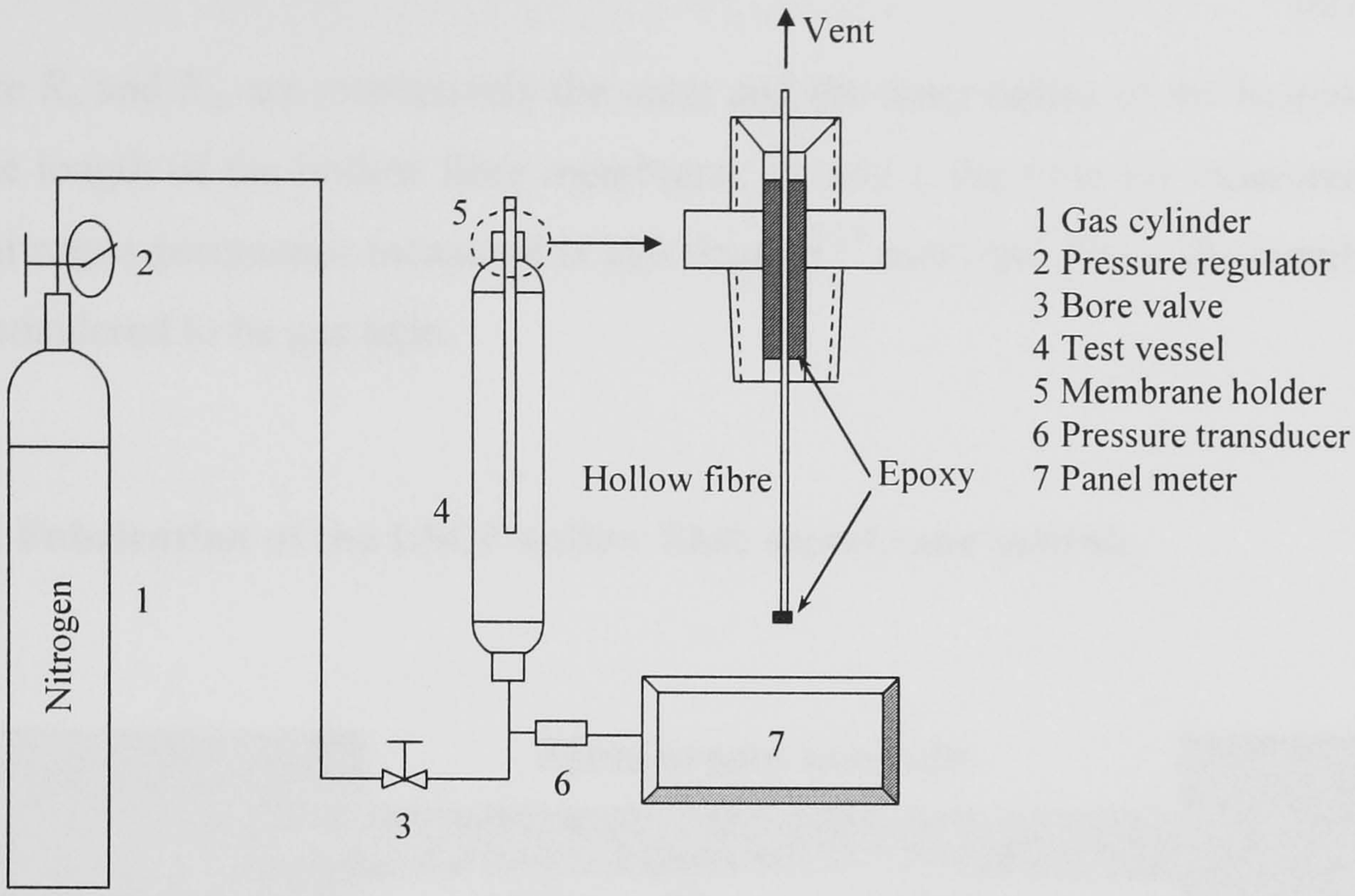


Fig. 7-1 Experimental setup for gas-tightness test.

The preparation of the LSCF hollow fibre membranes had been discussed in the Chapter 6. The LSCF hollow fibre membranes for air separation were same as used for oxygen permeation test in Chapter 6. Gas-tightness of the prepared hollow fibre membranes was tested using a gas permeation apparatus as shown schematically in Fig. 7-1. The hollow fibre membrane for the test was glued onto a stainless steel sample holder with an epoxy resin (UKR-135 resin with UKH-136 hardener, supplied by UK Epoxy Resins). It was then assembled into a cylinder with a volume capacity of 500 cm^3). Nitrogen was used as a test gas. The pressure change with time of the cylinder was measured with a pressure transducer (Model PX300-050GV, from Omega Inc) attached to the test cylinder and was recorded through a panel meter (Model DP25B-S, supplied by Omega Inc). The gas permeance is, thus, obtained based on the cylinder pressure change with time:

$$P = \frac{V}{RT \cdot A_m t} \ln\left(\frac{p_0 - p_a}{p_t - p_a}\right) \tag{7-1}$$

where P is the permeance of the test membrane, mol/m^2.s.Pa; V, the volume of the test cylinder m^3; R, gas constant, 8.314 J/mol.K; and T, the measured temperature, K. p_0 and p_t are the initial and final measured pressures in test cylinder, Pa; p_a, the atmospheric pressure, Pa. A_m (m^2) is the membrane area, i.e. $A_m = \frac{2\pi(R_o - R_{in})L}{\ln(R_o / R_{in})}$

where R_o and R_{in} are respectively the outer and the inner radius of the hollow fibre, m; L, the length of the hollow fibre membrane, m; and t, the time for measurement, s. If the nitrogen permeance measured is less than 10^{-14} mol/(cm^2.Pa.s), the membrane may be considered to be gas tight.

7.2.2 Fabrication of the LSCF hollow fibre membrane module

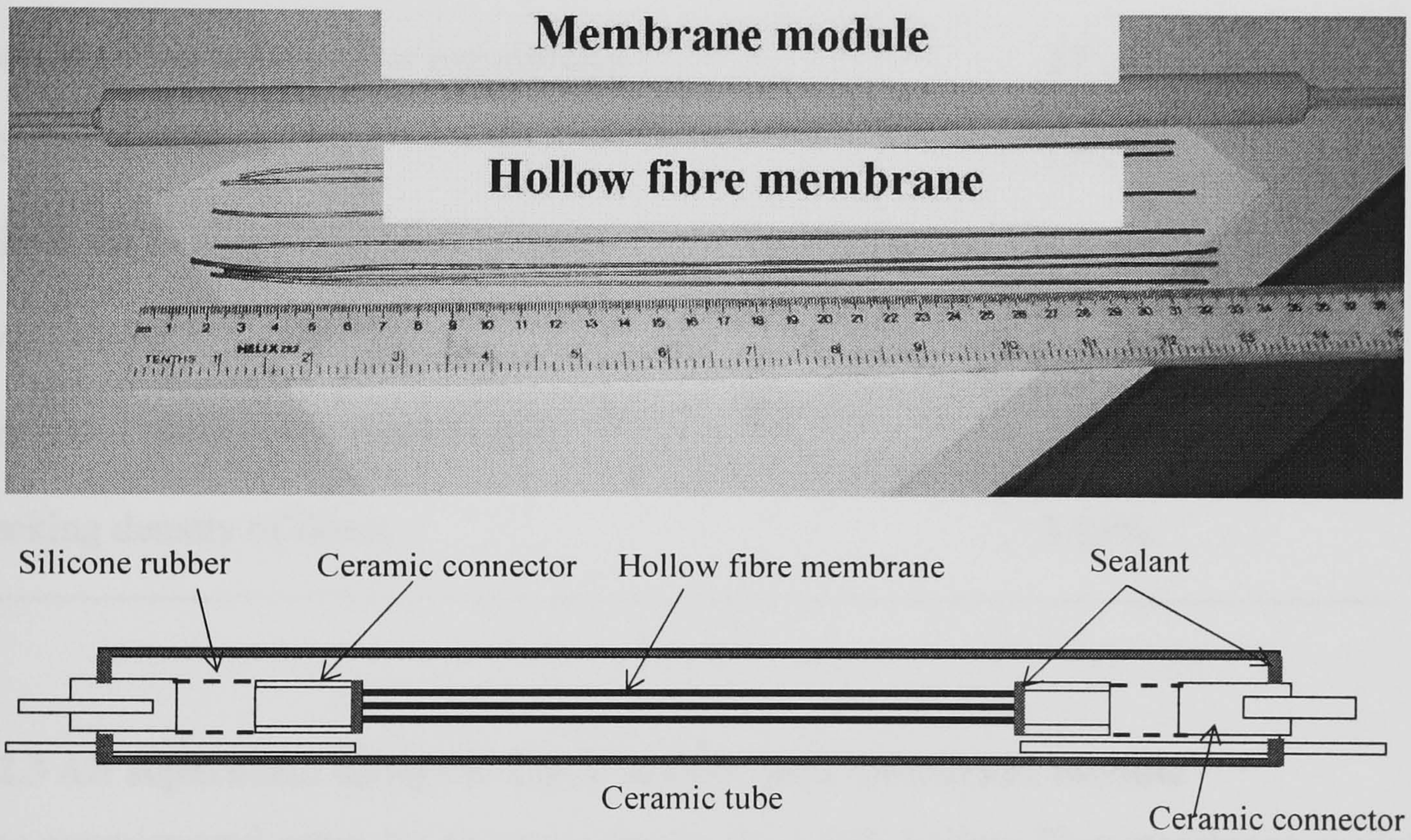


Fig. 7-2 Configuration of the LSCF hollow fibre membrane module.

Although problems of high temperature sealing can be avoided using a long hollow fibre membrane (Liu *et al.*, 2001), the thermal expansion of the fibres must also be taken into consideration. It was found that the LSCF hollow fibre membrane would break into pieces at temperatures above 500°C if both ends of the fibre were fixed with the module shell. Therefore, in this work, soft silicone rubber tubes were used to offset the thermal expansion of the hollow fibre membranes. Fig. 7-2 shows schematically

the characteristics of the prepared membrane module as well as the LSCF hollow fibres. As can be seen in Fig. 7-2, two ends of the LSCF hollow fibre membranes were indirectly glued onto the module shell via flexible silicone rubber tubes and ceramic connectors. The sealant used for the module is the high temperature resistant adhesive named 'Light' supplied by FortaFix Inc. Values of the characteristic parameters of the prepared LSFC hollow fibre membrane module are given in Table 7-1.

Table 7-1 Properties of the hollow fibre membrane module.

Item	**Parameter**
OD of the hollow fibre membranes	1.46 mm
ID of the hollow fibre membranes	1.14 mm
Number of the hollow fiber membranes	6
Length of the hollow fiber membranes	27 cm
ID of the alumina tube	1.4 cm
OD of the alumina tube	1.8 cm
Total length of the module	40 cm
Length of the silicone rubber tube	4.0 cm
Packing density of fibres	3.95%

7.2.3 Air separation using the LSCF hollow fibre membrane module

The experimental setup for air separation in the LSCF hollow fibre membrane module is shown in Fig. 7-3. The membrane module was placed in a CARBOLITE tubular furnace with the length of 15 cm. Thus, the sealing joints were kept 6 cm away from the inlet of the furnace tube. Before experiments, the temperature profile within the module (inside the alumina tube) was measured using a type C thermocouple with a thermometer supplied by Omega Engineering Inc. The feed gas flow rates were controlled and measured using a mass flow controller (Smart Mass Flow meter with Read out & Control Electronics Model 0152, Brooks Instrument). Argon was used as a sweep gas and was introduced either in the shell side (lumen-feed mode) or in the fibre

lumen (shell-feed mode). In the vacuum operation, a self-cleaning dry vacuum system (Model 2025, from Welch Inc.) was applied to the fibre lumen while the air stream was flowing through the shell side. Oxygen concentrations in both the air stream and the argon stream effluents were measured online using an oxygen meter (Oxygen Analyser 572, Servomex). The overall oxygen permeation rate is calculated from the concentration changes of oxygen in the argon stream or in the air stream:

$$N_t = \frac{F_{Ar} y_e}{(1 - y_e)} \text{ from the argon stream} \tag{7-2a}$$

or

$$N_t = \frac{F_{Air}(0.21 - x_e)}{(1 - x_e)} \text{ from the air stream} \tag{7-2b}$$

where F is the feed gas flow rate, mol/s; x_e and y_e are, respectively, oxygen concentrations in the air or in the argon effluents.

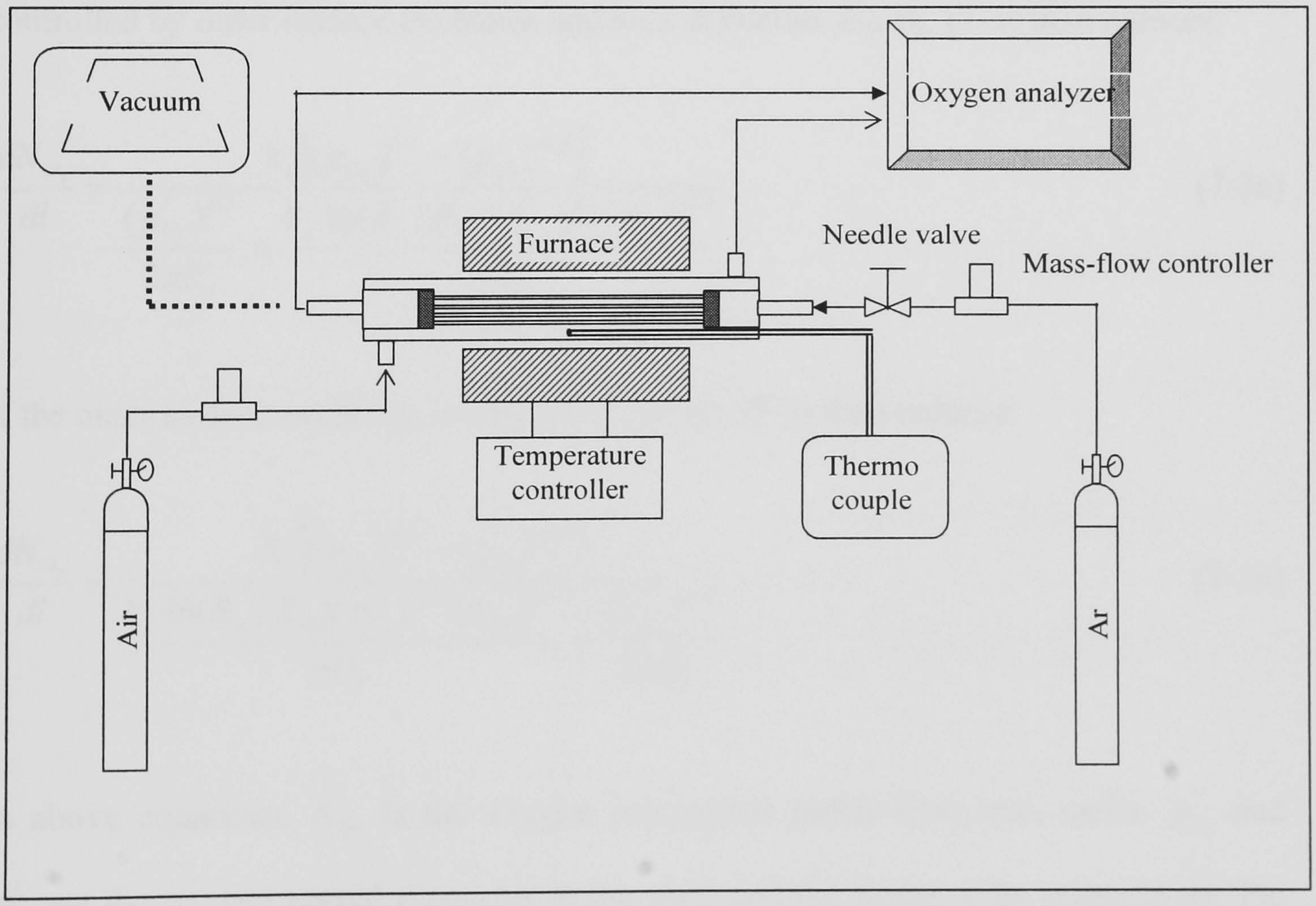


Fig. 7-3 Experimental setup for air separation.

7.3 Theory description

7.3.1 Oxygen permeation rate through a hollow fibre membrane

Oxygen permeation through a mixed ionic-electronic conducting perovskite membrane may not be controlled by the oxygen diffusion rate (or the diffusion rate of oxygen vacancy) in the membrane, but also the surface oxygen exchange kinetics on both sides of the membrane (Xu and Thomson, 1999; Stefan and Herle, 2004). The local oxygen permeation rate through a hollow fibre (or tubular) membrane can be given as (Tan and Li, 2002):

$$\frac{dN_{O_2}}{dl} = \frac{k_r\left[(p_{O_2}^{'})^{0.5} - (p_{O_2}^{''})^{0.5}\right]}{\frac{(p_{O_2}^{''})^{0.5}}{2\pi R_o} + \frac{k_f \ln(R_o / R_{in})(p_{O_2}^{'})^{0.5}(p_{O_2}^{''})^{0.5}}{\pi D_V} + \frac{(p_{O_2}^{'})^{0.5}}{2\pi R_{in}}} \tag{7-3}$$

It can be seen that the total permeation resistance is consisted of three parts: exchange reaction at outer membrane surface (shell side), bulk diffusion and exchange reaction at inner membrane surface (lumen side). The above equation can be simplified if one or two steps of the resistances are negligible. For example, if the oxygen permeation is controlled by outer surface exchange and bulk diffusion, the eq. (7-3) then reduces:

$$\frac{dN_{O_2}}{dl} = \frac{k_r\left[(p_{O_2}^{'})^{0.5} - (p_{O_2}^{''})^{0.5}\right]}{\frac{(p_{O_2}^{''})^{0.5}}{2\pi R_o} + \frac{k_f \ln(R_o / R_{in})(p_{O_2}^{'})^{0.5}(p_{O_2}^{''})^{0.5}}{\pi D_V}} \tag{7-3a}$$

If the outer surface exchange is negligible, the eq. (7-3) then reduces:

$$\frac{dN_{O_2}}{dl} = \frac{k_r\left[(p_{O_2}^{'})^{0.5} - (p_{O_2}^{''})^{0.5}\right]}{\frac{k_f \ln(R_o / R_{in})(p_{O_2}^{'})^{0.5}(p_{O_2}^{''})^{0.5}}{\pi D_V} + \frac{(p_{O_2}^{'})^{0.5}}{2\pi R_{in}}} \tag{7-3b}$$

In above equations, N_{O_2} is the oxygen permeation molar flow rate, mol/s. $p_{O_2}^{'}$ and $p_{O_2}^{''}$ are the oxygen partial pressures in the shell and the lumen side, respectively, Pa;

D_V, the diffusion coefficient of oxygen vacancy, m^2/s. k_f and k_r are, respectively, the forward and the reverse reaction rate constants for the surface exchange reaction:

$$\frac{1}{2}O_2 + V_O^{\cdot\cdot} \xleftrightarrow{k_f / k_r} O_O^x + 2h^{\cdot} \tag{7-4}$$

where the charged defects are defined using the Kröger-Vink notation. That is, $O_O^{\times}$ stands for lattice oxygen, $V_O^{\bullet\bullet}$ for oxygen vacancy and $h_i^{\bullet}$ for electron hole.

It should be noted that eq. (7-3) is suitable for both the shell-feed and the lumen-feed operating modes. In the lumen-feed operation, the local oxygen permeation rate is negative, which means oxygen permeates from lumen to shell.

7.3.2 Models for air separation in a hollow fibre membrane module

Models for air separation in a membrane module consisting of *m* LSCF hollow fibres are developed below, which depend on the practical operating modes as schematically illustrated in Fig. 7-4.

In the formulation of mathematical models, following general assumptions have been made:

(1) The mass transfer resistance in gas phase is negligible.
(2) Gas streams in the shell side and in the lumen are both plug flow. Besides, the axial dispersion is negligible.
(3) The transfer of charged defects (oxygen vacancy and electron) in the membrane occurs only in the radial direction of the membrane.
(4) Both the diffusion coefficient of oxygen vacancy and the surface exchange rate constants are independent of oxygen partial pressures.
(5) Ideal gas law is applicable to describe the gas behavior of both single component and gas mixture.
(6) The operation runs at steady state.

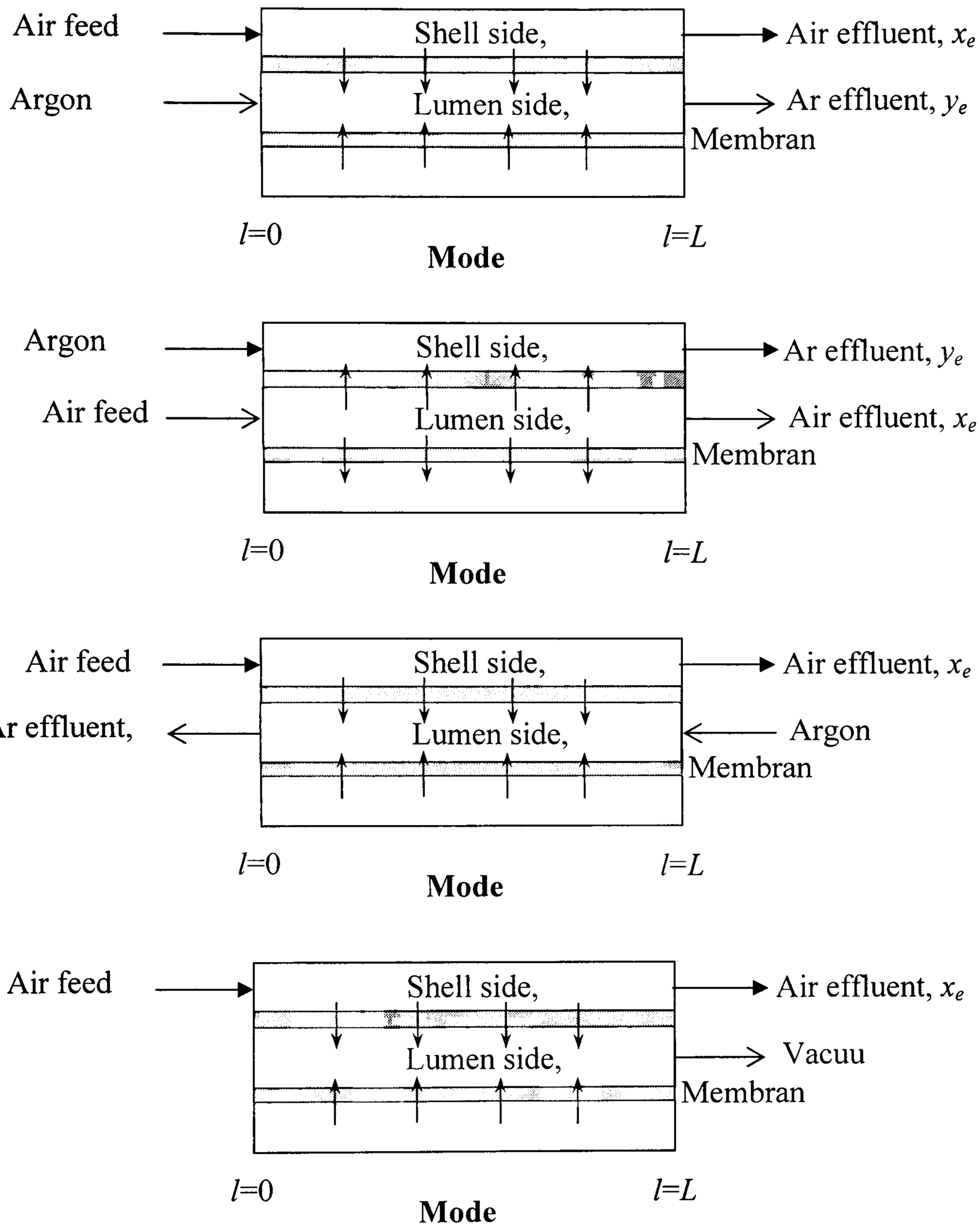


Fig. 7-4 Operating modes of the membrane module for air separation.

Mode 1: Shell- feed, cocurrent flow operation

In this operating mode, air is introduced into the shell side of the module, while argon is cocurrently fed into the fibre lumen. The material balance equations for the shell and lumen gas streams are given, respectively, as:

Shell side for oxygen:
$$\frac{d}{dl}\left(\frac{p'_{O_2}\upsilon_s}{RT}\right) = -m\frac{dN_{O_2}}{dl} \tag{7-5a}$$

Shell side for nitrogen:
$$\frac{(p_s - p'_{O_2})\upsilon_s}{RT} = 0.79F_{Air} \tag{7-5b}$$

Lumen side for oxygen: $$\frac{d}{dl}\left(\frac{p_{O_2}^{''}\upsilon_l}{RT}\right) = m\frac{dN_{O_2}}{dl} \tag{7-6a}$$

Lumen side for argon: $$\frac{(p_l - p_{O_2}^{''})\upsilon_l}{RT} = F_{Ar} \tag{7-6b}$$

The boundary conditions are:

$$l = 0, \quad p_{O_2}^{'} = 0.21p_a, \quad p_{O_2}^{''} = 0 \tag{7-7}$$

where υ_l and υ_s are the volumetric flow rates of the lumen and the shell gas streams, respectively, m^3/s. p_l and p_s are respectively the pressures in the fibre lumen and the shell side, and equal to atmosphere pressure, i.e., 1.013×10^5 Pa.

Mode 2: lumen-feed, cocurrent flow operation

This operating mode shows that air is introduced into the fibre lumen while argon flows cocurrently in the shell side of the module.

Shell side for oxygen: $$\frac{d}{dl}\left(\frac{p_{O_2}^{'}\upsilon_s}{RT}\right) = -m\frac{dN_{O_2}}{dl} \tag{7-8a}$$

Shell side for argon: $$\frac{(p_s - p_{O_2}^{'})\upsilon_s}{RT} = F_{Ar} \tag{7-8b}$$

Lumen side for oxygen: $$\frac{d}{dl}\left(\frac{p_{O_2}^{''}\upsilon_l}{RT}\right) = m\frac{dN_{O_2}}{dl} \tag{7-9a}$$

Lumen side for nitrogen: $$\frac{(p_l - p_{O_2}^{''})\upsilon_l}{RT} = 0.79F_{Air} \tag{7-9b}$$

with the boundary conditions:

$$l = 0, \quad p_{O_2}^{'} = 0, \quad p_{O_2}^{''} = 0.21 p_a \tag{7-10}$$

Mode 3: shell- feed, countercurrent flow operation

In this operating mode, air is introduced into the shell side of the module while argon is fed into the fibre lumen from the opposite end of the feed air inlet. The governing equations for this operation are:

Shell side for oxygen:
$$\frac{d}{dl}\left(\frac{p_{O_2}^{'} \upsilon_s}{RT}\right) = -m\frac{dN_{O_2}}{dl} \tag{7-11a}$$

Shell side for nitrogen:
$$\frac{(p_s - p_{O_2}^{'})\upsilon_s}{RT} = 0.79 F_{Air} \tag{7-11b}$$

Lumen side for oxygen:
$$\frac{d}{dl}\left(\frac{p_{O_2}^{''} \upsilon_l}{RT}\right) = -m\frac{dN_{O_2}}{dl} \tag{7-12a}$$

Lumen side for argon:
$$\frac{(p_l - p_{O_2}^{''})\upsilon_l}{RT} = F_{Ar} \tag{7-12b}$$

with the boundary conditions:

$$l = 0, \quad p_{O_2}^{'} = 0.21 p_a; \quad l = L, \quad p_{O_2}^{''} = 0 \tag{7-13}$$

where L is the membrane's length in the furnace tube, m.

Mode 4: shell- feed, cocurrent flow with vacuum operation

In this operation, air flows in the shell side of the module while a vacuum is applied to the fibre lumen side at the same end of the module as the air effluent outlet. The mass conservation equations on the shell side are:

Shell side for oxygen:
$$\frac{d}{dl}\left(\frac{p_{O_2}^{'} \upsilon_s}{RT}\right) = -m\frac{dN_{O_2}}{dl} \tag{7-14a}$$

Shell side for nitrogen: $$\frac{(p_s - p_{O_2}^{'})\upsilon_s}{RT} = 0.79F_{Air} \tag{7-14b}$$

On the lumen side, the gas stream is pure oxygen:

$$\frac{d}{dl}\left(\frac{p_{O_2}^{''}\upsilon_l}{RT}\right) = m\frac{dN_{O_2}}{dl} \tag{7-15}$$

For vacuum operation, pressure drop may occur in the fibre lumen. Hagen-Poiseuille equation can be used to describe the oxygen pressure profile in the lumen for laminar flow:

$$\frac{dp_{O_2}^{''}}{dl} = -\frac{8\mu\upsilon_l}{m\pi R_{in}^4} \tag{7-16}$$

The boundary conditions are:

$$l = 0, \quad p_{O_2}^{'} = 0.21p_a, \quad \upsilon_l = 0; \quad l = L, \quad p_{O_2}^{''} = p_v \tag{7-17}$$

where μ is the viscosity of oxygen, Pa.s; p_v is the operating vacuum level (absolute pressure), Pa.

As can be seen, the governing equations for each operating mode are a group of ordinary differential equations, and thus can be solved numerically using the Runge-Kutta method.

7.4 Results and discussion

7.4.1 Gas-tightness of the hollow fibre membranes

As is known, the perovskite membranes for oxygen permeation must be gas-tight without any defects. The gas-tightness test was conducted for all the hollow fibres in the membrane module. Fig. 7-5 illustrates typical results of one of the hollow fibres, where the pressure in the test cylinder is plotted against the time. The gas permeance of the fibre was calculated according to eq. (7-1) and was found to be 2.82×10^{-14} mol/(cm^2.Pa.s). This value is much lower than the oxygen permeability through the hollow fibres at elevated temperatures (2.2×10^{-8} mol/(cm^2.Pa.s))at 800 ^{o}C, which is described in detail in the following section). It should be noted that a slight decrease in pressure in the test cylinder is not only due to the negligible gas permeation through the membrane, but also the possible leak from joints of the system. Therefore, the actual permeance value of the fibre is even lower than the above-calculated result and the hollow fibre of the membrane module is, thus, considered to be gas-tight.

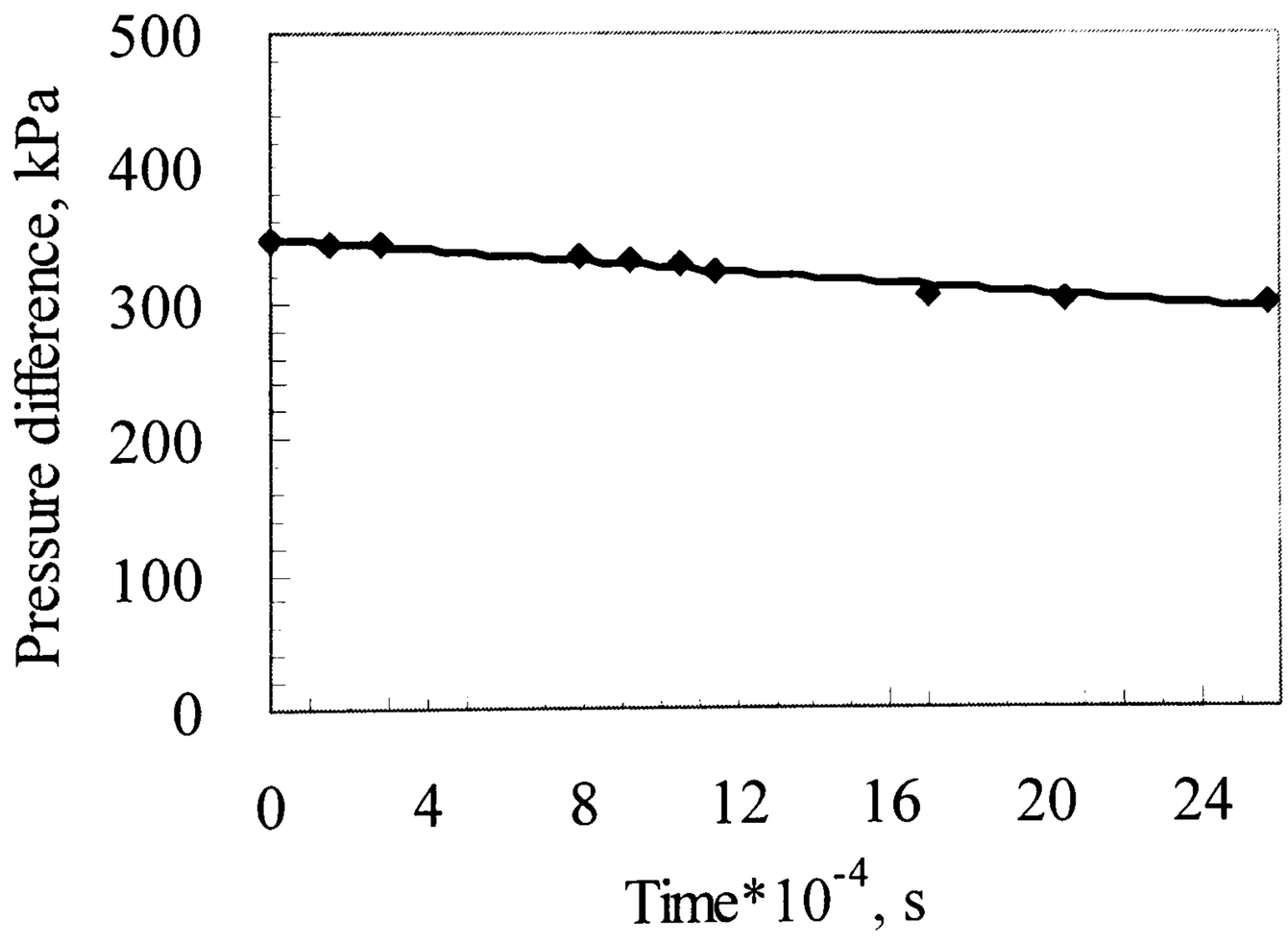


Fig. 7-5 Pressure change with time in the gas-tightness test of hollow fibre membranes.

7.4.2 Temperature profile in the membrane module

The temperature uniform zone of the furnace given by the manufacture is only 4 cm in length. However, the actual length of the hollow fibre membranes for oxygen permeation should be different depending on the temperature settings. Since any parts of the hollow fibre membranes where the temperature is high enough are able to make the contribution to oxygen permeation, it is necessary to know the real temperature profile in the membrane module so as to analyse the experimental data accurately. Fig. 7-6 illustrates the temperature profile of the furnace at a given temperature. It can be seen that the actual temperature in the temperature uniform zone for air separation is lower than the setting value because of the insulation effect of ceramic tube. By the least-square regression, a correlation is obtained with the R^2 value of 0.998:

$$T = -(0.0086T_s + 2.5621)\cdot l^2 + (0.1201T_s + 43.46)\cdot l + (0.5854T_s - 205.59) + 273 \tag{7-18}$$

where T_s is the setting value, respectively, ^{o}C.

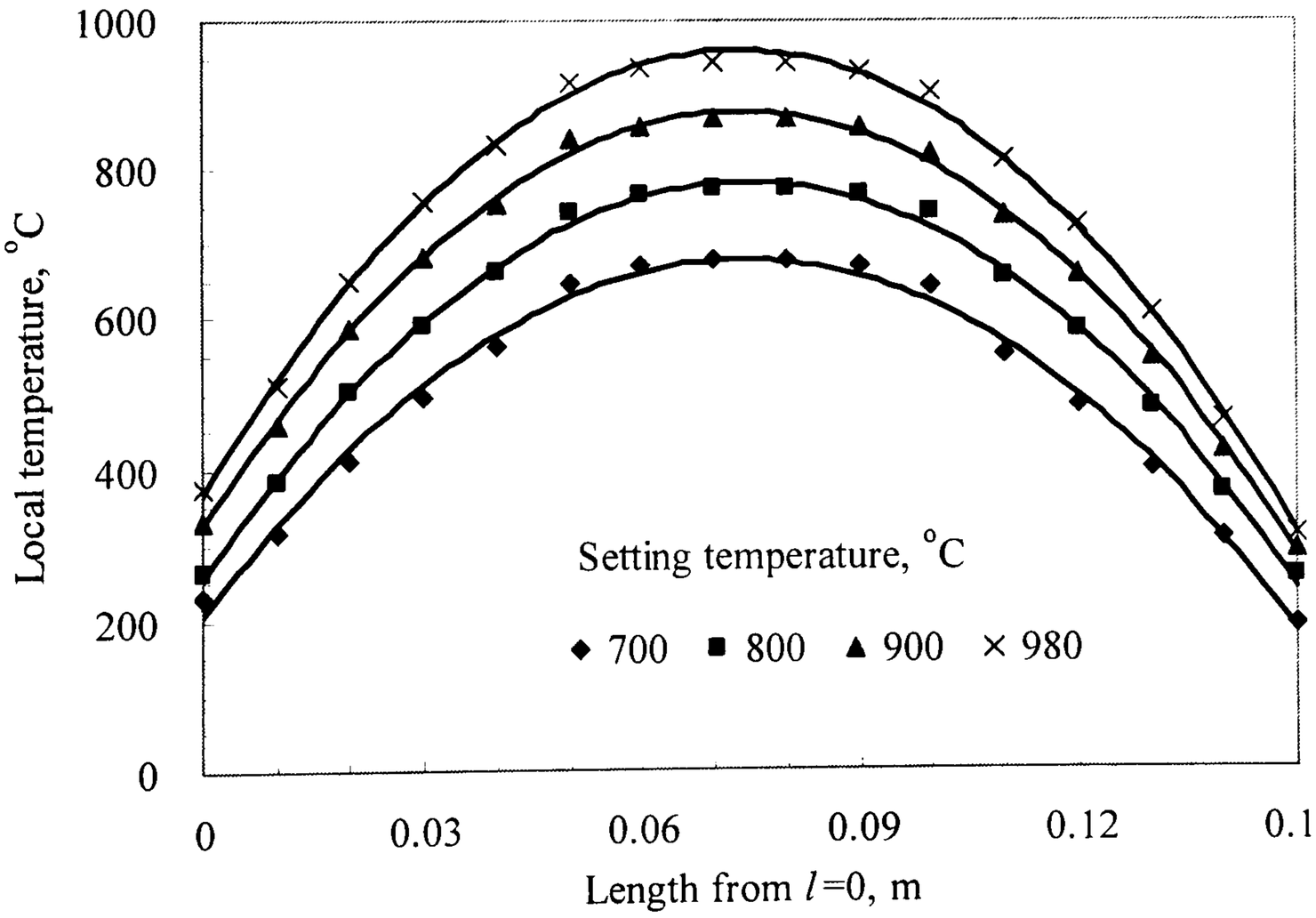


Fig. 7-6 Temperature profile in the membrane module.

Obviously, the higher the setting temperature, the larger the membrane area provided for oxygen permeation in the module. In the following simulations, the temperature

profile or eq. (7-18) is incorporated in the modeling equations. However, for illustration purpose, the furnace setting temperature will be depicted in the subsequent figures.

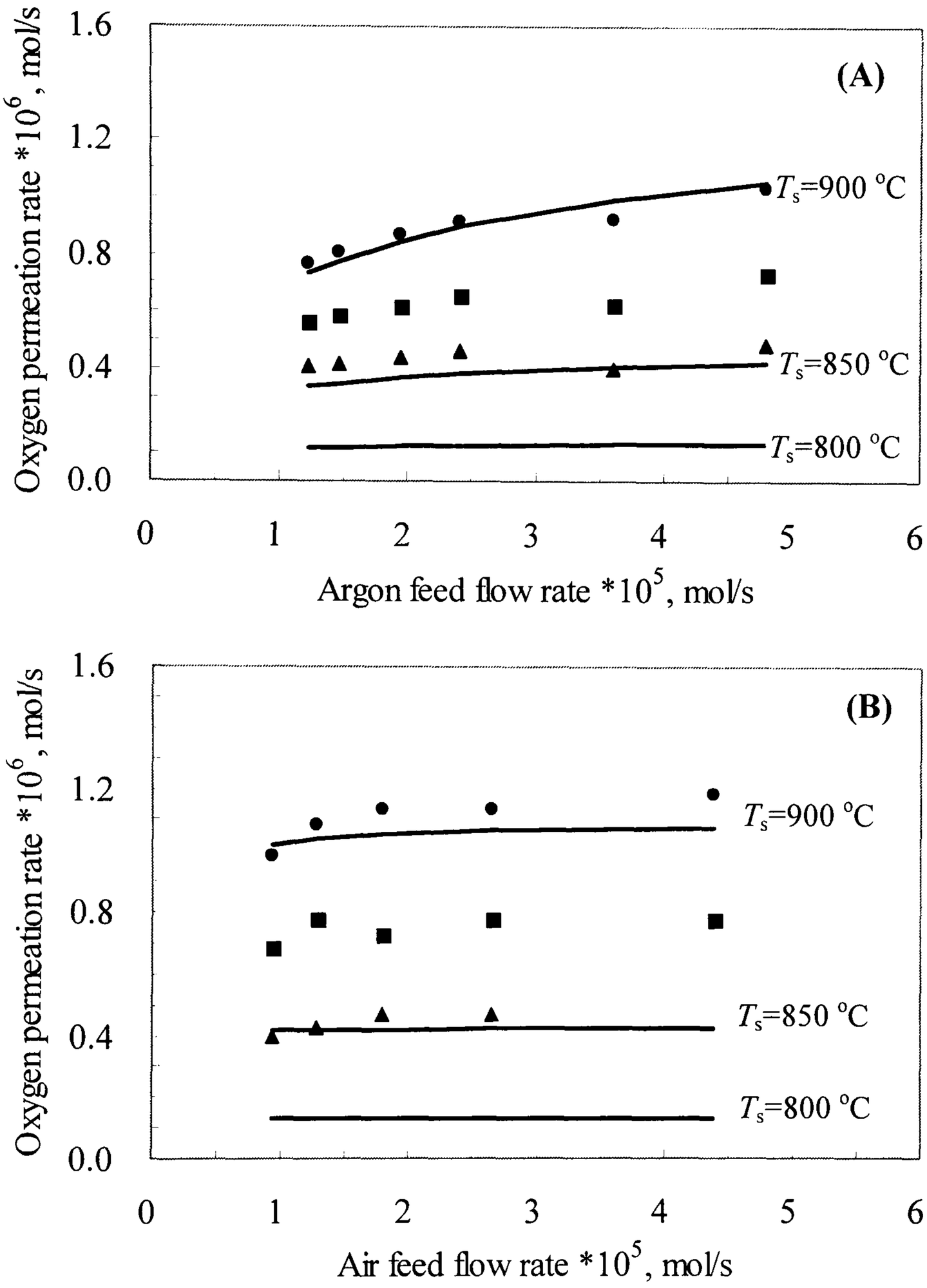


Fig. 7-7 Oxygen permeation rate as a function of the gas flow rate for the shell-feed and cocurrent operating mode (A) Air feed flow rate is constant; (B) Argon feed flow rate is constant (Experimental data: ▲800°C, ■ 850°C, ● 900°C).

7.4.3 Air separation results

Fig. 7-7 shows the experimental and theoretical results for the shell-feed and cocurrent flow operation where the oxygen permeation rate is plotted against the argon or air flow rates at different operating temperatures. In Fig. 7-7(A), the effect of argon flow

rate on oxygen permeation rate is illustrated, keeping airflow rate constant at 24.1cm^3/min. As expected, the oxygen permeation rate increase with increasing argon flow rate because the oxygen partial pressure in the downstream decreases as the argon flow rate is increased, giving an increased driving force for oxygen permeation. In Fig. 7-7(B), the effect of airflow rate on oxygen permeation is depicted with the argon flow rate kept constant at 32.4 cm^3/min for 800 °C, and at 64.5 cm^3/min for 850 and 900 °C, respectively. It can be seen that effect of airflow rate on the oxygen permeation is, in general, negligible, especially at low temperatures. This is because for the operating conditions employed, the amount of oxygen permeated is small compared to the amount of oxygen introduced into the module. Therefore, the oxygen driving force remains relatively unchanged, hence the oxygen permeation rate. As operating temperature increases, the effect of airflow on oxygen permeation rate becomes noticeable, indicating that the operating temperature plays a more important role in oxygen permeation compared to the oxygen driving force.

In Fig. 7-7, modeling results using literature kinetic parameters obtained from a disc-shaped symmetric membrane (Xu and Thomson, 1999) are also plotted in solid lines and compared with the experimental data. As can be seen, both experimental and modeling results show the same trend. However, the experimental results are better than the modeling ones except for the operating temperature of 900 °C. This difference may be resulted from the different membrane structure, as the LSCF hollow fibre membranes prepared using the phase inversion/sintering technique possess an asymmetric structure where the inner surface layer of the membranes is porous and thus the membrane area for the surface exchange reaction is higher than that of symmetric membrane (Xu and Thomson, 1999). Therefore, the downstream surface exchange resistance is greatly decreased due to the higher surface area. As a result, the experimental results are better than modeling values at lower temperatures where the downstream surface exchange is, in general, the controlling step (which is further illustrated theoretically in Fig. 7-9 below). As the temperature increases, the bulk diffusion plays an increasingly important role in oxygen permeation and gradually becomes the controlling step. Therefore, the enhancement of oxygen permeation due to the better membrane surface structure would be diminished as the operating temperature increases; hence the experimental data is close to the modeling results (900 °C).

Fig. 7-8 compares the results between the lumen-feed operation and the shell-feed operation at 850 °C. As can be seen, the experimental data for the lumen-feed operation is much inferior than that obtained from the shell-feed operation, further confirming that the downstream surface exchange kinetics play the important role in oxygen permeation at low operating temperatures.

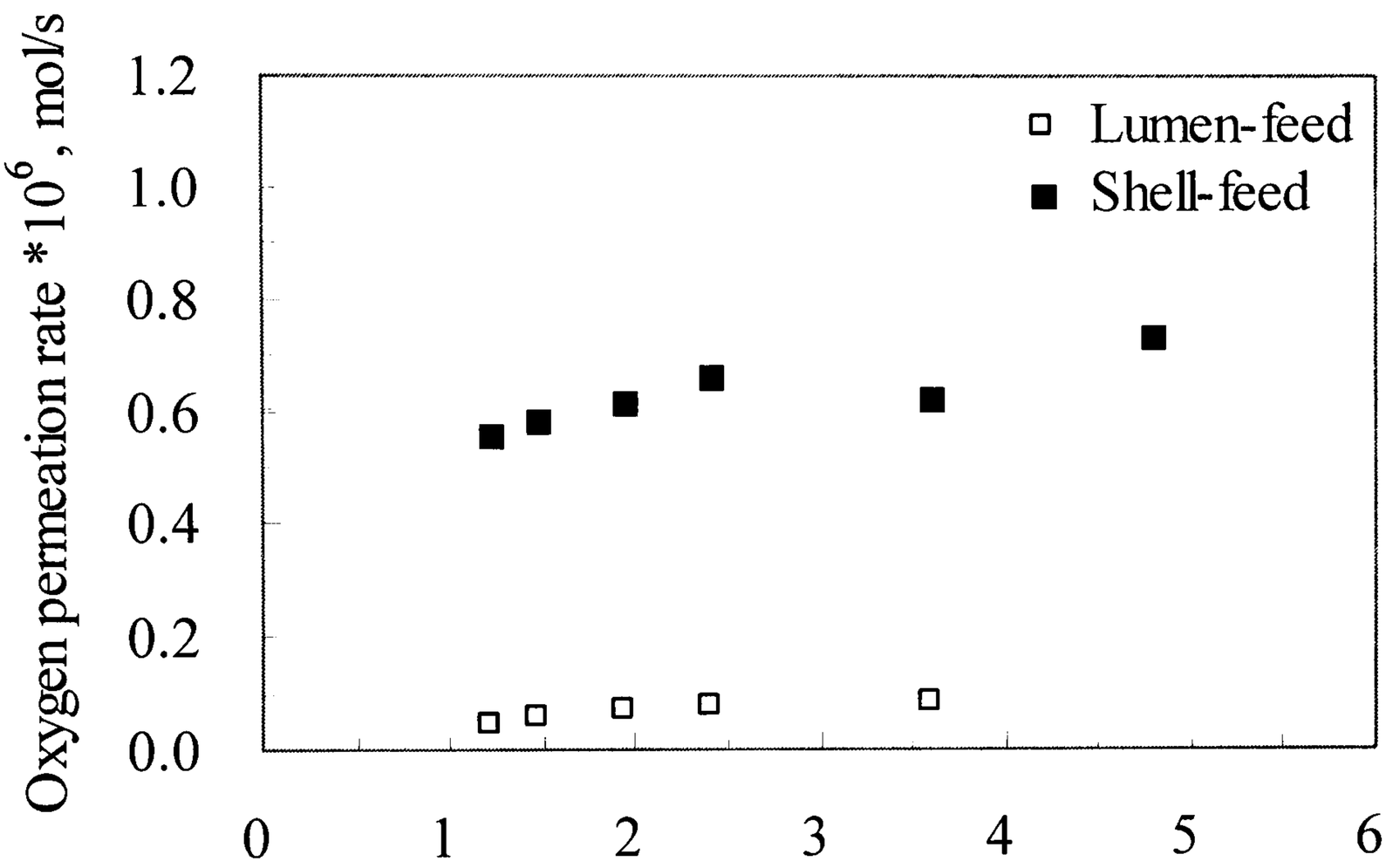


Fig. 7-8 Comparison between the lumen-feed and shell-feed operations (T_s=850°C).

Fig. 7-9 illustrates theoretically importance of each resistance (upstream surface exchange, bulk diffusion and downstream surface exchange) for oxygen permeation at 800 and 1000 °C, respectively. It can be seen that at the low operating temperature, i.e., 800 °C, the upstream surface exchange resistance shows a negligible effect, as the simulation results obtained without considering upstream surface exchange resistance (dashed line) is overlapped with the solid line calculated for the actual case, i.e. considering all three resistances. As the downstream surface exchange resistance is assumed to be negligible, the oxygen permeation rate (dotted line) is considerably higher, suggesting that the downstream surface exchange is the controlling step for oxygen permeation. When the temperature is elevated to 1000 °C, the difference is dramatically reduced, which indicates that the contribution of the downstream surface

exchange to the overall resistance becomes small at high temperatures, and the bulk diffusion gradually becomes the controlling step.

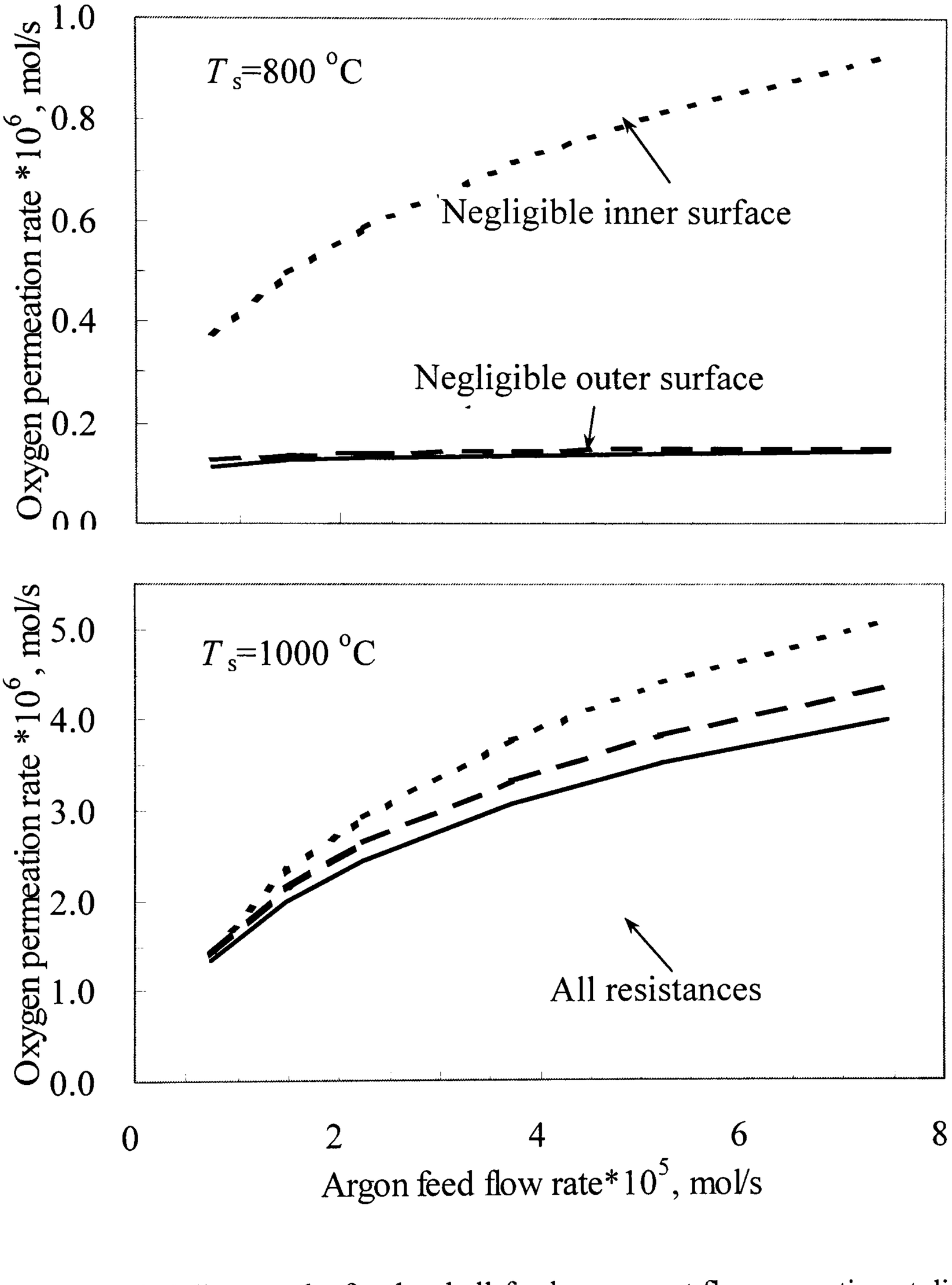


Fig. 7-9 Modeling results for the shell-feed, cocurrent flow operation at different temperatures.

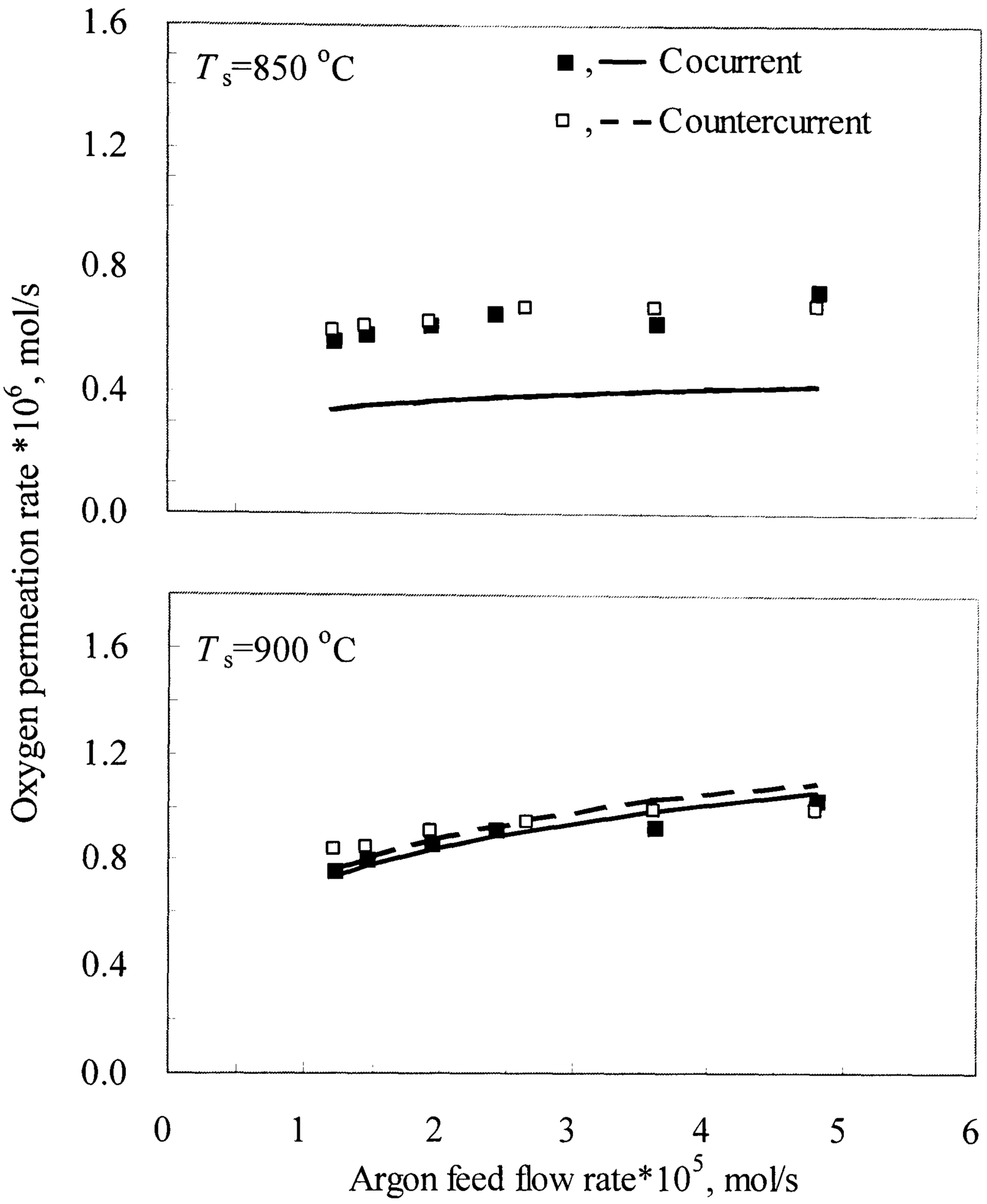


Fig. 7-10 Comparison between the countercurrent and cocurrent flow patterns.

Fig. 7-10 compares the results between countercurrent flow and cocurrent flow patterns at two different temperatures for shell-feed operation. Both the experimental and modeling results indicate that the oxygen permeation rate in the countercurrent flow operation is slightly higher than that in the cocurrent flow operation. This is because the permeation driving force in countercurrent flow is larger than that in cocurrent flow, although the difference is not so noticeable as expected. At low operating temperature, the experimental data is better than the modeling values due to the asymmetric structure of the membrane developed. More positive effect of

countercurrent flow on oxygen permeation at high temperature than at lower temperatures can be expected as shown in Fig. 7-, as the bulk diffusion plays an increasingly important role in permeation as temperature increases.

The effect of the vacuum level on the performance of the membrane module is given in Fig. 7-11 where the oxygen permeation rate is plotted against the absolute pressures at different operating temperatures. In this experiment, air flows in the shell side of the module while the vacuum is applied to the fibre lumen at the same end of the module as the air effluent outlet. As is expected, the oxygen permeation rate increases as the applied vacuum level is increased (i.e. the absolute pressure is decreased). The theoretical results are also plotted in the figure with the solid curves. It can be seen that the experimental data is in good agreement with modeling results. Unlike the sweep gas operation, the experimental data is greater than the corresponding modeling values in the vacuum operation. This may be due to the fact that the oxygen molecules in the inner porous layer (down stream) are able to be released easily from the membrane surface under vacuum operation. Conclusively, the vacuum operation favors the oxygen permeation kinetically in the LSCF hollow fibre membrane modules.

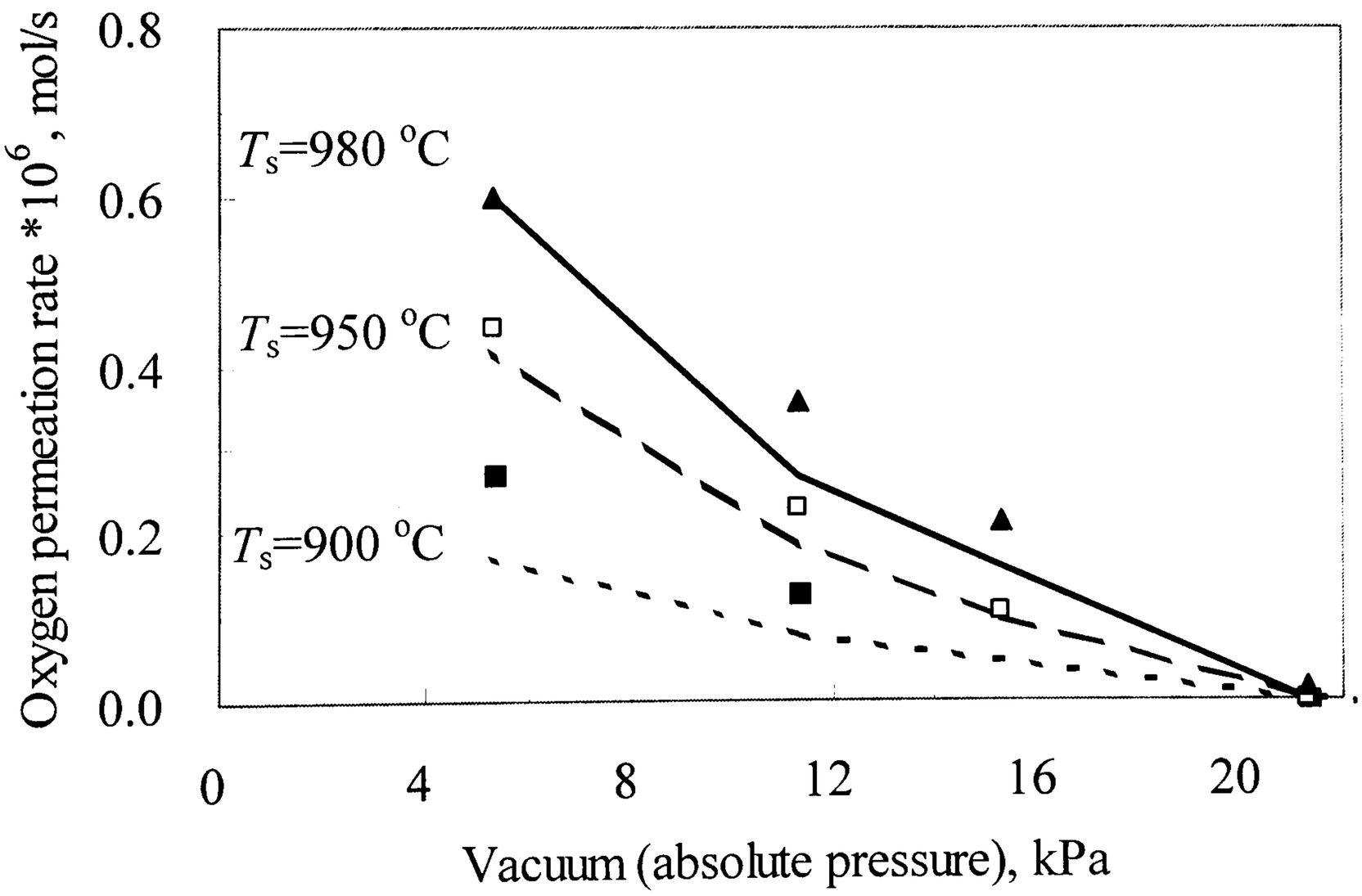


Fig. 7-11 Oxygen permeation rate against vacuum level (absolute pressure).

7.5 Conclusions

Gas-tight LSCF hollow fibre membranes that possess an asymmetric structure have been prepared via a phase inversion spinning, followed by sintering at 1280°C for 4 hours. Using the prepared LSCF hollow fibre membranes, a membrane module was designed and fabricated for air separation. For oxygen permeation, the downstream surface exchange plays an important role compared to the upstream surface exchange especially at low operating temperatures. The porous inner surfaces of the prepared LSCF hollow fibre membranes favour oxygen permeation considerably when air is fed in the shell side of the membrane module. At high temperatures, oxygen permeation can be enhanced by the countercurrent flow operation. Vacuum operation favours the oxygen permeation kinetically in the LSCF hollow fibre membrane modules.

Notations

A_m	-	Membrane area, $A_m = \frac{2\pi(R_o - R_{in})L}{\ln(R_o / R_{in})}$, m^2
D_V	-	Effective diffusivity of oxygen vacancy, m^2/s
F	-	Feed gas flow rate, mol/s
k_r	-	Reverse surface reaction rate constant of (4), $mol/(m^2\ s)$
k_f	-	Forward surface reaction rate constant of (4), $m/(Pa^{0.5}\ s)$
l	-	Variable length of hollow fibre membrane, m
L	-	Length of hollow fibre membrane, m
m	-	Number of hollow fibre membranes
N_{O_2}	-	Oxygen permeation molar flow rate, mol/s
P	-	Gas permeance of membrane, $mol/(m^2.s.Pa)$
p_t	-	Pressure at t, Pa
P_0	-	Initial pressures in the test cylinder, Pa
p_a	-	Atmospheric pressure, 1.013×10^5 Pa
p_l		Pressure in the fibre lumen, Pa
p'_{O_2}	-	Oxygen partial pressures in the shell side, Pa
p''_{O_2}	-	Oxygen partial pressures in the lumen side, Pa
p_s		Pressure in the shell side of the module, Pa
p_v	-	Operating vacuum level, Pa
R	-	Gas constant, 8.314 J/(mol.K)
R_{in}	-	Inner radius of hollow fibre, m
R_o	-	Outer radius of hollow fibre, m
T	-	Operating temperature, K
T_s	-	Setting value of the operating temperature, ^oC
t	-	Time for measurement, s
V	-	Volume of the test cylinder, m^3
x_e		Oxygen concentration in air effluent, %
y_e		Oxygen concentration in argon effluent, %
μ	-	Oxygen viscosity, Pa s
υ_l		Volumetric flow rate of the lumen gas stream, m^3/s
υ_s		Volumetric flow rate of the shell gas stream, m^3/s

References

Abrutis, A., A. Teiserskis, G. Garcia, V. Kubilius, Z. Saltyte, Z. Salciunas, V. Faucheux, A. Figueras and S. Rushworth (2004). Preparation of dense, ultra-thin MIEC ceramic membranes by atmospheric spray-pyrolysis technique, *J. Membr. Sci.*, **Vol.** 240, **pp.** 113-122.

Dyer, P. N., R. E. Richards, S. L. Russek and D. M. Taylor (2000). Ion transport membrane technology for oxygen separation and syngas production, *Solid State Ionics*, **Vol.** 134, **pp.** 21-33.

Kharton, V. V., A. A. Yaremchenko, A. V. Kovalevsky, A. P. Viskup, E. N. Naumovich and P. F. Kerko (1999). Perovskite-type oxides for high-temperature oxygen separation membranes, *J. Membr. Sci.*, **Vol.** 163, **pp.** 307-317.

Lee, K., S. Lee, J. Kim and S. Woo (2002). Enhancement of oxygen permeation by $La_{0.6}Sr_{0.4}CoO_{3-\delta}$ coating in $La_{0.7}Sr_{0.3}Ga_{0.6}Fe_{0.4}O_{3-\delta}$ membrane, *Desalination*, **Vol.** 147, **pp.** 439-444.

Lee, S., K. Lee, S. Woo, J. Kim, T. Ishihara and D. Kim (2003). Oxygen-permeating property of $LaSrBFeO_3$ (B=Co, Ga) perovskite membrane surface-modified by $LaSrCoO_3$, *Solid State Ionics*, **Vol.** 158, **pp.** 287-296.

Li, S., W. Jin, P. Huang, N. Xu, J. Shi and Y. S. Lin (2000). Tubular lanthanum cobalitite perovskite type membrane for oxygen permeation, *J. Membr. Sci.*, **Vol.** 166, **pp.** 51-61.

Li, S., W. Jin, X. N. and J. Shi (1999). Synthesis and oxygen permeation properties of $La_{0.2}Sr_{0.8}Co_{0.2}Fe_{0.8}O_{3-\delta}$ membranes, *Solid State Ionics*, **Vol.** 124, **pp.** 161-170.

Liu, S., X. Tan, L. K. and R. Hughes (2001). Preparation and characterization of $SrCe_{0.95}Yb_{0.05}O_{2.975}$ hollow fibre membranes, *J. Membr. Sci.*, **Vol.** 193, **pp.** 249-260.

Luyten, J., A. Buekenhoudt, W. Adriansens, J. Cooymans, H. Weyten, F. Servaes and R. Leysen (2000). Preparation of $LaSrCoFeO_{3-x}$ membranes, *Solid State Ionics*, **Vol.** 135, **pp.** 637-642.

Stefan, D. and J. Herle (2004). Oxygen transport through dense $La_{0.6}Sr_{0.4}Fe_{0.8}Co_{0.2}O_{3-\delta}$ perovskite-type permeation membranes, *J. Eur. Ceram. Soc.*, **Vol.** 24, **pp.** 1319-1323.

Tan, X. and K. Li (2002). Modeling of air separation in a LSCF hollow-fiber membrane module, *AIChE J.*, **Vol.** 48, **pp.** 1469-1477.

Tan, X., S. Liu and K. Li (2001). Preparation and characterization of inorganic hollow fibre membranes, *J. Membr. Sci.*, **Vol.** 188, **pp.** 87-95.

Teraoka, Y., Y. Honbe, J. Ishii, H. Furukawa and I. Moriguchi (2002). Catalytic effects in oxygen permeation through mixed-conductive LSCF perovskite membranes, *Solid State Ionics*, **Vol.** 152, **pp.** 681-687.

Ullmann, H. and N. Trofimenko (1999). Composition, structure and transport properties of perovskite-type oxides, *Solid State Ionics*, **Vol.** 119, **pp.** 1-8.

Wang, H., R. Wang, D. T. Liang and W. Yang (2004). Experimental and modeling studies on $Ba_{0.5}Sr_{0.5}Co_{0.8}Fe_{0.2}O_{3-\delta}$ (BSCF) tubular membranes for air separation, *J. Membr. Sci.*, **Vol.** 243, **pp.** 405-415.

Xu, S. J. and W. J. Thomson (1999). Oxygen permeation rates through ion-conducting perovskite membranes, *Chemical Engineering Science*, **Vol.** 54, **pp.** 3839-3850.

Chapter 8

Conclusions and recommendations

8.1 Conclusions

Two types of novel mixed-conducting ceramic hollow fibre membranes made from mixed proton-hole conducting materials were prepared via a combined phase inversion and sintering method where polyethersulfone (PESf) is used as a binder, N-methyl-2-pyrrollidone (NMP) as solvent and polyvinylpyrrolidone (PVP) as an additive. A mixed proton-hole conducting material, $SrCe_{0.95}Yb_{0.05}O_{3-\delta}$ (SCYb), was used to produce hollow fibre membrane for methane coupling reaction. An oxygen permeable material $La_{0.6}Sr_{0.4}Co_{0.2}Fe_{0.8}O_{3-\delta}$ (LSCF) was used for air separation. The following conclusions in terms of preparation and characterization of ceramic hollow fibre membranes and their applications in separation and reaction could be drawn based on the research findings.

1. Feasibility of producing mixed conducting ceramic hollow fibre membrane using combined phase inversion and sintering method is clearly demonstrated in this study. Two types of dense ceramic hollow fibre membranes were prepared successfully in the lab using SCYb and LSCF as membrane materials, respectively. SCYb is a mixed proton-hole conducting material, with smaller particle size and the sintering of SCYb membranes is difficult since high sintering temperature is required. LSCF is a mixed oxygen ion-electron conducting material, with larger particle size and the sintering temperature is much lower than that of SCYb. These membranes usually possess an asymmetric structure, i.e. a relative thin dense layer integrated with a porous support, and good mechanical strength. The highly asymmetric structure and relatively thin dense layer of such membranes are resulted from the fast phase inversion process which is frequently used in the fabrication of the polymeric membranes. Good mechanical strength of these ceramic hollow fibre membranes can be obtained if the preparation conditions are well controlled, especially the sintering conditions. In order to obtain the gas tight property, the preparation conditions such as the composition of the starting solutions, spinning process and sintering process must be controlled properly.

2. Problems of high temperature sealing in the making of ceramic hollow fibre membranes modules were overcome by extending the length of the hollow fibre membranes. A few sealants were tested in this study. It was found that all the sealants fail to seal the LSCF hollow fibres to the ceramic tubes at high temperatures (300~1000°C) by resulting in brittleness of the fibres, especially near the glued area and by losing the sealing performance. The mixed conducting hollow fibre membranes with length about 30 cm were prepared in the lab in order to overcome the sealing problems. With this additional fibre length, the sealing ends of the hollow fibre membrane modules could be kept far enough away from the high temperature zone of a furnace. As such, commercially available low temperature sealants such as epoxy could be utilised without compromising its sealing performance. Another problem faced in the making of ceramic hollow fibre membrane module was the thermal expansion of the fibres. It was found that the prepared hollow fibre membrane would break into pieces at temperatures above 500°C if both ends of the fibre were fixed with the module shell. Therefore, in this work, soft silicone rubber tubes were used to offset the thermal expansion of the hollow fibre membranes, as illustrated schematically in chapter 4 and 7. Studies on two applications, i.e. methane coupling reaction and the air separation, were carried out successfully using the prepared mixed conducting hollow fibre membranes.

3. Sintering process is one of the most crucial processes in the fabrication of ceramic hollow fibre membranes, especially in obtaining the gas tight property and also in maintaining the mechanical strength. In order to well control the sintering process, the sintering behaviour of the SCYb hollow fibre membranes was investigated by evaluation of the degree of fibre shrinkage and the change in fibre surface morphology with the sintering temperature and sintering time. Gas tight property was achieved by using a programmed sintering process. This includes a long term sintering at lower temperature for compacting particles and followed by a short term sintering at higher temperature for closing the pores. Specifically, SCYb hollow fibre membranes with excellent gas tight property was obtained by performing the second stage sintering at 1450 °C for 4 hours. Similarly, LSCF hollow fibre membranes with gas tight property were produced by performing the second stage sintering at 1280 °C for 4 hours. Experimental results also revealed the strong dependence between the mechanical strength of SCYb hollow fibre with the sintering conditions. The mechanical strength of SCYb hollow fibre membranes

decreased proportionally with the increase in the sintering temperature from 1350 to 1550 °C. In this study, SCYb hollow fibre membranes with mechanical strength at the level of 200-300 MPa were successfully accomplished using the prescribed preparation conditions.

4. The prepared SCYb hollow fibre membranes showed very good mixed proton-hole conduction at elevated temperature. The mixed proton conducting property of the prepared SCYb hollow fibre membranes was investigated under various operating conditions including temperature and hydrogen/oxygen partial pressure. The obvious hydrogen permeation (or proton conduction) through the resulting dense SCYb hollow fiber membranes generally occurred at the temperatures beyond 700 °C. The hydrogen permeation flux increases with increasing the hydrogen and oxygen concentrations following a nonlinear relationship. The increase in hydrogen permeation flux is especially evident at temperature above 850 °C. Comparison between experimental data and theoretical results suggests that the surface exchange reactions may have resulted in resistances to hydrogen permeation. Further study on the surface exchange reaction will be helpful for a thorough understanding on the proton conducting mechanism. The proton conduction efficiency could be also affected when long SCYb hollow fibers were employed.

5. Based on the principle of the mixed proton-hole conducting of SCYb material, methane coupling reactions were investigated by continuous removal of hydrogen from methane. Extraction of hydrogen through the membrane promotes the formation of ethylene more than that of ethane. The increase in temperature also favours the formation of ethylene over ethane. This can be reversed by increasing the methane flow rate. In addition to the C_2 compounds (namely C_2H_4 and C_2H_6), C_3-C_5 compounds were also formed in the SCYb hollow fibre membrane reactor. Due to the methane carbonisation and formation of higher hydrocarbons, the C_2 selectivity of only about 60% was achieved. Meanwhile, low C_2 yield at 9% indicates that the catalytic activity of SCYb remained low.

6. The gas tight $La_{0.6}Sr_{0.4}Co_{0.2}Fe_{0.8}O_{3-\alpha}$ (LSCF) hollow fibre membranes were obtained under sintering temperature of 1280°C for 4 hours. These membranes showed considerable oxygen permeability at the temperature range from 700 to 1000 °C. The oxygen permeation results indicated that the operating temperature plays an important role in

oxygen permeation through the LSCF membranes than the concentration driving force. At operating temperature above 700 °C, the oxygen permeation flux increased sharply due to the order–disorder transition of oxygen vacancy. The oxygen permeation flux through the LSCF hollow membrane is generally higher than LSCF disk-shaped or tubular membranes because of the improved membrane design, i.e. better membrane surface morphology and reduced membrane thickness. In addition, oxygen permeation at higher temperature can be further enhanced by using countercurrent flow operation.

8.2 Future work and recommendations.

The development of mixed conducting hollow fibre membranes with highly asymmetric structure is still at its infancy stage. This study clearly demonstrates that it is technically feasible to produce mixed conducting hollow fibre membranes with acceptable performance and good mechanical strength via a combined phase inversion and sintering method. In essence, membrane performance in terms of permselectivity and mechanical strength are the two key factors dictating its practicality in industrial application. Further research is required especially in the following areas:

Membrane preparation.

In the fabrication of ceramic membranes, the first problem to be tackled is the dispersion of ceramic particles in the starting solutions. Aggregation of particles is frequently present in starting solution and makes the solution to be not very homogeneous. The defects will be developed in the final membranes due to bad dispersion of particles. The dispersion will become even worse in a concentrated solution or/and if the particle size is as small as colloidal-size. Therefore, the particle dispersion remains as a basic concern in achieving a homogeneous starting solution, which will then warrant the development of a defect free ceramic membrane and improvement of the mechanical strength as well.

Adjustment of the membrane structure is another concern in the preparation of the membranes which may improve membrane performance. It was believed that porous surface on the downstream side of the membrane could reduce the resistance of the surface exchange reaction. A sandwich structure with a relative thin dense layer in the middle and very porous support layers integrated on the both sides is highly recommended here. The

major advantage of this structure is the increase in the effective membrane area on both sides. Another advantage is that proper catalyst can be loaded onto the porous substrates and form a compact and efficient membrane reactor.

Membranes modification

The results from methane coupling reaction suggest that the catalytic activity of the SCYb remained low. Hence, modification on the catalytic properties of the SCYb hollow fibre membranes may be essential. This can be achieved by depositing an additional catalyst, such as, K/PbO, Li/MgO and Na-Mn-W/SiO_2, etc., on the membrane surface via dip coating or incipient wetness impregnation methods, and the overall performance of the mixed conducting SCYb membranes in the methane coupling reactions may be improved. Similar idea can also be applied in order to improve the oxygen permeation rate of LSCF membranes with the assistance of some impregnated proper catalyst.

Another potential modification method is based on the concept of a dual phase membrane, as discussed in the literature review. It is believed that membrane conductivity and mechanical strength could be improved using this method.

Transport mechanism

The influence of surface exchange reaction on both oxygen permeation LSCF membranes and proton conduction SCYb membranes was clearly noticeable in this study. The mechanism as to how the surface exchange reaction took place and the associated governing parameters remained unclear. The resistance of the porous support layer of the asymmetric membrane also needs to be investigated in order to understand on the overall transport mechanism.

LIST OF PUBLICATIONS

1. S.M. Liu, Y. Liu and K. Li (2003). Development of mixed conducting perovskite hollow fibre membranes for dehydrogenation reactions, *3rd International Symposium on Multifunctional Reactors and 18th Colloquium on Chemical Reaction Engineering*, 27-29 August, Bath, UK.

2. Y. Liu and K. Li (2005). Preparation of $SrCe_{0.95}Yb_{0.05}O_{3-\delta}$ hollow fibre membranes: Study on sintering processes, *J. Membr. Sci.*, **Vol.** 259, **pp.** 47-54.

3. X. Tan, Y. Liu and K. Li (2005). Preparation of LSCF ceramic hollow fibre membrane for oxygen production by a phase-inversion/sintering technique, *Ind. Eng. Chem. Res.*, **Vol.** 44, **pp.** 61-66.

4. Y. Liu and K. Li (2005). Preparation of $SrCe_{0.95}Yb_{0.05}O_{3-\delta}$ (SCYb) hollow fibre membranes and applications in methane coupling reaction, *5th International Symposium on Catalysis in Multiphase Reactors and 4th International Symposium on Multifunctional Reactors*, edited by Janez Levec and Albin Pintar, 15-18 June, Portoroz-Portorose, Slovenia.

5. X. Tan, Y. Liu and K. Li (2005). Mixed conducting ceramic hollow-fiber membranes for air separation, *AIChE J.*, **Vol.** 51, **pp.** 1991-2000.

6. Y. Liu, X. Tan, and K. Li, $SrCe_{0.95}Yb_{0.05}O_{3-\delta}$ hollow fiber membrane and its property in proton conduction, *AIChE J.*, in press.

7. Y. Liu, X. Tan, and K. Li, Non-oxidative methane coupling in a $SrCe_{0.95}Yb_{0.05}O_{3-\delta}$ (SCYb) hollow fibre membrane reactor, submitted to *Ind. Eng. Chem. Res.*.

8. Y. Liu, X. Tan, and K. Li, Mixed conducting ceramics for catalytic membrane processing, submitted to *Cata. Rew.*.

APPENDIX A

Data tables of the experimental results

Table Appendix A-1Temperature profile of the tube furnace.

Length of the tube (m)	Setting temperature (°C)			
	980	**900**	**800**	**700**
0	375.4	329.4	263.2	232.1
0.01	508.4	458.9	381.1	316.3
0.02	650.6	586.5	502.5	412.2
0.03	756.3	681.1	588.0	493.8
0.04	830.7	754.1	661.5	561.5
0.05	915.6	839.7	742.5	646.8
0.06	***935.9***	***858.2***	***763.2***	***667.5***
0.07	***945.6***	***868.7***	***774.5***	***678.0***
0.08	***943.7***	***866.8***	***774.5***	***678.0***
0.09	***931.7***	***855.8***	***763.4***	***668.5***
0.1	906.3	820.5	740.3	643.0
0.11	813.0	736.0	655.3	550.4
0.12	723.4	658.5	580.0	482.8
0.13	604.9	546.0	476.5	400.2
0.14	461.7	421.0	366.0	305.4
0.15	312.0	289.3	253.2	192.1

Table Appendix A-2 Effect of sintering temperature on the weight loss of the SCYb hollow fibre membranes.

Temperature (ºC)	600	800	1000	1100	1200	1300	1400	1450	1500	1570
Loss of weight (%)	2.5	7.4	8.7	8	9.3	8.7	9.7	9.8	--	--

Table Appendix A-3 Effect of sintering temperature and time on the shrinkage of the hollow fibre membranes.

Temperature (ºC)	**Shrinkage (%)**					
	Sintering time (minute)					
	30	**60**	**120**	**240**	**480**	**600**
800	0.5±0.2	0.8±0.2	0.9±0.2	1.0±0.2	1.0±0.2	1.0±0.2
1000	1.0±0.1	1.0±0.2	1.0±0.1	2.8±0.1	2.9±0.1	2.9±0.1
1200	4.2±0.1	5.4±0.1	6.2±0.1	6.3±0.1	6.9±0.1	7.0±0.1
1300	9.2±0.1	9.9±0.1	11.0±0.2	12.5±0.1	13.2±0.1	16.9±0.1
1400	20.6±0.1	20±0.1	23.3±0.2	23.6±0.1	23.5±0.1	24.7±0.1
1450	--	--	24.8±0.1	--	--	25.1±0.1
1500	--	--	25.2±0.1	--	--	25.6±0.1
1570	--	--	25.7±0.1	--	--	26.4±0.1

Table Appendix A-4 Effect of sintering temperature on the nitrogen permeability of SCYb hollow fibre membranes sintered for 4 hours.

Temp. (ºC)	**Permeability (mol/cm^2.s.pa)x10^{10}**	
	Sintering I	**Sintering II**
1350	285	35.3
1400	83.2	1.94
1450	7	0.0
1500	4.54	0.0
1550	0.0	0.0

Table Appendix A-5 Effect of sintering time on the nitrogen permeability of SCYb hollow fibre membranes sintered at 1400 ºC.

Time (hr)	**Permeability (mol/cm^2.s.pa)x10^{10}**	
	Sintering I	**Sintering II**
0.5	185	--
2	86.6	--
4	83.2	1.94
8	34.2	0.0

Table Appendix A-6 Effect of sintering conditions on the three-point-bending strength of SCYb hollow fibre membranes.

Temp. (°C)	Mechanical strength (MPa)		
	Sintering I		Sintering II
	2 hr	4 hr	4 hr
1350	441.0	400.7	427.3
1400	352.3	325.7	358.3
1450	300.9	209.6	233.1
1500	224.1	172.7	196.3
1550	--	--	104.6

Table Appendix A-7 Effect of sintering time on the three-point-bending strength of SCYb hollow fibre membrane sintered at 1400 °C.

Time (hr)	Mechanical strength (MPa)	
	Sintering I	Sintering II
0.5	423	383.6
1	438.4	--
2	352.3	419.1
4	325.7	358.3
8	255.4	228.0

Table Appendix A-8 Effects of hydrogen concentration of feed on the hydrogen permeation rate at different temperatures (oxygen concentration at downstream side: 21%).

Temp. (°C)	Hydrogen permeation rate (ml/cm^2.min)					
	Hydrogen concentration of feed (vol%)					
	3.5%	7.1%	14.3%	21.4%	28.8%	35.9%
700	0.00256	0.00309	0.00355	0.00359	0.00444	0.00599
750	0.00374	0.00540	0.00582	0.00626	0.00647	0.00671
800	0.003563	0.005791	0.008274	0.009389	0.012174	0.017397
850	0.00839	0.01764	0.02337	0.02750	0.03627	0.04435
900	0.01737	0.03207	0.05525	0.07708	0.09825	0.11639
950	0.03579	0.05966	0.09376	0.12846	0.16227	0.19884

Table Appendix A-9 Effects of temperature and hydrogen concentration of feed on the hydrogen permeation rate (oxygen concentration at downstream side: 9.9%).

Temp. (°C)	Hydrogen permeation rate (ml/cm^2.min)					
	Hydrogen concentration of feed (vol%)					
	3.5%	7.1%	14.3%	21.4%	28.8%	35.9%
700	0.00061	0.00122	0.00245	0.00363	0.00394	0.00394
750	0.00119	0.00238	0.00295	0.00472	0.00532	0.00532
800	0.00310	0.00559	0.00745	0.00868	0.01055	0.01118
850	0.00813	0.01136	0.01724	0.02221	0.03045	0.03803
900	0.01772	0.02321	0.04336	0.06300	0.08076	0.09747
950	0.02909	0.04637	0.07372	0.10022	0.12848	0.15640

Table Appendix A-10 Effects of hydrogen concentration of feed on the hydrogen permeation rate at different temperatures (oxygen concentration at downstream side: 6.3%).

Temp. (°C)	Hydrogen permeation rate (ml/cm^2.min)					
	Hydrogen concentration of feed (vol%)					
	3.5%	7.1%	14.3%	21.4%	28.8%	35.9%
700	0	0	0	0	0	0
750	0.00127	0.00190	0.00253	0.00316	0.00346	0.00346
800	0.00249	0.00441	0.00570	0.00762	0.00890	0.01018
850	0.00703	0.00887	0.01215	0.01421	0.01753	0.02210
900	0.01460	0.01892	0.02884	0.04126	0.05137	0.06496
950	0.02634	0.03774	0.06575	0.09100	0.11421	0.14145

Table Appendix A-11 Effects of hydrogen concentration of feed on the hydrogen permeation rate at different temperatures (oxygen concentration at downstream side: 1.7%).

Temp. (°C)	Hydrogen permeation rate (ml/cm^2.min)					
	Hydrogen concentration of feed (vol%)					
	3.5%	7.1%	14.3%	21.4%	28.8%	35.9%
700						
750	0.00053	0.00079	0.00165	0.00153	0.00177	0.00177
800	0.00082	0.00167	0.00285	0.00462	0.00664	0.00723
850	0.00627	0.00835	0.01047	0.01284	0.01435	0.01435
900	0.00728	0.00894	0.01216	0.01584	0.01779	0.02032
950	0.01397	0.01539	0.01941	0.02529	0.03382	0.03980

Table Appendix A-12 Effect of concentration of CH_4 of feed and concentration of oxygen of downstream side on the formation rate of C_2-C_5 hydrocarbons and hydrogen during the methane coupling reaction in the SCYb hollow fibre membrane at 750 ºC.

CH_4 Conc. %	**CH_4 +Ar**	**Air**	**C_2H_4**	**C_2H_6**	**C_3**	**C_4**	**C_5**
	ml/min		**Formation rate (μmol/cm^2.min)**				
9.2	4.3	40		0.041	0.00029		0.00093
6.7	3.8	40		0.0196			
O_2 Conc. %	**10% CH_4**	**Air+Ar**	**C_2H_4**	**C_2H_6**	**C_3**	**C_4**	**C_5**
	ml/min		**Formation rate (μmol/cm^2.min)**				
20.6	4.3	40.0		0.041	0.00029		0.00093
12.0	4.3	37		0.0442			
7.4	4.3	38.7		0.0659			
1	4.3	36.6		0.0477			

Table Appendix A-13 Effect of concentration of CH_4 of feed and concentration of oxygen of downstream side on the formation rate of C_2-C_5 hydrocarbons and hydrogen during the methane coupling reaction in the SCYb hollow fibre membrane at 800 °C.

CH_4 Conc. %	CH_4 +Ar	Air	C_2H_4	C_2H_6	C_3	C_4	C_5
	ml/min	ml/min	Formation rate (μmol/cm^2.min)				
9.2	4.3	40.1	0.18772	0.144	0.00464	0.00085	0.00108
6.3	4.3	38.7	0.12168	0.12225			
5.3	3.8	37	0.06604	0.07635			
3.8	3.6	40.3	0.06604	0.0567			
2.9	3.9	40	0.06	0.04455			
O_2 Conc. %	10% CH_4	Air+Ar	C_2H_4	C_2H_6	C_3	C_4	C_5
	ml/min		Formation rate (μmol/cm^2.min)				
20.6	4.3	40.0	0.18772	0.144	0.00464	0.00085	0.00108
14.9	4.3	40	0.0759	0.101			
11.9	4.3	40	0.08316	0.116			
6.8	4.3	40	0.08558	0.121			
2.8	4.3	40	0.05	0.081			

Table Appendix A-14 Effect of concentration of CH_4 of feed and concentration of oxygen of downstream side on the formation rate of C_2-C_5 hydrocarbons and hydrogen during the methane coupling reaction in the SCYb hollow fibre membrane at 850 °C.

CH_4 Conc. %	CH_4 +Ar	Air	C_2H_4	C_2H_6	C_3	C_4	C_5
	ml/min	ml/min	Formation rate (μmol/cm^2.min)				
9.2	4.3	40	0.2117	0.1840	0.00953	0.00142	0.00218
6.8	4.3	40	0.1695	0.1197	0.00251		
6.0	3.8	40	0.1185	0.1130	0.00254		
3.8	3.6	40	0.0768	0.0502	0.00236	0.00385	
2.9	3.9	40	0.0627	0.0437		0.00239	
O_2 Conc. %	10% CH_4	Air+Ar	C_2H_4	C_2H_6	C_3	C_4	C_5
	ml/min		Formation rate (μmol/cm^2.min)				
20.6	4.3	40.0	0.2117	0.1840	0.00953	0.00142	0.00218
16.3	4.3	46	0.1738	0.1340	0.00826	0.00644	
14.8	4.3	37.4	0.1861	0.1365	0.00812	0.00602	
6.4	4.3	38.7	0.1697	0.1307	0.00877	0.00345	
2.3	4.3	40.1	0.0377	0.0745	0.00614	0.00141	

Table Appendix A-15 Effect of concentration of CH_4 of feed and concentration of oxygen of downstream side on the formation rate of C_2-C_5 hydrocarbons and hydrogen during the methane coupling reaction in the SCYb hollow fibre membrane at 900 °C.

CH_4 Conc. %	CH_4 +Ar	Air	C_2H_4	C_2H_6	C_3	C_4	C_5
	ml/min	ml/min	Formation rate (μmol/cm^2.min)				
9.2	4.3	43.9	0.3439	0.1742	0.01693	0.00338	0.00500
6.8	4.3	44.2	0.2302	0.1489	0.00659	0.00333	
6.0	3.8	38.4	0.1421	0.0736	0.00453		
3.8	3.6	46	0.0871	0.0464	0.00291	0.00313	
2.9	3.9	40	0.0965	0.0707	0.00257	0.00289	

O_2 Conc. %	10% CH_4	Air+Ar	C_2H_4	C_2H_6	C_3	C_4	C_5
	ml/min		Formation rate (μmol/cm^2.min)				
20.6	4.3	40.0	0.3439	0.1742	0.01693	0.00338	0.00500
16.1	4.3	40	0.2244	0.1424	0.00966	0.00360	
14.5	4.3	40	0.2374	0.1546	0.01110	0.00354	
6.1	4.3	40	0.1765	0.1502	0.00949	0.00276	
3.3	4.3	40	0.1792	0.1745	0.00874	0.00193	

Table Appendix A-16 Effect of concentration of CH_4 of feed and concentration of oxygen of downstream side on the formation rate of C_2-C_5 hydrocarbons and hydrogen during the methane coupling reaction in the SCYb hollow fibre membrane at 950 °C.

CH_4 Conc. %	CH_4 +Ar	Air	C_2H_4	C_2H_6	C_3	C_4	C_5
	ml/min		Formation rate (μmol/cm^2.min)				
9.2	4.3	40	0.4325	0.1687	0.01807	0.00305	0.01100
6.8	4.3	40	0.2665	0.1289	0.00907	0.00712	
5	3.8	40	0.1454	0.0607	0.00300		
3.8	3.6	46	0.1500	0.0500			
2.9	3.9	40	0.1300	0.0400			
O_2 Conc. %	10% CH_4	Air+Ar	C_2H_4	C_2H_6	C_3	C_4	C_5
	ml/min		Formation rate (μmol/cm^2.min)				
20.6	4.3	40.0	0.4325	0.1687	0.01807	0.00305	0.01100
16.6	4.3	46	0.3339	0.1532	0.00843	0.00158	0.01047
12.2	4.3	47	0.2966	0.1512	0.01070	0.00184	
7.8	4.3	35.5	0.2094	0.1812	0.00889	0.00442	
2.8	4.3	43.9	0.1903	0.1558	0.01056	0.00319	

Table Appendix A-17 Effect of resident time on the formation rate of C_2-C_5 hydrocarbons during methane coupling reaction in the SCYb hollow fibre membrane.

Resident time (second)	**C_2H_4**	**C_2H_6**	**C_3**	**C_4**	**C_5**
	Formation rate (μmol/cm^2.min)				
0.35	4.11E-01	1.51E-01	1.81E-02	3.05E-03	7.60E-03
0.19	4.33E-01	1.69E-01	2.36E-02	4.42E-03	1.10E-02
0.12	3.27E-01	1.90E-01	2.82E-02	4.95E-03	2.10E-03
0.06	2.91E-01	2.30E-01	2.14E-02	3.20E-03	

Table Appendix A-18 Measurement results of gas tight property of LSCF hollow fibre membrane.

Time x 10^4 (s)	**Pressure (kPa)**
0.00	345.6
1.49	344.2
2.79	342.7
7.93	333.6
9.23	331.6
10.50	327.3
11.41	322.2
16.97	305.4
20.43	303.0
25.68	300.3

Table Appendix A-19 Effect of temperature on the oxygen flux.

Temp. °C	Conc. Of permeate side %	Permeation flux $*10^7$ mol/cm^2.s
100	0	0.000
360	0.1	0.064
574	0.2	0.128
600	0.2	0.128
620	0.3	0.193
640	0.4	0.257
653	0.5	0.322
666	0.6	0.387
700	1	0.648
712	1.1	0.713
718	1.2	0.779
723	1.3	0.844
728	1.4	0.910
733	1.5	0.976
738	1.6	1.042
743	1.7	1.109
748	1.8	1.175
766	2	1.308
770	2.1	1.375
780	2.4	1.576
788	2.6	1.711
792	2.8	1.847
800	3.1	2.051
810	3	1.983
820	3.4	2.256
830	3.7	2.463
840	4.1	2.741
850	4.6	3.091
911	6.7	4.604
920	7.2	4.974
932	7.6	5.273
940	8	5.575
950	8.5	5.955

Table Appendix A-20 Oxygen flux against down stream oxygen partial pressure at different temperatures*.

700 °C		750 °C		800 °C		850 °C		900 °C		950 °C	
p_d	jo_2	p_d	jo_2	p_d	jo_2	p_d	jo_2	p_d	jo_2	p_d	jo_2
0.014	0.459	0.027	0.898	0.048	1.631	0.072	2.510	0.098	3.516	0.122	4.496
0.01	0.648	0.019	1.242	0.037	1.893	0.046	3.091	0.064	4.383	0.085	5.955
0.004	0.385	0.01	0.967	0.031	2.051	0.033	3.268	0.048	4.828	0.065	6.656
		0.007	0.898	0.024	1.965	0.026	3.402	0.039	5.172	0.045	7.499
		0.005	0.800	0.02	1.954	0.021	3.414	0.032	5.261	0.034	7.832
				0.015	1.941	0.015	3.389	0.024	5.472	0.024	7.810
				0.012	1.933	0.01	3.208	0.017	5.493		

* $jo_{2:}$ oxygen permeation flux 10^7 mol/cm^2.s; p_d: downstream oxygen partial pressure atm.

Table Appendix A-21 Effect of air flow rate on the oxygen permeation rate.

Air flow rate 10^5 mol/s	Oxygen permeation rate 10^5 mol/s		
	900°C	850°C	800°C
0.93	0.979	0.681	0.398
1.27	1.079	0.781	0.426
1.79	1.129	0.731	0.467
2.66	1.129	0.780	0.471
4.38	1.180	0.780	

Table Appendix A-22 Effect of Ar flow rate on the oxygen permeation rate.

Ar flow rate 10^5 mol/s	Oxygen permeation rate 10^5 mol/s		
	900°C	850°C	800°C
1.22	0.764	0.561	0.403
1.46	0.807	0.583	0.412
1.93	0.869	0.619	0.435
2.41	0.916	0.659	0.457
3.60	0.924	0.623	0.401
4.80	1.029	0.731	0.485

Table Appendix A-23 Effect of Ar flow rate on the oxygen permeation rate when air going lumen and shell side.

Ar flow rate 10^5 mol/s	**Oxygen permeation rate 10^5 mol/s**	
	Lumen feed	**Shell feed**
1.22	0.561	0.0428
1.46	0.583	0.0556
1.93	0.619	0.0699
2.41	0.659	0.0774
3.60	0.623	0.0867
4.80	0.731	

Table Appendix A-24 Oxygen permeation rate at different operation modes.

Ar flow rate 10^5 mol/s	**Oxygen permeation rate 10^5 mol/s**			
	Counter-current		**Cocurrent**	
	850 °C	**900 °C**	**850 °C**	**900 °C**
1.22	0.597	0.838	0.561	0.764
1.46	0.610	0.849	0.583	0.807
1.93	0.628	0.912	0.619	0.869
2.65	0.674	0.945	0.659	0.916
3.60	0.673	0.983	0.623	0.924
4.80	0.682	0.990	0.731	1.029

Table Appendix A-25 Oxygen permeation rate at vacuum operation mode.

Vacuum kPa	**Oxygen permeation rate 10^6 mol/s**		
	980°C	**950°C**	**900°C**
21.33	0.015	0.000	0.042
15.33	0.214	0.104	0.000
11.33	0.356	0.229	0.127
5.33	0.600	0.446	0.271

APPENDIX B

Computing programs

Appendix B-Computer program for proton conduction simulation

Proton-main-1

```
clear
% Hollow fiber membrane module for hydrogen permeation-cocurrent flow pattern
global Pl Ps NAr Nn2 Lth Am
global Ke1 Ke2 Ke3 Cyb Dv Dp Dh
global Cv1 Cp1 Ch1 Cv2 Cp2 Ch2

% Basic parameters
Temt=850+273; %K
Pl=1;%lumen pressure, atm
Ps=1;%shell pressure, atm
n=1;%number of hollow fibres
Ro=0.145/2;%outer radius of fibre, cm
Rin=0.065/2;%inner radius of fibre, cm
Lr=20;%Lenth of the membranes, cm
Rm=(Ro-Rin)/log(Ro/Rin);% Average radius of hollow fibre, cm
Lth=(Ro-Rin)*1;% membrane thickness
Lth=0.004; % cm
Am=2*n*pi*Rm;
Cyb=1.06e-3;%mol/cm3
Vf1=136/60;%flow rate of hydrogen feed, cm3/s
Ysw=4e-4;%
YH2=0.2;%molar fraction of the hydrogen feed stream
Vf2=60/60;%flow rate of air feed, cm3/s
Ylw=4e-4;%
YO2=0.21;%molar fraction of oxygen in air feed

% Experimental data-varying hydrogen pressure
Hcon=[0.035     0.071     0.143     0.214     0.288     0.359];
for KK=1:6
      YH2=Hcon(KK);

Nsf=Vf1/(82.06*298.15);%mol/s
Nlf=Vf2/(82.06*298.15);%mol/s
NAr=Nsf*(1-YH2-Ysw);Nn2=Nlf*(1-YO2-Ylw);

% Diffusivity and equilibrium constants
Dp=0.122*exp(-7851/Temt);
```

```
Dh=49.38*exp(-12588.7/Temt);
Dv=24.24*exp(-23467/Temt); %cm2/s
Ke1=3.24e-8*exp(1371.3/Temt); %
if Temt<1073
Ke2=2.087e-2*exp(1368.4/Temt);
else
Ke2=1.77e-10*exp(21911/Temt);
end
Kw=1.188e-3*exp(29709/Temt);
Ke3=Kw*Ke2/Ke1;

% integration of the model equations
Tol=1e-12;
Y0=[Nsf*Ysw Nsf*YH2 Nlf*Ylw Nlf*YO2];
[zout,yout]=ode45('p1fun',0,Lr,Y0,Tol);
nn=max(size(zout));

Jhydrog(KK)=(Y0(2)-yout(nn,2))/(Am*Lr)*22400*60;% ml/cm2.min
Jproton(KK)=(yout(nn,3)-Y0(3))*2/(Am*Lr)*1e8 % % mol/cm2.s
Jvacancy(KK)=(yout(nn,1)-Y0(1))/(Am*Lr)*1e10

end
Flux=Jproton'*1e-8*22400*60/2
plot(Hcon,Expf,'bo',Hcon,Flux,'r*')
%plot(Water,Jhydrog,'bo')
%figure(2)
%plot(Water,Jproton,'r*',Water,Jvacancy,'bo')
%plot(Length,Jproton,'r*',Length,Jvacancy,'bo')
```

Proton-p1fun

```
function ydot=pfun(t,x)
global Pl Ps NAr Nn2 Am
global Cyb Ke1 Ke2 Ke3 Dv Dp Dh
global Lth Jv Jp Cv1 Cp1 Ch1 Cv2 Cp2 Ch2

Nw1=x(1);Nh2=x(2);Nw2=x(3);No2=x(4);

Pw1=Ps*Nw1/(Nw1+Nh2+NAr);Ph1=Ps*Nh2/(Nw1+Nh2+NAr);
Pw2=Pl*Nw2/(Nw2+No2+Nn2);Po2=Pl*No2/(Nw2+No2+Nn2);

% At interface I
alfa1=1+1/sqrt(Ke3*Ph1);
Cp1=(sqrt(alfa1*alfa1+8*Cyb/(Ke2*Pw1))-alfa1)/(4/(Ke2*Pw1));
Cv1=Cp1^2/(Ke2*Pw1);
```

```
Ch1=Cp1/sqrt(Ke3*Ph1);

% At interface II
alfa2=sqrt(Ke1*sqrt(Po2))+sqrt(Ke2*Pw2);
Cv2=(sqrt(alfa2*alfa2+8*Cyb)-alfa2)^2/16;
Ch2=sqrt(Ke1*sqrt(Po2)*Cv2);
Cp2=sqrt(Ke2*Pw2*Cv2);

options(1)=0;options(2)=1e-12;options(3)=1e-15;options(14)=400;
Jopt=fmins('fluxopt',[1e-10 1.2e-8],options);
Jv=Jopt(1);Jp=Jopt(2);
%Jv=6.8317e-009;Jp=5.8134e-008;
Tol=1e-12;
[tout,yout]=ode45('efluxfun',0,Lth,[Cv1 Cp1 Ch1],Tol);
nn=max(size(tout));
Er=sqrt((yout(nn,1)-Cv2)^2+(yout(nn,2)-Cp2)^2+(yout(nn,3)-Ch2)^2);
%Pressure=[Pw1 Ph1;Pw2 Po2]
gkk=[Cv1 Cp1 Ch1;Cv2 Cp2 Ch2;yout(nn,1) yout(nn,2) yout(nn,3)];
ggs=[Jv Jp Er]

ydot(1)=Am*Jv;
ydot(2)=-ydot(1)-Am*Jp/2;
ydot(3)=Am*Jp/2;
ydot(4)=-ydot(3)/2-Am*Jv/2;
```

Proton-efluxfun

```
function ydot=fluxfun(t,x)
global Dv Dp Dh Jv Jp
%Value=[Jv Jp]
%pause
cv=x(1);cp=x(2);ch=x(3);
sigm=4*Dv*cv+Dp*cp+Dh*ch;
tv=4*Dv*cv/sigm;tp=Dp*cp/sigm;th=Dh*ch/sigm;
A(1,1:3)=[1-tv -2*tp*cv/cp -2*th*cv/ch];
A(2,1:3)=[-0.5*tv*cp/cv 1-tp -th*cp/ch];
A(3,1:3)=[2 1 1];
B=-[Jv/Dv Jp/Dp 0]';
ydot(1)=det([B A(:,2:3)])/det(A);
ydot(2)=det([A(:,1) B A(:,3)])/det(A);
ydot(3)=det([A(:,1:2) B])/det(A);
```

Proton-main-2

```
clear
```

```
% Hollow fiber membrane module for proton permeation-countercurrent flow pattern
global Pl Ps Nsf Nlf Ysw YH2 Ylw YO2 NAr Nn2 Lth Lr Am
global Ke1 Ke2 Ke3 Cyb Dv Dp Dh
global Cv1 Cp1 Ch1 Cv2 Cp2 Ch2

% Basic parameters
Temt=850+273; %K
Pl=1;%lumen pressure, atm
Ps=1;%shell pressure, atm
n=1;%number of hollow fibres
Ro=0.145/2;%outer radius of fibre, cm
Rin=0.065/2;%inner radius of fibre, cm
Lr=20;%Lenth of the membranes, cm
Rm=(Ro-Rin)/log(Ro/Rin);% Average radius of hollow fibre, cm
Lth=(Ro-Rin)*1;% membrane thickness
Am=2*n*pi*Rm;
Cyb=1.06e-3;%mol/cm3
Vf1=136/60;%flow rate of hydrogen feed, cm3/s
Ysw=4e-4;%
YH2=0.2;%molar fraction of the hydrogen feed stream
Vf2=60/60;%flow rate of air feed, cm3/s
Ylw=4e-4;%
YO2=0.21;%molar fraction of oxygen in air feed
Temt=850+273;YO2=0.21;

%for KK=1:4
%       YO2=Acon(KK);

%Water=[4e-4 6e-4 1e-3 2e-3 5e-3];
%for KK=1:5
%       Ysw=Water(KK);

Nsf=Vf1/(82.06*298.15);%mol/s
Nlf=Vf2/(82.06*298.15);%mol/s
NAr=Nsf*(1-YH2-Ysw);Nn2=Nlf*(1-YO2-Ylw);

% Diffusivity and equilibrium constants
Dp=0.122*exp(-7851/Temt);
Dh=49.38*exp(-12588.7/Temt);
Dv=24.24*exp(-23467/Temt); %cm2/s
Ke1=3.24e-8*exp(1371.3/Temt); %
if Temt<1073
Ke2=2.087e-2*exp(1368.4/Temt);
else
```

```
Ke2=1.77e-10*exp(21911/Temt);
end
Kw=1.188e-3*exp(29709/Temt);
Ke3=Kw*Ke2/Ke1;

%options(1)=0;options(2)=1e-6;options(3)=1e-6;options(14)=400;
%Yoxyg=fmins('p2oxyg',[1.05e-3 0.209]);
%Ylwc=Yoxyg(1);YO2c=Yoxyg(2);
Ylwc=2.446e-3;YO2c=2.0895e-1;

% integration of the model equations
Tol=1e-12;
Y0=[Nsf*Ysw Nsf*YH2 Nlf*Ylwc Nlf*YO2c];
[zout,yout]=ode45('p2fun',0,Lr,Y0,Tol);
nn=max(size(zout));

for I=1:nn
Nw1=yout(I,1);Nh2=yout(I,2);Nw2=yout(I,3);No2=yout(I,4);
Pw1=Ps*Nw1/(Nw1+Nh2+NAr);Ph1=Ps*Nh2/(Nw1+Nh2+NAr);
Pw2=Pl*Nw2/(Nw2+No2+Nn2);Po2=Pl*No2/(Nw2+No2+Nn2);

% At interface I
alfa1=1+1/sqrt(Ke3*Ph1);
Cp1=(sqrt(alfa1*alfa1+8*Cyb/(Ke2*Pw1))-alfa1)/(4/(Ke2*Pw1));
Cv1=Cp1^2/(Ke2*Pw1);
Ch1=Cp1/sqrt(Ke3*Ph1);

% At interface II
alfa2=sqrt(Ke1*sqrt(Po2))+sqrt(Ke2*Pw2);
Cv2=(sqrt(alfa2*alfa2+8*Cyb)-alfa2)^2/16;
Ch2=sqrt(Ke1*sqrt(Po2)*Cv2);
Cp2=sqrt(Ke2*Pw2*Cv2);

options(1)=0;options(2)=1e-12;options(3)=1e-15;options(14)=400;
Jopt=fmins('fluxopt',[1e-12 1.2e-9],options);
Jv(I)=Jopt(1);Jp(I)=Jopt(2);
end

figure(1)
plot(zout,Jv,'bo')
figure(2)
plot(zout,Jp,'b*')
figure(3)
plot(zout,yout(:,3)/(Nlf*Ylw),'ro')
figure(4)
```

```
plot(zout,yout(:,4)/(Nlf*YO2),'r*')
```

Proton-p2fun

```
function ydot=pfun(t,x)
% countercurrent flow
global Pl Ps NAr Nn2 Am
global Cyb Ke1 Ke2 Ke3 Dv Dp Dh
global Lth Jv Jp Cv1 Cp1 Ch1 Cv2 Cp2 Ch2

Nw1=x(1);Nh2=x(2);Nw2=x(3);No2=x(4);
Pw1=Ps*Nw1/(Nw1+Nh2+NAr);Ph1=Ps*Nh2/(Nw1+Nh2+NAr);
Pw2=Pl*Nw2/(Nw2+No2+Nn2);Po2=Pl*No2/(Nw2+No2+Nn2);

% At interface I
alfa1=1+1/sqrt(Ke3*Ph1);
Cp1=(sqrt(alfa1*alfa1+8*Cyb/(Ke2*Pw1))-alfa1)/(4/(Ke2*Pw1));
Cv1=Cp1^2/(Ke2*Pw1);
Ch1=Cp1/sqrt(Ke3*Ph1);

% At interface II
alfa2=sqrt(Ke1*sqrt(Po2))+sqrt(Ke2*Pw2);
Cv2=(sqrt(alfa2*alfa2+8*Cyb)-alfa2)^2/16;
Ch2=sqrt(Ke1*sqrt(Po2)*Cv2);
Cp2=sqrt(Ke2*Pw2*Cv2);

options(1)=0;options(2)=1e-12;options(3)=1e-15;options(14)=400;
Jopt=fmins('fluxopt',[1e-10 1.2e-8],options);
Jv=Jopt(1);Jp=Jopt(2);
%Jv=6.8317e-009;Jp=5.8134e-008;
Tol=1e-12;
[tout,yout]=ode45('efluxfun',0,Lth,[Cv1 Cp1 Ch1],Tol);
nn=max(size(tout));
Er=sqrt((yout(nn,1)-Cv2)^2+(yout(nn,2)-Cp2)^2+(yout(nn,3)-Ch2)^2);
%Pressure=[Pw1 Ph1;Pw2 Po2]
%gkk=[Cv1 Cp1 Ch1;Cv2 Cp2 Ch2;yout(nn,1) yout(nn,2) yout(nn,3)]
%ggs=[Jv Jp Er]

ydot(1)=Am*Jv;
ydot(2)=-ydot(1)-Am*Jp/2;
ydot(3)=-Am*Jp/2;
ydot(4)=Am*Jp/4+Am*Jv/2;
```

Proton-fluxopt

```
function Er=fluxopt(x)
```

```
% find the optimum flux, Jv, Jp and Jh
global Lth Jv Jp Cv1 Cp1 Ch1 Cv2 Cp2 Ch2
Tol=1e-12;
Jv=x(1);Jp=x(2);
[tout,yout]=ode45('efluxfun',0,Lth,[Cv1 Cp1 Ch1],Tol);
nn=max(size(tout));
Er=sqrt((yout(nn,1)-Cv2)^2+(yout(nn,2)-Cp2)^2+(yout(nn,3)-Ch2)^2);

%gkk=[Cv1 Cp1 Ch1;Cv2 Cp2 Ch2;yout(nn,1) yout(nn,2) yout(nn,3)]
%gms=[Jv Jp Er]
```

Proton-p2oxyg

```
function Er=p2oxyg(x)
% find the compositions of the effluent from fibre lumen
global Pl Ps Nsf Nlf Ysw YH2 Ylw YO2 NAr Nn2 Lth Lr Am
global Ke1 Ke2 Ke3 Cyb Dv Dp Dh
global Cv1 Cp1 Ch1 Cv2 Cp2 Ch2

Ylwc=x(1);YO2c=x(2);

% integration of the model equations
Tol=1e-12;
Y0=[Nsf*Ysw Nsf*YH2 Nlf*Ylwc Nlf*YO2c];
[zout,yout]=ode45('p2fun',0,Lr,Y0,Tol);
nn=max(size(zout));

Er=sqrt((1-yout(nn,3)/(Nlf*Ylw))^2+(1-yout(nn,4)/(Nlf*YO2))^2);

gff=[Ylwc YO2c yout(nn,3)/Nlf yout(nn,4)/Nlf Ylw YO2 Er]
```

Appendix B-Computer program for methane coupling reaction simulation

OCM-main-1

```
clear
% Hollow fiber membrane reactor for OCM-cocurrent flow pattern
global Pl Ps Temt Ns0 YCH4 Nl0 YO2 n Rin Rm Lme Am Lr Rt1 Rt2
global Ke1 Ke2 CYb Kr1 Kr2
global Dv Dp Dh Flux

% Basic parameters
Temt=1173; %K
Pl=1;%lumen pressure, atm
Ps=1;%shell pressure, atm
n=1; %number of hollow fibres
Ro=0.145/2;%outer radius of fibre, cm
Rin=0.065/2;%inner radius of fibre, cm
CYb=1.06e-3;%mol/cm3
Lr=4;%Lenth of reactor, cm
Vf1=3.94/60;%flow rate of hydrocarbon feed, cm3/s
YCH4=0.0922;%molar fraction of methane in hydrocarbon feed
Vf2=40/60;%flow rate of air feed, cm3/s
YO2=0.21;%molar fraction of oxygen in air feed
Rm=(Ro-Rin)/log(Ro/Rin);% Average radius of hollow fibre, cm
Lme=Ro-Rin;% membrane thickness
Am=2*n*pi*Lr*Lme/log(Ro/(Ro-Lme));
Ns0=Vf1/(82.06*298.15);%mol/s
Nl0=Vf2/(82.06*298.15);%mol/s

Tm=[700 750 800 850 900 950 1000];% temperature
Rc2h6=[0.054 0.097 0.148 0.689 0.661 0.537 0.140];% *1e8 mol/s
Rc2h4=[0.021 0.090 0.192 0.668 0.973 1.290 1.442];
Krct1(1)=1.7000e+002;Krct2(1)=4.4000e+004;
Krct1(2)=4.6719e+002;Krct2(2)=9.2258e+004;
Krct1(3)=9.9400e+002;Krct2(3)=1.3000e+005;
Krct1(4)=6.1623e+003;Krct2(4)=1.6208e+005;
Krct1(5)=6.9581e+003;Krct2(5)=2.1155e+005;
Krct1(6)=7.4922e+003;Krct2(6)=2.9648e+005;
Krct1(7)=5.9969e+003;Krct2(7)=9.2623e+005;

for KK=1:7
    Temt=Tm(KK)+273;
    Rt1=Rc2h6(KK);Rt2=Rc2h4(KK);

% Diffusivity and Kinetic parameter
```

```
Dp=0.122*exp(-7851/Temt);
Dh=49.402*exp(-12588.7/Temt);
Dv=24.24*exp(-23467/Temt); %cm2/s
Ke1=3.24e-8*exp(1371.3/Temt); %
if Temt<1073
Ke2=2.087e-2*exp(1368.4/Temt);
else
Ke2=1.77e-10*exp(21911/Temt);
end
%Kr1=1.e4;Kr2=5.5e5;
%Krconst=fmins('ocmkr',[1.42e3 1e5])
%Kr1=Krconst(1);Kr2=Krconst(2);
%Kr1=Krct1(KK);Kr2=Krct2(KK);
%if Temt<1123
%       Kr1=4.911e13*exp(-25840/Temt);
%else
%       Kr1=68128*exp(-2691.5/Temt);
%end
%Kr2=2.9246e8*exp(-8398.9/Temt);

Kr1=4.46e5*exp(-5929/Temt);
Kr2=3.246e8*exp(-8619/Temt);

% integration of the model equations
Tol=1e-12;
z0=0;zf=Lr;
Y0=[0 0 1e-20];
[zout,yout]=ode45('ocmfun',z0,zf,Y0,Tol);
nn=max(size(zout));
%Cons=2*(yout(:,1)+yout(:,2))/(Ns0*YCH4);
%Rat=yout(:,2)./yout(:,1);
Conv(KK)=2*(yout(nn,1)+yout(nn,2))/(Ns0*YCH4)*100;
Rato(KK)=yout(nn,2)/yout(nn,1);
Rate1(KK)=yout(nn,1)*1e6/Am*60;% *1e6 mol/cm2.min
Rate2(KK)=yout(nn,2)*1e6/Am*60;
Results=[Rc2h6(KK) Rate1(KK);Rc2h4(KK) Rate2(KK)]

end
React1=Rate1'
React2=Rate2'
plot(Tm,Rate1,'b-',Tm,Rc2h6,'bo',Tm,Rate2,'r-',Tm,Rc2h4,'r*')
```

OCM-ocmfun

```
function ydot=hffun(t,x)
```

```
global Pl Ps Temt Ns0 YCH4 Nl0 YO2 n Rin Rm Lme
global Ke1 Ke2 CYb Kr1 Kr2
global CCH4 CC2H6 PO2 PH2O

NC2H6=x(1);NC2H4=x(2);NH2O=x(3);

CCH4=Pl/(82.06*Temt)*(Ns0*YCH4-2*(NC2H6+NC2H4))/(Ns0-NC2H6-NC2H4);
CC2H6=Pl/(82.06*Temt)*NC2H6/(Ns0-NC2H6-NC2H4);
PO2=Ps*(Nl0*YO2-0.5*NH2O)/(Nl0+0.5*NH2O);
PH2O=Ps*NH2O/(Nl0+0.5*NH2O);
```

```
options(2)=1e-10;options(3)=1e-10;
Chs=fmin('ocmopt',0,CYb,options);

alfa=sqrt(Ke1*sqrt(PO2))+sqrt(Ke2*PH2O);
Cv2=(sqrt(alfa*alfa+8*CYb)-alfa)^2/16; %mol/cm3
Ch2=sqrt(Ke1*sqrt(PO2)*Cv2);
Cp2=sqrt((Ke2*PH2O)*Cv2);
Flux=Rin/Rm*2*(Kr1*CCH4*Chs+Kr2*CC2H6*Chs);

Tol=1e-12;
t0=0;tfinal=Lme;
y0=[Cv2 Cp2 Ch2];
[tout,yout]=ode45('ocmperm',t0,tfinal,y0,Tol);
nn=max(size(tout));
Ch1=yout(nn,3);
Ag=[Chs Ch1];

ydot(1)=2*n*pi*Rin*(Kr1*CCH4*Ch1-Kr2*CC2H6*Ch1);
ydot(2)=2*n*pi*Rin*Kr2*CC2H6*Ch1;
ydot(3)=2*n*pi*Rm*Flux/2;
```

OCM-ocmopt

```
function Er=ocmkr(Kr)
% find the reaction constants
global Pl Ps Temt Ns0 YCH4 Nl0 YO2 n Rm Lme Am Lr Rt1 Rt2
global Ke1 Ke2 CYb Kr1 Kr2
global Dv Dp Dh Flux

Kr1=Kr(1);Kr2=Kr(2);

% integration of the model equations
Tol=1e-12;
z0=0;zf=Lr;
```

```
Y0=[0 0 1e-20];
[zout,yout]=ode45('ocmfun',z0,zf,Y0,Tol);
nn=max(size(zout));
Rate1=yout(nn,1)*1e8;
Rate2=yout(nn,2)*1e8;

Er=sqrt((Rate1-Rt1)^2+(Rate2-Rt2)^2);
gms=[Kr Er]
Results=[Rt1 Rate1;Rt2 Rate2]
```

OCM-ocmperm

```
function ydot=dlxfun(t,x)
global Dv Dp Dh Flux

cv=x(1);cp=x(2);ch=x(3);
sigm=4*Dv*cv+Dp*cp+Dh*ch;
tv=4*Dv*cv/sigm;tp=Dp*cp/sigm;th=Dh*ch/sigm;
A(1,1:3)=[1-tv -2*tp*cv/cp -2*th*cv/ch];
A(2,1:3)=[-0.5*tv*cp/cv 1-tp -th*cp/ch];
A(3,1:3)=[2 1 1];
B=[0 Flux/Dp 0]';
```

OCM-main-2

```
clear
% Hollow fiber membrane reactor for OCM-cocurrent flow pattern-effect of feed flow
rate
global Pl Ps Temt Ns0 YCH4 Nl0 YO2 n Rin Rm Lme Am Lr Rt1 Rt2
global Ke1 Ke2 CYb Kr1 Kr2
global Dv Dp Dh Flux

% Basic parameters
Temt=950+273; %K
Pl=1;%lumen pressure, atm
Ps=1;%shell pressure, atm
n=1; %number of hollow fibres
Ro=0.145/2;%outer radius of fibre, cm
Rin=0.065/2;%inner radius of fibre, cm
CYb=1.06e-3;%mol/cm3
Lr=4;%Lenth of reactor, cm
Vf1=3.94/60;%flow rate of hydrocarbon feed, cm3/s
YCH4=0.0922;%molar fraction of methane in hydrocarbon feed
Vf2=40/60;%flow rate of air feed, cm3/s
YO2=0.21;%molar fraction of oxygen in air feed

Rm=(Ro-Rin)/log(Ro/Rin);% Average radius of hollow fibre, cm
```

```
Lme=Ro-Rin;% membrane thickness
Am=2*n*pi*Lr*Lme/log(Ro/(Ro-Lme));
Nl0=Vf2/(82.06*298.15);%mol/s

Temt=950+273;Kr1=3.57e+003;Kr2=2.92e+005;
Feed=[2.143 3.940 6.445 12.000];% feed flow rate, ml/min
Rc2h4=[0.617 0.558 0.491 0.523];% *1e6 mol/cm2.min
Rc2h6=[0.257 0.410 0.285 0.345];% *1e6 mol/cm2.min

% Diffusivity and Kinetic parameter
Dp=0.122*exp(-7851/Temt);
Dh=49.402*exp(-12588.7/Temt);
Dv=24.24*exp(-23467/Temt); %cm2/s
Ke1=3.24e-8*exp(1371.3/Temt); %
if Temt<1073
Ke2=2.087e-2*exp(1368.4/Temt);
else
Ke2=1.77e-10*exp(21911/Temt);
end
%Kr1=1.e4;Kr2=5.5e5;
%Krconst=fmins('ocmkr',[1.42e3 1e5])
%Kr1=Krconst(1);Kr2=Krconst(2);
%Kr1=Krct1(KK);Kr2=Krct2(KK);
%if Temt<1123
%       Kr1=4.911e13*exp(-25840/Temt);
%else
%       Kr1=68128*exp(-2691.5/Temt);
%end
%Kr2=2.9246e8*exp(-8398.9/Temt);

for KK=1:4
    Vf1=Feed(KK)/60;
Ns0=Vf1/(82.06*298.15);%mol/s

% integration of the model equations
Tol=1e-12;
z0=0;zf=Lr;
Y0=[0 0 1e-20];
[zout,yout]=ode45('ocmfun',z0,zf,Y0,Tol);
nn=max(size(zout));
%Cons=2*(yout(:,1)+yout(:,2))/(Ns0*YCH4);
%Rat=yout(:,2)./yout(:,1);
Conv(KK)=2*(yout(nn,1)+yout(nn,2))/(Ns0*YCH4)*100;
Rato(KK)=yout(nn,2)/yout(nn,1);
Rate1(KK)=yout(nn,1)*1e6/Am*60;% *1e6 mol/cm2.min
```

```
Rate2(KK)=yout(nn,2)*1e6/Am*60;
Results=[Rc2h6(KK) Rate1(KK);Rc2h4(KK) Rate2(KK)]

end
React1=Rate1'
React2=Rate2'
plot(Feed,Rate1,'b-',Feed,Rc2h6,'bo',Feed,Rate2,'r-',Feed,Rc2h4,'r*')
```

Appendix B-Computer program for air separation simulation

Airsept-main-1

```
clear
% Operating mode: shell feed, cocurrent operation
% Argon feed flow rate is changed while air feed flow rate is kept constant
global Ts m Ro Rin Lr FAir FAr XX Conx Cony

% Basic parameters
Ts=800; % oC
m=6;%number of hollow fibres
Ro=0.1562/2;%outer radius of fibre, cm
Rin=0.1125/2;%inner radius of fibre, cm
Lr=15;%Lenth of module, cm

Ts=980;FAir=35.69/60/22400;%flow rate of air feed, mol/s
XX=[16.37 19.58 26.00 32.41 48.44 80.51];%Exptl Argon flowrate, ml/min
Conx=[18.0 17.8 17.5 17.3 16.8 16.3];%Exptl oxygen concentration in air stream, %
Cony=[8.40 7.40 6.10 5.20 4.00 2.70];%Exptl oxygen concentration in argon stream,
%

Permflow=Conx./(100-Cony).*XX/60/22400;

for KK=1:6
      FAr=XX(KK)/60/22400;
% integration of the model equations
Tol=1e-12;
z0=0;zf=Lr;
Y0=[0.21 0];
[zout,yout]=ode45('mod1fun',z0,zf,Y0,Tol);
nn=max(size(zout));
Calx(KK)=yout(nn,1)*100;
Caly(KK)=yout(nn,2)*100;
Prc(KK)=Caly(KK)/(100-Caly(KK))*FAr;%mol/s
end

plot(XX,Cony,'ro',XX,Caly,'b-')
```

Airsept-mod1fun

```
function ydot=m1fun(t,x)
% In the case of a negligible pressure drop in the fibre lumen
global Ts m Ro Rin FAir FAr

X=x(1);Y=x(2);
```

```
T=-(0.0086*Ts+2.5621)*t^2+(0.1203*Ts+43.46)*t+(0.5854*Ts-205.59)+273;
Dv=1.58e-2*exp(-8852.5/T);
Kf=5.9e6*exp(-27291/T);
Kr=2.07e4*exp(-29023/T);

Resum=Kf*log(Ro/Rin)*(X*Y)^0.5/Dv+X^0.5/(2*Rin)+Y^0.5/(2*Ro);

ydot(1)=-pi*m* (1-X)^2/(0.79*FAir)*Kr*(X^0.5-Y^0.5)/Resum;
ydot(2)=pi*m* (1-Y)^2/FAr*Kr*(X^0.5-Y^0.5)/Resum;
```

Airsept-main-2

```
clear
% Operating mode: shell feed, cocurrent operation,
% Argon feed flow rate is kept constant while air feed flow rate is changed
global Ts m Ro Rin Lr FAir FAr Flow Conx Cony

% Basic parameters
Ts=800; % oC
m=6;%number of hollow fibres
Ro=0.1562/2;%outer radius of fibre, cm
Rin=0.1125/2;%inner radius of fibre, cm
Lr=15;%Lenth of module, cm

Ts=980; FAr=80.51/60/22400;%flow rate of air feed, mol/s
Flow=[12.49 17.13 24.09 35.69 58.89 89.05];%Exptl Air flowrate, ml/min
Conx=[10.4 12.4 14.3 16.3 18.1 19.2];%Exptl oxygen concentration in air stream, %
Cony=[1.90 2.20 2.40 2.70 2.80 2.90];%Exptl oxygen concentration in argon stream,
%

Permflow=(21-Conx)./(100-Conx).*Flow/60/22400;

for KK=1:6
    FAir=Flow(KK)/60/22400;
% integration of the model equations
Tol=1e-12;
z0=0;zf=Lr;
Y0=[0.21 0];
[zout,yout]=ode45('mod1fun',z0,zf,Y0,Tol);
nn=max(size(zout));
Calx(KK)=yout(nn,1)*100;
Caly(KK)=yout(nn,2)*100;
%Prc(KK)=Caly(KK)/(100-Caly(KK))*FAr;%mol/s
Prc(KK)=(21-Calx(KK))/(100-Calx(KK))*FAir;%mol/s
end
```

```
plot(Flow,Conx,'ro',Flow,Calx,'b-')
%plot(Flow,Cony,'ro',Flow,Caly,'b-')
```

Airsept-main-3

```
clear
% Operating mode 2: lumen feed, cocurrent flow
% Argon feed flow rate is changed while air feed flow rate is kept constant
global Ts m Ro Rin Lr FAir FAr XX Conx Cony

% Basic parameters
Ts=800; % oC
m=6;%number of hollow fibres
Ro=0.1562/2;%outer radius of fibre, cm
Rin=0.1125/2;%inner radius of fibre, cm
Lr=15;%Lenth of module, cm

Ts=980; FAir=35.69/60/22400;%flow rate of air feed, mol/s
XX=[16.37 19.58 26.00 32.41 48.44 64.48];%Exptl Argon flowrate, ml/min
Conx=[18.8 18.6 18.4 18.3 18.1 17.9];%Exptl oxygen concentration in air stream, %
Cony=[6.80 6.10 4.90 4.10 3.00 2.3];%Exptl oxygen concentration in argon stream, %

Permflow=Cony./(100-Cony).*XX/60/22400;

for KK=1:6
      FAr=XX(KK)/60/22400;
% integration of the model equations
Tol=1e-12;
z0=0;zf=Lr;
Y0=[0 0.21];
[zout,yout]=ode45('mod3fun',z0,zf,Y0,Tol);
nn=max(size(zout));
Calx(KK)=yout(nn,1)*100;
Caly(KK)=yout(nn,2)*100;
Prc(KK)=Calx(KK)/(100-Calx(KK))*FAr;%mol/s
end

plot(XX,Cony,'ro',XX,Caly,'b-')
```

Airsept-mod3fun

```
function ydot=m3fun(t,x)
% In the case of a negligible pressure drop in the fibre lumen
global Ts m Ro Rin FAir FAr
```

```
X=x(1);Y=x(2);
T=-(0.0086*Ts+2.5621)*t^2+(0.1201*Ts+43.46)*t+(0.5854*Ts-205.59)+273;
Dv=1.58e-2*exp(-8852.5/T);
Kf=5.9e6*exp(-27291/T);
Kr=2.07e4*exp(-29023/T);

Resum=Kf*log(Ro/Rin)*(X*Y)^0.5/Dv+X^0.5/(2*Rin)+Y^0.5/(2*Ro);

ydot(1)=-pi*m* (1-X)^2/FAr*Kr*(X^0.5-Y^0.5)/Resum;
ydot(2)=pi*m* (1-Y)^2/(0.79*FAir)*Kr*(X^0.5-Y^0.5)/Resum;
```

Airsept-main-4

```
clear
% Operating mode: shell feed, countercurrent flow
% Air feed flow rate is kept constant, 24.09 ml/min
global Ts m Ro Rin Lr FAir FAr XX Conx Cony

% Basic parameters
Ts=800; % oC
m=6;%number of hollow fibres
Ro=0.1562/2;%outer radius of fibre, cm
Rin=0.1125/2;%inner radius of fibre, cm
Lr=15;%Lenth of module, cm

Ts=900;FAir=24.09/60/22400;%flow rate of air feed, mol/s
XX=[16.37 19.58 26.00 35.62 48.44 64.48];%Exptl Argon flowrate, ml/min
Cony=[4.90 4.20 3.50 2.70 2.10 1.60];%Exptl oxygen concentration, %

options(2)=1e-6;options(3)=1e-6;

for KK=1:6
      FAr=XX(KK)/60/22400;
% integration of the model equations
ye=fmin('mod4opt',0,1,options);

Tol=1e-12;
z0=0;zf=Lr;
Y0=[0.21 ye];
[zout,yout]=ode45('mod4fun',z0,zf,Y0,Tol);
nn=max(size(zout));
gf=[ye yout(nn,2)]
Calx(KK)=yout(nn,1)*100;
Caly(KK)=ye*100;
Prc(KK)=Caly(KK)/(100-Caly(KK))*FAr;%mol/s
```

```
end

plot(XX,Cony,'ro',XX,Caly,'b-')
```

Airsept-mod4opt

```
function Er=m4opt(Yout)
% Operating mode: shell feed, countercurrent operation
global Ts m Ro Rin Lr FAir FAr XX Conx Cony
ye=Yout;

% integration of the model equations
Tol=1e-12;
z0=0;zf=Lr;
Y0=[0.21 ye];
[zout,yout]=ode45('mod4fun',z0,zf,Y0,Tol);
nn=max(size(zout));
yin=yout(nn,2);

Er=abs(yin);
gs=[ye yin Er];
```

Airsept-mod4fun

```
function ydot=m4fun(t,x)
% In the case of a negligible pressure drop in the fibre lumen
global Ts m Ro Rin FAir FAr

X=x(1);Y=x(2);
T=-(0.0086*Ts+2.5621)*t^2+(0.1203*Ts+43.46)*t+(0.5854*Ts-205.59)+273;
Dv=1.58e-2*exp(-73600/8.314/T);
Kf=5.9e6*exp(-226900/8.314/T);
Kr=2.07e4*exp(-241300/8.314/T);

Resum=Kf*log(Ro/Rin)*(X*Y)^0.5/Dv+X^0.5/(2*Rin)+Y^0.5/(2*Ro);

ydot(1)=-pi*m *(1-X)^2/(0.79*FAir)*Kr*(X^0.5-Y^0.5)/Resum;
ydot(2)=-pi*m*fr*1-Y)^2/FAr*Kr*(X^0.5-Y^0.5)/Resum;
```

Airsept-main-5

```
clear
% Operating mode: shell feed, cocurrent flow, vacuum operation
```

```
% Air feed flow rate is kept constant, 24.09 ml/min
global Ts m Ro Rin Lr FAir Pa Pv Vis

% Basic parameters
Ts=800; % oC
m=6;%number of hollow fibres
Ro=0.1562/2;%outer radius of fibre, cm
Rin=0.1125/2;%inner radius of fibre, cm
Lr=15;%Lenth of module, cm
Vis=2.42e-5;%viscosity of oxygen, Pa.s
Pa=1;

Ts=980;fr=0.5567;FAir=24.09/60/22400;%flow rate of air feed, mol/s
Pvac=[61.33 41.33 21.33 11.33 5.33];%Exptl Argon flowrate, kPa
Pfr=[0.102 0.296 0.434 0.624 0.952]/60/22400*1e6;%Exptl oxygen permeation flow
rate, mol/min

for KK=1:5
      Pv=Pvac(KK)/101.3;
% integration of the model equations
Pin=fmin('mod5opt',1,1.1,options);

Tol=1e-12;
z0=0;zf=Lr;T0=0.5854*Ts-205.59+273;
Y0=[0.21 Pin T0 0];
[zout,yout]=ode45('mod5fun',z0,zf,Y0,Tol);
nn=max(size(zout));
gf=[Pv Pin yout(nn,2)]
Xe=yout(nn,1);
Prc(KK)=Pv*yout(nn,4)/(82.06*yout(nn,3))*1e6;%mol/s
end

plot(Pvac,Pfr,'ro',Pvac,Prc,'b-')
```

Airsept-mod5opt

```
function Er=m5opt(Pclose)
global Ts Lr

Pin=Pclose;

% integration of the model equations
Tol=1e-12;
z0=0;zf=Lr;T0=0.5854*Ts-205.59+273;
Y0=[0.21 Pin T0 0];
```

```
[zout,yout]=ode45('mod5fun',z0,zf,Y0,Tol);
nn=max(size(zout));
end

Er=abs(yout(nn,2)-1);
gs=[Pin yout(nn,2) Er];
```

Airsept-mod5fun

```
function ydot=m5fun(t,x)
global Ts m Ro Rin Lr FAir Pa Pv Vis

X=x(1);Y=x(2);T=x(3);Vl=x(4);
Dv=1.58e-2*exp(-8852.5/T);
Kf=5.9e6*exp(-27291/T);
Kr=2.07e4*exp(-29023/T);

Resum=Kf*log(Ro/Rin)*sqrt(Pa*Pv)*(X*Y)^0.5/Dv+(Pa*X)^0.5/(2*Rin)+(Pv*Y)^0.
5/(2*Ro);

ydot(1)=-pi*m* (1-X)^2/(0.79*FAir)*Kr*((Pa*X)^0.5-(Pv*Y)^0.5)/Resum;
ydot(2)=-8*Vis*Vl/(m*pi*Rin^4*Pv*1.013e5);
ydot(3)=-2*(0.0086*Ts+2.5621)*t+(0.1201*Ts+43.46);
ydot(4)=T/Y*(82.06*m*fr/Pv*Kr*((Pa*X)^0.5-(Pv*Y)^0.5)/Resum-Vl/T*ydot(2)+Y*
Vl/T^2*ydot(3));
```

GRL. LOND. IN. UNIV